



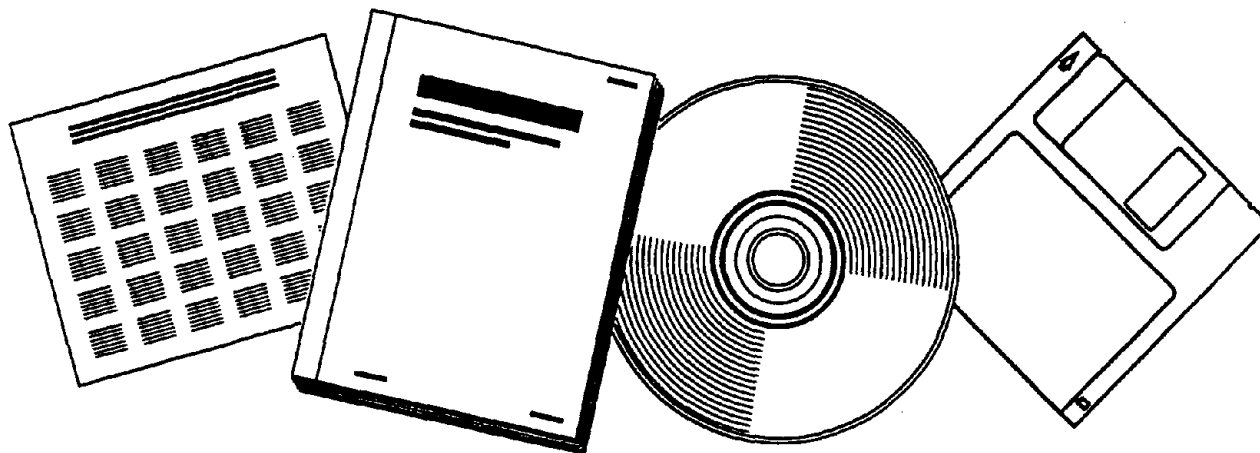
PB97-186803

NTIS[®]
Information is our business.

EXPERIMENTAL AND ANALYTICAL STUDIES OF STEEL CONNECTIONS AND ENERGY DISSIPATORS

CALIFORNIA UNIV., RICHMOND

DEC 95



U.S. DEPARTMENT OF COMMERCE
National Technical Information Service



PB97-186803

REPORT NO.
UCB/EERC-95/13
DECEMBER 1995


EARTHQUAKE ENGINEERING RESEARCH CENTER

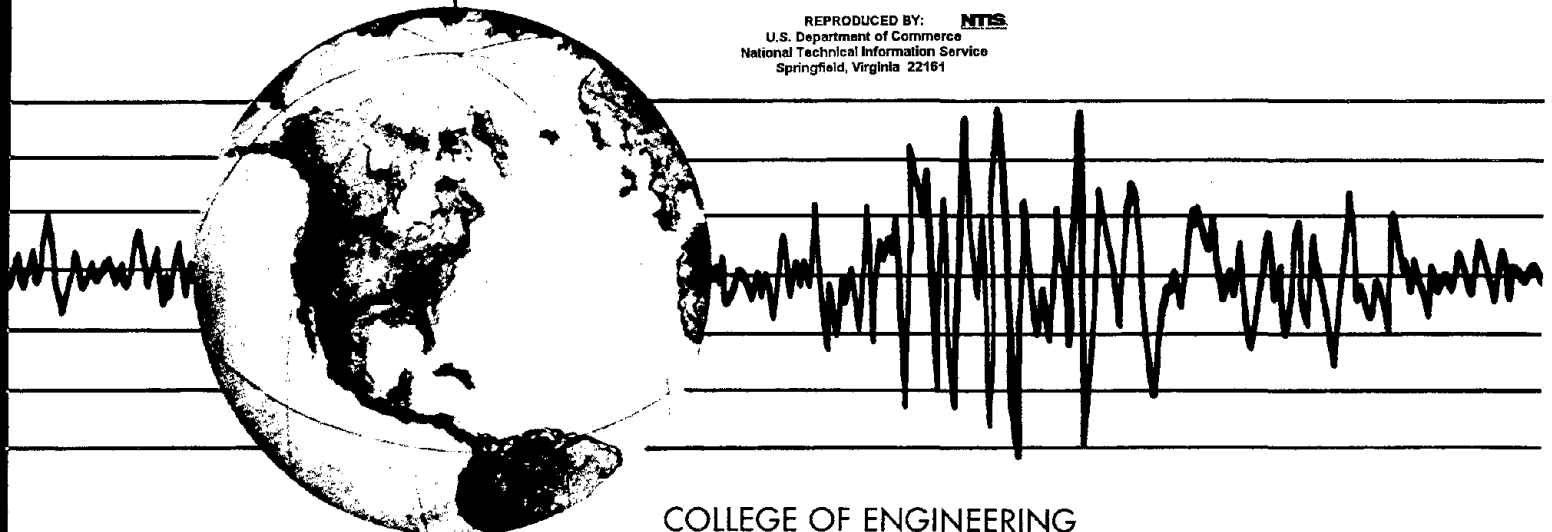
EXPERIMENTAL AND ANALYTICAL STUDIES OF STEEL CONNECTIONS AND ENERGY DISSIPATORS

by

TZONG-SHUOH YANG
EGOR P. POPOV

A report to: National Science Foundation
American Institute of Steel Construction

REPRODUCED BY: 
U.S. Department of Commerce
National Technical Information Service
Springfield, Virginia 22161



COLLEGE OF ENGINEERING
UNIVERSITY OF CALIFORNIA AT BERKELEY

For sale by the National Technical Information Service, U.S. Department of Commerce, Springfield, Virginia 22161

See back of report for up to date listing of EERC reports.

DISCLAIMER

Any opinions, findings, and conclusions or recommendations expressed in this publication are those of the authors and do not necessarily reflect the views of the Sponsors or the Earthquake Engineering Research Center, University of California at Berkeley.

Experimental and Analytical Studies of Steel Connections and Energy Dissipators

by

Tzong-Shuoh Yang
and
Egor P. Popov

Report to Sponsors:
National Science Foundation
American Institute of Steel Construction

Report No. UCB/EERC-95/13
Earthquake Engineering Research Center
College of Engineering
University of California at Berkeley

December, 1995



REPORT DOCUMENTATION PAGE

Form Approved
OMB No. 0704-0188

Public reporting burden for this collection of information is estimated to average 1 hour per response, including the time for reviewing instructions, searching existing data sources, gathering and maintaining the data needed, and completing and reviewing the collection of information. Send comments regarding this burden estimate or any other aspect of this collection of information, including suggestions for reducing this burden, to Washington Headquarters Services, Directorate for Information Operations and Reports, 1215 Jefferson Avenue, Washington, DC 20540, and to the Office of Management and Budget, Paperwork Reduction Project (0704-0188), Washington, DC 20503.

PB97-186803



2. REPORT DATE December 1995		3. REPORT TYPE AND DATES COVERED Final	
4. TITLE AND SUBTITLE Experimental and Analytical Studies of Steel Connections and Energy Dissipators		5. FUNDING NUMBERS NSF/BCS-9016781 NSF/BCS-9222110 NSF/CMS-9416457	
6. AUTHOR(S) Tzong-Shuoh Yang, Egor P. Popov			
7. PERFORMING ORGANIZATION NAME(S) AND ADDRESS(ES) Earthquake Engineering Research Center University of California, Berkeley 1301 S. 46th Street Richmond, California 94804		8. PERFORMING ORGANIZATION REPORT NUMBER UCB/EERC-95/13	
9. SPONSORING/MONITORING AGENCY NAME(S) AND ADDRESS(ES) National Science Foundation 1800 G Street, N.W. Washington, D.C. 20550		10. SPONSORING/MONITORING AGENCY REPORT NUMBER American Inst. of Steel Construction 1 East Wacker Dr., Ste 3100 Chicago, IL 60601-2001	
11. SUPPLEMENTARY NOTES			
12a. DISTRIBUTION / AVAILABILITY STATEMENT		12b. DISTRIBUTION CODE	
13. ABSTRACT (Maximum 200 words) <p>After a brief overview of the building seismic design, nonlinear structural response spectra for strength, ductility, energy and number of yield reversals as a function of building period and structure strength for several strong motion earthquakes are presented. These results are compared with conventionally evaluated elastic response spectra and code criteria.</p> <p>The basic reasons for the fractures that occurred in steel moment-resisting connections during the 1994 Northridge earthquake are examined. The possible modes of failure are examined, showing the very limited view in the code design. Three SAC pre-Northridge specimen tests subjected to cyclic loading are critically examined.</p> <p>Next, the beam strength is reduced by drilling holes in flanges to protect the steel connection. Experiments on eight W12x26 beams with different perforation patterns are reported. Two large size connections with perforated beam flanges are tested.</p> <p>The design method of braced frames with Slotted Bolted Connections (SBCs) are reported. The Rotational Slotted Bolted Connection (RSBC), a new variety of SBC which is in essence a rotational friction damper, is designed for use in steel moment-resisting connections. Two large size RSBC specimens are designed and tested. A simple analytical model can predict the behavior of the RSBC with reasonable accuracy.</p>			
14. SUBJECT TERMS		15. NUMBER OF PAGES 192	
		16. PRICE CODE	
17. SECURITY CLASSIFICATION OF REPORT Unclassified	18. SECURITY CLASSIFICATION OF THIS PAGE Unclassified	19. SECURITY CLASSIFICATION OF ABSTRACT Unclassified	20. LIMITATION OF ABSTRACT

Abstract

After a brief overview of the building seismic design, nonlinear structural response spectra for strength, ductility, energy and number of yield reversals as a function of building period and structure strength for several strong motion earthquakes are presented. These results are compared with conventionally evaluated elastic response spectra and code criteria.

The basic reasons for the fractures that occurred in steel moment-resisting connections during the 1994 Northridge earthquake are examined from a fundamental point of view. The possible modes of failure are examined, showing the very limited view in the code design. The unfused material between a column face and a backing bar forms an “artificial” edge crack. The methods of nonlinear finite element analysis combined with fracture mechanics were brought to bear. Three SAC pre-Northridge specimen tests subjected to cyclic loading are critically examined. Good comparisons are found using the above theory.

Next, the beam strength is reduced by drilling holes in flanges to protect the steel connection. Experiments on eight W12×26 beams with different perforation patterns are reported. The results show that a well-designed perforated beam can have its moment capacity reduced and its ductility increased. Two large size connections with perforated beam flanges are tested. Test results show that the ductility of both specimens is enhanced without severe strength degradation.

The design methods of braced frames with Slotted Bolted Connections (SBCs) are reported. The advantages of using such frictional connections are demonstrated by comparing seismic structural responses. Finally, the Rotational Slotted Bolted Connection (RSBC), a new variety of SBC which is in essence a rotational friction damper, is designed for use in steel moment-resisting connections. Two large size RSBC specimens are designed and tested. A simple analytical model can predict the

behavior of the RSBC with reasonable accuracy. Test results show that the energy dissipation capacity of RSBC is outstanding. This non-destructive connection shows no degradation in hysteresis loops or damage in material after a severe test, making it durable enough to withstand several strong earthquake events without retrofit.

Acknowledgements

Special thanks are due to Drs. S.-C. Liu and M. P. Singh of NSF for encouraging this study and providing the necessary funds, under grants BCS-9016781 and BCS-9222110, for carrying out the work. Part of this report was completed with the support of the National Science Foundation under the grant (CMS-9416457) entitled “Re-evaluation of Conventional Seismic Beam-to-Column Flange Steel Connections”. Professors Egor P. Popov and Stephen A. Mahin were the co-PIs.

The authors also sincerely thank Nestor Iwankiw of AISC for providing supplementary funds and arranging for delivery at no cost of several tons of steel to proceed with the experimental phase of the project.

Special thanks are offered to Professors Stephen Mahin and John Strain for serving as the dissertation committee for the first author.

Gratis fabrication of very large specimens for validating some of the analyses, made by PDM Strockal, Inc. with Fred Long in charge, and by the Herrick Corporation with Vice-President Roger Ferch, were essential for the success of the project.

The authors wish to express their gratitude to postdoctoral researcher Chao-Tung Chang for contributing much time and effort to the progress of this project. The help of Brent Blackman, Hana Mori, Dr. Lev Stepanov, and Dr. Bozidar Stojadinovic are much appreciated. Thanks are due to Professor Motoo Saisho of Kumamoto University, Japan, for his contribution in the analysis of the test setup.

Thanks to advisors A. L. Collin, L. A. Napper, and F. R. Preece for their careful review of many design drawings. Dr. Carl Grigorian is also thanked for his review of the rotational slotted bolted connections.

The authors appreciate Civil Engineering staff Dr. Marcial Blondet, Todd Mersport, Chris Moy, Jon Asselanis and Bill MacCracken for their help in instrumentation, video recording and data acquisition. Machine shop staff Doug Zulaica, Dick Par-

sons, Jeff Higginbotham, Mark Troxler and Larry Baker are also thanked for their assistance. The authors are grateful to Carol Cameron for editing the report.

The kindness of Professor Albert P. Pisano of the Mechanical Engineering Department deserves special mention, as he provided access to his powerful computer facilities for the extensive analyses presented in this report.

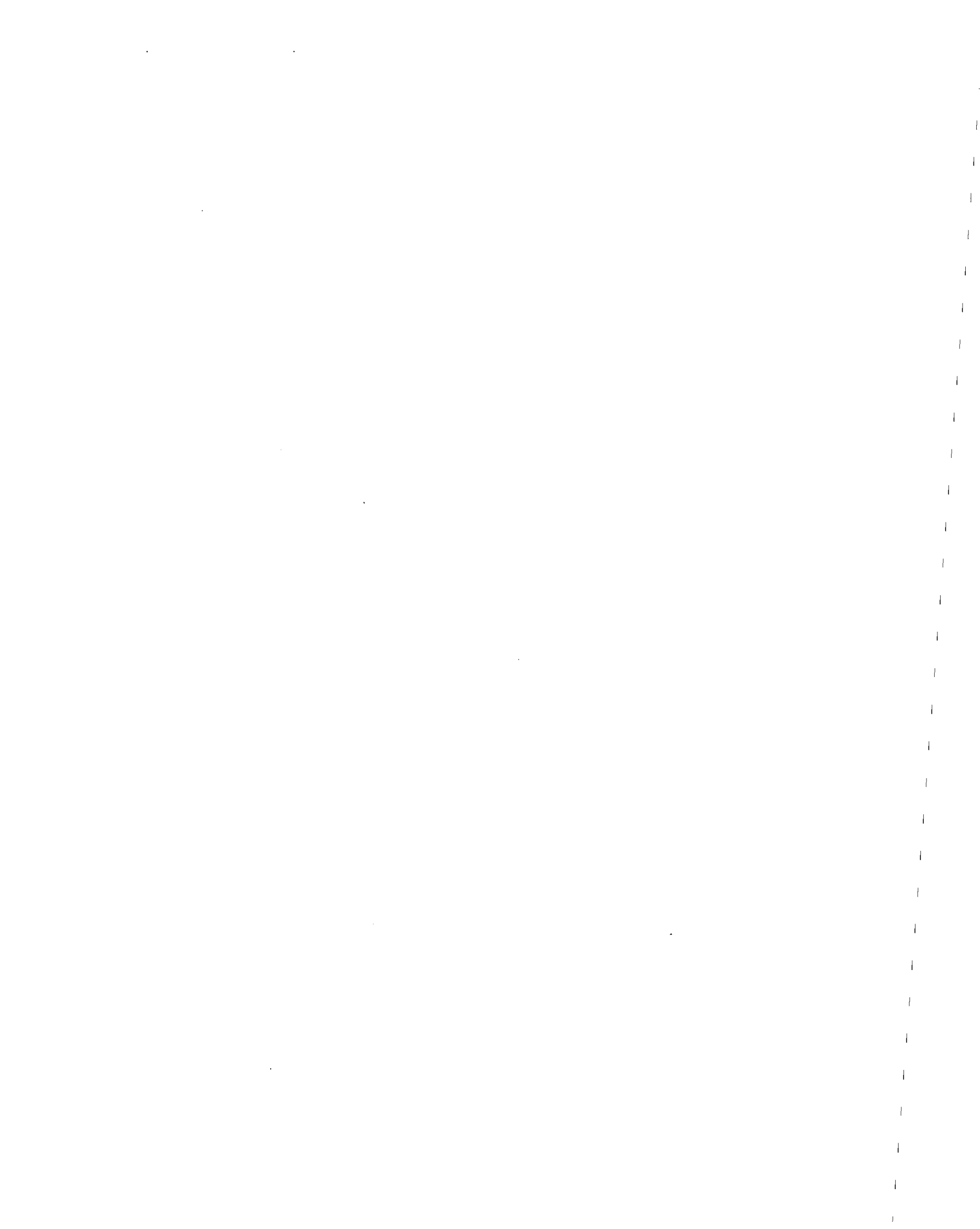
The availability of data from the SAC experiments was necessary for some formulations. In this regard, the cooperation of Stephen A. Mahin of SAC and UCB as well as of James O. Malley of SAC and Degenkolb Engineers is also greatly appreciated.

Thanks are also due to Ian Searle for his development of the RjaB computer program, and for providing help in a Macintosh port. This free software made the data reduction an enjoyable task. Thanks to Maurice LeBrun and Geoffrey Furnish for doing such a nice job with PLPLOT plotting library, with which many xy and xyz graphs in this report were generated.

Finally, the first author is deeply grateful to his wife, Wen-Jing Chang, who has been a source of steady support and encouragement.

Special Remarks

All of the designs and findings in this report are placed in the public domain. No organization or person may use the materials or similar designs presented in this report to apply for patents in the U.S. or in the world.



Contents

Abstract	i
Acknowledgements	iii
Special Remarks	v
1 Introduction	1
1.1 Seismic Structural Design	1
1.2 Nonlinear Seismic Spectra	3
1.3 Seismic Energy Demand	8
1.4 Conclusion	13
2 Behavior of Pre-Northridge Steel Moment-Resisting Connections	15
2.1 Introduction	15
2.2 Material Properties of Structural Steel	16
2.3 Design Strategy	21
2.4 Simplified Stress Analysis	23
2.5 Three SAC Pre-Northridge Specimen Tests	27
2.6 Stress Concentration Caused by the Backing Bar	37
2.7 Nonlinear Finite Element Analysis	41
2.8 Conclusion	58
3 Steel Joint Protection by Beam Flange Perforation	63
3.1 Introduction	63
3.2 The Dog-Bone Connections	65
3.3 Beam Flange Perforation	66
3.4 Design of Perforated Connection	68
3.5 Specimens and Test Setup Designs	71
3.6 Test Results of Eight Perforated Beams	74
3.7 Cyclic Test of Large Size Specimens	80
3.8 Conclusions	90

4	Design of Frames with Slotted Bolted Connection	93
4.1	Introduction	93
4.2	The Slotted Bolted Connection	94
4.3	Analytical Model of SBC	96
4.4	Design Methods	100
4.4.1	Design by Special Spectra	101
4.4.2	Design by Energy Balance	102
4.4.3	Design by Force Reduction	104
4.4.4	Design Methods for MDOF system	104
4.5	Temperature Rise of SBC	108
4.6	Design Examples	109
4.6.1	Single-story Shear Building with SBC	109
4.6.2	Multi-story Shear Building with SBCs	118
4.7	Conclusions and Remarks	124
5	Rotational Slotted Bolted Connection (RSBC)	129
5.1	Introduction	129
5.2	The Constitutive Model for RSBC	130
5.3	Specimen Design and Testing	134
5.4	Structural Test Results	147
5.5	Alternative RSBCs	156
5.6	Seismic Structural Design with RSBC	157
5.7	Conclusions and Remarks	158
	Epilogue	161
	A Nonlinear Dynamic Response Analysis	169
	B Seismic Response Spectra	173
B.1	Displacement Spectra Diagrams	174
B.2	Displacement Ductility Diagrams	176
B.3	Number of Yield Reversals Diagrams	178
B.4	Seismic Input Energy Mesh Diagrams	180
B.5	Hysteresis Energy Mesh Diagrams	182

List of Figures

1.1	Four types of structure and their primary lateral deformed shapes. Dots shown in (a) and (d) are the possible energy dissipation locations.	2
1.2	(a) A single-story moment-resisting frame, (b) the corresponding single degree-of-freedom model, and (c) The elastic-perfectly plastic constitutive law of the system.	4
1.3	Seismic force spectra for the UBC allowable stress design C_w (solid curve), for first yield design C_s ($\Omega = 1$), and for overstrength design of $\Omega = 2$ and 3.	7
1.4	Displacement ductility diagram for the 1994 Northridge earthquake at Sylmar Hospital.	8
1.5	Displacement ductility (left column) and Number of yield reversals (right column) diagrams for the UBC force response spectra for 1940 El Centro, 1989 Loma Prieta, and 1994 Northridge earthquakes.	9
1.6	Seismic input energy spectrum for the 1994 Northridge earthquake at Sylmar Hospital: (a) 3D mesh, (b) contours.	11
1.7	Seismic hysteresis energy spectrum for the 1994 Northridge earthquake at Sylmar Hospital: (a) 3D mesh, (b) contours.	12
2.1	A typical welded beam-to-column connection.	17
2.2	Some failure modes of the welded beam-to-column connection.	17
2.3	Simple tensile test of steel specimens with the same critical cross section area: (a) cylindrical bar, and (b) grooved cylindrical bar.	18
2.4	Stress-strain curves of a series of tensile tests for A36 steel.	19
2.5	Two alternative plastic hinge mechanisms for a typical MRF: (a) Type 3 mechanism and (b) Type 4 mechanism.	22
2.6	Critical points in the connection - point A on beam flange, point B on beam-weldment junction, and C at column flange.	23
2.7	Stress concentration factors at juncture of beam-to-column connection calculated by elastic finite element analysis. The external load is uniformly distributed unit tensile stress σ_{zz} applied on the beam flange.	25

2.8	Detail of the SAC PN specimens.	28
2.9	Connection detail for SAC PN specimens.	29
2.10	Photograph showing specimen tested horizontally in laboratory. Left side of the beam is the <i>upper</i> side of the specimen.	29
2.11	Photograph showing the clevis connected to beam end-plate and hydraulic actuator.	30
2.12	Photograph showing the top of the column.	31
2.13	Photograph showing the bottom of the column.	31
2.14	Moment-rotation and moment ratio-plastic rotation diagrams for SAC PN1, PN2 and PN3 specimens.	34
2.15	Photograph of SAC specimen PN1 after test.	35
2.16	Fracture pattern of SAC specimen PN2 is similar to specimen PN1.	36
2.17	Photograph showing the fractured bottom beam flange of SAC PN3 specimen after test.	37
2.18	The unfused backing bar surface forms an artificial edge crack.	38
2.19	The three modes of loading that can be applied to a crack: Mode-I (Opening), Mode-II (In-plane shear), and Mode-III (Out-of-plane shear).	39
2.20	A semi-infinite plate with (a) edge crack, (b) center crack subject to a remote axial stress σ	39
2.21	Finite element mesh for SAC Pre-Northridge PN connection. Only one half of the specimen is modeled.	42
2.22	(a) Imposed tip displacements used in testing SAC PN1 specimen, and (b) imposed tip displacements used in finite element analysis.	44
2.23	(a) Experimental and (b) analytical hysteresis loops of SAC PN1 specimen (Displacements are measured in the loading direction).	44
2.24	(a) Imposed tip displacements used in testing SAC PN3 specimen, and (b) imposed tip displacements used in finite element analysis. The dashed line represents the imposed displacements after the bottom beam flange was fractured.	45
2.25	(a) Experimental and (b) analytical hysteresis loops of SAC PN3 specimen (Displacements are measured in the loading direction). The dashed curve represents the response after the fracture of the bottom beam flange.	45
2.26	(a) Experimental and (b) analytical total strain energy diagrams of SAC PN1 and PN2 specimens.	46
2.27	(a) Experimental and (b) analytical total strain energy diagrams of SAC PN3 specimen.	46

2.28	(a) Imposed displacements and (b) hysteresis loops of SAC PN2 specimen (Displacements are measured in the loading direction). The dashed curves represent the response after the fracture of the bottom beam-column juncture.	47
2.29	Von Mises Stress contours for SAC PN1/PN2 under 225 kips tip load.	48
2.30	Web and panel zone stress contours for SAC PN1/PN2 under 225 kips tip load.	49
2.31	Top beam flange and continuity plate contours for SAC PN1/PN2 under 225 kips tip load.	50
2.32	Bottom beam flange and continuity plate contours for SAC PN1/PN2 under 225 kips tip load.	51
2.33	Stress distribution across the bottom beam flange at weld for SAC PN1 and PN2 specimens: (a) σ_{xx} , (b) σ_{yy} , (c) σ_{zz} , and (d) von Mises stress.	52
2.34	Center panel zone strains vs tip load for SAC PN1, PN2 and PN3 specimens.	53
2.35	Stress intensity factors plotted against temperatures obtained from 1.5-in.-thick plates of A572 steel.	55
2.36	Stress-intensity factors plotted across beam width and number of analysis steps at (a) top and (b) bottom backing bars for SAC PN1 and PN2 specimens.	56
2.37	Maximum stress-intensity factors vs. tip load at (a) top and (b) bottom backing bars for SAC PN1 and PN2 specimens.	57
2.38	Maximum stress-intensity factor vs. tip displacement at (a) top and (b) bottom backing bars for SAC PN1 and PN2 specimens.	59
3.1	The dog-bone connections designed by (a) Plumier, and (b) Chen & Yeh.	65
3.2	Simple tensile tests for coupons of different lengths.	66
3.3	Connection protection by beam flange perforation.	67
3.4	Projection of moment diagram on beam flange to help determining hole sizes and locations.	69
3.5	Hole patterns for Specimens A to H.	72
3.6	Test setup for beams with flange holes.	73
3.7	Photograph showing Specimen C after the test.	75
3.8	Photograph showing Specimen E after the test.	76
3.9	Photograph showing Specimen F after the test.	77
3.10	Photograph showing Specimen G after the test.	77
3.11	Photograph showing Specimen H after the test.	78
3.12	Typical stress-strain curve of a flange coupon test.	80

3.13	Load-deflection diagrams for Specimens A to H.	81
3.14	Load-plastic deflection diagrams for Specimens A to H.	82
3.15	Moment ratio-plastic rotation diagrams for Specimens A to H.	83
3.16	The cyclic test setup and overall dimensions.	84
3.17	Original hole pattern of Specimen 3.	85
3.18	Original hole pattern of Specimen 8.	85
3.19	Connection details of Specimen 3.	86
3.20	Connection details of Specimen 8.	87
3.21	Hysteresis loops for Specimen (a) 3 and (b) 8.	87
3.22	Plastic rotation against moment ratio for Specimen (a) 3 and (b) 8.	88
3.23	Photograph after test of white-washed Specimen 3.	89
3.24	Total energy diagrams for Specimen (a) 3 and (b) 8.	89
3.25	Cumulative ductility diagrams for Specimen (a) 3 and (b) 8.	90
4.1	(a) A Concentrically braced frame with SBCs, (b) the top view and side view of an SBC.	94
4.2	Typical detail of a Slotted Bolted Connection (SBC).	95
4.3	Hysteresis loops for a two-bolted SBC test specimen.	96
4.4	(a) A single-story concentrically braced frame with a friction damper, and (b) the corresponding single degree-of-freedom model.	97
4.5	Selection of friction force and slip distance.	98
4.6	Special displacement spectrum for the 1971 Pacoima earthquake. This spectra is constructed for 5% stiffness ratio and 2% damping ratio.	99
4.7	Special displacement spectrum for the 1971 Pacoima earthquake. Both the stiffness and damping ratios are 5%.	100
4.8	A 3-story shear building with SBC dampers.	105
4.9	A single-story concentrically braced warehouse frame.	110
4.10	The accelerogram of the 1971 Pacoima earthquake.	110
4.11	The Fourier amplitude spectrum of the 1971 Pacoima earthquake ground acceleration.	110
4.12	Displacement response, in <i>inches</i> , of the single story building with the SBC for the 1971 Pacoima earthquake.	112
4.13	Absolute energy history, in <i>kip-inches</i> , of the single story building with the SBC for the 1971 Pacoima earthquake.	112
4.14	Analytical hysteretic loops of the SBC for the 1971 Pacoima earthquake.	113
4.15	Experimental hysteretic loops of the SBC for the 1971 Pacoima earthquake. (Tested by C. E. Grigorian)	113
4.16	Displacement response, in <i>inches</i> , of the single story building <i>without</i> the SBC for the 1971 Pacoima earthquake.	114

4.17	Absolute energy history, in <i>kip-inches</i> , of the single story building <i>without</i> the SBC for the 1971 Pacoima earthquake.	114
4.18	Trajectory diagram, in <i>inches</i> and <i>inches/sec</i> , of the single story building <i>without</i> the SBC for the 1971 Pacoima earthquake.	115
4.19	Trajectory diagram, in <i>inches</i> and <i>inches/sec</i> , of the single story building <i>with</i> the SBC for the 1971 Pacoima earthquake.	115
4.20	Displacement Fourier amplitude spectrum of the single story building <i>without</i> the SBC for the 1971 Pacoima earthquake.	115
4.21	Displacement Fourier amplitude spectrum of the single story building <i>with</i> the SBC for the 1971 Pacoima earthquake.	115
4.22	Displacement response of the single story building for the 1989 Loma Prieta earthquake.	116
4.23	SBC slip history of the single story building for the 1989 Loma Prieta earthquake.	116
4.24	Displacement response of the single story building for the 1940 El Centro earthquake times two.	116
4.25	SBC slip history of the single story building for the 1940 El Centro earthquake times two.	116
4.26	(a) The required friction force f_1 , f_2 , and f_3 are applied as external loads to reduce the largest drift to allowable value. (b) The equivalent static loads calculated from the first mode shape. (c) The shear force distribution calculated from (b).	121
4.27	The first mode shape of the 3-story shear building.	122
4.28	The second mode shape of the 3-story shear building.	122
4.29	The third mode shape of the 3-story shear building.	123
4.30	The displacement and SBC slip history of the 3-story shear building for the 1971 Pacoima earthquake.	125
4.31	The displacement and SBC slip history of the 3-story shear building for the 1989 Loma Prieta earthquake.	126
4.32	The displacement and SBC slip history of the 3-story shear building for the 1940 El Centro earthquake times two.	127
5.1	RSBC for Moment Resisting Connections.	130
5.2	(a) An RSBC consists of two SBCs. (b) Two tees in an RSBC will be bent when the connection rotates.	131
5.3	Load-deflection curve for an RSBC.	133
5.4	Detail of a rotational friction damper: Specimen 7A (Sheet 1/3).	135
5.5	Detail of a rotational friction damper: Specimen 7A (Sheet 2/3).	136
5.6	Detail of a rotational friction damper: Specimen 7A (Sheet 3/3).	137

5.7	Detail of a rotational friction damper: Specimen 7B (Sheet 1/3). . . .	138
5.8	Detail of a rotational friction damper: Specimen 7B (Sheet 2/3). . . .	139
5.9	Detail of a rotational friction damper: Specimen 7B (Sheet 3/3). . . .	140
5.10	Photograph showing Specimen 7A in testing.	143
5.11	Photograph showing one of the tees for Specimen 7A after the test. .	144
5.12	Photograph showing one of the steel tees of Specimen 7A after the test.	145
5.13	Shear plate of Specimen 7A shows no damage after the test. The beam has been pulled away from the column for half inch.	145
5.14	Beam web under the shear plate of Specimen 7A shows no damage after the test. The center pivot bolt hole was enlarged by load reversals.	146
5.15	Photograph showing the brass shims and bolts taken out from Specimen 7A after the test.	147
5.16	Photograph showing the pivot bolt of Specimen 7B. The bolt hole in beam web is reinforced.	148
5.17	Photograph showing the shear plate and the pivot bolt of Specimen 7B after test.	148
5.18	Photograph showing Specimen 7B after test, the connection is in good condition without damage.	149
5.19	Imposed displacements for Specimen (a) 7A and (b) 7B.	150
5.20	Hysteresis loops for Specimen (a) 7A and (b) 7B.	152
5.21	Analytical hysteresis loops for Specimen (a) 7A and (b) 7B.	152
5.22	Top and bottom SBC slip for Specimen (a) 7A and (b) 7B.	153
5.23	“Plastic” rotations for Specimen (a) 7A and (b) 7B.	153
5.24	Total strain energy diagram for Specimen (a) 7A and (b) 7B.	154
5.25	Strain near bolt holes for Specimen (a) 7A and (b) 7B.	155
5.26	Strain gauge was placed on the tee root surface for Specimen 7B. . .	155
5.27	Tee root strains vs. tip load for Specimen 7B.	156
5.28	An alternative RSBC for Moment Resisting Connections.	157
5.29	An alternative RSBC for composite construction.	158
A.1	Newton iterations in a time-step.	172

List of Tables

1.1	Ten earthquake components for response analysis.	5
2.1	Specified minimum strengths of certain ASTM steels.	20
2.2	Four possible failure types of a steel MRF connection.	22
2.3	Material properties of the SAC Joint Venture PN specimens.	32
2.4	Test results of the SAC Joint Venture PN specimens.	35
3.1	Comparison table for eight A36 W12×26 specimens.	79
3.2	Material properties of Specimen 3 and 8 (from Mill Certificates).	84
5.1	Bolt tension range using DTI gap of 0.015 in.	132
5.2	Material properties of Specimen 7A and 7B. Both specimens share the same column.	142
5.3	Force indicating value of DTIs used in Specimen 7A and 7B.	142

Chapter 1

Introduction

1.1 Seismic Structural Design

In the earthquake-resistant design of building structures, the primary task is to avoid collapse and to limit structural and non-structural damage that may jeopardize human lives during a severe earthquake. To achieve this goal, a structure must possess adequate strength, high ductility, and long durability.

At present, the displacement ductility ratio is the most widely used parameter for limiting damage and for expressing damage in terms of earthquake-resistant design criteria. The procedure for the construction of inelastic design response spectra for a given ductility ratio has been established by Newmark and Hall [50]. Based on this procedure, design spectra have been developed and adopted by most current building codes. However, this method considers only the peak response of the structure and does not account for many other important effects such as the available cumulative ductility, number of yielding reversals, hysteresis energy capacity, and low-cycle fatigue. These shortcomings have led to the development of energy based design methods [3, 70, 71]. In general, in an energy approach, it is required that the available structural energy absorption or dissipation capacity be larger than the seismic energy demand. The duration of an earthquake is implicitly considered in the analysis. The combination of these two methods in design is now a standard practice.

There are many building framing systems in use. Because it is too expensive to design structures elastically to resist earthquakes, they must be made to rely on different deformation or yielding mechanisms to dissipate seismic input energy. One

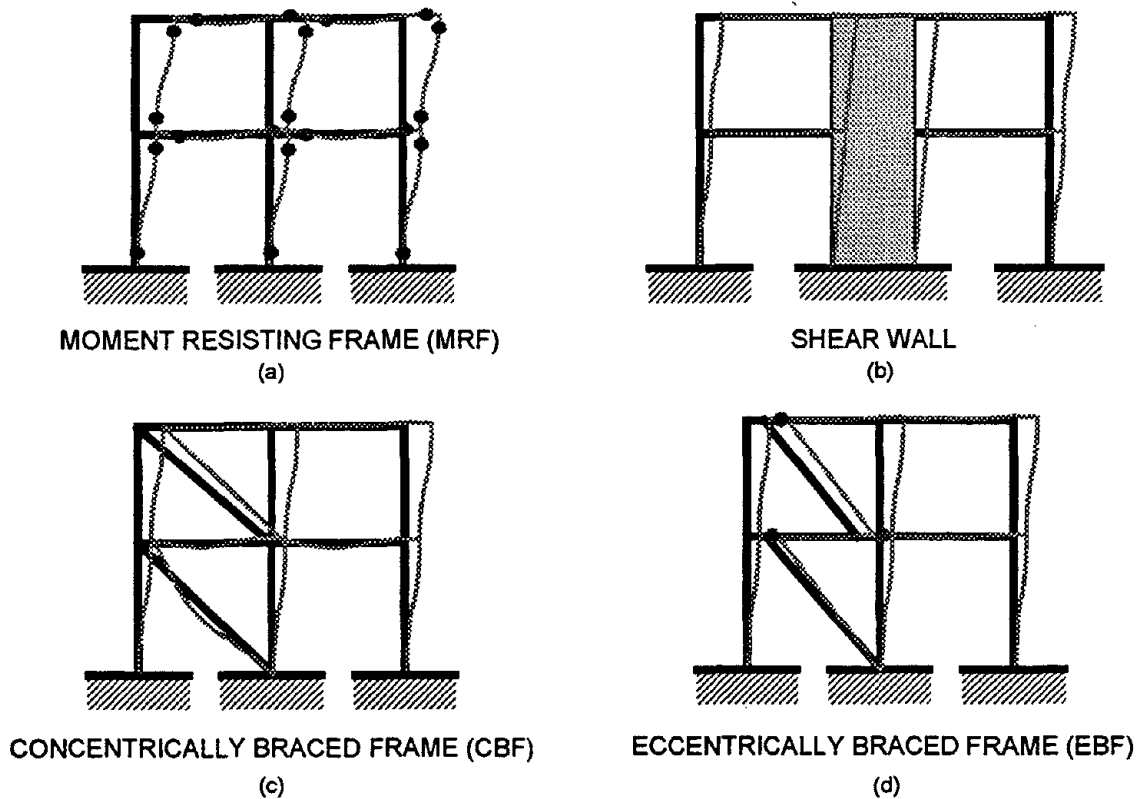


Fig. 1.1: Four types of structure and their primary lateral deformed shapes. Dots shown in (a) and (d) are the possible energy dissipation locations.

approach has been the use of plastic hinges near the connections in Moment Resisting Frames (MRFs) (dots in Fig. 1.1a). The energy capacity of this type of system is, in general, limited. The failure type may be brittle. A detailed investigation of MRF connections is given in Chapter 2. Another approach has been the use of concentrically braced frames (CBFs) (Fig. 1.1c) and shear walls (Fig. 1.1b). Both of these are rigid designs with very little energy absorption capacity. Braces in a CBF have to be very strong in order to prevent buckling. The Eccentrically Braced Frame (EBF) as shown in Fig. 1.1d is another kind of structural system in which energy dissipation takes place in active links [37, 59, 60]. The rotation of such a connection can deliver up to 8% rad.

These structural systems are mostly statically indeterminate, and their failure mechanisms are not easy to determine, especially for random seismic excitation situations. The energy dissipation capacity of a structural member depends not only

on the loading path but also on the deformation path. Also, there is no appropriate criteria to judge whether or not a retrofit is needed after a strong earthquake if the structural member has yielded. Even if the damage locations in the main structure are known, the retrofit can be costly and time consuming. These difficulties require structural engineers to design structures with specific critical locations for energy dissipation. Therefore, using a deterministic mechanism with energy dissipation or absorption capability becomes a rational approach. A number of different energy dissipative methods and devices have been developed and put into use in recent years [1, 2, 25, 38, 65, 66, 74]. Three major types of energy dissipating devices are available today, namely (1) material yielding type, (2) viscoelastic type, and (3) frictional type. Structures equipped with such devices can be designed to dissipate energy without yielding in the primary or gravity supporting structure, thus protecting structures from damage and failure. Another advantage of using energy dissipating devices is that they are removable and inexpensive, and can be easily fixed or replaced after a major earthquake.

1.2 Nonlinear Seismic Spectra

To investigate the seismic demand and to compare them with seismic code provisions, an array of nonlinear response spectra are constructed. The response spectrum is a plot of the *maximum* response (displacement, velocity, acceleration, ductility, energy, or any other quantity) to a specified earthquake or excitation for all possible single degree-of-freedom systems. The primary purpose of this nonlinear spectra study is to find the inadequacies in conventional ductility design such that improvements can be suggested.

In Fig. 1.2a, the single-story moment resisting frame can be idealized as a single degree-of-freedom (SDOF) system, as shown in Fig. 1.2b. The equation of motion in terms of relative displacement u can be written as

$$m\ddot{u} + c\dot{u} + f_s(u) = -m\ddot{u}_g \quad (1.1)$$

where m is the mass, c is the viscous damping coefficient, and \ddot{u}_g the ground acceleration. The constitutive law of the spring force $f_s(u)$ is assumed to be linearly elastic-perfectly plastic with stiffness k_s , and u_y the displacement at first positive

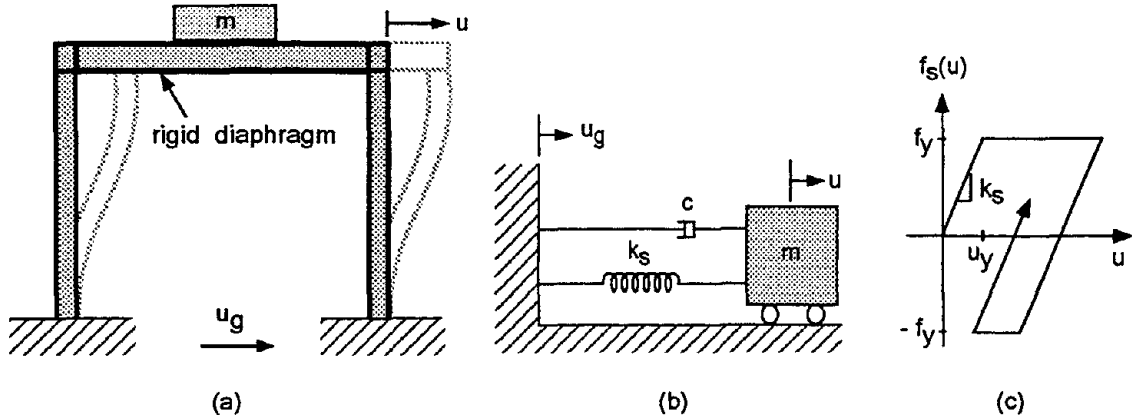


Fig. 1.2: (a) A single-story moment-resisting frame, (b) the corresponding single degree-of-freedom model, and (c) The elastic-perfectly plastic constitutive law of the system.

yield, thus the yield force f_y is $k_s u_y$ (see Fig. 1.2c). The spring force $f_s(u)$ is a function of u with internal plastic deformation offset memory. Defining the displacement ductility $\mu = u/u_y$, the natural circular frequency $\omega = \sqrt{k_s/m}$, the damping ratio $\xi = c/(2m\omega)$, and the period $T = 2\pi/\omega$, the equation of motion Eq. (1.1) becomes:

$$\ddot{\mu} + \frac{4\pi}{T}\xi\dot{\mu} + \frac{1}{m u_y} f_s(\mu) = -\frac{\ddot{u}_g}{u_y} \quad (1.2)$$

In this system, the spring force depends on the nonlinear constitutive law of the structure. Iterations for equilibrium are commonly needed in solving the dynamic response using Eqs. (1.1) and (1.2). In this study, the Newmark method is used to solve the dynamic equilibrium equation [10, 11, 12, 13, 46, 49]. The algorithm is summarized in Appendix A.

The seismic coefficient C_y is defined as the ratio of the yielding force f_y and the weight of the structure W

$$C_y = \frac{f_y}{W} \quad (1.3)$$

where W is equal to mg , and C_y is a dimensionless parameter representing the idealized plastic capacity of the system.

The various spectra in this study were determined for points on a rectangular grid with periods T varying from 0.04 to 3 seconds, at increments of 0.04, and for the seismic coefficients C_y varying along the ordinate from 0.04 to 1.2, also at increments

Earthquake	Date	Record	Component	PGA (g)	Duration (sec)
Imperial Valley	05/18/40	El Centro	N00E	0.35	53.74
San Fernando	02/09/71	Pacoima Dam	S16E	1.17	41.80
Kern County	07/21/52	Taft	N21E	0.16	54.36
Chile	03/03/85	Lolleo	N10E	0.67	116.42
San Salvador	10/10/86	GIC	E00W	0.69	9.04
San Fernando	02/09/71	Derived Pacoima	S16E	0.40	14.99
Mexico City	09/19/85	SCT	N90W	0.17	180.06
Landers	06/28/92	Joshua Tree	Ch1 90 Deg	0.28	79.98
Miyagi-Ken-Ok	06/12/78	Tohoku Sendai	N00E	0.26	39.99
Loma Prieta	10/17/89	Corralitos	Ch1 90 Deg	0.63	40.00

Table 1.1: Ten earthquake components for response analysis.

of 0.04. All the response spectra were computed by the DANS computer program [75]. Ten earthquake components, as shown in Table 1.1, were selected for this study.

Appendix B.1 shows 12 displacement spectrum contours of the selected earthquakes by solving Eq. (1.1). Appendix B.2 shows 12 displacement ductility spectrum contours of the same earthquakes by solving Eq. (1.2), where μ varies from 1 (elastic) to 8 (significant yield). In both cases, an internal damping ratio ξ of 5% is assumed. The response spectra can be calculated by either Eq. (1.1) or Eq. (1.2), the value of μ is related to u by

$$u = \mu u_y = \mu \frac{f_y}{k} = \mu \frac{f_y}{mg} \frac{mg}{k} = \mu C_y g \left(\frac{T}{2\pi} \right)^2 \quad (1.4)$$

Thus, both spectra are equivalent. Many earthquakes have similar contour shapes of displacement ductility spectra, e.g. 1985 Chile and 1986 San Salvador (see Figs. (d) & (e) in Appendix B.2), but with different levels of destruction. One good explanation for this difference is the number of yield reversals (NYR). The NYR spectrum contours for the selected earthquakes are shown in Appendix B.3. A yield reversal is defined as a positive yield followed by a negative yield, or vice versa. Since NYR is closely related to the low-cycle fatigue or fracture of the structural members, an earthquake with the same displacement ductility but with larger NYR is considered to be more destructive. The 1985 Chile earthquake has larger NYR than the 1986

San Salvador earthquake (see Figs. (d) & (e) in Appendix B.3), thus the 1985 Chile earthquake is more destructive, although both earthquakes had similar ductility spectra. It is important to note the large number of reversals that may occur for low C_y . But if a structure is equipped with energy dissipators, the threat from large NYR can be eliminated. The code specified equivalent lateral force seismic design considers only the magnitude of load but ignores the importance of NYR. From the displacement ductility spectra, it is seen that the rate of reduction in the demanded seismic coefficient, C_y , decreases with increasing ductility, μ . This contrasts with the codes in which the required seismic resistance is decreased linearly with increasing μ .

For comparison, the nonlinear seismic spectrum for the 1994 Uniform Building Code (UBC) [33] lateral force specification is studied next. The UBC total base shear specification for seismic design is

$$V_B = \frac{ZIC}{R_w}W \quad \text{and} \quad C = \frac{1.25S}{T^{2/3}} \leq 2.75 \quad (1.5)$$

where V_B is the total design base shear, Z is the zone factor, I is the importance factor, S is the site coefficient, R_w is the structural system coefficient, and T is the period of the structure. By taking $Z = 0.4$, $I = 1$, $S = 1.2$, and $R_w = 8$, the equation reduces to

$$\frac{V_B}{W} = \frac{0.075}{T^{2/3}} \leq 0.1375 \quad (1.6)$$

The plot of this equation is shown by a solid black curve in Fig. 1.3 which is the allowable working stress seismic coefficient C_w . The overstrength factor $\Omega = 1$ defines the response spectrum for the strength design (first yield). For codes formulated on the allowable stress basis, the relationship $C_y = 1.4\Omega C_w$ applies for reinforced concrete structures. For steel structures, C_y is slightly higher. The plots of these strength design curves of $\Omega = 1, 2$, and 3 are also shown in Fig. 1.3. For some steel frames, Ω is estimated to be on the order of 2 [70, 73].

The displacement ductility diagram of the 1994 Northridge earthquake is shown in Fig. 1.4. In this figure, displacement ductility curves of $\mu = 1, 2, 4, 8$, and 12 , together with the UBC curve of $\Omega = 2$, are plotted for comparison. By comparing the $\mu = 8$ curve with the UBC curve, it appears that the UBC code underestimates the seismic forces in the low period range below about 0.5 s.

Another method to compare the code specifications with earthquake responses is using the code curves shown in Fig. 1.3 under the excitation of real earthquakes.

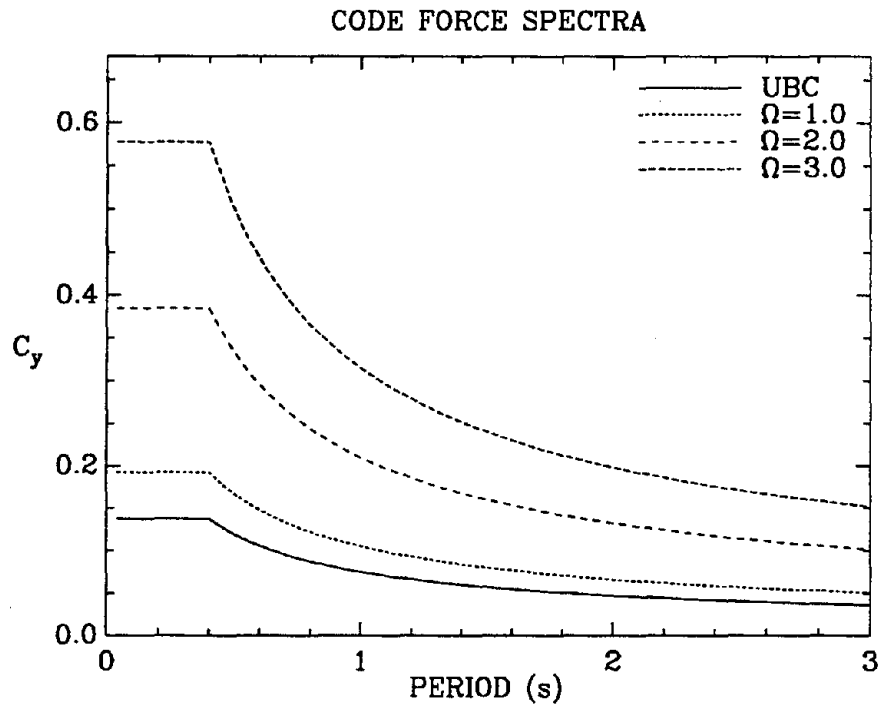


Fig. 1.3: Seismic force spectra for the UBC allowable stress design C_w (solid curve), for first yield design C_s ($\Omega = 1$), and for overstrength design of $\Omega = 2$ and 3.

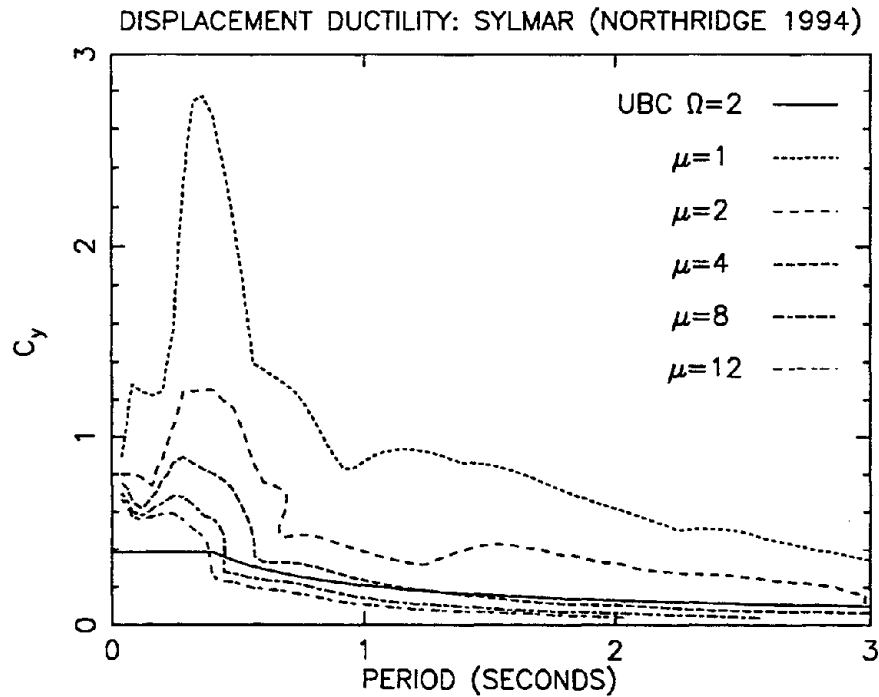


Fig. 1.4: Displacement ductility diagram for the 1994 Northridge earthquake at Sylmar Hospital.

In Fig. 1.5, displacement ductilities and the number of yield reversals for the force response spectra of Fig. 1.3 are plotted against the structural period T . These diagrams clearly show the inadequacy of code specifications for short period structures with overstrength factors less than 2. Similar inadequacy is also found in the Mexico City seismic code [57].

The above study shows the displacement ductility and number of yield reversals based on the UBC code force spectra. Each yield in the plastic hinges contributes some damage to the structure. Because the displacement in every yield reversal cycle is different, it is difficult to judge the extent of the actual damage. The cumulative effects must be considered concurrently. A rational approach is to use hysteresis energy as the damage index.

1.3 Seismic Energy Demand

To study the characteristics of strong motions for the purpose of seismic design by the energy approach, investigation of the seismic input energy should be made first.

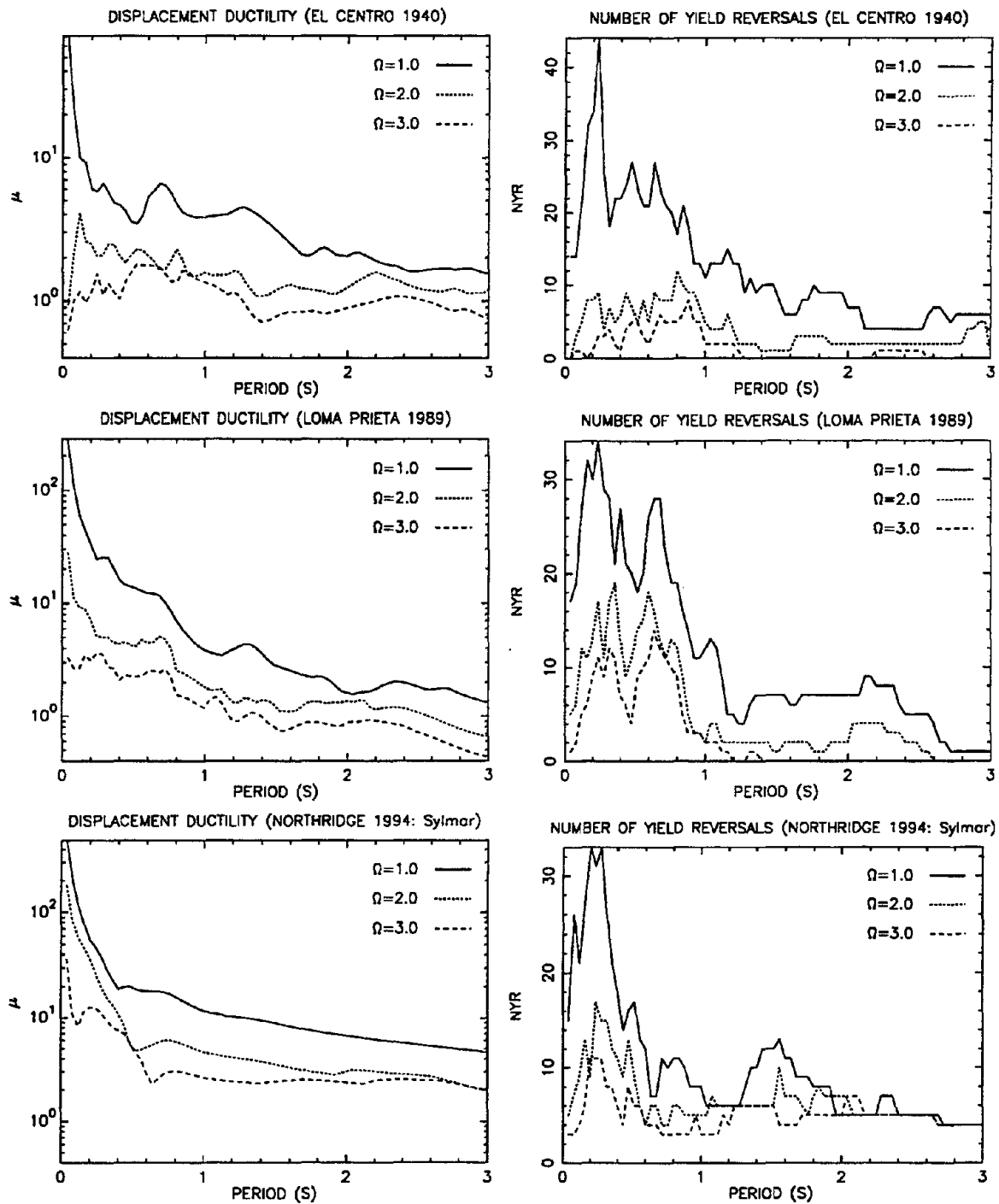


Fig. 1.5: Displacement ductility (left column) and Number of yield reversals (right column) diagrams for the UBC force response spectra for 1940 El Centro, 1989 Loma Prieta, and 1994 Northridge earthquakes.

Structures with different periods and strengths receive different amounts of seismic input energy. Analogous to calculations for displacement ductility, a rectangular $T-C_y$ region is considered. The formula for the absolute seismic input energy calculation is

$$E_I = \int m \ddot{u}_t du_g \quad (1.7)$$

where $u_t = u + u_g$ is the total displacement, $\ddot{u}_t = \ddot{u} + \ddot{u}_g$ is the total acceleration, and u_g is ground displacement.

The input energy diagram for the 1994 Northridge earthquake is shown in Fig. 1.6. A set of 3D mesh surfaces of the calculated seismic input energy for the selected earthquakes is shown in Appendix B.4. From these diagrams, it is clear as to which structures are vulnerable to a given earthquake. For example, in Fig. (g) of Appendix B.4, the dramatic absence of any need for seismic protection for a low period structure is evident for the 1985 Mexico City earthquake. The same figure also shows that structures with a period near 2 seconds receive the largest seismic energy input.

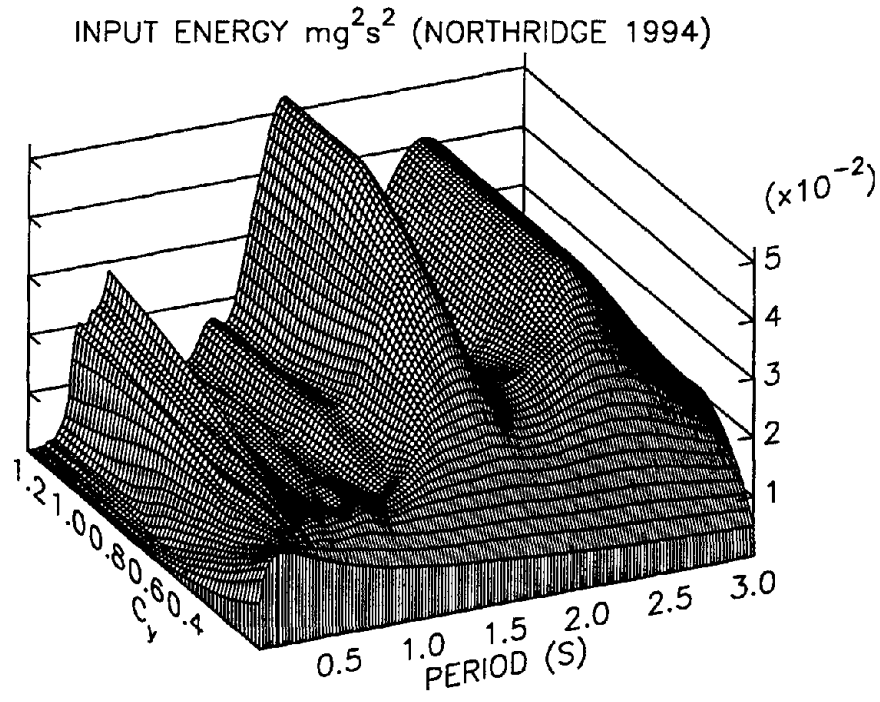
Structures can dissipate seismic input energy via hysteresis energy. If the hysteresis energy is caused by material yielding, then hysteresis energy represents the seismic damage energy. Hysteresis energy is calculated as the total area enclosed in the hysteretic loops. The calculation of hysteresis energy can be expressed as

$$E_H = \int f_s(u) du \quad (1.8)$$

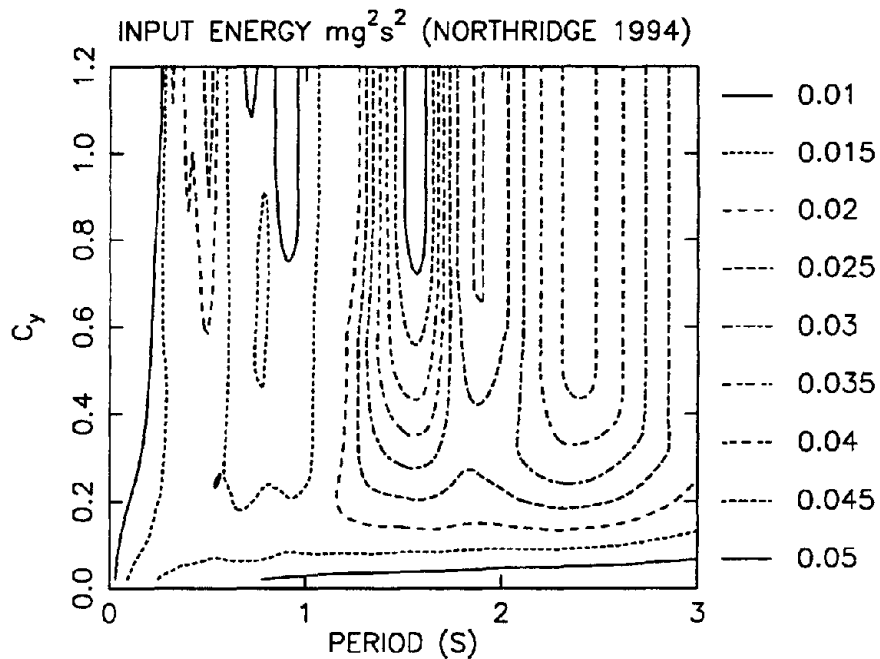
The hysteresis energy for the 1994 Northridge earthquake is shown in Fig. 1.7. A set of 3D mesh surfaces of calculated hysteresis energies for selected earthquakes is shown in Appendix B.5.

By integrating the volume under the mesh surfaces, it is possible to obtain meaningful indices of earthquake strength and damage potential [56]. The volume under the mesh surface for the absolute seismic energy input can be related to the strength of the earthquake; the volume under the mesh surface for the hysteresis energy can be treated as the potential damage that would be caused by an earthquake.

Hysteresis energy is calculated for the whole duration of an earthquake. If an energy dissipating device is used, the hysteresis energy represents the minimum energy capacity requirement of the energy dissipating device. An energy dissipating device that cannot supply the seismic hysteresis energy demand is inadequate. Durability tests to verify the energy capacity of energy dissipating devices are essential.



(a)



(b)

Fig. 1.6: Seismic input energy spectrum for the 1994 Northridge earthquake at Sylmar Hospital: (a) 3D mesh, (b) contours.

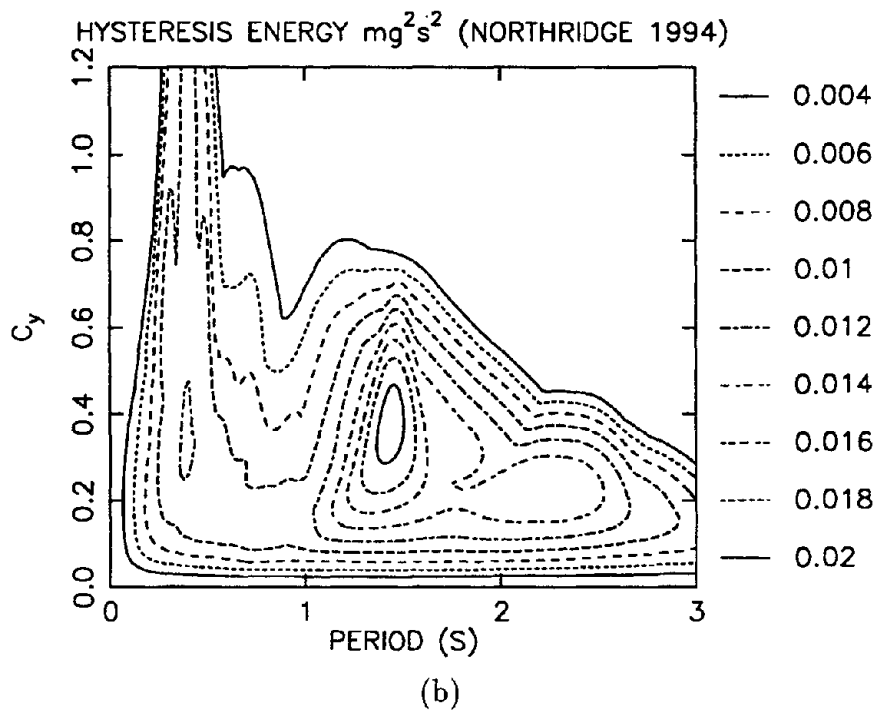
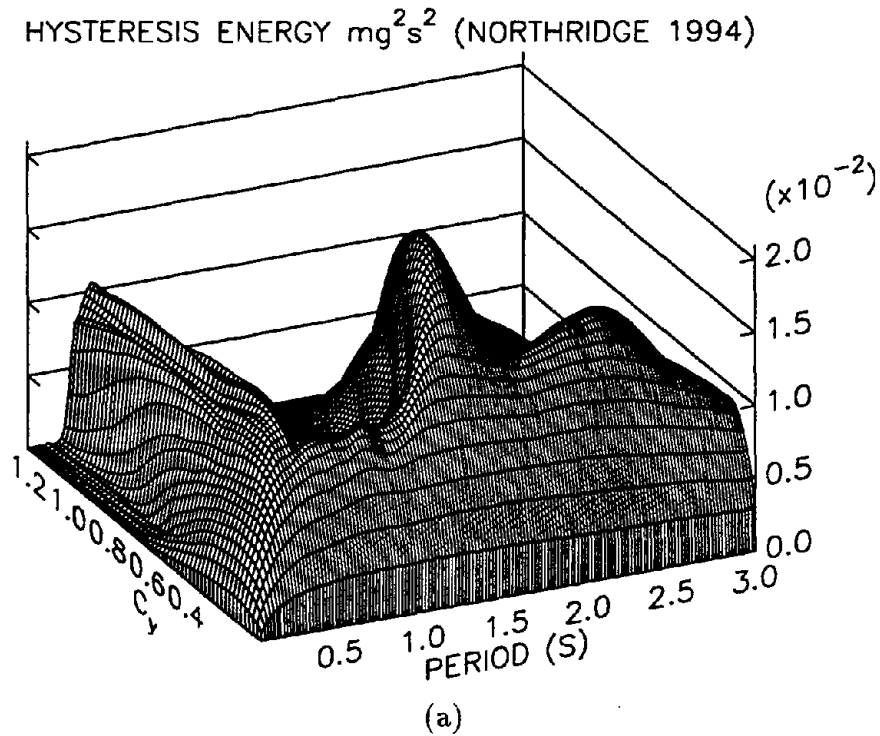


Fig. 1.7: Seismic hysteresis energy spectrum for the 1994 Northridge earthquake at Sylmar Hospital: (a) 3D mesh, (b) contours.

1.4 Conclusion

Based on the seismic response studies, the code specified force spectra are considered to be at times inadequate in the low period range, especially for structures with small overstrength factor. This can have serious consequences for low rise buildings. The nonlinear response spectra for ductility force decreases in an exponential manner with μ . Codes do not recognize this variation.

Nonlinear response spectra for the number of yield reversals are of great value in assessing building response. Such spectra are very sensitive to the duration of earthquakes, and indirectly provide a measure of input energy. Examination of the seismic demands on energy and number of yield reversals would indicate that conventional ductile structures may not have enough seismic capacity, unless larger members, good connection detailing, or base-isolation systems are used. But, these requirements can be attained easily by using well-designed energy dissipating connections or devices.

Displays of three-dimensional mesh surfaces for seismic energy input and for hysteresis energy provide guidance for establishing seismic zones.

Chapter 2

Behavior of Pre-Northridge Steel Moment-Resisting Connections

2.1 Introduction

Before the 1994 Northridge earthquake, steel moment-resisting frames (MRFs) were considered ductile by engineers. The dream was broken suddenly after the earthquake. Many brittle failures were reported throughout the greater Los Angeles area [16, 76]. Most serious fractures occurred at the welded beam-to-column connections. This has called into question the strength and ductility of such connections.

This chapter presents the analytical studies of pre-Northridge welded beam-to-column connections used in typical steel MRFs. In the analysis, no defects in welding material, welding procedure, or workmanship are assumed. The purpose of these studies is to give explanations for both fracture locations and failure modes of the aforementioned connections in quantitative and rational ways. The stress concentration at the juncture of a welded beam flange and a column flange is analyzed by three-dimensional elastic-plastic finite elements based on the von Mises yield criterion with associated plastic flow. The results clearly explain that the weak beam flange breaks off right at the weld due to the triaxial state of stress in this region. The important effect of the weak column panel zone was not fully explored before. In this chapter, it is shown that the column web fractures are closely related to the weak panel zone. The important effect of the backing bar in the connection failure is analyzed next by fracture mechanics methods. The unfused backing bar side next to

the column flange is interpreted as an artificial crack. Flange tension due to bending of the beam opens the artificial crack between the backing bar and the column flange, and initiates the rupture. The stress-intensity factors at the artificial crack tips of both top and bottom backing bars are calculated by the J-integral method. The results clarify why the rupture generally was initiated at the bottom flange but not at the top flange. Finally, the analytical cyclic load-deflection curve and plastic energy dissipation are compared with the three SAC¹ Joint Venture full-size specimens tested at the University of California at Berkeley. Good agreement between the analytical results and the experimental tests conclude the chapter.

2.2 Material Properties of Structural Steel

A typical welded beam-to-column moment resisting connection is shown in Fig. 2.1. The top and bottom flanges of the beam are welded directly to the column by full penetration groove welds. The beam web is bolted or welded to a shear plate, which is attached to the column by welding. The most serious rupture modes of such connections are shown in Fig. 2.2. The failure modes are catastrophic because they fracture at extremely high speeds without exhibiting prior ductile behavior. This violates the precept of the ductile MRF.

Before studying the non-ductile failure of the connection, some remarks on the material properties need to be made. The stress-strain curve of a small diameter uniform cylindrical steel bar ((a) in Fig. 2.3) loaded longitudinally to failure, will be ductile (curve (a) in Fig. 2.3). A small diameter bar of uniform cross-section is not restrained in the lateral direction, and allows Poisson contraction, which leads to specimen necking down and the development of shear slip layers (Lueders lines) during failure. However, for a cylindrical bar with a groove or notch, such as bar (b) in Fig. 2.3, even though the cross sectional area at the groove is the same as bar (a), the tensile stress-strain curve is completely different. When loaded in tension, the grooved part will have the largest stress, but due to the constraint of the larger sections outside the groove, no lateral contraction or shear flow can develop at the groove. The failure of bar (b) is caused by triaxial tension resulting in a brittle failure

¹SAC is an acronym for Structural Engineers Association of California, Applied Technology Council, and California Universities for Research in Earthquake Engineering.

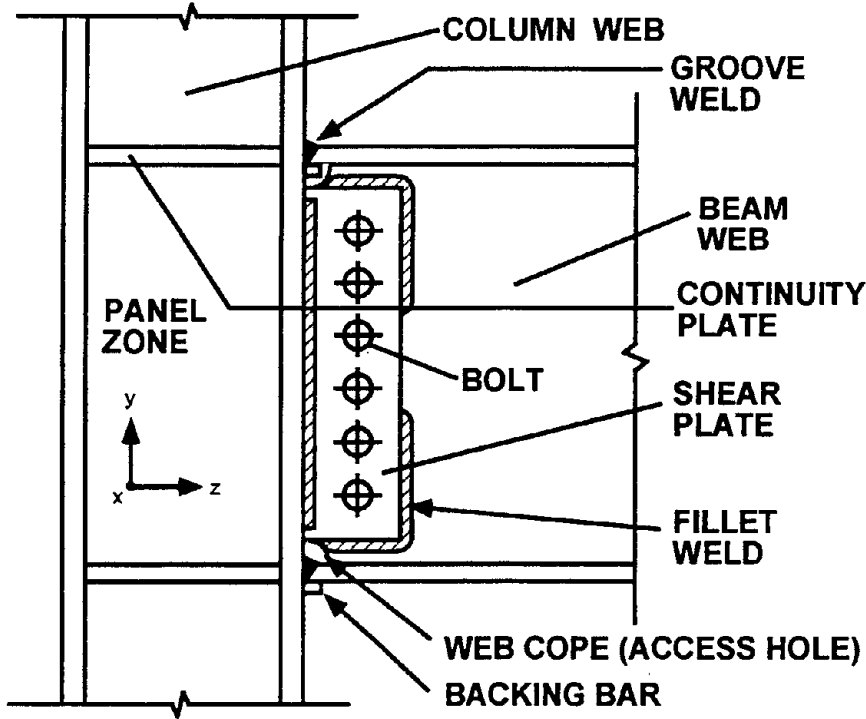


Fig. 2.1: A typical welded beam-to-column connection.

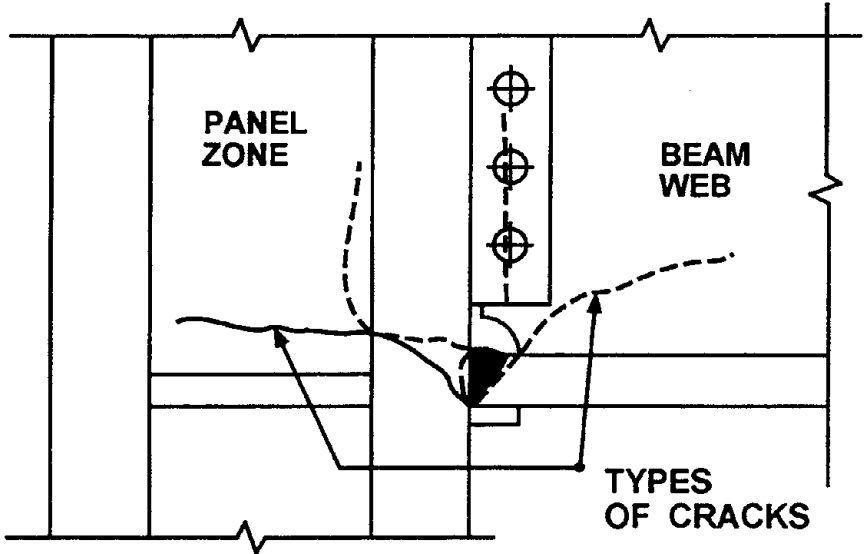


Fig. 2.2: Some failure modes of the welded beam-to-column connection.

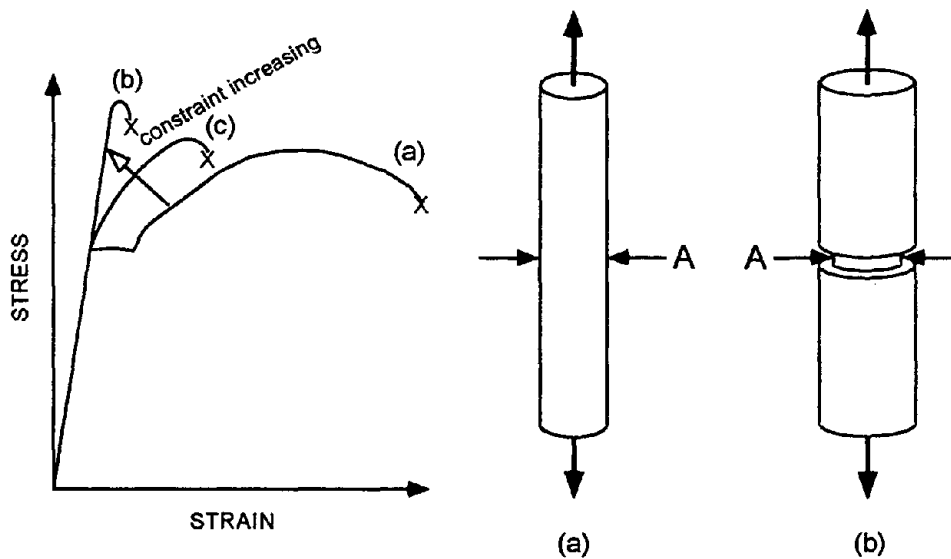


Fig. 2.3: Simple tensile test of steel specimens with the same critical cross section area: (a) cylindrical bar, and (b) grooved cylindrical bar.

with no apparent yielding. The stress at breaking is near the cohesion strength of the material; its stress-strain curve is similar to curve (b) in Fig. 2.3. Timoshenko on page 435 of his book says [68]:

Because most of the grooved specimen remains elastic during a tensile test to failure, it will have a very small elongation, and hence only a small amount of work is required to produce fracture. A small impact force can easily supply the work required for failure. The specimen is brittle because of its shape not because of any mechanical property of the material.

There have been many research studies on grooved specimens, such as Kirkaldy [39], Ludwik and Scheu [44], and MacGregor [45]. Stress concentration factors for a variety of grooved bars can be found, for example, in Neuber [48] and Peterson [52].

It can be seen in Fig. 2.1 that the welded beam flange cannot be deformed in both x and y directions because it is welded to a relatively large column flange with continuity plates. The welded beam flange also has to resist the largest bending moment caused by the loads on its span and frame drift. The stress on the beam flange outside the weld is smaller because of reduced moment and lesser lateral strain constraint. The welded beam-to-column connection has the strain constraint and the

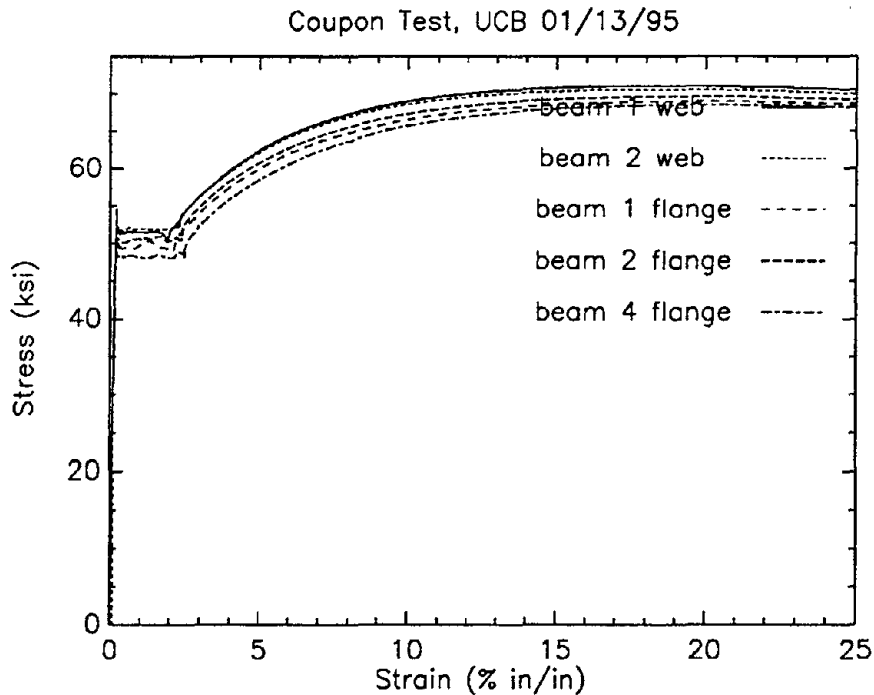


Fig. 2.4: Stress-strain curves of a series of tensile tests for A36 steel.

largest stress, which make it essentially like a grooved bar except with a different shape. It can be expected that the tensile stress-strain curve right at the beam flange weld will be between curves (a) and (b) in Fig. 2.3 depending on the degree of constraint, web cope (access hole) size, and bending moment gradient.

Another important fact regarding the mechanical properties of today's steel is that the yield strength of A36 steel is no longer 36 ksi. Fig. 2.4 shows a series of tested stress-strain curves of coupons cut from A36 W12×26 beams. The average yield strength of A36 steel is about 48 ksi, the ultimate strength of A36 steel is about 70 ksi.

Table 2.1 lists *minimum* yield strength, F_y , and minimum ultimate strength, F_u , for certain ASTM steels given in the AISC specifications. The ANSI-ASTM standard B483-78 defines minimum strength as follows:

Standard mechanical property limits for the respective size ranges are based on an analysis of data from standard production material and are established at a level [at] which at least 99 percent of the production of values obtained from all standard material in the size range meets the established value.

ASTM Number	A36	A592	A572 Gr50	A588	A514
Steel Type	Carbon	Carbon	Low alloy	Stainless	Alloy Q&T†
Minimum F_y (ksi)	36	42	50	50	100
Minimum F_u (ksi)	58	60	65	70	110

†Q&T: Quenching and Tempering

Table 2.1: Specified minimum strengths of certain ASTM steels.

The unqualified word *minimum* may be misleading, since there is a chance that the materials involved may have a strength much higher than the minimum. In the statement, there is no specification for the upper bound of steel strength. For structural elements loaded to the allowable stress level, the statement is adequate for design. However, in seismic resisting structures, many elements can be stressed beyond the yield strength during a strong earthquake to develop the needed ductile behavior. The ASTM specifications provide no information for designers to control deformation because the material strength can be much higher than the minimum value. The A36 materials tested in the laboratory have an average yield strength 33% over the specified minimum value (Fig. 2.4). Such high variance on strength makes stress analysis meaningless.

The AISC specification states that:

Certified mill test reports or certified reports of tests made by the fabricator or a testing laboratory in accordance with ASTM A6 or A568, as applicable, and the governing specification shall constitute sufficient evidence of conformity with one of the ASTM standards. Additionally, the fabricator shall, if requested, provide an affidavit stating that the structural steel furnished meets the requirements of the grade specified.

The AISC statement ensures that materials having these minimum strengths are actually used in the construction, but the designers have no way to know the actual material strengths during design until the materials reach the fabrication stage.

A more appropriate material specification would be to give the average material strength with a specified small variance. Designers can use the average as the nominal design value and use the variance for reliability analysis.

2.3 Design Strategy

The most essential characteristic of the MRF is the requirement that plastic hinges be formed near connections during severe loading conditions. These plastic hinges provide strength and ductility to dissipate energy hysteretically. As was stated earlier, it is impossible to develop large plastic deformation right at the beam-column weld location. Thus, the plastic hinges can only be formed at the beam or column section near the connection.

In order to establish the design strategy, let the resisting capacity at the connection be defined by the following symbols:

- C_m^b = Moment resisting capacity of beam at the connection
- C_v^b = Shear resisting capacity of beam at the connection
- C_m^c = Moment resisting capacity of column at the connection
- C_v^c = Shear resisting capacity of column in the panel zone
- C_{cr}^b = Local buckling strength of beam near the connection
- C_{cr}^c = Local buckling strength of column near the connection

The superscripts *b* and *c* are used to designate *beam* and *column*, respectively. The actual resisting capacity of a connection is controlled by the minimum of these six values². The minimum resisting capacity is based on the failure type. The four possible failure types are given in Table 2.2. In this table, Types 1 and 2 correspond to sudden fractures and should be avoided. By developing plastic hinges near the connections, Type 3 and 4 mechanisms assure good strength and ductility (Fig. 2.5). For beam flange connections welded directly to the column flange, the resisting capacity C_m^b is always smaller than the ultimate moment capacity of the beam. In such a situation, in order to develop a Type 3 mechanism, a non-compact beam section must be used. The derivations for C_m^b and C_{cr}^b are given in the next section. It is to be noted that the kinematic mechanisms shown in Fig. 2.5 are associated with early inelastic action and do not represent collapse mechanisms.

²The resisting capacity is also affected by backing bars at the welds. This will be discussed later.

Failure Type	Minimum Capacity	Failure Mode
1	C_m^b or C_v^b	beam flange or shear plate rupture (crack 3 in Fig. 2.6)
2	C_m^c or C_v^c	fracture through column web or divot pullout from column flange (crack 1 or 2 in Fig. 2.6)
3	C_{cr}^b	buckling of beam near connection and formation of plastic hinge (weak beam-strong column connection)
4	C_{cr}^c	buckling of column near connection and formation of plastic hinge (strong beam-weak column connection)

Table 2.2: Four possible failure types of a steel MRF connection.

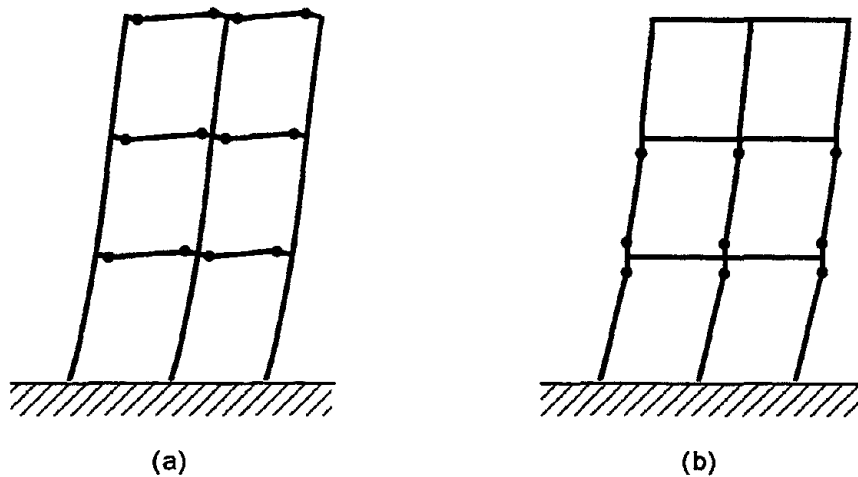


Fig. 2.5: Two alternative plastic hinge mechanisms for a typical MRF: (a) Type 3 mechanism and (b) Type 4 mechanism.

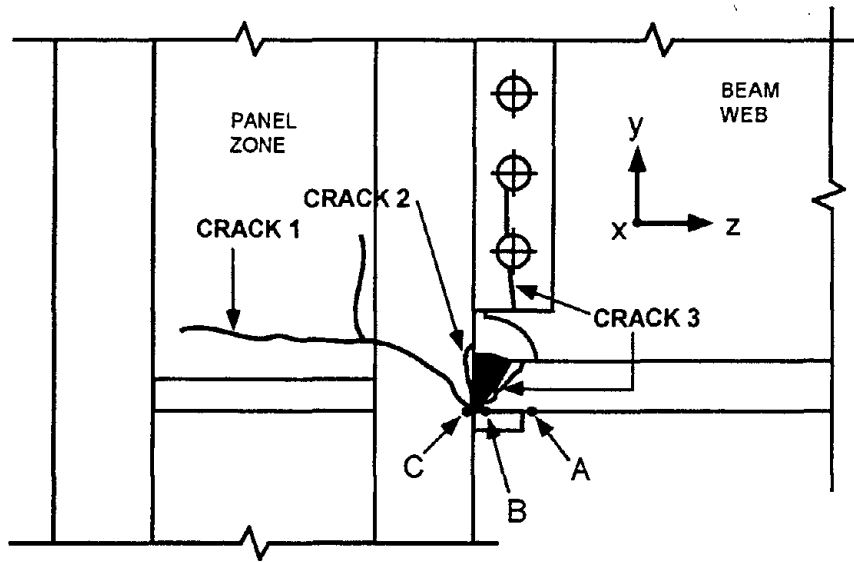


Fig. 2.6: Critical points in the connection - point A on beam flange, point B on beam-weldment junction, and C at column flange.

2.4 Simplified Stress Analysis

In the linear elastic range, the stress in the z direction at the outer-most fiber point A, shown in Fig. 2.6 near the weld to the connection, is denoted as σ_{zz}^A . The nominal value of σ_{zz}^A can be calculated from

$$\sigma_{zz}^A = \frac{M}{S_x^b} \quad (2.1)$$

where M is the applied bending moment, and S_x^b is the section modulus of the beam. The corresponding strain is expressed as

$$\epsilon_{zz}^A = \sigma_{zz}^A / E \quad (2.2)$$

where E is the Young's modulus of the beam.

Point A is not constrained by the weldment. On the other hand, point B is also at the outer-most fiber of the beam at the center of the beam-column junction. As shown in Fig. 2.6, point B is restrained by the weldment, which is directly attached to a wide thick column flange and cannot displace in either the x or y direction, hence $\epsilon_{xx}^B = \epsilon_{yy}^B = 0$. The stress state of point B is in the transition zone from plane stress to plane strain. Because point B is so close to point A, its strain ϵ_{zz}^B in direction z can

be assumed to be equal to ϵ_{zz}^A , and the stresses at point B can then be determined by Hooke's law:

$$\sigma_{zz}^B = \frac{(1-\nu)E}{(1+\nu)(1-2\nu)}\epsilon_{zz}^B = \frac{(1-\nu)E}{(1+\nu)(1-2\nu)}\epsilon_{zz}^A = \frac{(1-\nu)}{(1+\nu)(1-2\nu)}\sigma_{zz}^A \quad (2.3)$$

$$\sigma_{xx}^B, \sigma_{yy}^B = \frac{\nu E}{(1+\nu)(1-2\nu)}\epsilon_{zz}^B = \frac{\nu E}{(1+\nu)(1-2\nu)}\epsilon_{zz}^A = \frac{\nu}{(1+\nu)(1-2\nu)}\sigma_{zz}^A \quad (2.4)$$

where ν is Poisson's ratio. Since for steel, $\nu = 0.3$ and $E = 29,000$ ksi, approximately, the above equations reduce to

$$\sigma_{zz}^B = 1.35\sigma_{zz}^A \quad (2.5)$$

$$\sigma_{xx}^B, \sigma_{yy}^B = 0.58\sigma_{zz}^A \quad (2.6)$$

To verify the adequacy of the estimated stress concentration factors derived above, a series of elastic finite element analyses was performed based on the geometry of the SAC specimen (see next section) by varying the column flange thickness while keeping the beam flange thickness constant. The results are shown in Fig. 2.7. The stress concentration factor of each component of stress is plotted against the beam/column flange thickness ratio. The stress concentration factors of σ_{zz} range from 1.2 to 1.46, which is very close to the calculated simplified value of 1.35, but the stress concentration factors for σ_{xx} and σ_{yy} are much less than the estimated value 0.58. The lower three curves in the figure show how small the flange shear stresses are at the juncture. Because of the low shear stresses, no shear slip can form, resulting in no ductility. For the same reason, the beam fracture is governed by the maximum-normal-stress criterion. The maximum-normal-stress criterion states that failure occurs whenever one of the three principal stresses equals the uniaxial material strength. The maximum principal tension stress σ_{max} of the beam flange at the juncture of the beam-column connection is plotted in Fig. 2.7, which is very close to the σ_{zz} curve.

In the inelastic range, the stress across the flange will re-distribute to become much more evenly distributed, although the greatest stress value remains at the flange center. All rolled steel members (W, M, C, etc.) possess residual stresses due to differential cooling. The flange tips and interior web parts always cool more quickly than the other parts of the flange. In this manner, the flange tips develop compressive stresses, while the residual stresses are tensile in the middle of the flange.

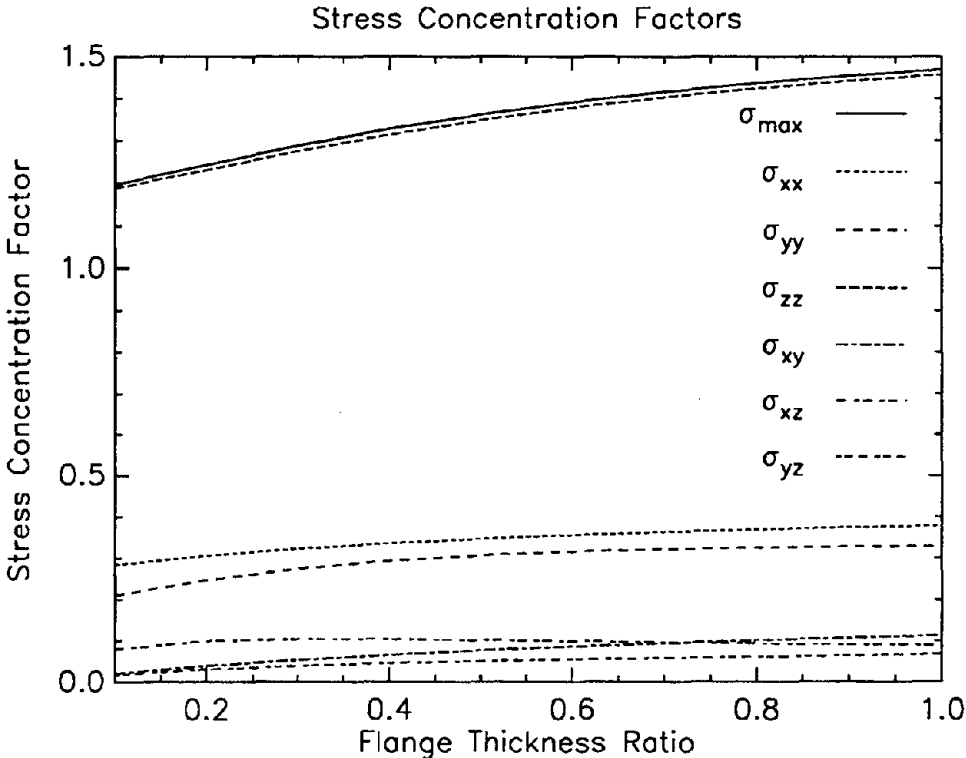


Fig. 2.7: Stress concentration factors at juncture of beam-to-column connection calculated by elastic finite element analysis. The external load is uniformly distributed unit tensile stress σ_{zz} applied on the beam flange.

The yielding moment of a member can be calculated with a sufficient degree of accuracy by the following equation

$$M_{yield}^b = (F_y - F_r)S_x^b \quad (2.7)$$

where F_r is the maximum compressive residual stress in either flange tip of the beam. The average compressive residual stress at the flange tips of small to medium size rolled shapes is about 13 ksi for A36 steel with 36 ksi yield strength [15, 22]. It is reasonable therefore to assume that the value of the residual stress is a fraction of the yield strength

$$F_r = \frac{13}{36}F_y = 0.36F_y \quad (2.8)$$

The residual stresses for large hot-rolled sections can be found in Alpsten [4]. The plastic moment capacity of a rolled section is hardly affected by the presence of residual stresses and can be calculated simply as

$$M_{plastic}^b = F_y Z_x^b \quad (2.9)$$

where Z_x^b is the plastic modulus of the beam. The ultimate moment capacity of a beam can be reached by bending a plastic section into the strain-hardening range. Hence the ultimate bending capacity is expressed as

$$M_{ultimate}^b = F_u Z_x^b \quad (2.10)$$

For a directly welded beam-to-column connection without cover plate, the bending beam moment is transferred primarily through the beam flanges into the column regardless of the size of the shear plate. The ultimate moment capacity of the connection therefore can be calculated by

$$C_m^b = F_u Z_f^b \quad (2.11)$$

where Z_f^b is the plastic modulus of the beam flanges. Because Z_x^b is larger than Z_f^b , the ultimate moment capacity of the beam $M_{ultimate}^b$ is always larger than the connection moment capacity C_m^b . If the rolled shape section is compact, no local buckling will occur before $M_{ultimate}^b$ is reached, and the rapid failure occurs by tearing off the flange.

The local buckling stress of a beam flange can be derived from the plate buckling stress. In general, the plate buckling stress in the elastic range is given by the *Bryan*

equation³

$$\sigma_{cr} = k \frac{\pi^2 E}{12(1 - \nu^2)} \left(\frac{t}{b}\right)^2 \quad (2.12)$$

where t and b are the thickness and the width of the plate, respectively. k is the plate buckling coefficient, which depends on the plate geometry and boundary conditions. For the beam flange of a wide-flange rolled shape, k is 0.7. The plate buckling stress in the inelastic range can be shown to be [18]

$$\sigma_{cr} = k \frac{\pi^2 \sqrt{E E_t}}{12(1 - \nu^2)} \left(\frac{t}{b}\right)^2 \quad (2.13)$$

where E_t is the tangent modulus of the material. From the buckling stress, the critical beam moment capacity C_{cr}^b can be calculated from

$$C_{cr}^b = \sigma_{cr} Z_f^b \quad (2.14)$$

To safely design a beam-column connection, it is desirable that

$$C_{cr}^b < C_m^b < M_{ultimate}^b \quad (2.15)$$

But for economic use of the material, the critical stress should obey the following relation

$$F_y \leq \sigma_{cr} < F_u \quad (2.16)$$

2.5 Three SAC Pre-Northridge Specimen Tests

In order to help understand the strength and ductility of the welded moment resisting connections, three specimens have been fabricated according to the standards used before the 1994 Northridge earthquake. These were tested at UC Berkeley under the guidance of the SAC Joint Venture. The dimensions of these specimens are shown in Fig. 2.8. The connection detail is shown in Fig. 2.9. These specimens were tested in a horizontal position. The test setup is shown in Fig. 2.10. An end-plate is welded to the cantilever beam and bolted to a clevis, which connects to a computer-controlled 350 kips hydraulic actuator (see Fig. 2.11). Slowly varying cyclic loads are applied to the beam tip by the actuator. The column is simply supported at the ends by

³After the English naval engineer who derived it in 1891.

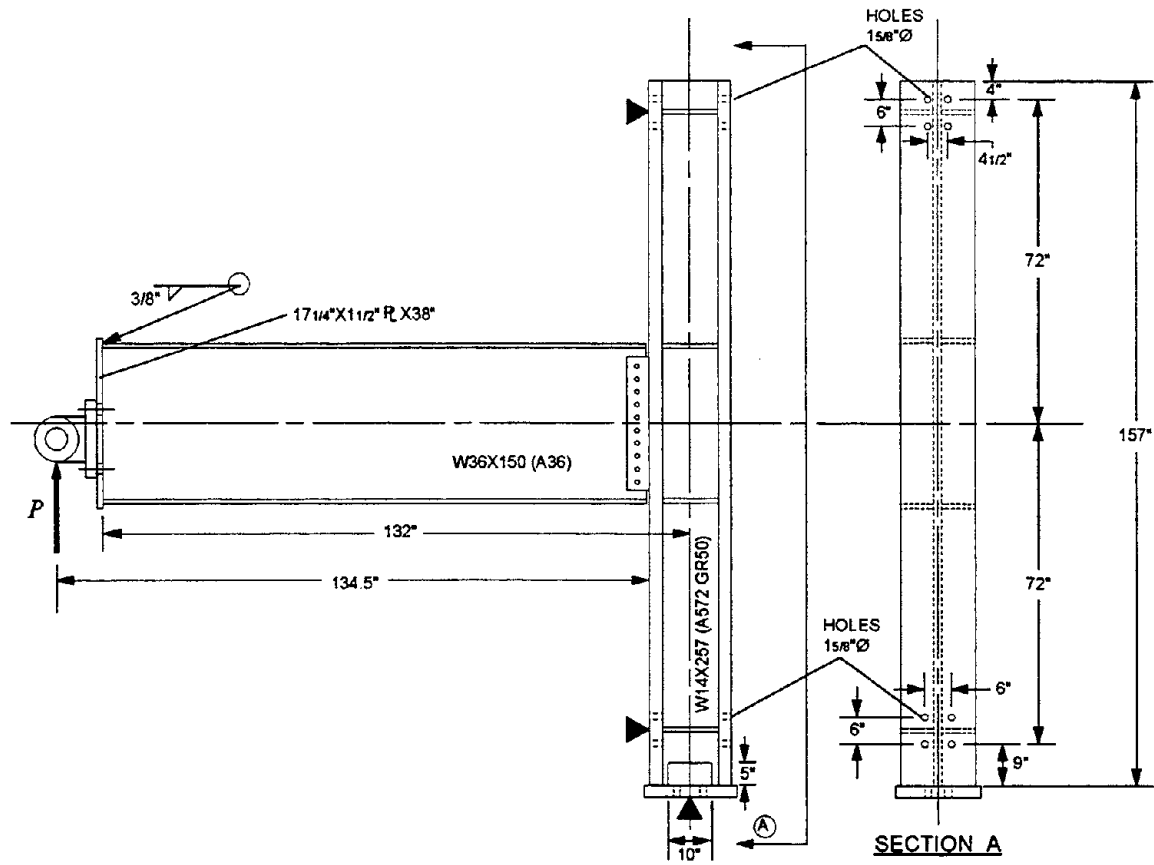


Fig. 2.8: Detail of the SAC PN specimens.

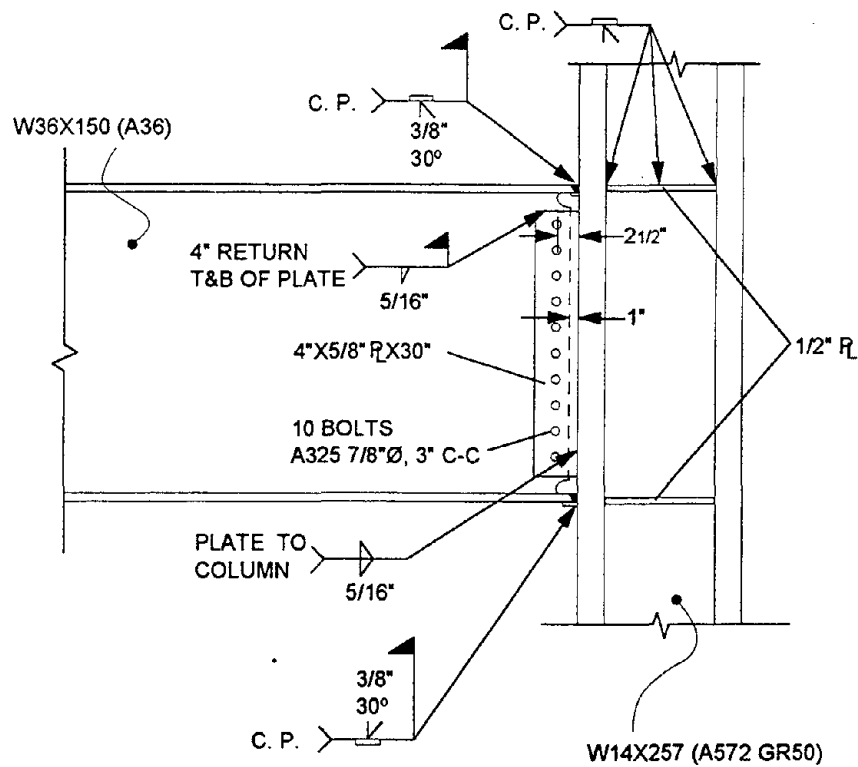


Fig. 2.9: Connection detail for SAC PN specimens.

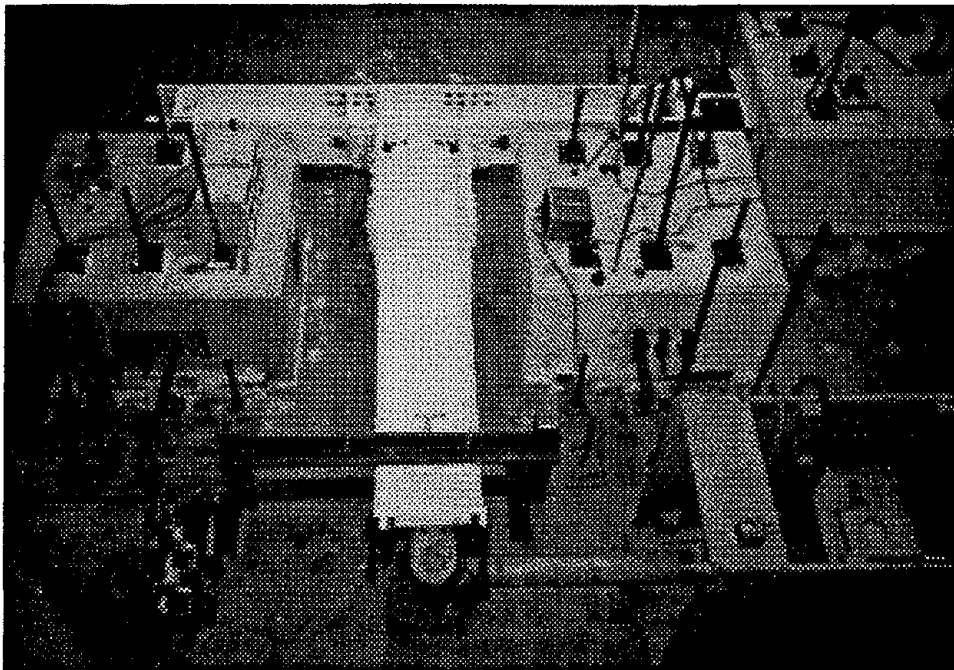


Fig. 2.10: Photograph showing specimen tested horizontally in laboratory. Left side of the beam is the *upper* side of the specimen.

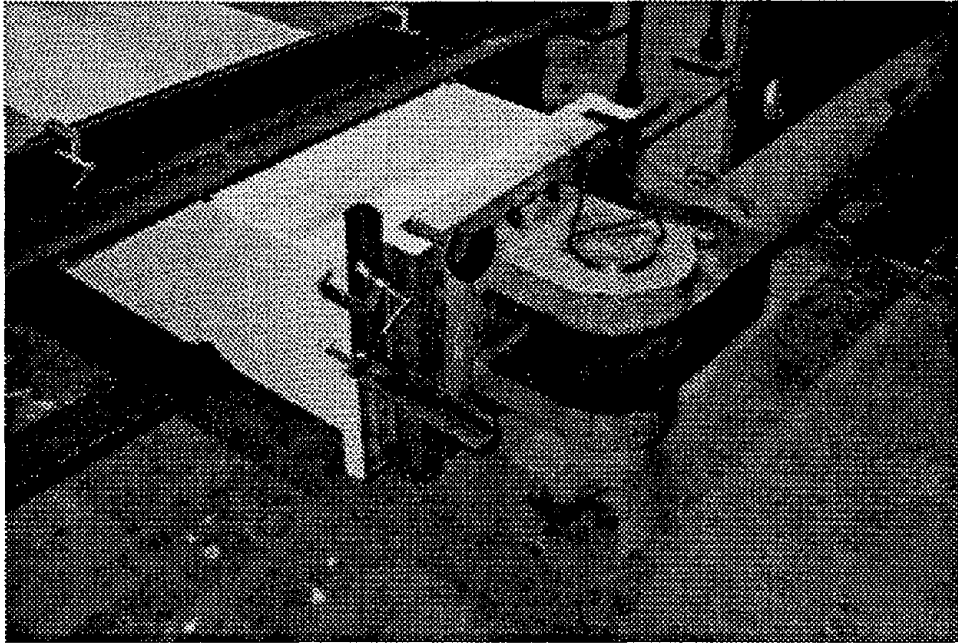


Fig. 2.11: Photograph showing the clevis connected to beam end-plate and hydraulic actuator.

prestressed rods tightened to three reinforced concrete blocks. These reaction blocks are prestressed to the floor by high-strength rods. The reaction and loading points simulate the inflection points occurring at mid span of a frame. At the top of the column, in order to simulate a roller support at the end, the column is tightened to a reaction block by four prestressing rods (Fig. 2.12). At the bottom of the column, in order to simulate a hinged end, the column is tightened to the reaction blocks by prestressed rods in two directions (Fig. 2.13). Detailed information of the setup can be found in the thesis by Blackman [17]. During the fabrication of the specimens, two A572-Gr50 beams were mistakenly used in the first two specimens PN1 and PN2. Only the third specimen PN3 was made of the correct materials. The material properties of these three specimens, as determined from mill certificates, are given in Table 2.3. Notice that the yield strength of the A572 Grade 50 PN1 and PN2 beam is 25% over the ASTM minimum, the yield strength of the A36 PN3 beam is 58% over the ASTM minimum. The high scatter in material strengths may result in inadequate structures.

Each SAC specimen has a cantilever beam with a concentrated force P applied

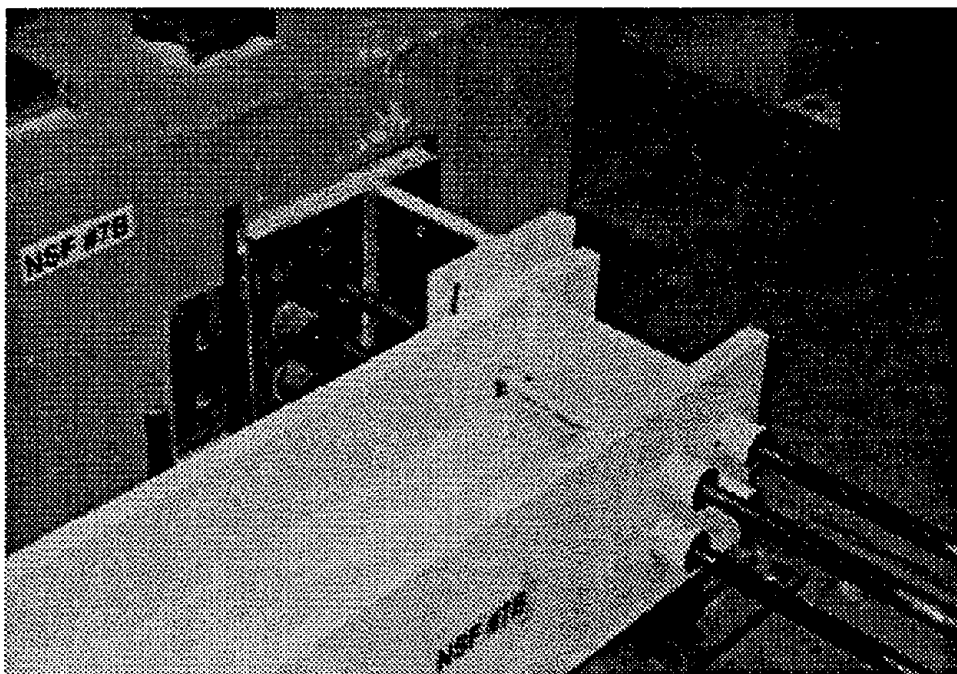


Fig. 2.12: Photograph showing the top of the column.

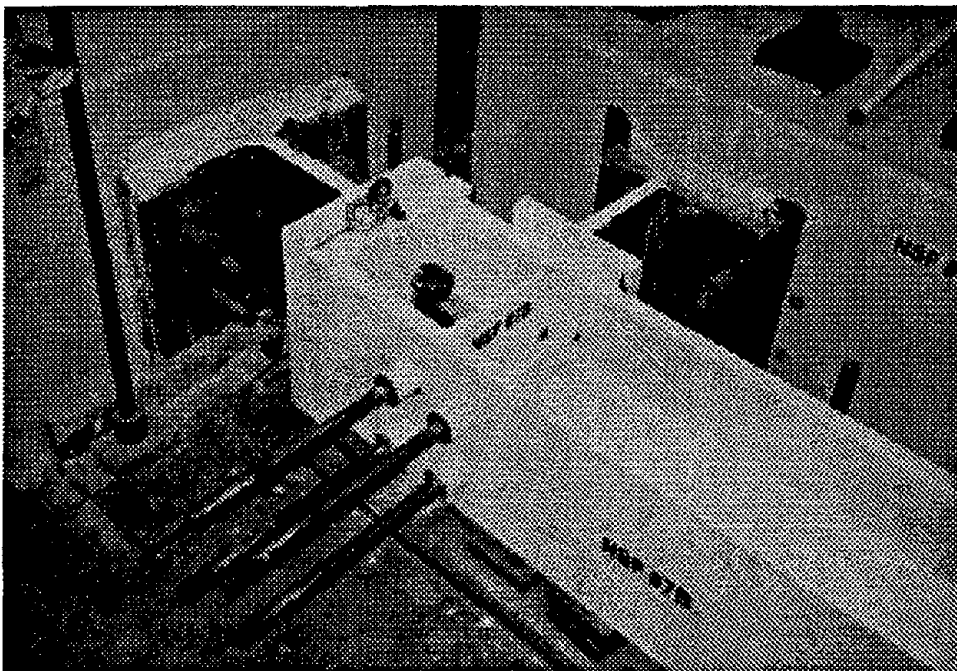


Fig. 2.13: Photograph showing the bottom of the column.

Material Properties
(from Mill Certificates)

Specimen Number	Material Size & Spec	Yield Strength F_y (Elongation)	Ultimate Strength F_u (Elongation)
PN1, PN2 & PN3 Column	W14×257 A572-Gr50	53.5 ksi (0.18%)	72.5 ksi (N/A)
PN1 & PN2 Beam	W36×150 A572-Gr50	62.6 ksi (0.22%)	74.7 ksi (22.5%)
PN3 Beam	W36×150 A36	56.8 ksi (0.20%)	68.7 ksi (28.0%)

Table 2.3: Material properties of the SAC Joint Venture PN specimens.

at its free end (see Fig. 2.8). The arm length L of the concentrated force to the face of the column flange is 134.5 inches. The moment capacities of these specimens can be calculated by Eqs. 2.7-2.11. The corresponding concentrated forces can also be calculated by dividing the moment by the moment arm. For PN1 and PN2 specimens, the yield force can be calculated as

$$P_{yield} = M_{yield}^b / L = S_x^b (F_y - F_r) / L = 504(62.6 - 0.36 \times 62.6) / 134.5 = 150 \text{ kips} \quad (2.17)$$

and the peak force can be calculated as

$$P_{peak} = C_m^b / L = Z_f F_u / L = 392.96 \times 74.7 / 134.5 = 218 \text{ kips} \quad (2.18)$$

Similarly, the yield and peak forces of the PN3 specimen can be calculated as

$$P_{yield} = S_x^b (F_y - F_r) / L = 504(56.8 - 0.36 \times 56.8) / 134.5 = 136 \text{ kips} \quad (2.19)$$

$$P_{peak} = C_m^b / L = Z_f F_u / L = 392.96 \times 68.7 / 134.5 = 201 \text{ kips} \quad (2.20)$$

The shear force in the column below and above the connection due to tip load P can be calculated as

$$V^c = P(L + \frac{d^c}{2}) / 138 = P(134.5 + 16.38/2) / 138 = 1.03P \quad (2.21)$$

where d^c is the depth of the column (refer to Fig. 2.8). The axial force at the beam flange can be expressed as

$$T^b = \frac{PL}{d^b - t_f^b} = \frac{134.5P}{35.85 - 0.94} = 3.85P \quad (2.22)$$

where d^b is the depth of the beam and t_f^b is the flange thickness of the beam. Thus the shear force in the panel zone is

$$V^{pz} = T^b - V^c = 2.82P \quad (2.23)$$

and the shear capacity of the column is

$$C_v^c = 0.95d^c t_w^c \frac{F_y^c}{\sqrt{3}} = 0.95 \times 16.38 \times 1.175 \times \frac{53.5}{\sqrt{3}} = 565 \text{ kips} \quad (2.24)$$

where 0.95 is the effective shear area coefficient, t_w^c is the web thickness of the column, and $1/\sqrt{3}$ comes from the von Mises yield criterion. As long as the tip load is over 200 kips, the column will have shear yielding in the panel zone.

The maximum column bending moment occurs at the section outside the panel zone. Its value is

$$M^c = V^c(69 - d^b/2) = 52.8P \quad (2.25)$$

The moment capacity of the column is

$$C_m^c = F_u^c Z_x^c = 72.5 \times 542 = 39,300 \text{ kip-in} \quad (2.26)$$

The column is very safe in bending. The shear plate of the connection is very well designed, and its strength is enough to resist the applied load.

The test results of these specimens are shown in Table 2.4. These values agree well with the calculated values. The moment-rotation and moment ratio-plastic rotation diagrams for three SAC specimens are given in Fig. 2.14.

Since the beams of three SAC specimens have compact sections and strong material, the failure modes are of a rapid fracture type. The crack in the PN1 specimen initiated at the center of the bottom beam flange-column juncture. The crack rapidly propagated through the column flange and forked out into two cracks in the column web (see Fig. 2.15). At the peak load of 225 kips, the panel zone is unable to resist the applied shear force. The PN2 specimen has the same material properties as the PN1 specimen. Its fracture pattern is also similar to PN1 (see Fig. 2.16) except that the

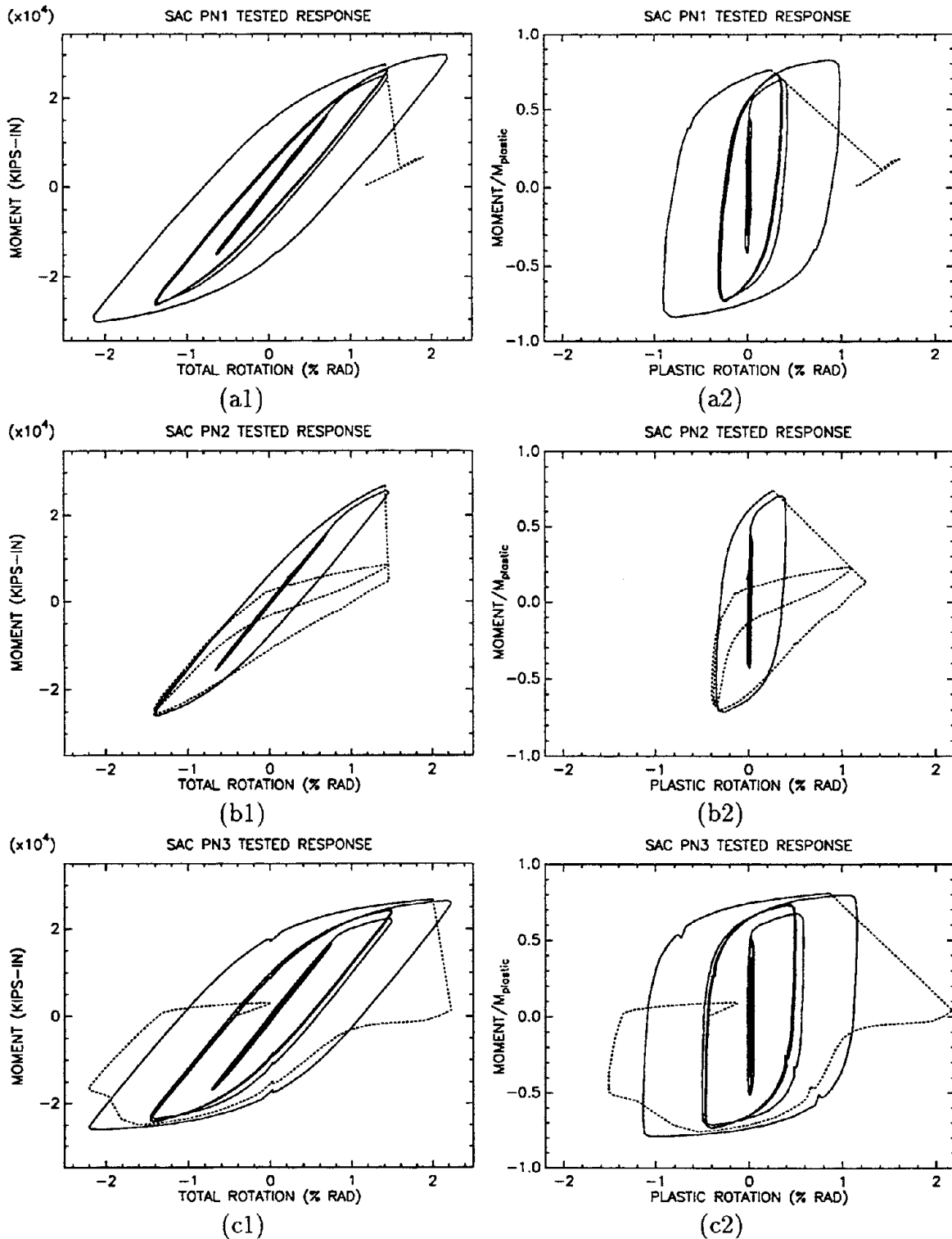


Fig. 2.14: Moment-rotation and moment ratio-plastic rotation diagrams for SAC PN1, PN2 and PN3 specimens.

Specimen Number	Load (kips)	Displacement Total (inches)	Displacement Beam (inches)	Post-yield cycles	Date & Temperature
PN1 - P_{yield}	154	1.31	1.15	$4\frac{1}{4}$	02/09/95 60° F
P_{peak}	225	2.91	2.63		
PN2 - P_{yield}	153	1.34	1.11	$1\frac{1}{4}$	02/16/95 50° F
P_{peak}	201	1.94	1.71		
PN3 - P_{yield}	138	1.12	1.02	$4\frac{1}{4}$	02/28/95 60° F
P_{peak}	199	3.02	2.88		

Table 2.4: Test results of the SAC Joint Venture PN specimens.

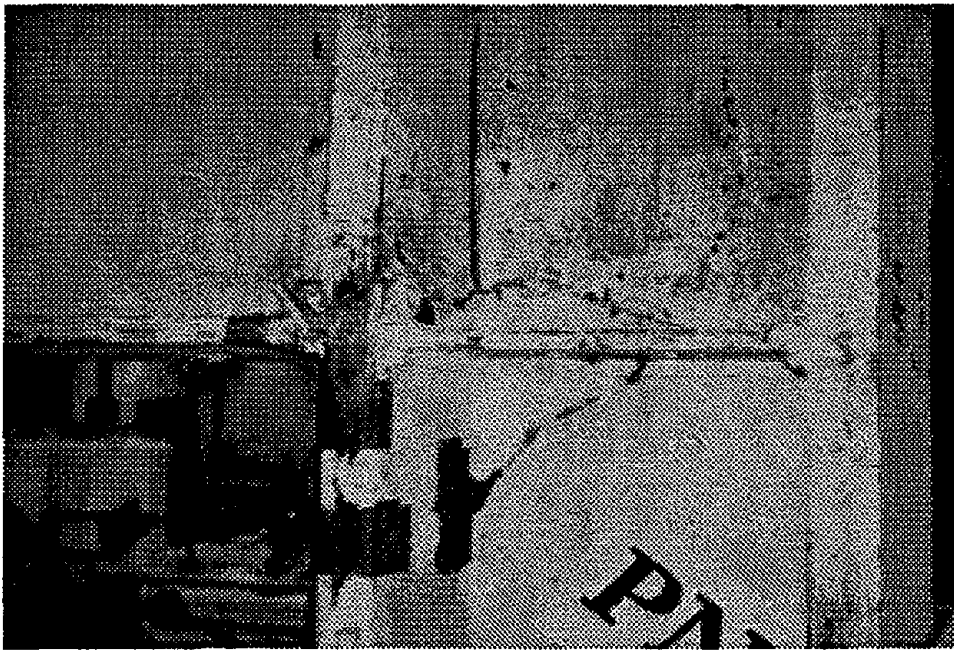


Fig. 2.15: Photograph of SAC specimen PN1 after test.

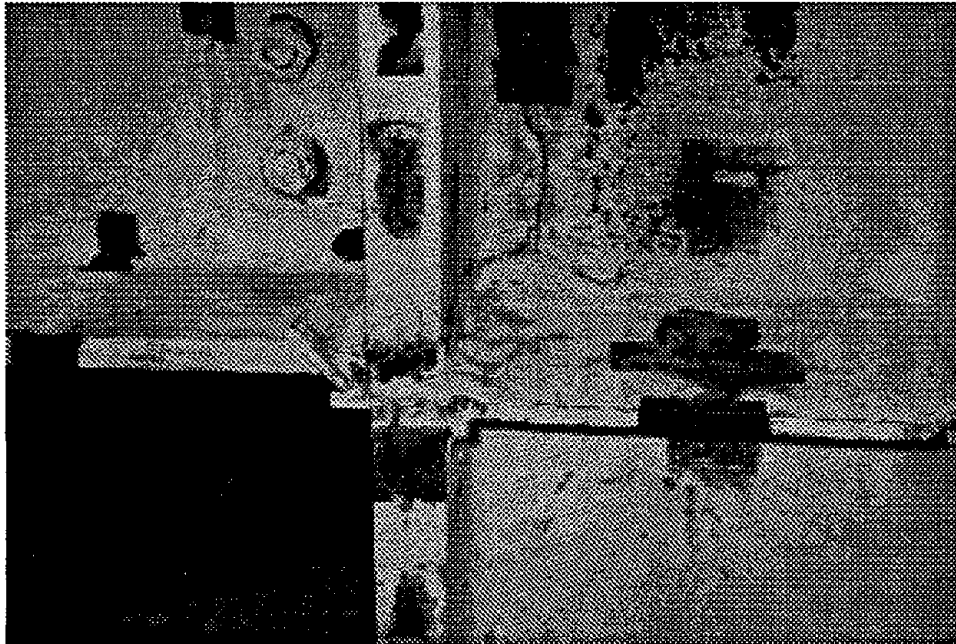


Fig. 2.16: Fracture pattern of SAC specimen PN2 is similar to specimen PN1.

post-yield cycles are smaller. The peak load of 201 kips is a little over the panel zone shear capacity. Specimen PN3 had a different fracture pattern compared with that of PN1 and PN2 specimens. The crack initiated at the center of the bottom beam flange-column juncture, then fractured the entire bottom beam flange (see Fig. 2.17). According to the classification in Table 2.2, PN1 and PN2 had failures of Type 2 because both had a strong beam and a relatively weak panel zone. The failure mode of PN3 is Type 1. All three specimens performed unsatisfactorily and failed in abrupt fractures. The imposed displacements and hysteresis loops for these specimens will be presented together with the analytical results in a later section.

It is interesting to note that if the beams of the SAC specimen had a yield strength of 36 ksi and an ultimate strength of 58 ksi, the performance of the connections would be much better and the failure mode would also be different. Compared with many successful connection tests back in the 1970s [54, 55], the design method and procedure are almost the same today. The most significant difference is that the material strength in the 1970s was much nearer to the ASTM specified minimum.

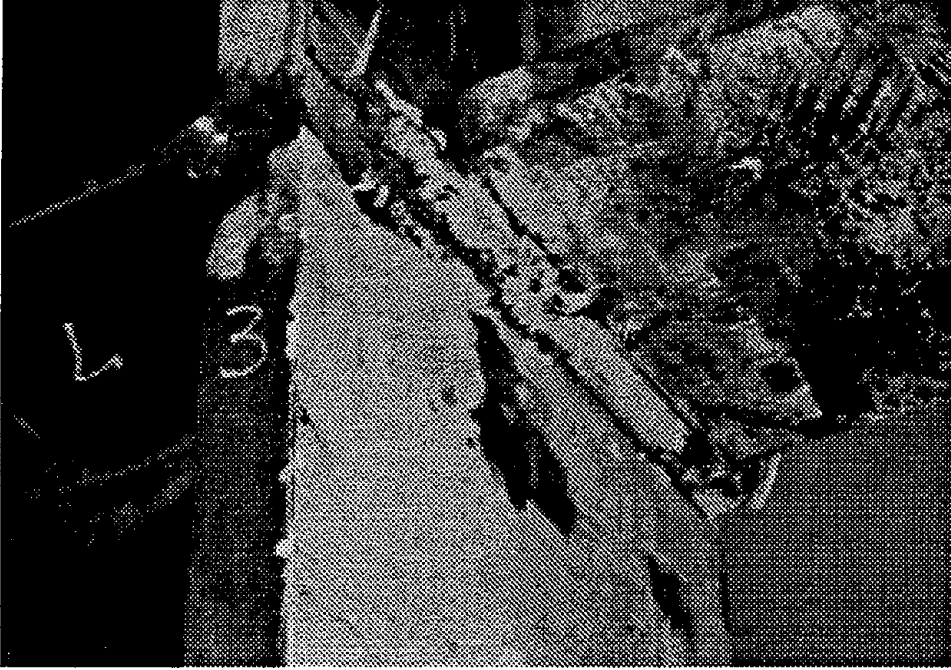


Fig. 2.17: Photograph showing the fractured bottom beam flange of SAC PN3 specimen after test.

2.6 Stress Concentration Caused by the Backing Bar

If the backing bar has not been removed after welding, the unfused interface between the backing bar and the column flange acts as a fine crack. The length of the crack is equal to the thickness of the backing bar (Fig. 2.18). Theories for analyzing the stress field near cracks are now well-established and can be found in many standard texts such as Anderson [5], Broek [19], Rolfe and Barsom [61], and Suresh [67]. The stresses in the vicinity of a crack tip in an elastic material can be expressed as [34, 35, 72]

$$\begin{aligned}
 \sigma_{xx} &= \frac{K}{\sqrt{2\pi r}} \cos\left(\frac{\theta}{2}\right) \left[1 - \sin\left(\frac{\theta}{2}\right) \sin\left(\frac{3\theta}{2}\right)\right] \\
 \sigma_{yy} &= \frac{K}{\sqrt{2\pi r}} \cos\left(\frac{\theta}{2}\right) \left[1 + \sin\left(\frac{\theta}{2}\right) \sin\left(\frac{3\theta}{2}\right)\right] \\
 \sigma_{xy} &= \frac{K}{\sqrt{2\pi r}} \cos\left(\frac{\theta}{2}\right) \sin\left(\frac{\theta}{2}\right) \cos\left(\frac{3\theta}{2}\right)
 \end{aligned} \tag{2.27}$$

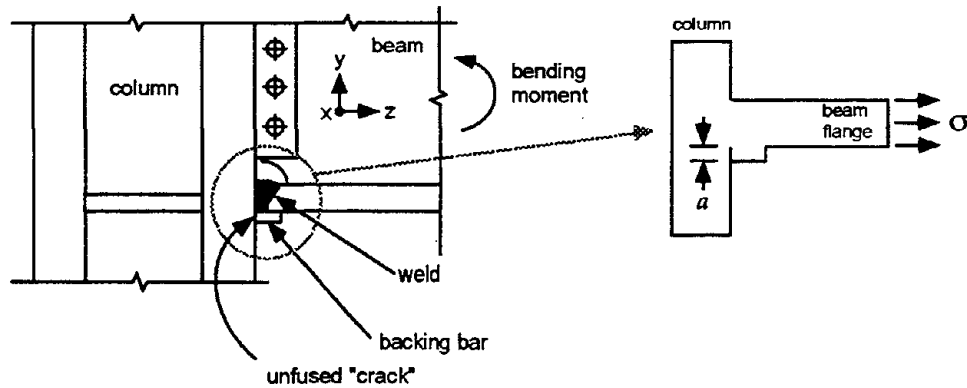


Fig. 2.18: The unfused backing bar surface forms an artificial edge crack.

for a crack aligned in the x direction, where K is the stress intensity factor and, r , θ are the cylindrical polar coordinates of a point with respect to the crack tip. Thus, each case is characterized by the stress intensity factor having a spatial distribution of stresses. One of the underlying principles of fracture mechanics is that unstable fracture occurs when the stress-intensity factor K at the crack tip reaches a critical value K_c . To prevent a fracture failure, the computed stress-intensity factor K must be less than the critical stress-intensity factor, or fracture toughness, K_c .

The “artificial crack” between the unfused backing bar and the column flange can be characterized as an edge crack. There are three possible fracture modes of a crack (Fig. 2.19), namely Mode-I (Opening), Mode-II (In-plane shear), and Mode-III (Out-of-plane shear). Tension in a beam flange due to bending opens the crack in mode-I⁴. The Mode-I stress-intensity factor for the edge crack is shown to be

$$K_I = 1.12\sigma\sqrt{\pi a} \quad (2.28)$$

where a is the crack length, here the thickness of the backing bar, and σ is the applied nominal Mode-I stress (Fig. 2.20a). The critical stress-intensity factor K_{Ic} of Mode-I can be obtained by following the ASTM standard for determining K_{Ic} [6]. K_{Ic} is temperature sensitive. For carbon steel, the transition is quite steep at temperatures above 0°F.

⁴The shear and torsional forces in the beam can also open the crack in mode-II and mode-III, respectively, but their magnitudes are relatively small and can be ignored.

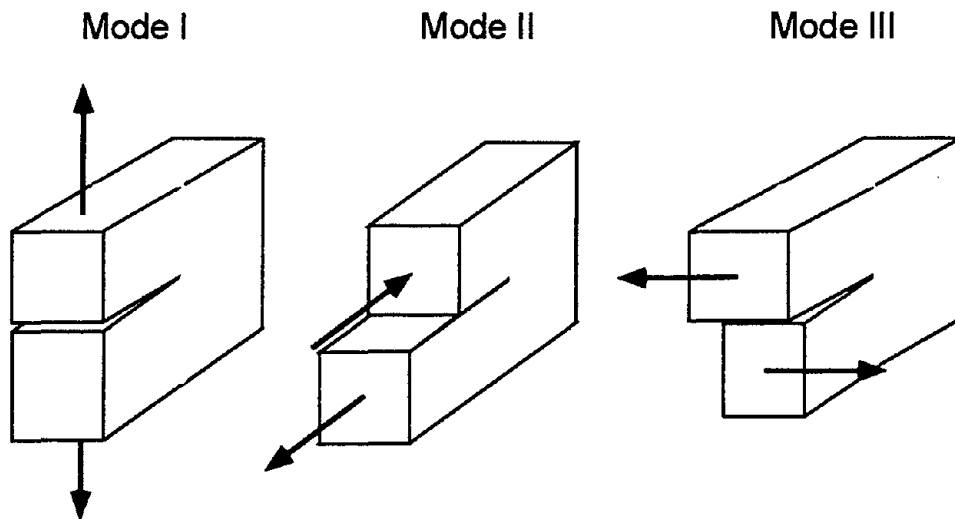


Fig. 2.19: The three modes of loading that can be applied to a crack: Mode-I (Opening), Mode-II (In-plane shear), and Mode-III (Out-of-plane shear).

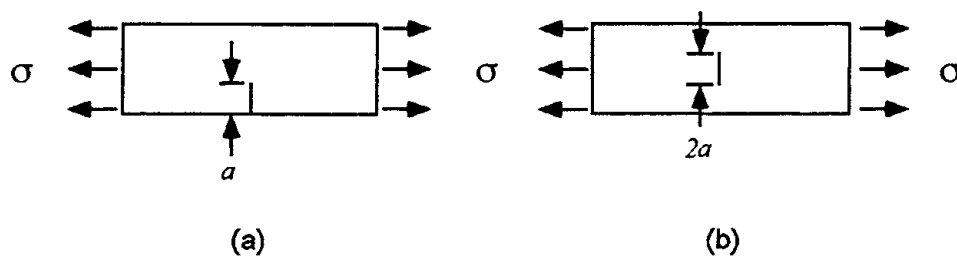


Fig. 2.20: A semi-infinite plate with (a) edge crack, (b) center crack subject to a remote axial stress σ .

K_{Ic} can also be obtained from the critical energy release rate \mathcal{G} (after Griffith [24]) of the material from

$$K_{Ic} = \sqrt{\mathcal{G}E'} \quad (2.29)$$

where E' is the modified modulus of elasticity, it can be computed as

$$E' = \begin{cases} E & \text{for plane stress} \\ E/(1 - \nu^2) & \text{for plane strain} \end{cases} \quad (2.30)$$

where E is the Young's modulus and ν the Poisson's ratio. The crack between the backing bar and column flange is long enough to be considered as a plane strain problem.

The critical energy release rate \mathcal{G} is temperature sensitive. For structural carbon steel, it is known that \mathcal{G} is at least 15 lb-ft (see [9, 62]). The critical stress-intensity factor can be calculated to be

$$K_{Ic} = 75.7 \text{ ksi}\sqrt{\text{in}} \quad (2.31)$$

Based on this value and in the case that $K_I = K_{Ic}$, if the thickness of the backing bar is 3/8 inch, then according to Eq. 2.28, the nominal stress σ_{zz} in the beam flange cannot be more than 62.3 ksi⁵.

There are two ways to reduce the deleterious effect of the backing bar. A direct method is to remove it using a carbon arc. Once the backing bar has been removed, the artificial crack no longer exists. The advantage of this method is that the root pass of the weld can be examined. But this method has a high probability of damaging a good weld above the backing bar. Another method to reduce the stress concentration caused by the backing bar is to apply a fillet weld under it to close the crack. But one must use other non-destructive tests to ensure that the root pass of the weld is good. A center crack of length $2a$ occurring away from the edges, such as the one shown in Fig. 2.20b, has a smaller stress-intensity factor, namely,

$$K_I = \sigma\sqrt{\pi a} \quad (2.32)$$

Here, a is half of the backing bar thickness. For a center crack and in the case that $K_I = K_{Ic}$, if the thickness of the backing bar is 3/8 inch, then according to Eq. 2.32,

⁵ $1.12\sigma\sqrt{\pi(3/8)} = 75.7$, hence $\sigma = \sigma_{zz} = 62.3$ ksi

the nominal stress $\sigma_{zz} = \sigma$ in the beam flange cannot be more than 98.6 ksi⁶. An additional small fillet weld under the backing bar will reduce the stress-intensity factor by a ratio of $62.3/98.6 = 0.63$ and substantially improve the connection fracture resisting capability.

In this section, it is assumed that the stress σ across the beam flange is uniform with linear elastic behavior, but in reality, σ is not uniform. The geometry of the backing bar crack is not similar to the edge or center crack shown in Fig. 2.20. Applying Eqs. (2.28) and (2.32) to the backing bar crack problem is oversimplified. To account for the effects of the geometry, non-uniform stress distribution, and elastic-plastic material behavior, the numerical J contour integration by finite element method must be used.

2.7 Nonlinear Finite Element Analysis

In order to accurately evaluate the stress distribution and the stress-intensity factor at the connection, the SAC specimens are modeled on eight-node brick elements in the ABAQUS finite element package [30]. The element mesh of the connection part of the specimen is shown in Fig. 2.21. Note that the backing bars together with the artificial cracks mentioned previously are introduced in the model. As of this writing, the SAC specimens are being retrofitted for re-testing, and no tension tests for the material are available at the moment. Because the true material properties are unknown, the material properties used in the finite element model are based on the Mill Certificates as given in Table 2.3. The coupon test will be scheduled right after the completion of structural testing of the retrofitted connections. The material properties were modeled by von Mises yield criterion with associated plastic flow.

To fully understand the stress distribution and propagation during the structural testing, the same imposed beam tip displacements were used in the finite element computations. Because the applied loads are slowly varying in the test, the inertia loads are ignored in the finite element analysis. Figure 2.22 displays the imposed tip displacements for experimental and analytical studies of the PN1 specimen. The analysis steps shown in the figure are not evenly spaced because it requires more steps in the nonlinear region. To accelerate the analysis, low amplitude displacement

⁶ $\sigma\sqrt{\pi(3/8)(1/2)} = 75.7$, hence $\sigma = \sigma_{zz} = 98.6$ ksi

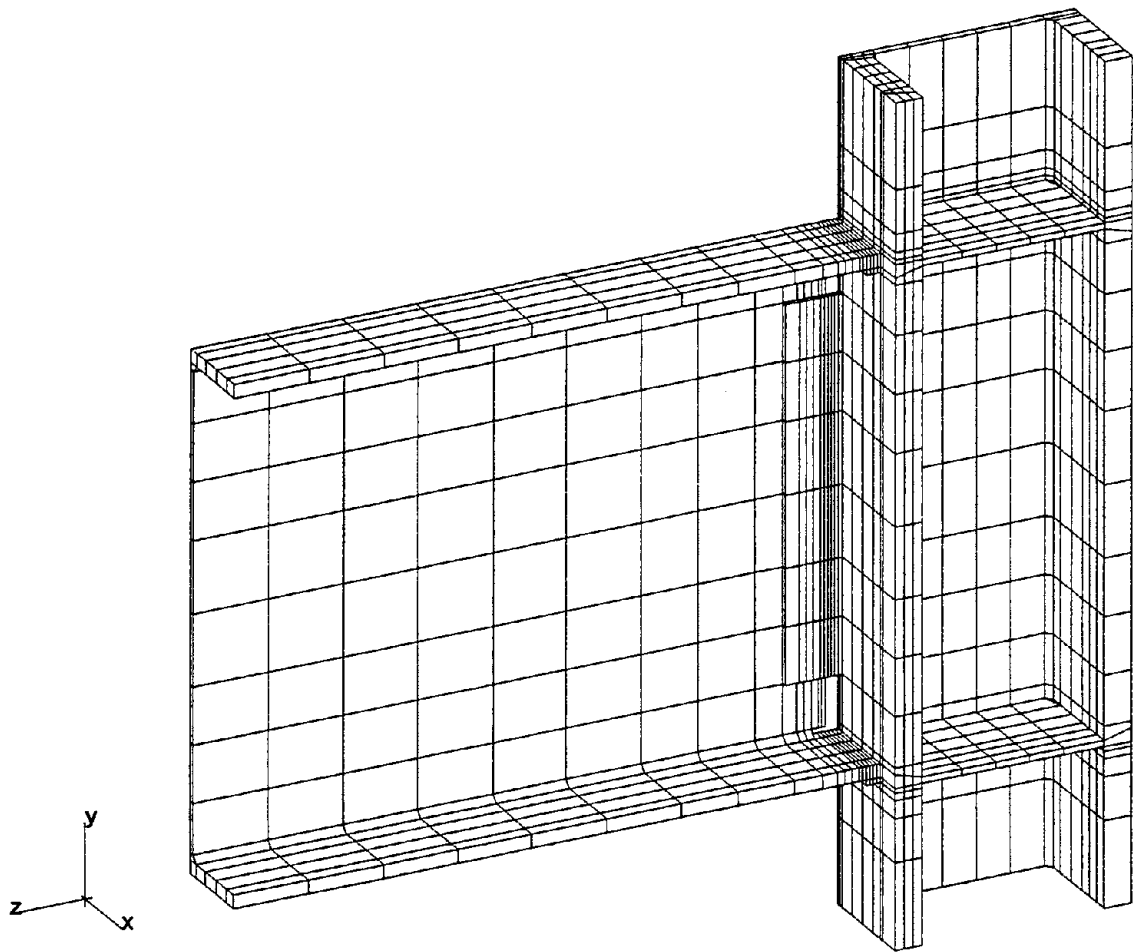


Fig. 2.21: Finite element mesh for SAC Pre-Northridge PN connection. Only one half of the specimen is modeled.

cycles are ignored, these including two 0.1 in. cycles, three 0.25 in. cycles, and three 0.5 in. cycles. Because the hot rolling residual stresses and the heat-affected zone residual stresses are not fully known, such effects are also ignored in analyses. Such simplifications make the corners in the analytical hysteresis loops sharper than the experimental ones. The experimental and analytical hysteresis loops for the SAC PN1 Specimen are presented in Fig. 2.23. The experimental and analytical imposed displacements and hysteresis loops for the SAC PN3 specimen are shown in Figs. 2.24 and 2.25, respectively. The low amplitude displacement cycles are also ignored in the PN3 analysis. By integrating the hysteresis loops step-by-step, the total energy diagram can be constructed. The total strain energies of PN1 and PN2 specimens are given in Fig. 2.26. The wavy shape curve in the total energy diagram is due to the restoration of elastic strain energy during load reversals. Those unrecoverable energies are dissipated energy. The same diagrams for the PN3 specimen are given in Fig. 2.27. These figures lead to the conclusion that none of the three SAC specimens possessed adequate energy dissipating capacities.

Among the three SAC specimens, PN2 has the least ductile behavior. The imposed displacements and load-deflection responses are shown in Fig. 2.28. Because the PN2 specimen is identical to the PN1 specimen, the analytical response of the PN1 specimen can be used for comparison. The total energy diagram for the PN2 specimen is given in Fig. 2.26a.

A perspective view of the connection stress distribution is shown in Fig. 2.29. The highest stressed spots are at the beam flange weld and in the panel zone. The material yielding in the panel zone starts at the center and then gradually expands outward. During the test, the whitewash was continuously breaking off in the panel zone. When the tip load reached about 200 kips, the entire panel zone yielded. The analytical stress contours in Fig. 2.30 agree with this observation. Figures 2.31 and 2.32, respectively, show views of the stress contours of the top and bottom beam flanges, together with the continuity plates and column section in the plastic range. In the elastic range, the largest stress occurs at the center of the beam flange-column juncture. The stresses become much more evenly distributed across the beam flange in the plastic range, but the center of the flange still has the largest stress. All the displacements in these figures are magnified 10 times. Even so, there is no obvious deformation observed in the axial direction of the beam flange.

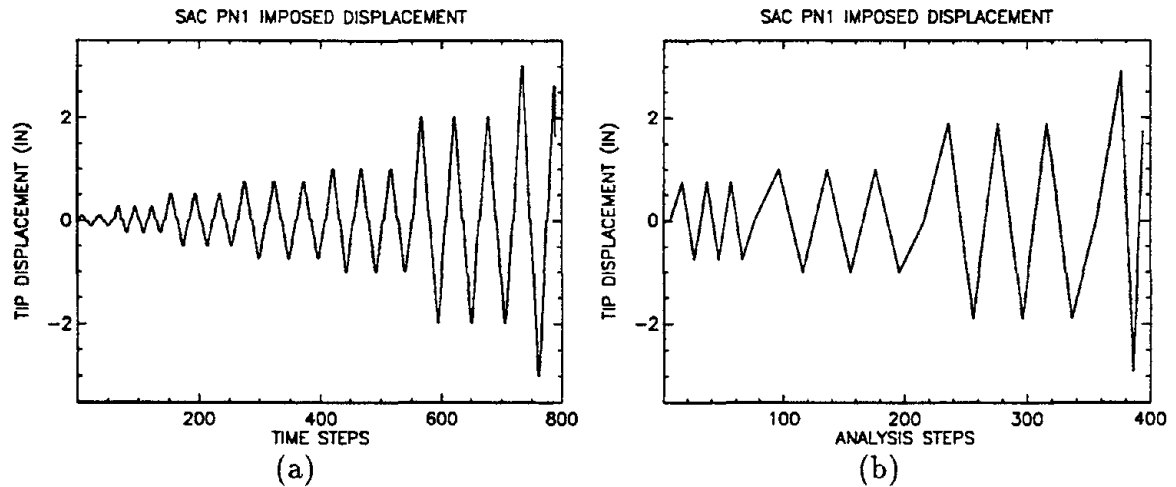


Fig. 2.22: (a) Imposed tip displacements used in testing SAC PN1 specimen, and (b) imposed tip displacements used in finite element analysis.

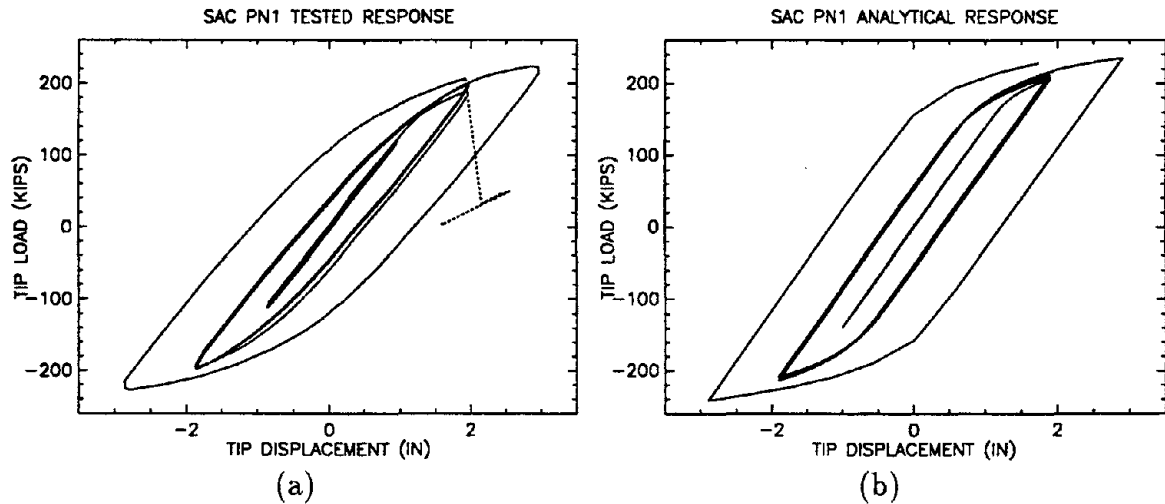


Fig. 2.23: (a) Experimental and (b) analytical hysteresis loops of SAC PN1 specimen (Displacements are measured in the loading direction).

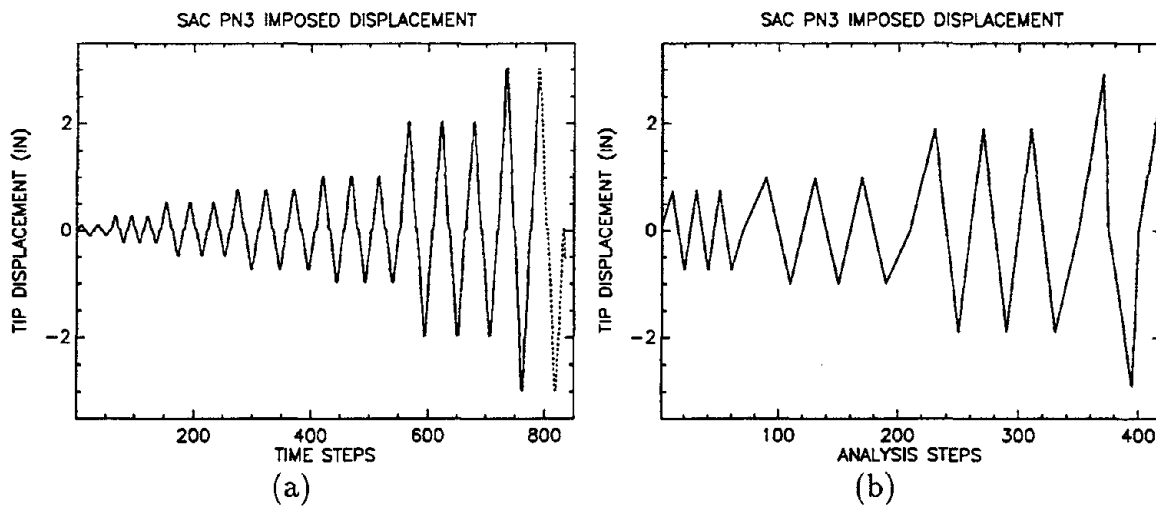


Fig. 2.24: (a) Imposed tip displacements used in testing SAC PN3 specimen, and (b) imposed tip displacements used in finite element analysis. The dashed line represents the imposed displacements after the bottom beam flange was fractured.

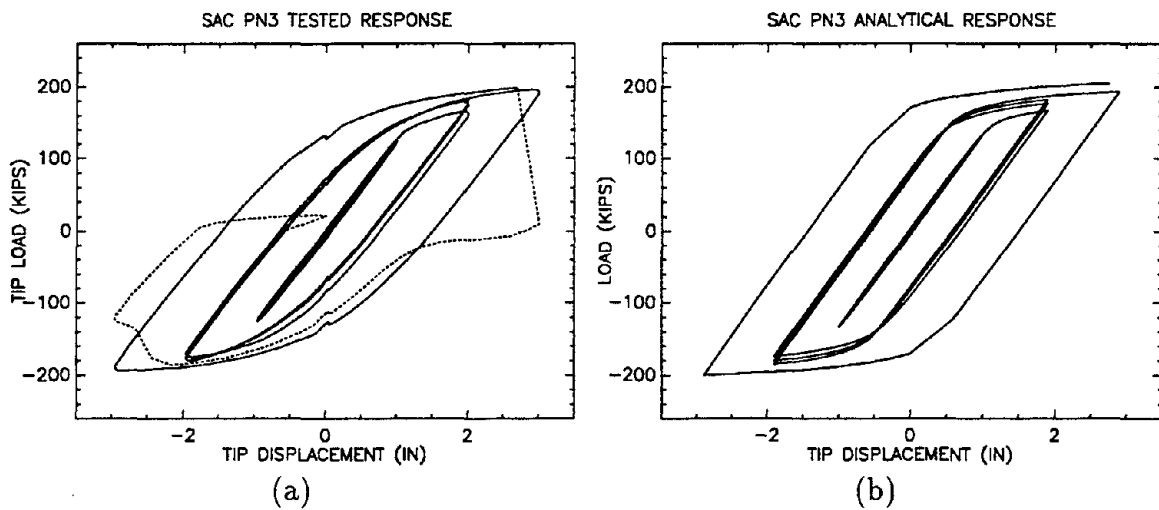


Fig. 2.25: (a) Experimental and (b) analytical hysteresis loops of SAC PN3 specimen (Displacements are measured in the loading direction). The dashed curve represents the response after the fracture of the bottom beam flange.

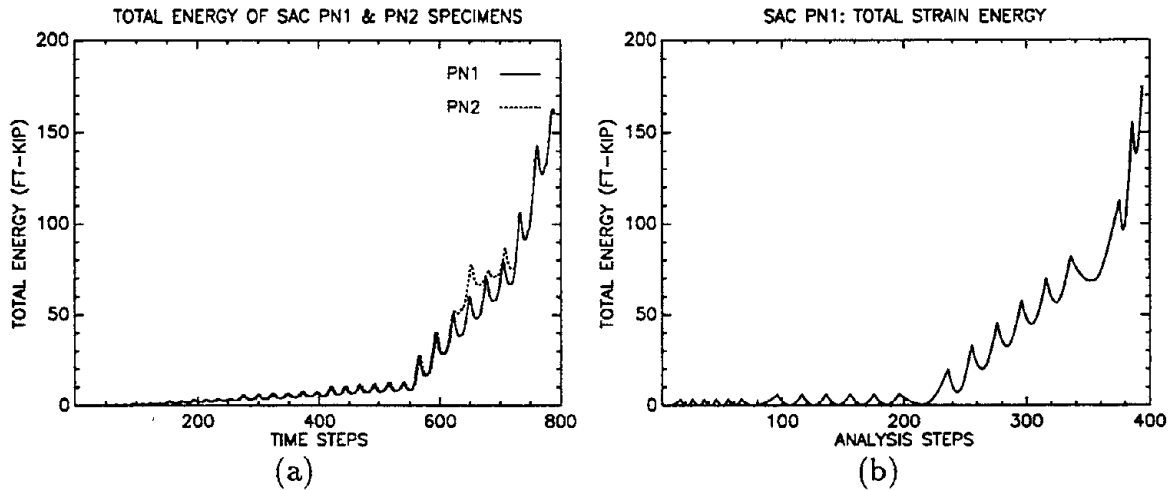


Fig. 2.26: (a) Experimental and (b) analytical total strain energy diagrams of SAC PN1 and PN2 specimens.

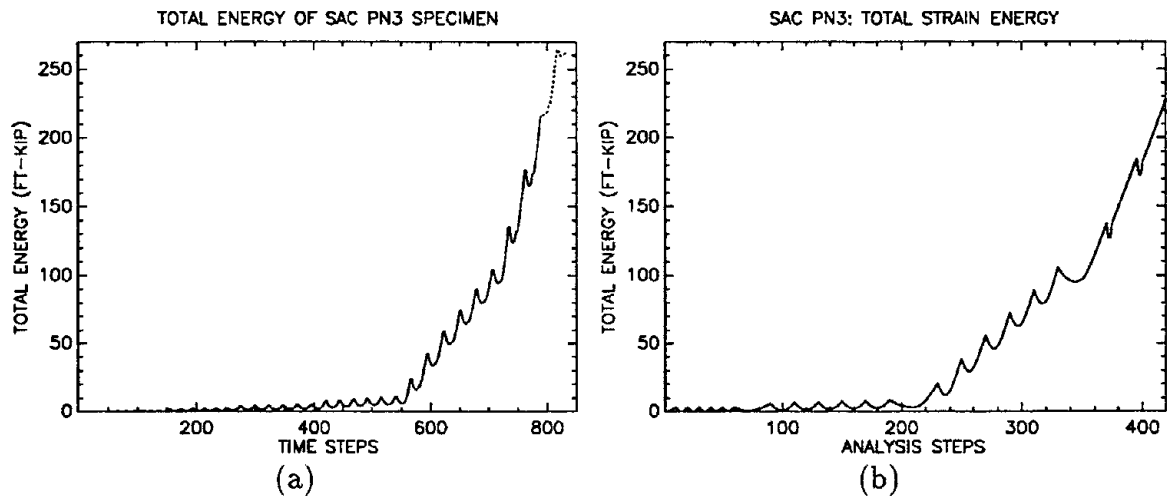


Fig. 2.27: (a) Experimental and (b) analytical total strain energy diagrams of SAC PN3 specimen.

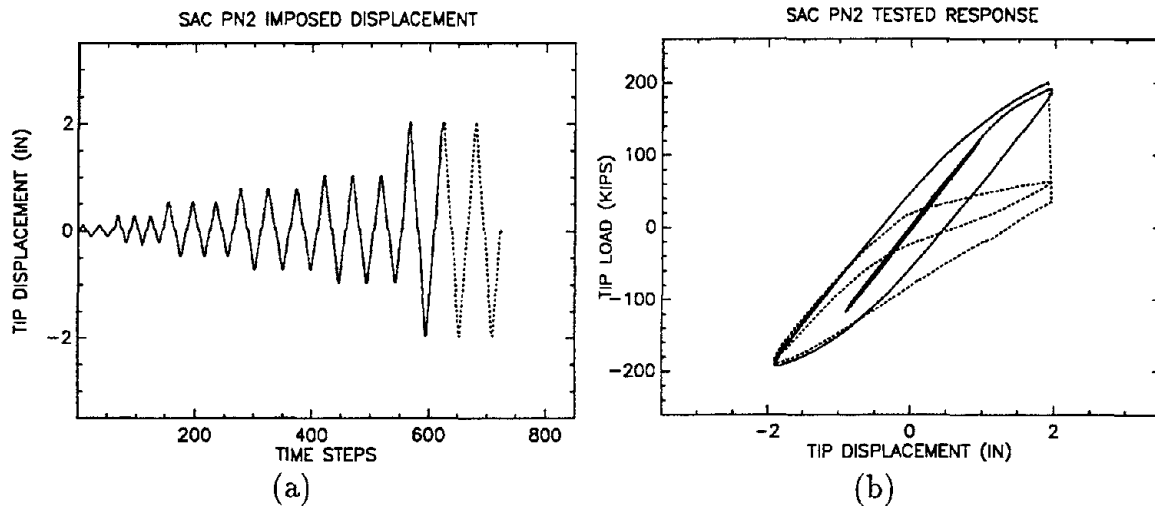


Fig. 2.28: (a) Imposed displacements and (b) hysteresis loops of SAC PN2 specimen (Displacements are measured in the loading direction). The dashed curves represent the response after the fracture of the bottom beam-column juncture.

The SAC PN1/PN2 stress distributions for the bottom beam flange along the line of groove weld are shown in Fig. 2.33. Curves shown are for beam tip loads of 21, 41, 62, 82, 103, 117, 142, 200, and 225 kips. Shearing stresses are not shown because their values are small. The maximum shearing stresses at 225 kips tip load are 3.6 ksi, -17.4 ksi, 17.5 ksi for σ_{xy} , σ_{xz} , and σ_{yz} , respectively. Small shearing stresses imply small shearing deformations and small ductility of the connection.

The experimental strains at the center of the panel zone are plotted against the applied tip load for three SAC specimens (see Fig. 2.34). The load-shear strain diagrams show large shear strain in the PN1 panel zone, but much smaller shear strain in the PN2 and PN3 panel zones. The PN3 panel zone resists smaller shear force, its panel zone shows only slight yielding but no fracture. From the material strength point of view, there is no doubt that PN1 failed in the panel zone by overstressing, but it is difficult to reach the same conclusion for PN2, although both have the same fracture pattern in the panel zone. It is much simpler to explain this by fracture mechanics.

The J contour integrals along the top and the bottom backing bar crack tip are evaluated. In calculating the J contour integral using the finite element method, the nonlinear elastic-plastic material properties are considered. Rice had formulated the

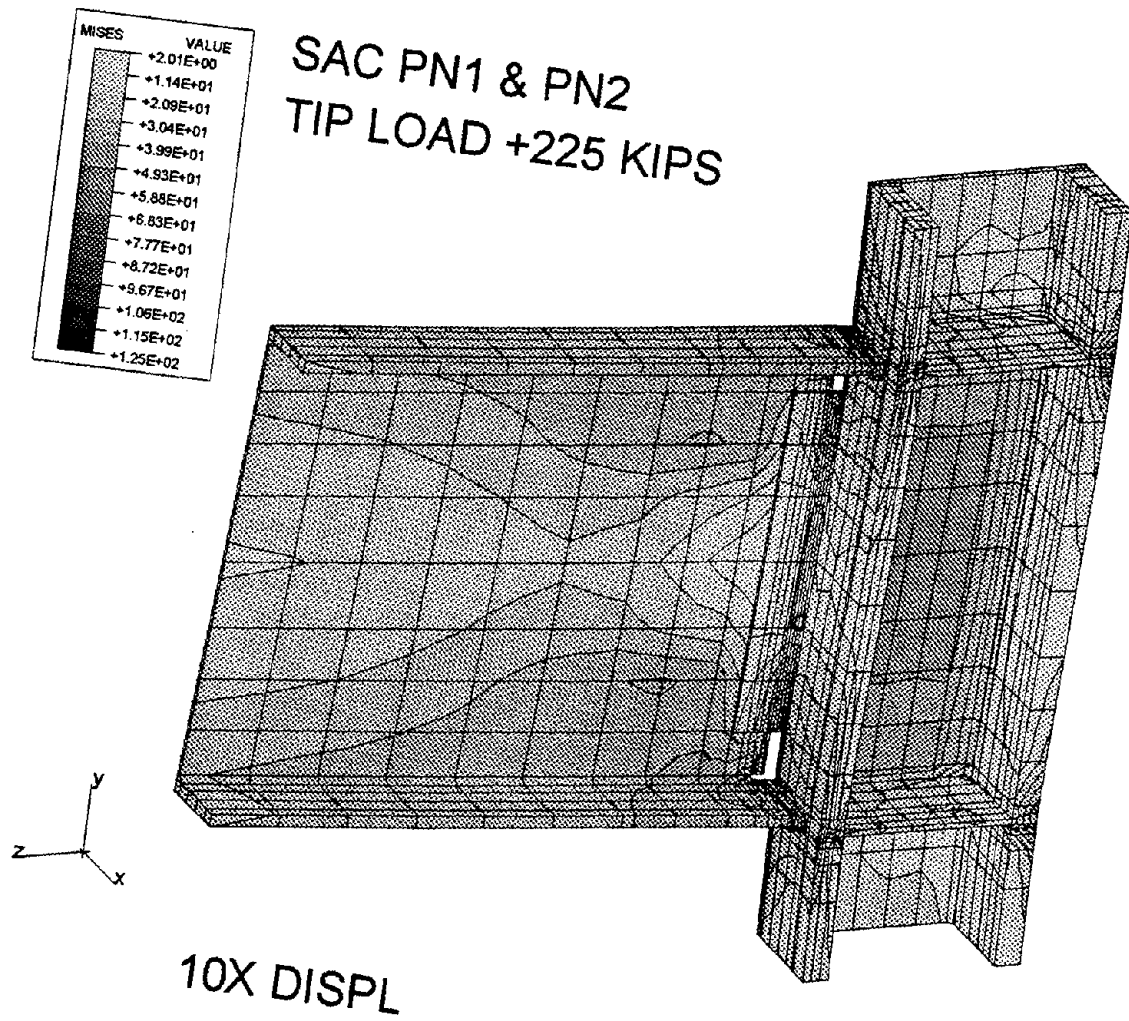


Fig. 2.29: Von Mises Stress contours for SAC PN1/PN2 under 225 kips tip load.

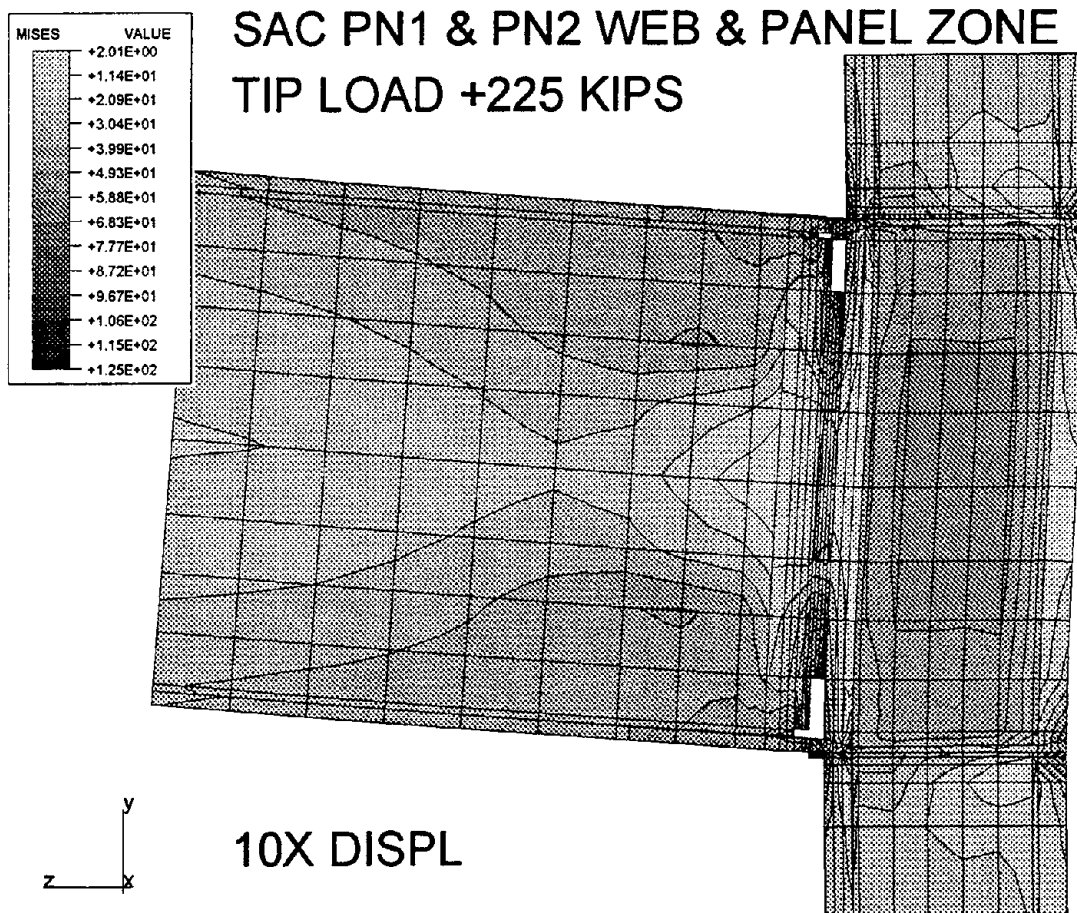


Fig. 2.30: Web and panel zone stress contours for SAC PN1/PN2 under 225 kips tip load.

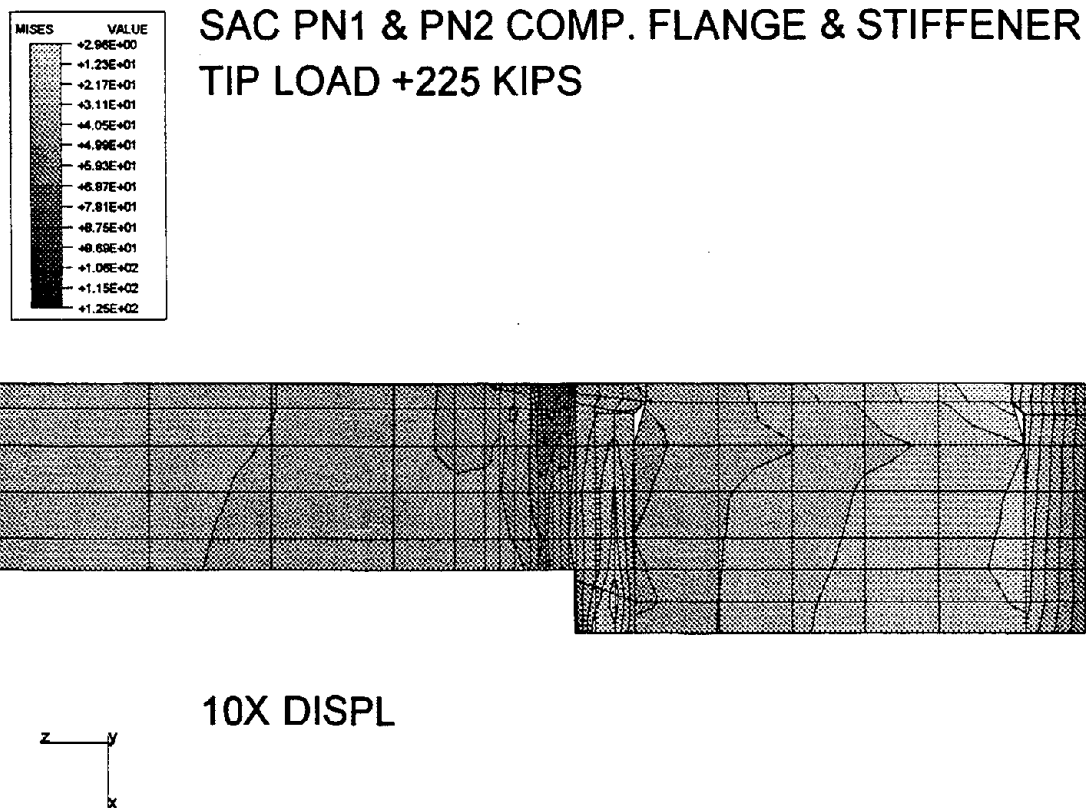


Fig. 2.31: Top beam flange and continuity plate contours for SAC PN1/PN2 under 225 kips tip load.

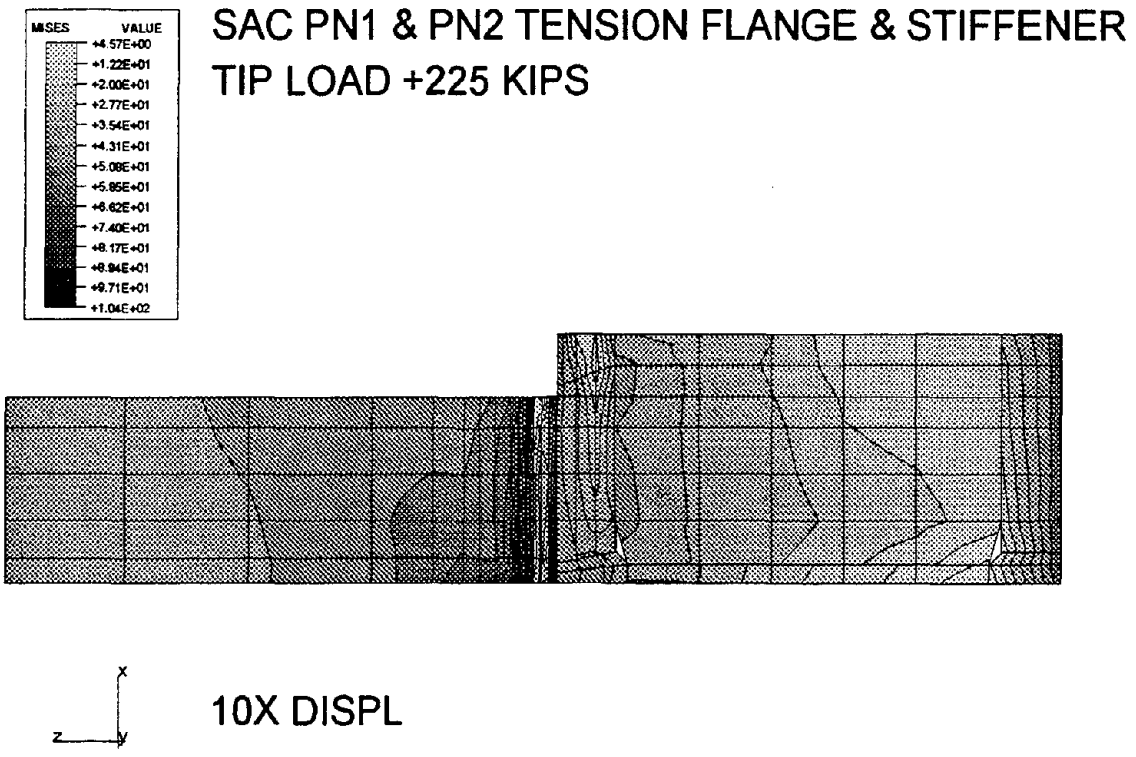


Fig. 2.32: Bottom beam flange and continuity plate contours for SAC PN1/PN2 under 225 kips tip load.

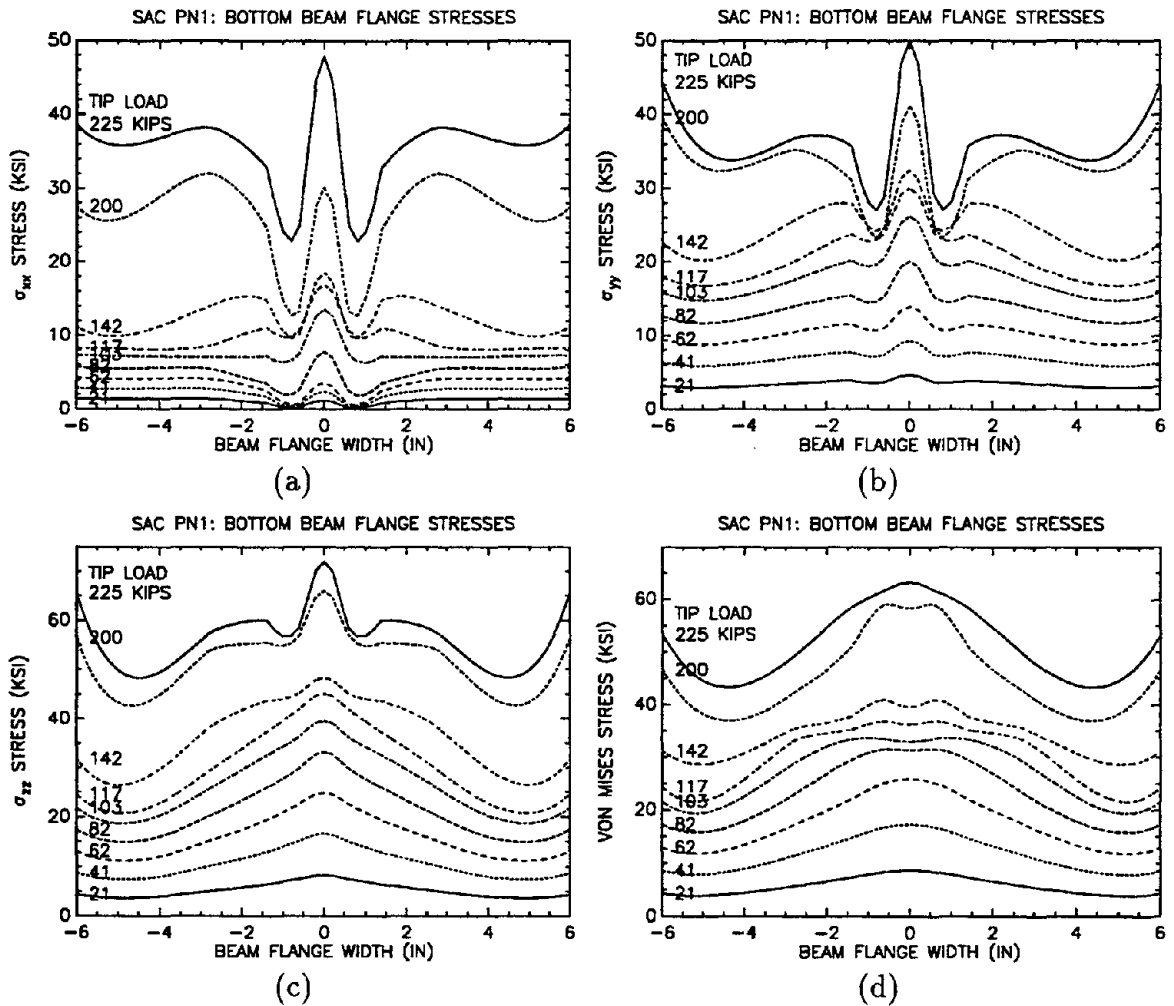


Fig. 2.33: Stress distribution across the bottom beam flange at weld for SAC PN1 and PN2 specimens: (a) σ_{xx} , (b) σ_{yy} , (c) σ_{zz} , and (d) von Mises stress.

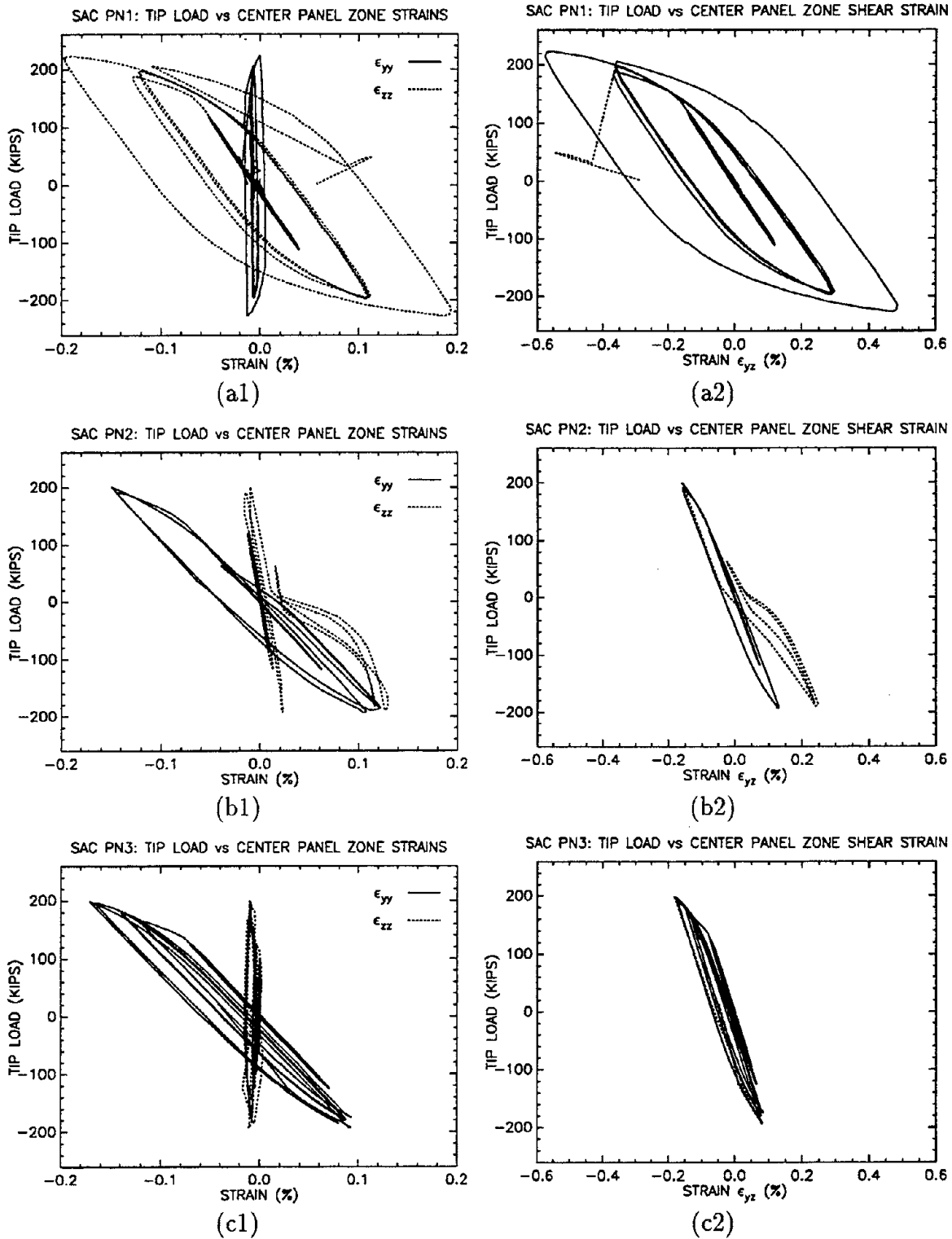


Fig. 2.34: Center panel zone strains vs tip load for SAC PN1, PN2 and PN3 specimens.

J contour integral defined to be [58]

$$J = \int_{\Gamma} \left(w dy - T_i \frac{du_i}{dx} ds \right) \quad (2.33)$$

for a crack aligned in the x direction. Here, Γ is any contour from the lower crack face counterclockwise around the crack tip to the upper face. The path length along this contour is s , w is the strain energy density defined as

$$w = \int_0^{\epsilon_{ij}} \sigma_{ij} d\epsilon_{ij} \quad (2.34)$$

where σ_{ij} and ϵ_{ij} are the stress and strain tensors, respectively. $T_i u_i$ are work terms for components of surface traction on the contour path, T_i , move through displacements, du_i . The J contour integral is equal to the energy release rate for a linear or nonlinear elastic material under quasi-static conditions. The integral was shown to be independent of choice of path for a crack with stress-free faces. Since the critical value J_c for A572 Grade 50 is unavailable, it is impossible to justify the initiation of fracture based on the computed J values. Fortunately, the specific temperature induced variation in stress intensity factors for the 1.5-in.-thick A572 Grade 50 specimens tested is available and presented in Fig. 2.35 [51]. In order to compare the calculated J values with the known K_{Ic} , an equivalent K_I is calculated [36]:

$$\frac{K_I^2}{E'} = J \quad (2.35)$$

where E' is defined in Eq. (2.30). It is thus conceptually equal to the Griffith term \mathcal{G} . Strictly speaking, the above equation only holds under elastic conditions. But if the plastic zone at the crack front is small, this equation is valid. The equivalent K_I values from the computed J values for the top and the bottom backing bars for PN1 and PN2 are shown in Fig. 2.36. In the figures, K_I values are plotted against beam width and analysis steps. It can be seen that the largest K_I occurs at the center of the beam flange-backing bar juncture. If the connection fractures, it will start at the point with the largest stress intensity factor. It is interesting to re-plot the largest stress intensity factor vs. the applied tip load (see Fig. 2.37). The growth of K_I due to cyclic load can be seen. The critical stress intensity factors at 0°F, 50°F and 60°F taken from Fig. 2.35 are also plotted in the diagram. The most interesting finding in the figure is that the bottom backing bar K_I at a given time is larger than that of the

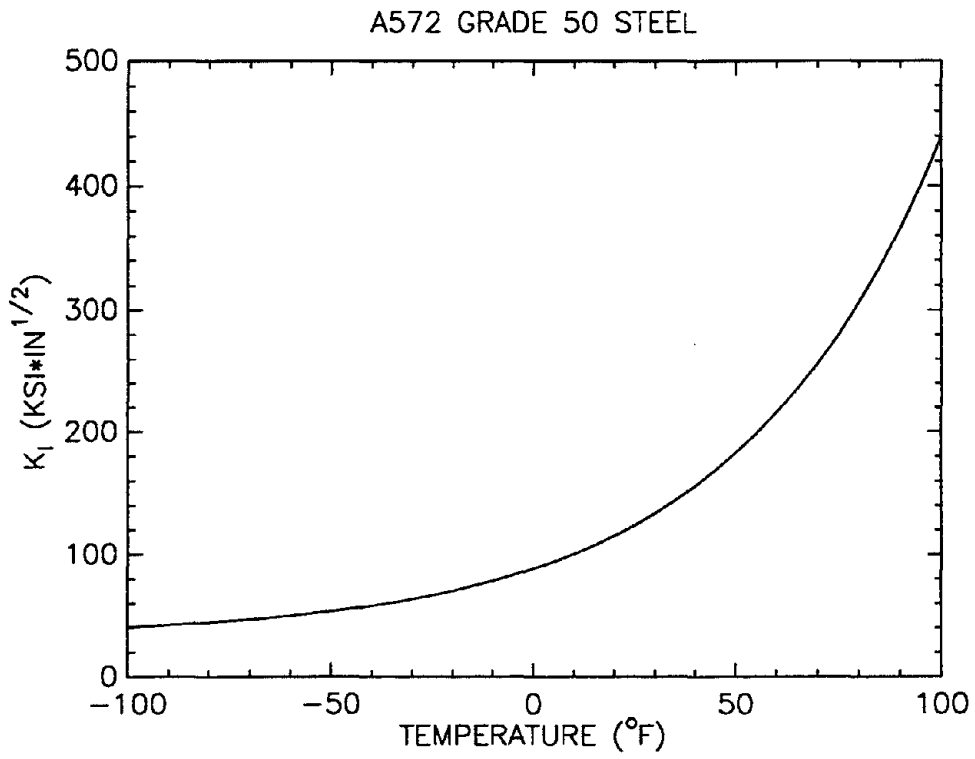


Fig. 2.35: Stress intensity factors plotted against temperatures obtained from 1.5-in.-thick plates of A572 steel.

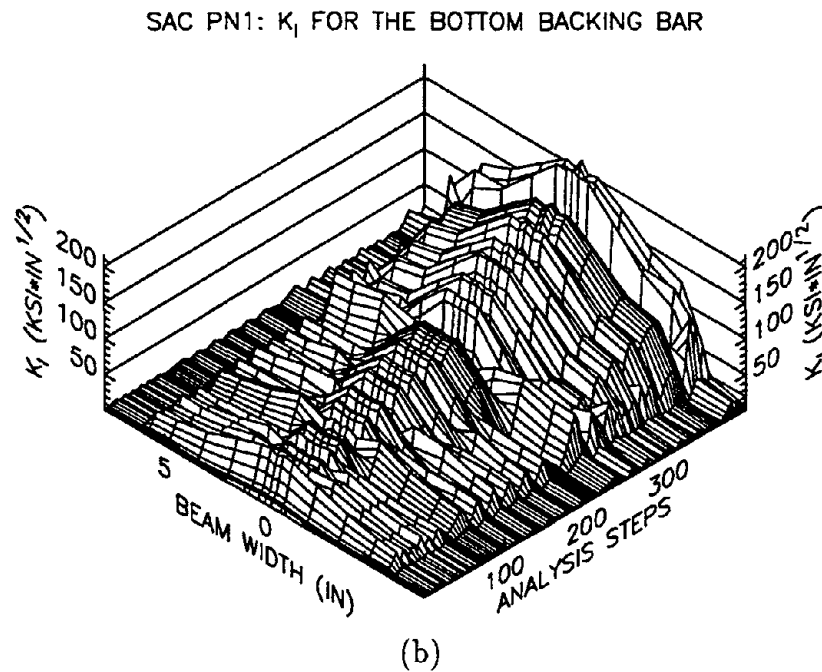
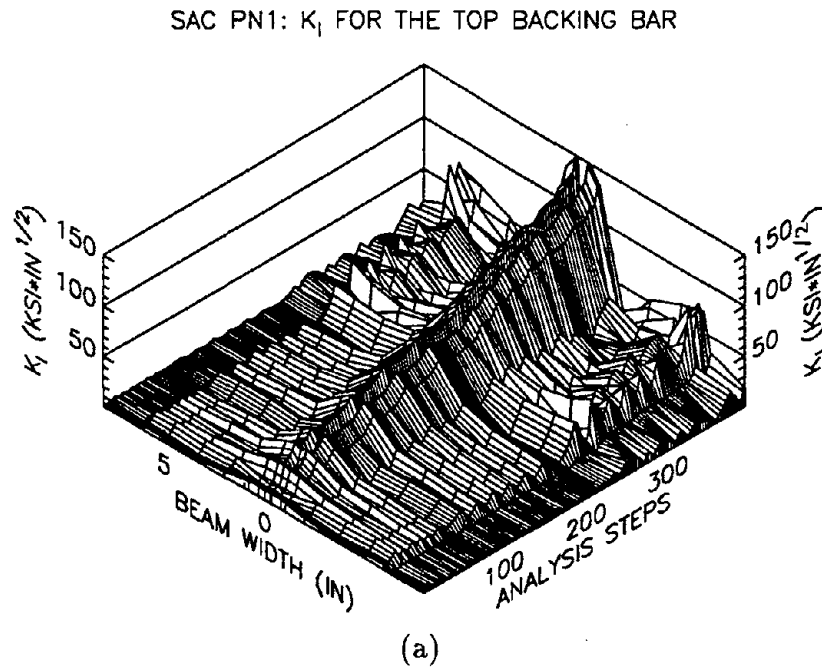
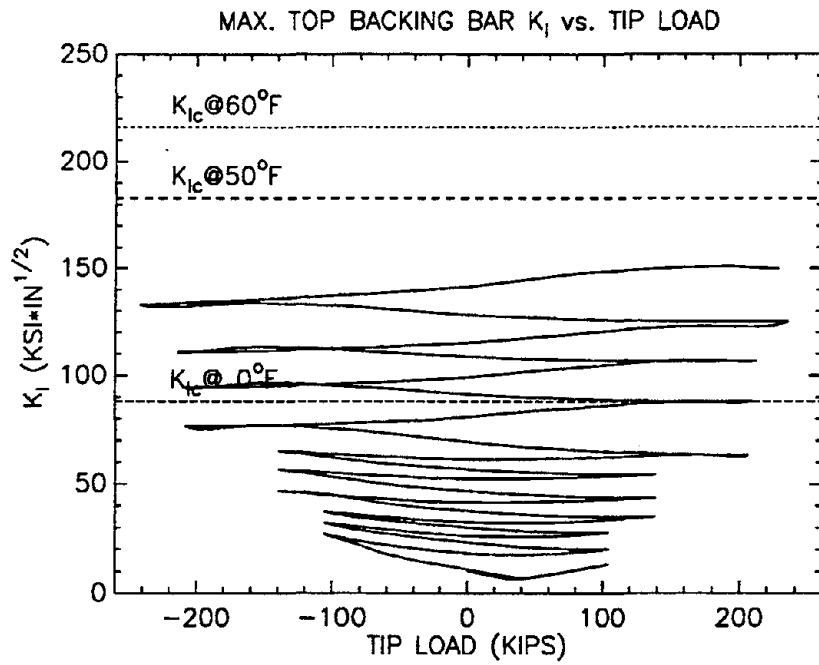
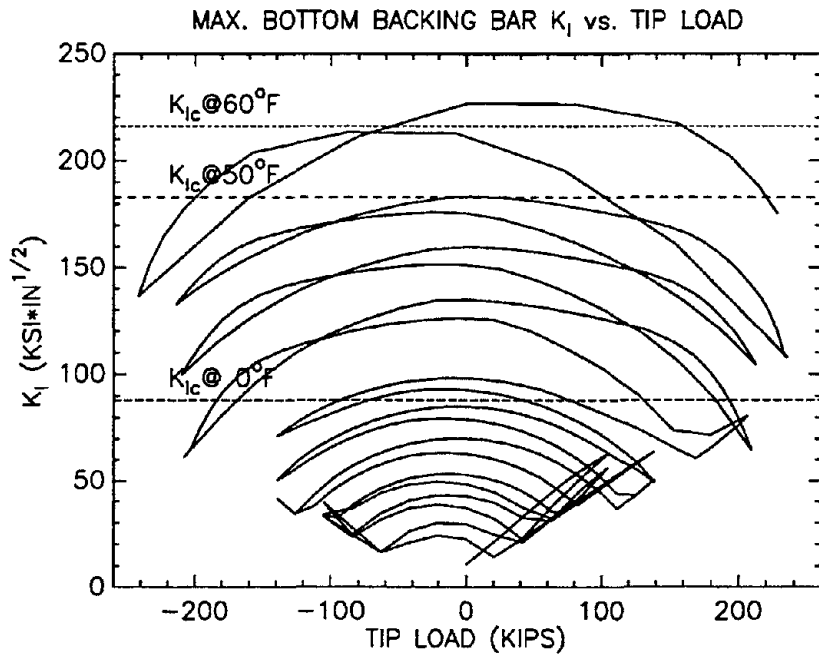


Fig. 2.36: Stress-intensity factors plotted across beam width and number of analysis steps at (a) top and (b) bottom backing bars for SAC PN1 and PN2 specimens.



(a)



(b)

Fig. 2.37: Maximum stress-intensity factors vs. tip load at (a) top and (b) bottom backing bars for SAC PN1 and PN2 specimens.

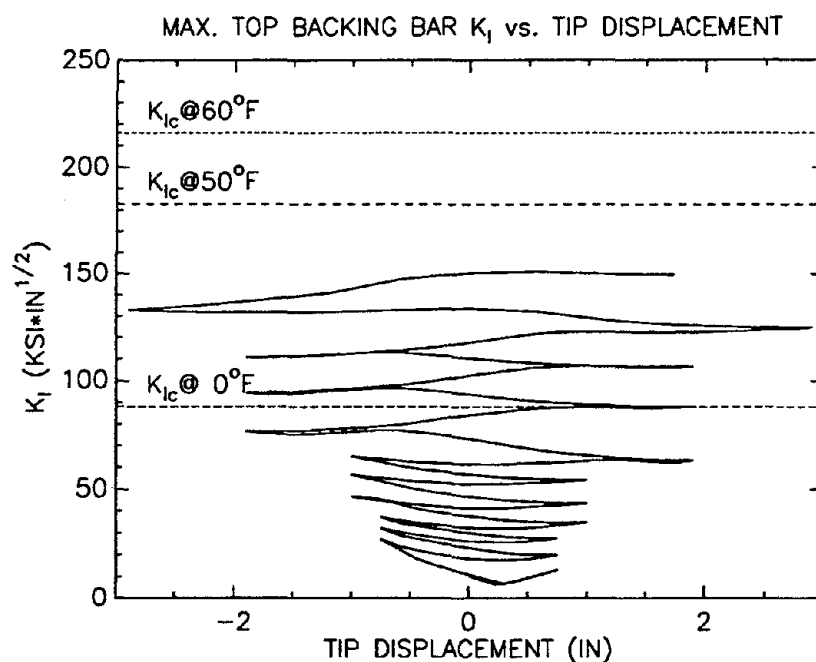
top backing bar. This clearly explains why most of the connection fractures during the Northridge earthquake initiated at the bottom backing bar.

It is also interesting to re-plot the largest K_I vs. tip displacement (see Fig. 2.38). It can be seen that the stress intensity factor keeps on growing under the same-amplitude cycles, elastic or inelastic; the larger the displacement amplitude, the larger the K_I growth rate. When K_I grows over the K_{Ic} , the connection will fracture. Based on the K_I growth rate, it is easy to predict the low-cycle fatigue fracture of the connection. The effect of temperature can be seen in these plots; the higher the temperature, the larger the K_{Ic} , and the less likely is the connection to fracture. The SAC PN1 and PN2 specimens are theoretically identical, but the PN1 specimen sustains more cycles of loading than PN2. One of the explanations for this is the different temperature. PN2 was tested on a cooler day. The low K_{Ic} value at the lower temperature meant PN2 fractured earlier.

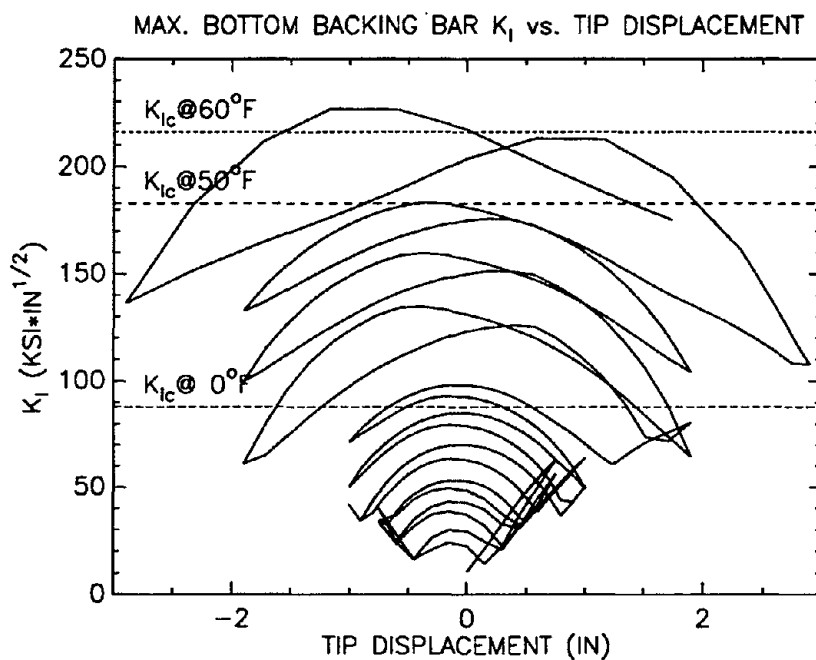
2.8 Conclusion

On the basis of these limited analytical and experimental studies, the following conclusions can be drawn:

1. Elementary mechanics calculations can predict the connection capacity very well as long as the material properties are known in advance.
2. The connection made by directly welding a compact beam flange to a column cannot attain the plastic moment of the beam. To protect the connection from failure, a weaker beam should be used or reinforcement of the connection should be made. A weaker beam means a beam with a non-compact section such that the local buckling moment is smaller than the connection moment capacity. If a compact beam must be used, the beam can be made weaker by drilling holes in the flange near the connection so that the moment transferred to the connection is smaller. There are several ways to reinforce the connection; one of the methods is by using flange cover plates with thickness greater than the beam flange thickness. But such connection requires two welds, a weld to the beam and a weld to the column, which increases the cost substantially.



(a)



(b)

Fig. 2.38: Maximum stress-intensity factor vs. tip displacement at (a) top and (b) bottom backing bars for SAC PN1 and PN2 specimens.

3. The elastic stress concentration factor at the beam flange of the welded beam-to-column connection can range between 1.2 to 1.46. The stresses will redistribute much more evenly across the flange when loaded into the plastic range. Nevertheless, the largest stress remains at the center of the welded flange.
4. Triaxial loading makes steel at a connection fail without exhibiting yielding ductile behavior. This is due to the state of stress and not because of the material property. The demand for ductility should be dependent on the material yielding near the connection area.
5. Material properties of steel, such as yield strength and ultimate strength, should be regulated to have a narrow range instead of prescribing only the minimum strength. Otherwise, an engineer cannot design a structure with tolerable bounds on response. Today's A36 steel has an average yield strength 33% over the minimum. This fact is not reflected in present design codes nor in education. This high strength does not enable the connection to develop a plastic hinge during a strong earthquake and causes its failure in brittle fracture.
6. The column web fracture is due to a weak panel zone. Using doubler plate in the panel zone may solve the problem, but will increase the construction cost. The best solution is to avoid connecting a strong beam to a column with weak web. Connecting a beam to the minor axis of a column allows for the use of column flanges to resist the shear.
7. The dimensions of many rolled shapes should be made to better proportions. For example, the W14×257 section used in the SAC specimens has a large moment capacity but a very small capacity in shear resistance.
8. The unfused surface between the backing bar and the column can be characterized as an edge crack. If the backing bar cannot be removed, an extra fillet weld under the backing bar can close the crack and makes the stress-intensity factor smaller, and thus safer. During load reversals, the stress intensity factor at the bottom backing bar crack is higher than that at the top backing bar, resulting in greater probability of initial fracture at the bottom weld during an earthquake.

9. Welded connections exposed to outside temperatures should be designed very carefully because steel has a lower critical stress-intensity factor at low temperatures. This is especially true for connections with backing bars and welding flaws.
10. Energy dissipation at a connection by the means of material yielding is notoriously unreliable. A small variation from the design value in beam or column strength will easily result in a totally different energy dissipating mechanism and failure mode.

The following important issues were not considered in this limited study, and require further research:

1. The relationships between connection strength, welding materials and welding methods require further investigation.
2. The dimensions of the panel zone (panel zone size and thickness, continuity plate thickness, and column flange thickness) are crucial to the strength of a connection. A parametric study of the panel zone is thus required.
3. Finite element analyses need to be re-done using the true material properties after the completion of the coupon test of the SAC PN specimens. High-order singularity elements should be used in modeling the crack for higher accuracy.
4. The residual stress distribution at the heat affected zone of a weld requires further investigation.
5. The internal flaw sizes between multiple layers of weld must be investigated, especially since the crack growth due to cyclic yield loads induces low cycles fatigue fracture. Such a problem will stand out in a long duration earthquake.
6. The databases of fracture toughness of structural steel and welding materials in the plastic range need to be established.
7. J contour integration analysis for the backing bar with additional under bar fillet weld is useful in understanding its merit quantitatively.
8. The welded connection, unlike the bolted connection, lacks crack resisting redundancy. Further investigation of the crack arresting design is required.

Chapter 3

Steel Joint Protection by Beam Flange Perforation

3.1 Introduction

In addition to some bad welds found and non-ductile materials used, the basic reasons for the fractures that occurred in steel moment-resisting connections during the 1994 Northridge earthquake are summarized below:

1. Today's steel strength is much higher than the ASTM specified minimum. The current specifications for steel provide a minimum strength requirement, but no ceiling for the upper limit. This makes it virtually impossible to design accurately.
2. For bolted web-welded flange moment connections, the moment capacity of the beam is always larger than the moment capacity of the connection. For a weak beam-strong column steel connection, the formation of a plastic hinge in the beam near the connection during a strong earthquake is desired. The plastic hinges provide both strength and ductility to dissipate seismic input energy. If the beam section is compact, the plastic hinge cannot develop before the fracture of the connection.
3. The column panel zone is unable to resist the shear force transmitted from the beam flanges because the current panel zone design equation is unconservative.

4. The unfused backing bar surface and the column form an artificial crack at the groove weld resulting in crack initiation due to moderate load.

The common point in the statements above is that a greater than intended strength is available in the provided steel beam. The remedy for items 2 and 3 is to use a non-compact beam section such that a plastic hinge can form by local buckling of the beam flanges. If a compact beam section must be used, then the beam strength should be locally reduced to limit the moment and shear that can be transferred to the connection and the panel zone.

The designer is unaware of the actual material properties until the material reaches the fabricator. Thus, during the fabrication stage, if the material strength of a beam is found, based on the mill certificates, to be much larger than the design value, the beam section size at the connection should be reduced to match the design moment value, thus preventing a brittle fracture.

There are many methods to reduce locally the strength of a beam, all of which are achieved by cutting off material either in a flange or web of the beam near the connection. Early research on rolled beams with drilled or punched holes was done by Dawance [21]. Dawance carried out many bending tests on rolled beams with holes in flanges and found that these holes do not appreciably affect the behavior of the section in elastic-plastic bending as long as the area cut does not exceed 15% of the total cross-sectional area of the flanges. Based on this, more than 15% of the beam flange cross-sectional area must be cut off in order to reduce the beam strength.

In this chapter, two recent research efforts on beam strength reduction by cutting off some of the flange area are reviewed. Next, the beam flange perforation method by drilling holes is introduced. In the analyses, the stress concentration factor near the line of holes in the flange is approximated by the elliptical hole formula. Then experiments on eight W12×26 beams with different perforation patterns are reported. The results show that a well-designed perforated beam can have its moment capacity reduced and its ductility increased. Next, two large size connections with perforated beam flanges are tested by cyclic loading. Test results show that both connections have a cumulative ductility of about 80 without severe strength degradation.

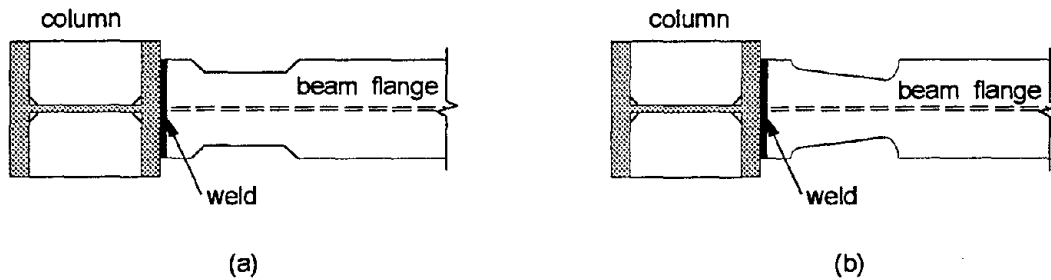


Fig. 3.1: The dog-bone connections designed by (a) Plumier, and (b) Chen & Yeh.

3.2 The Dog-Bone Connections

The underlying idea for beam strength reduction is simply to protect the beam-column connection from brittle fracture. There are not many research results available. The first known such connection is mentioned in Plumier [53], in which the flanges are torch cut in a trapezoidal shape. This patented connection is shown in Fig. 3.1a. Unfortunately, there are no quantitative performance reports of such connections. Because the shape of the beam flange for such connections resembles a dog-bone, the connections bear that name.

Another similar connection shown in Fig. 3.1b was designed and tested by Chen and Yeh [20]. The primary goal of such connections is to reduce beam strength and increase ductility. The beam flanges are cut along the bending moment gradient line such that, once a large force is applied, the material at the reduced cross-section will yield. Test results shows that the ductility increase of such connections is substantial, whereas the stiffness decreases only about 3%.

The basic idea of using yielding to increase the ductility of a member can be shown by simple tensile tests of short and long coupons (see Fig. 3.2). The situation is similar to the grooved bar test presented in the previous chapter. The longer specimen is easier to neck down, causing it to develop shear slips. The shorter specimen has greater constraint of the higher stressed material in the lateral direction, which prevents the plastic flow from developing. The ductility of the longer specimen is larger than that of the shorter one. The longer specimen has a larger volume of higher stressed material than the smaller one, and its durability in cyclic plastic deforma-

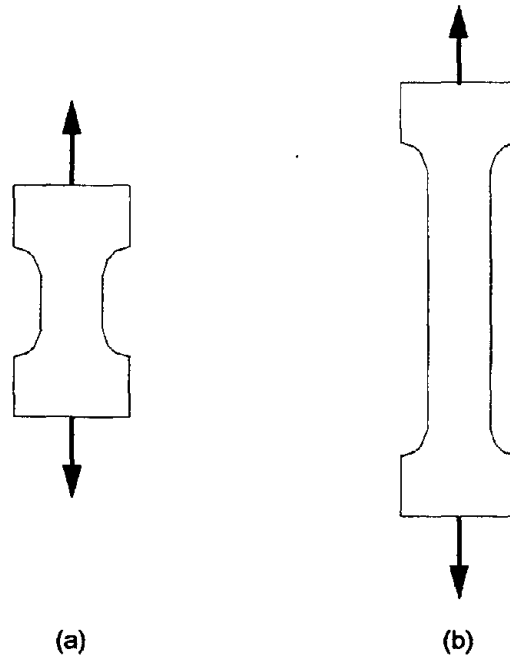


Fig. 3.2: Simple tensile tests for coupons of different lengths.

tion is better. It should be clearly recognized by the designers that, at a local level, the connection ductility is caused by shear in the flange. Equal triaxial stresses in the beam flange weld cause no shear. The ductility demand should be on the material yielding near the connection area. To make the material near the connection yield at a smaller moment than the virgin beam, some flange material should be removed to achieve a stress that does not exceed the stress in the weld.

3.3 Beam Flange Perforation

The dog-bone connections presented in the last section have two disadvantages. Firstly, the material around the torch cut is brittle and should be ground off. Secondly, the stress concentrations at the corners where the cutting lines meet are high.

To eliminate brittleness in the heat affected zone and stress concentration at the sharp corners, an alternative method in which circular holes are drilled in the beam flanges is devised (see Figure 3.3). The closely spaced circular holes in the flanges are aligned along a line such that the outline of these holes resembles a long slot of length h . If the diameter of the holes is D , then the stress at a side of the hole in the

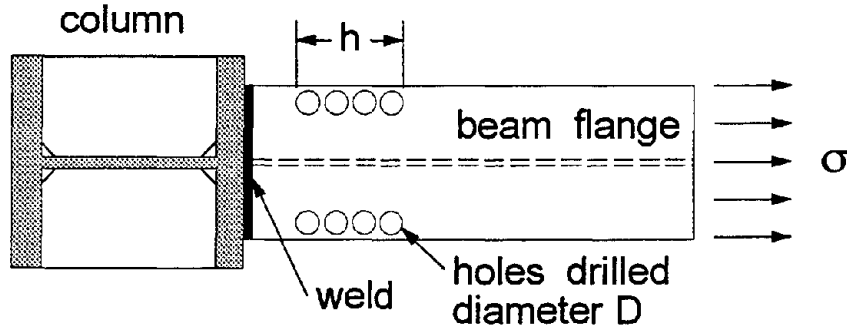


Fig. 3.3: Connection protection by beam flange perforation.

axial direction of the beam can be approximated by the elliptical hole formula:

$$\sigma' = \sigma \left(1 + \frac{2D}{h} \right) \quad (3.1)$$

where σ is the nominal longitudinal stress in the whole flange. For a single hole, $h = D$, and the stress concentration factor is 3. For two holes in a row with edges touching, $h = 2D$, the stress concentration factor is $1 + 2D/2D = 2$. According to the closed form solution of Ling [41, 42], the actual value is 2.57. Schoultz showed that, for a row of holes with edges touching, the stress concentration factor is 1.72 [64]. But if this row of holes has a distance D edge-to-edge, the stress concentration factor increases to 2.15. Thus, the longer the row of holes and the shorter the distance between them, the lower is the stress concentration. The stress concentration factors for more complex hole patterns can be found in Peterson [52] and Savin [63]. The stress concentration factor discussed here is relatively less important when material is in the plastic state and the stresses around the holes redistribute more evenly.

Beam flange perforated connections have the same advantages as the dog-bone connections, namely, strength reduction and an increase in ductility. The primary disadvantage of drilling holes in the beam flange is that it makes the beam more susceptible to buckling. The stability of the perforated beam sections is studied later.

3.4 Design of Perforated Connection

The yielding, plastic, and ultimate moment capacities of a beam can be calculated with a sufficient degree of accuracy by the following equations, respectively,

$$M_{yield}^b = (F_y - F_r)S_x^b \quad (3.2)$$

$$M_{plastic}^b = F_y Z_x^b \quad (3.3)$$

$$M_{ultimate}^b = F_u Z_x^b \quad (3.4)$$

where F_r is the maximum compressive residual stress in either flange tip of a beam; F_y and F_u are the yield and ultimate strengths, respectively, of the material; and S_x^b and Z_x^b are the beam section and plastic moduli, respectively.

For a directly welded beam-to-column connection, the bending beam moment is transferred primarily through the beam flange into the column, and the ultimate moment capacity, C_m^b , of the connection can be calculated from

$$C_m^b = F_u Z_f^b \quad (3.5)$$

where Z_f^b is the plastic modulus of the beam flanges. Because Z_x^b is larger than Z_f^b , the ultimate moment capacity of the beam, $M_{ultimate}^b$, is always larger than the connection capacity C_m^b .

To protect the connection from brittle failure during severe service, some holes can be drilled in the beam flanges near the connection as shown in Fig. 3.4. At the perforated beam section, the plastic modulus Z'^1 can be calculated based on the reduced area. Consider a cantilever beam with a concentrated load P at its free end (Fig. 3.4). The bending moment arm from the loading point to the connection is denoted as L . The bending moment arm from the loading point to the first hole center of the perforated section is L' . The bending moment arm from the loading point to the last hole center of the perforated section is L'' . From the material strength point of view, the reduced plastic modulus Z' must be selected such that the stress at the connection is smaller than the ultimate strength. To achieve this, the stress at the first hole section must be greater than the stress at the connection, namely,

$$\sigma = \frac{PL}{Z_f} \leq \frac{PL'}{Z'} \leq \alpha F_y < F_u \quad (3.6)$$

¹To simplify the notation, the superscript b is dropped in the remainder of the chapter.

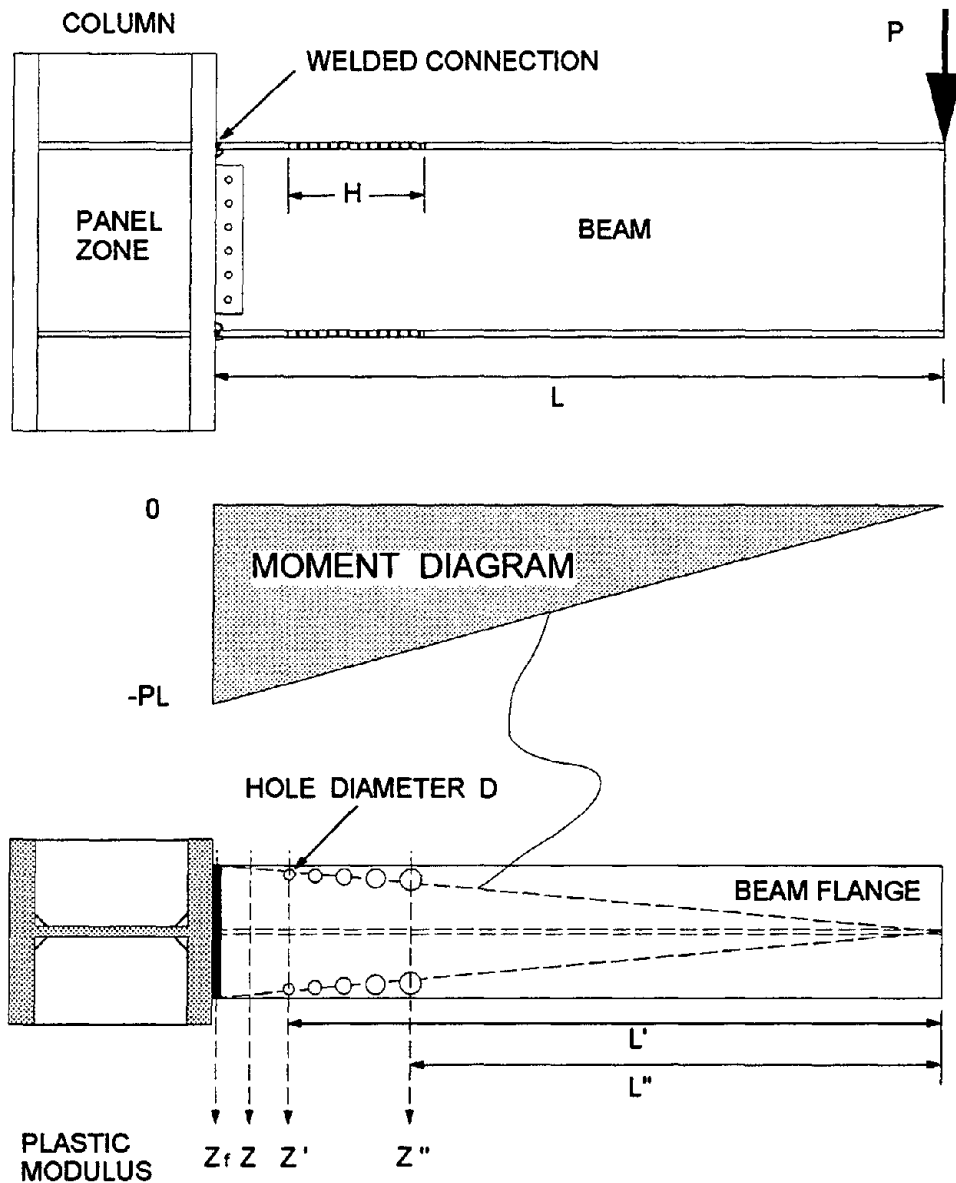


Fig. 3.4: Projection of moment diagram on beam flange to help determining hole sizes and locations.

where α is a strain hardening factor, $1 < \alpha < F_u/F_y$. For A36 steel, α is about 1.2, depending on the ductility demand. For A572 Grade 50 steel, α is smaller (about 1.1). By introducing a safety factor SF into the equation, the reduced plastic modulus can be expressed as

$$Z' = \frac{Z_f L' F_u}{SF L \alpha F_y} \quad (3.7)$$

where the safety factor SF must be greater than one. Once the reduced plastic modulus is known, the hole diameter can be determined. If the hole diameters are different, as is usually the case for obtaining maximum ductility, the reduced plastic modulus Z'' at the last hole section should also need to be calculated using Eq. 3.7 with Z' and L' replaced by Z'' and L'' , respectively. It is convenient to use the projected beam moment diagram on the beam flange as a design aid (refer to Fig. 3.4). The projected moment diagram on the beam flange corresponds to the area required for safety factor one if the plastic modulus of the beam web is ignored. In order for a plastic hinge to develop at the perforated area, the length of the row of holes h should be greater than one half of the beam depth. The starting position of the row of holes is about $b_f/2$ away from the connection. If the holes are drilled too close to the connection, the stress concentration around the holes will introduce high triaxial stresses at the connection. If the holes are drilled too far away from the connection, the hole diameters have to be large to satisfy Eq. 3.7, making the beam section prone to buckling.

After the reduced plastic modulus and its bending moment arm are known, the peak force can be calculated by

$$P_{peak} = \min \left(\frac{\alpha F_y Z'}{L'}, \frac{\alpha F_y Z''}{L''} \right) \quad (3.8)$$

If the strain corresponding to stress αF_y is ϵ' , then the plastic rotation θ_p at the perforated section can be estimated by

$$\theta_p = \frac{2h(\epsilon' - \epsilon_y)}{d} \quad (3.9)$$

where ϵ_y is the yield strain, and d is the depth of the beam. By adjusting α and h , the required plastic rotation can be attained. It is also important to check the panel zone shear capacity to ensure that the panel zone can resist the shear force transmitted from the beam flange axial forces at the connection.

From Bleich's formula [18], the critical stress for beam flange buckling in the strain-hardening range can be expressed as

$$\sigma_{cr} = k \frac{\pi^2 \sqrt{E E_t}}{12(1 - \nu^2) \left(\frac{b_f}{2t_f}\right)^2} \quad (3.10)$$

where k is the buckling coefficient, E and E_t are Young's and tangent moduli, respectively; ν is Poisson's ratio, b_f is the beam flange width, and t_f is the beam flange thickness. For a wide-flange beam flange, k is 0.7. Because this formula is conservative, the actual coefficient k should be higher and could be modified from experimental results for a specific rolled shape. If the holes are drilled symmetrically at both edges of a flange, the critical stress should be modified to take into account the effect of the holes. According to the research results of Kumai [40], another buckling coefficient, k_h , must be introduced into the critical stress equation. In such a condition, Eq. 3.10 becomes

$$\sigma_{cr} = k_h k \frac{\pi^2 \sqrt{E E_t}}{12(1 - \nu^2) \left(\frac{b_f}{2t_f}\right)^2} \quad (3.11)$$

Coefficient k_h depends on the diameter of the hole, D , and the flange width, b_f . By fitting the test results of Kumai to a parabolic curve, k_h can be approximated by the equation

$$k_h = 1 - 0.7826 \left(\frac{2D}{b_f}\right)^2 - 0.2205 \left(\frac{2D}{b_f}\right) \quad (3.12)$$

If no hole is drilled, $D = 0$ and $k_h = 1$, and Eq. 3.11 reduces to Eq. 3.10. The critical stress calculated by Eq. 3.11 is a nominal stress, that is, stress based on the original section without the hole.

3.5 Specimens and Test Setup Designs

To help understand the strength and ductility of the perforated beam, eight specimens of A36 W12×26 beam were fabricated and tested at the University of California at Berkeley in the last four months of 1994. The hole patterns of these eight specimens are shown in Fig. 3.5. Specimen A has no hole; it is used as a norm for comparing with other perforated beams. Specimens B to E were designed for a safety factor near 1.1 but with different hole patterns. Specimens F to H were designed for retrofitting,

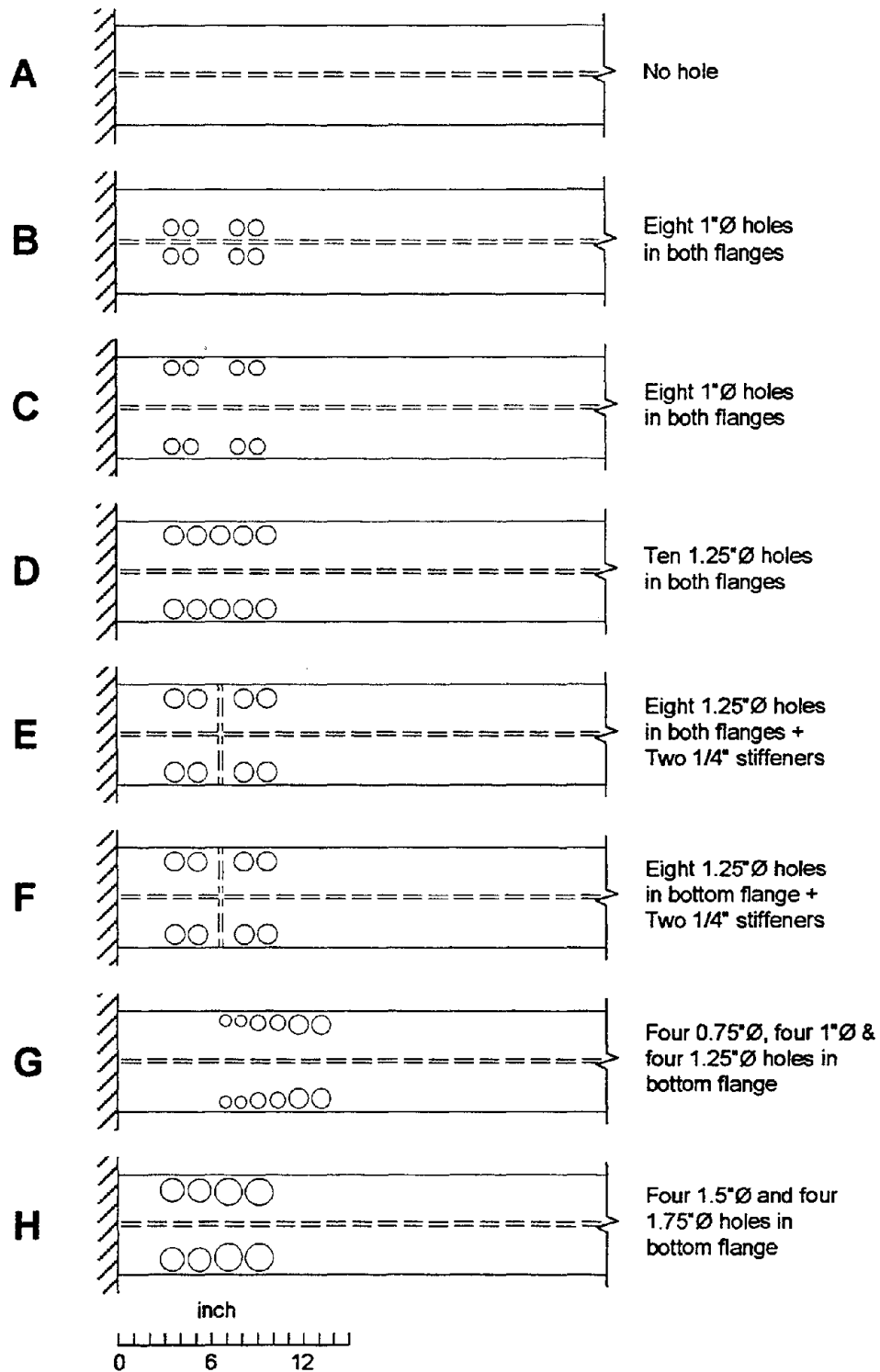


Fig. 3.5: Hole patterns for Specimens A to H.

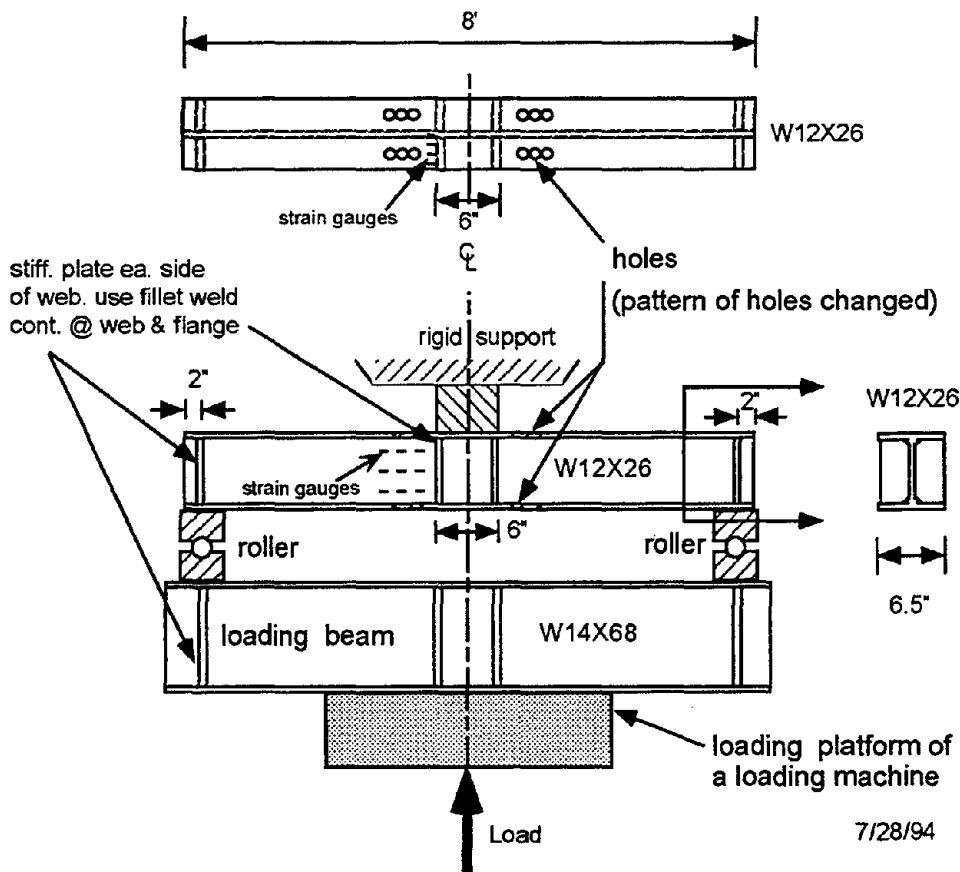


Fig. 3.6: Test setup for beams with flange holes.

thus only bottom flanges were perforated. Specimens E and F have two stiffeners between the two groups of holes to prevent early buckling.

These tests were used to determine the performance of the beams. They were not designed to test the beam-column connection as a whole, so only beams were fabricated. The test setup and the overall dimensions are shown in Fig. 3.6. The specimens were eight-foot simple beams with a center load, but each side of the beam can be considered as a cantilever beam. Two stiffeners were welded six inches apart at the center of the specimen to simulate the column flanges at the connections. The same hole patterns were drilled in both cantilever beams such that the deflections of both beams were symmetric with respect to the centerline. Strain gauges were placed on the beam flange near the holes and near the middle stiffener plates for stress concentration monitoring. Strain gauges were also placed on the beam web at the perforated beam flange to determine the plastic hinge rotation. Two Linear

Variable Displacement Transducers (LVDTs) measured the displacements at the ends and at the mid-span of the cantilever beams. The loading beam is a heavy W14×68 rolled shape with several vertical stiffeners. It is placed on the platform of the loading machine. Steel blocks separated by a round steel bar were placed on top of both ends of the loading beam to simulate roller supports. From the center of a roller to the face of the rigid support is the length of the bending moment arm L , which is 43 inches.

The loading machine can only apply a compressive force, and the rollers cannot resist tension. Therefore, in order to obtain a load reversal, the specimens were turned over after an upward push, and a second push was applied to the up-side-down specimen simulating a “pull”.

Since post-buckling behavior of the beam was not the major concern in these tests, the test was terminated right after the peak load was reached. But it is believed that if the pre-buckling ductility is large, the post-buckling ductility should also be high and less degrading.

3.6 Test Results of Eight Perforated Beams

In the early stage of testing, no previous results or literature were available for determining the pattern of holes. After a crude calculation, Specimen B was designed and tested first. It is known that two holes drilled side-by-side yield the lowest stress concentration factor, but it is difficult to drill such holes, thus a quarter inch separation was suggested by the shop technical staff. The subsequent specimens were designed using the quarter inch edge-to-edge rule.

Holes for Specimen B were drilled near the web of the beam. This test showed that Specimen B developed local buckling at the perforated portion of the flange. The next day, right after Specimen B was tested, Specimen A, which has no hole, was tested. By comparing the results, it was found that Specimen B had the expected strength reduction but the buckling occurred prematurely, resulting in worse ductility than that for Specimen A. It was soon discovered that drilling holes in the flange near the web releases the required constraint to prevent buckling. To verify this, the hole pattern of Specimen C was designed to be the same as that for Specimen B, except that the holes were drilled near the outer edges of the flange. The test results for this specimen show that Specimen C had a 16% strength reduction, but

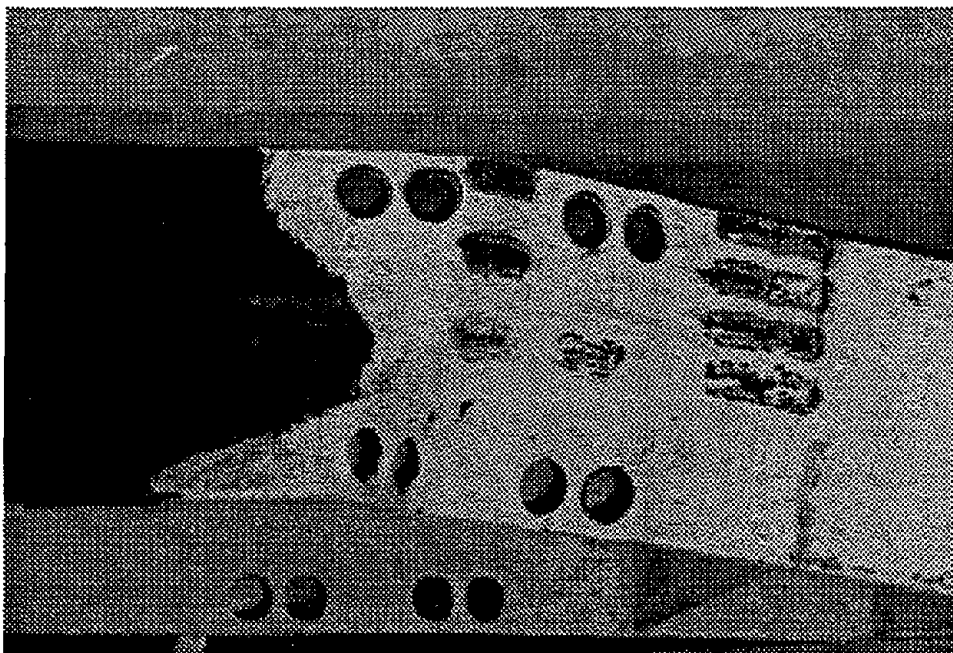


Fig. 3.7: Photograph showing Specimen C after the test.

the pre-buckling plastic rotation was 18% larger than for Specimen A. Thus, all the subsequent specimens had holes drilled in the outer flange area. The deflection mode of Specimen C was a flexure-torsional buckling shape (Fig. 3.7).

The outline of the hole pattern of Specimen D is similar to the dog-bone connection shown in Fig. 3.1a. The pattern consists of two rows of consecutive holes with the same diameter and spacing. Test results showed a 21% reduction in strength and a 7% gain over Specimen A in plastic rotation at the peak load.

In view of the buckling shape of Specimen C, one can envisage the new buckling shape if vertical stiffeners were added at the center of the perforation area. Specimen E was designed similarly to Specimen C, with stiffeners added. To compensate for the increased strength due to the added stiffeners, the hole diameter was enlarged by 25%. The test results for Specimen E were encouraging compared with Specimen A. The strength was reduced by 13%, whereas the pre-buckling plastic rotation had a 54% gain. The buckling shape of Specimen E is shown in Fig. 3.8.

For most retrofit projects, the top flange of a beam is difficult to drill because the floor deck is on top of it. Because of this concern, three specimens (F, G, and H) were tested with only the bottom flange perforated. Specimen F is identical to Specimen

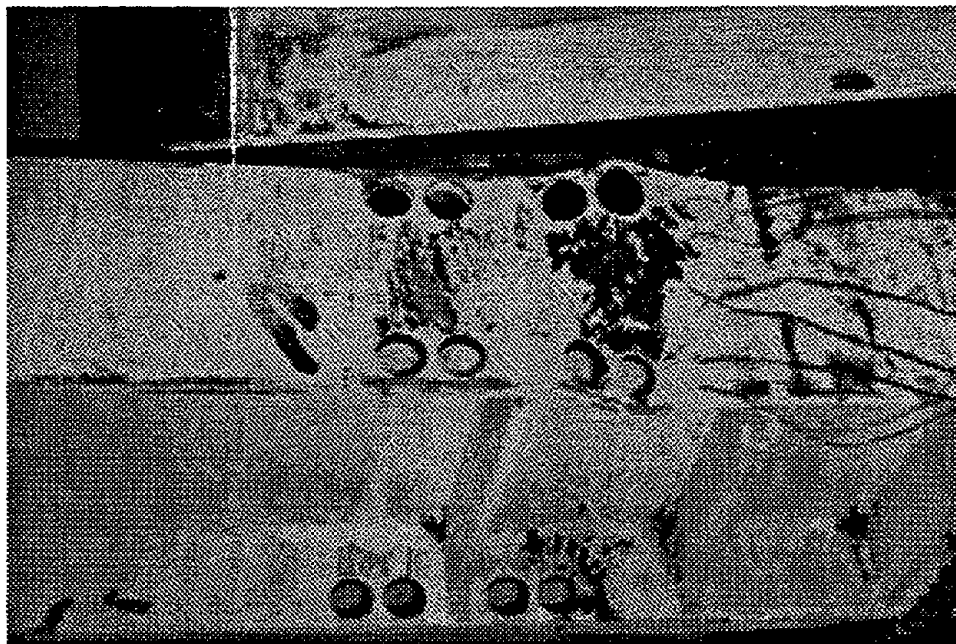


Fig. 3.8: Photograph showing Specimen E after the test.

E except that only the bottom flange has holes. Its strength was reduced only 5%, but its plastic rotation had a 71% gain. A photograph of Specimen F after the test is shown in Fig. 3.9.

A hole pattern to match the moment gradient line was used in Specimen G. The holes were drilled beginning a flange width distance from the connection. The hole sizes increase in the direction away from the connection. Thus the fabrication cost is higher. The strength reduction of this specimen was 9%. Unfortunately, in testing for the peak load, the holes were in the tension flange, thus the buckling occurred in the flange without holes (Fig. 3.10). Therefore, the plastic rotation at the peak load is the same as for Specimen A.

To develop an understanding of the effect of large holes, Specimen H was designed to have holes occupy about 50% of the bottom flange area. Experimental results show that such a design has stability problems. The quarter inch material between the holes and the beam flange edge is very slender. For this design, buckling occurred at a small load, causing the beam flange to warp (Fig. 3.11). The peak load of this specimen had a 25% reduction in strength.

During the tests, several material coupons were tested. The average beam flange

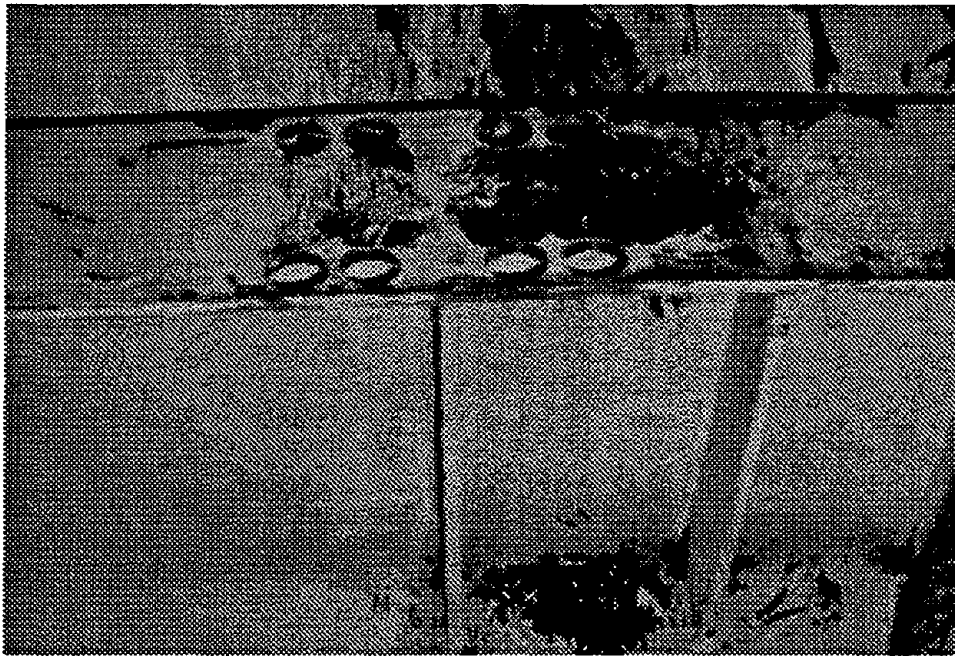


Fig. 3.9: Photograph showing Specimen F after the test.

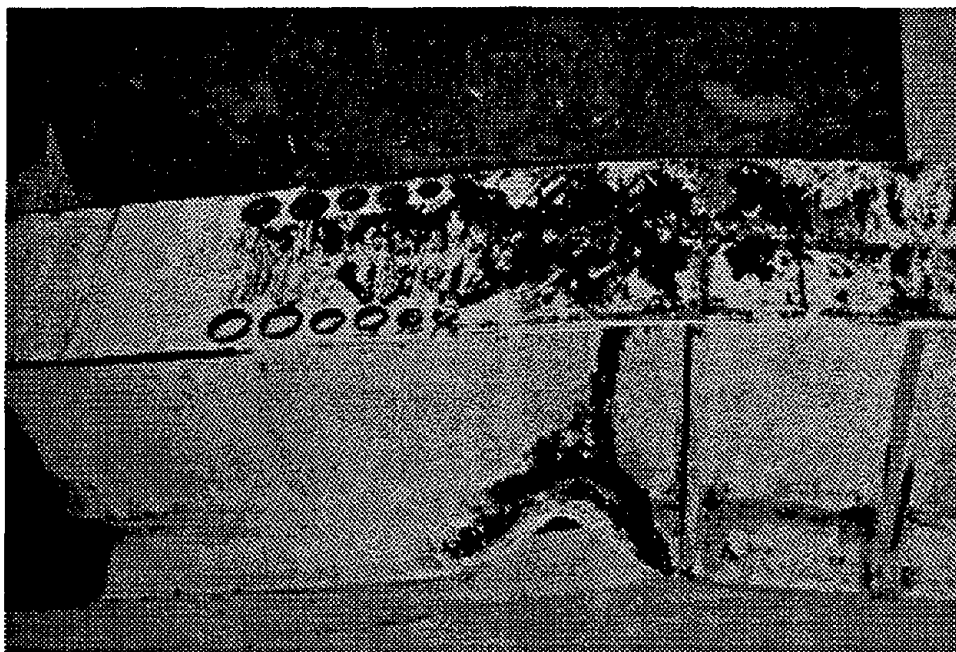


Fig. 3.10: Photograph showing Specimen G after the test.

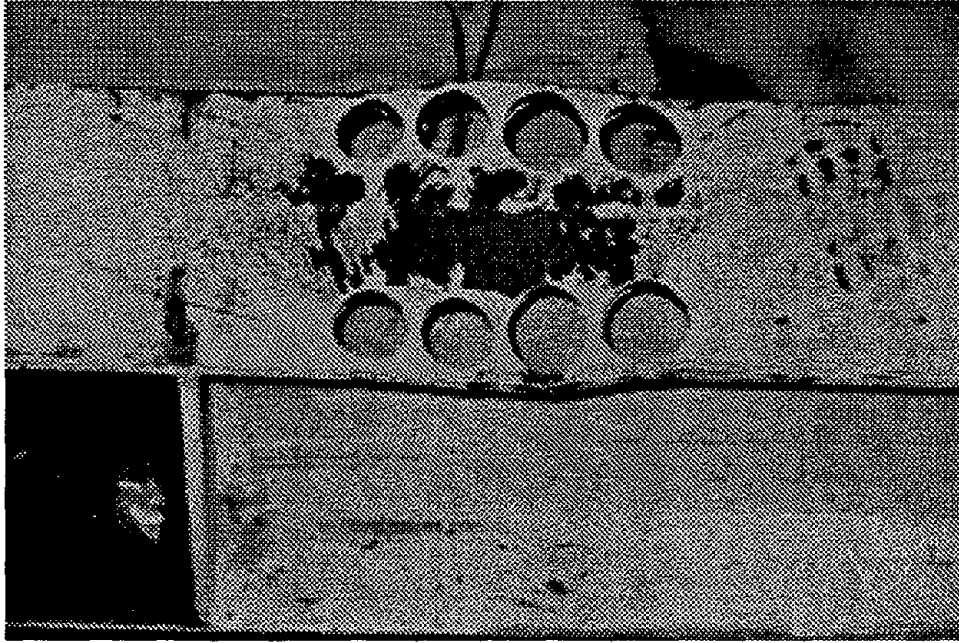


Fig. 3.11: Photograph showing Specimen H after the test.

yield strength was found to be 50 ksi, and the ultimate, 68 ksi. Figure 3.12 shows one of the test stress-strain curves.

The geometric data, theoretical values, and the test results for these eight specimens are summarized in Table 3.1. Theoretical peak loads agree well with the experimental values. The load-deflection curves of these eight specimens are shown in Fig. 3.13. The tip load-plastic displacement curves are shown in Fig. 3.14. From these plots, it is difficult to distinguish between the buckling load and the yielding load. Because the stress concentration factors around the holes are high, it is believed that the yielding started very early in the small areas around the holes. From these curves, it is found the the stiffness degradation due to the presence of holes ranges from 2% to 8%. The normalized moment ratio-plastic rotation curves are shown in Fig. 3.15. The normalized moment ratio in the plots is defined as

$$\frac{\text{Moment}}{M_{\text{plastic}}} = \frac{PL}{F_y Z_x} \quad (3.13)$$

The maximum value of this ratio, α , is found to be 1.2 shown in the plot for Specimen A.

Specimen	A	B	C	D	E	F	G	H
Test date	8/2/94	8/1/94	9/1/94	9/14/94	10/26/94	10/26/94	11/16/94	12/8/94
<i>Geometric data:</i>								
Arm, 1st hole, L' , in	43.0	39.5	39.5	39.4	39.4	39.4	36.0	39.5
Arm, last hole, L'' , in	43.0	34.0	34.0	33.4	33.4	33.4	29.5	33.9
Top flange area, in ²	2.47	1.71	1.71	1.52	1.52	2.47	2.47	2.47
Bottom flange area, in ²	2.47	1.71	1.71	1.52	1.52	1.52	1.90	1.33
							1.52*	1.14*
Plastic y centroid, in	0.0	0.0	0.0	0.0	0.0	2.07	1.24	2.48
							2.07*	2.89*
Plastic modulus, Z' , in ³ (Z'/Z , %)	37.2 (100)	28.2 (76)	28.2 (76)	25.9 (70)	25.9 (70)	30.5 (82)	33.4 (90)	29.0 (78)
Plastic modulus, Z'' , in ³ (Z''/Z , %)							30.5* (82)	27.4* (74)
Z_f/Z'	0.78	1.04	1.04	1.13	1.13	0.96	0.87	1.01
Z_f/Z''							0.96	1.07
$(Z_f/Z')(L'/L)$	0.78	0.96	0.96	1.04	1.04	0.88	0.73	0.93
$(Z_f/Z'')(L''/L)$	0.78	0.82	0.82	0.88	0.88	0.75	0.66	0.84
<i>Theoretical values:</i>								
Buckling stress σ_{cr} , ksi (Eq. 3.11)	44.3	38.0	35.4	35.4	35.4	35.4	40.2	32.4
							35.4*	29.0*
Buckling load, kips ($\sigma_{cr}S_x/L'$) (ratio, %)	41.2 (100)	32.1 (78)	32.1 (78)	30.0 (73)	30.0 (73)	30.0 (73)	37.3 (91)	27.4 (67)
Peak load, kips (Eq. 3.8)	51.9	42.8	42.8	39.4	39.4	46.4	55.7	44.1
							46.3*	48.5*
<i>Experimental results:</i>								
Stiffness, kips/in (ratio, %)	128 (100)	128 (100)	122 (95)	120 (94)	125 (98)	123 (96)	121 (95)	118 (92)
Buckling/yield load kips (ratio, %)	40 (100)	32 (80)	25 (63)	24 (60)	24 (60)	18 (45)	35 (89)	24 (60)
Peak load, kips (ratio, %)	51.6 (100)	44.5 (86)	43.5 (84)	40.9 (79)	44.8 (87)	49.1 (95)	47.1 (91)	38.5 (75)
Peak rotation, % rad (ratio, %)	2.8 (100)	2.1 (75)	3.3 (118)	3.0 (107)	4.3 (154)	4.8+ (171)	2.8+ (100)	0.75 (27)

For all specimens $S_x = 33.4 \text{ in}^3$, $Z = 37.2 \text{ in}^3$, $Z_f = 29.2 \text{ in}^3$, $L = 43 \text{ in.}$, $F_y = 50 \text{ ksi}$, and $F_u = 68 \text{ ksi}$.

* At the last hole section.

+ Buckling occurred in flange without hole.

Table 3.1: Comparison table for eight A36 W12×26 specimens.

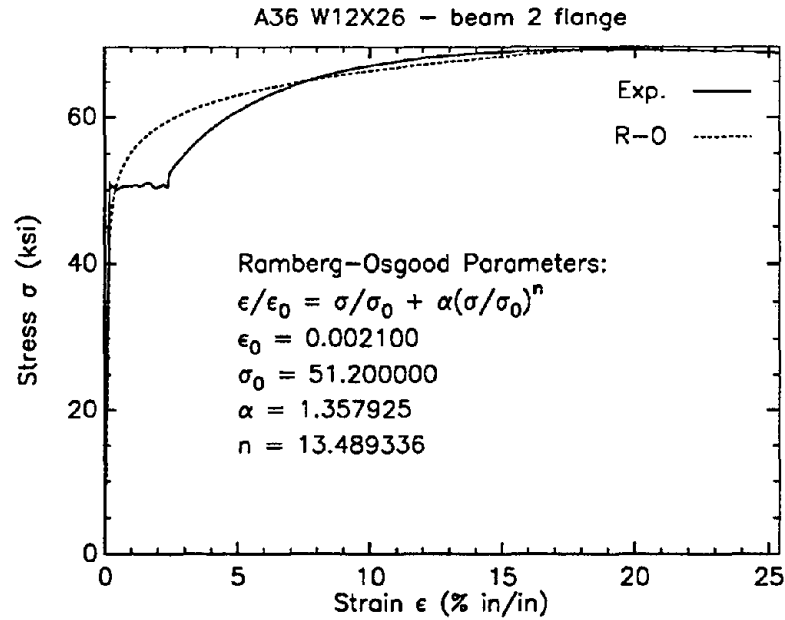


Fig. 3.12: Typical stress-strain curve of a flange coupon test.

3.7 Cyclic Test of Large Size Specimens

In order to help understand the strength and ductility of the perforated moment resisting connections under cyclic loading conditions, two specimens were fabricated. Both specimens consisted of an A36 W36×150 cantilever beam which connected to the middle of an A572 Grade 50 column of size W14×455 by groove welds. The test setup and the overall dimensions are shown in Fig. 3.16. The material properties of these two specimens are given in Table 3.2. Notice that the yield strength of beams is 61% over the ASTM minimum strength. The beams have to be weakened to protect the connection.

Due to a misunderstanding with the fabricator, the hole sizes of Specimen 3 and 8 were drilled too small. The original hole patterns for Specimen 3 and 8 are shown in Figs. 3.17 and 3.18, respectively. Because the bending moment capacity of the perforated section is larger than the connection strength, the perforated section had to be reduced to avoid the tear-off beam flange type failure at the connection. Since the edge distance was too small for hole redrilling, it was decided to drill extra holes near the existing ones. Figures 3.19 and 3.20 show the connection details and the new hole patterns for Specimen 3 and 8, respectively. Those added small holes did

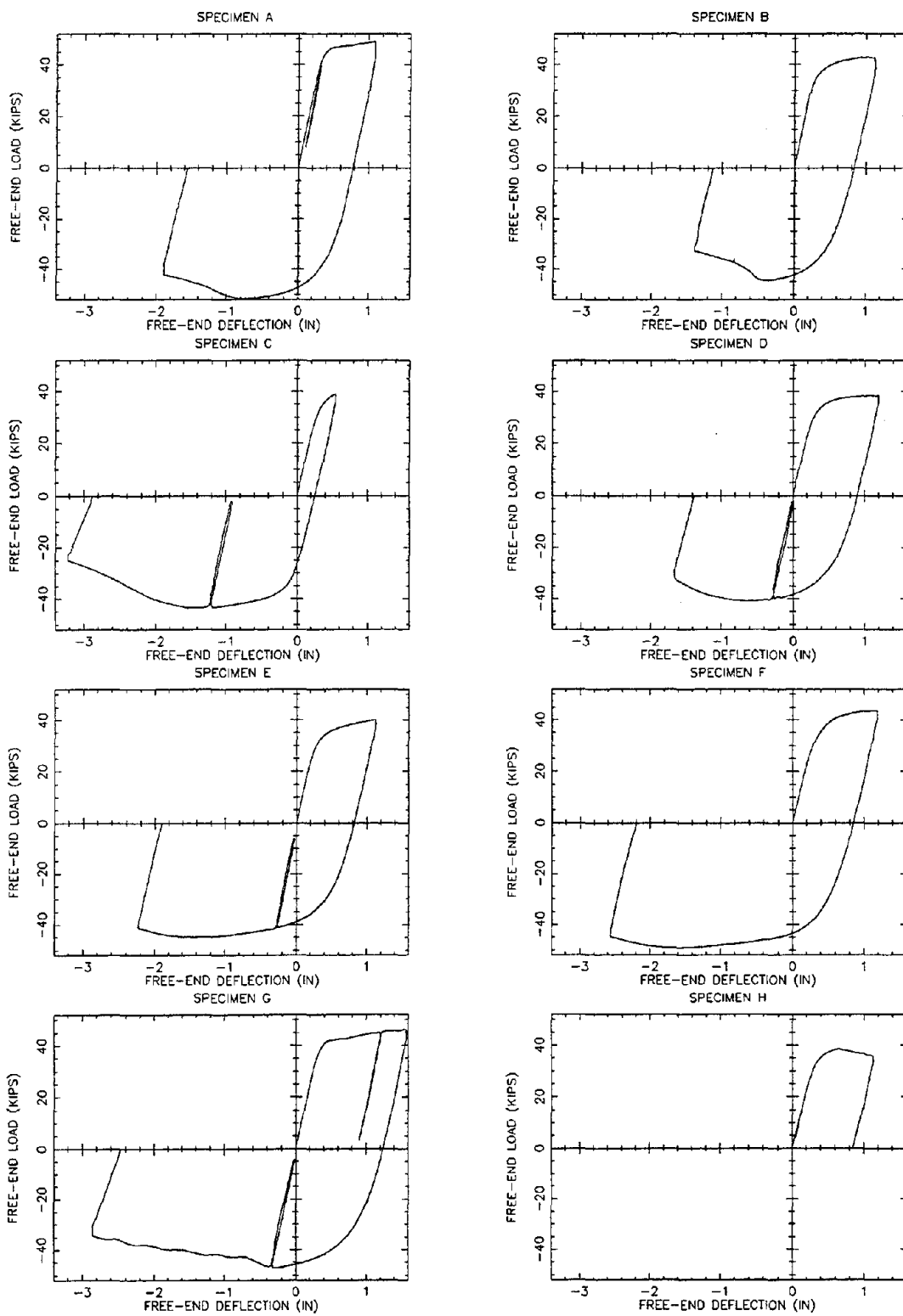


Fig. 3.13: Load-deflection diagrams for Specimens A to H.

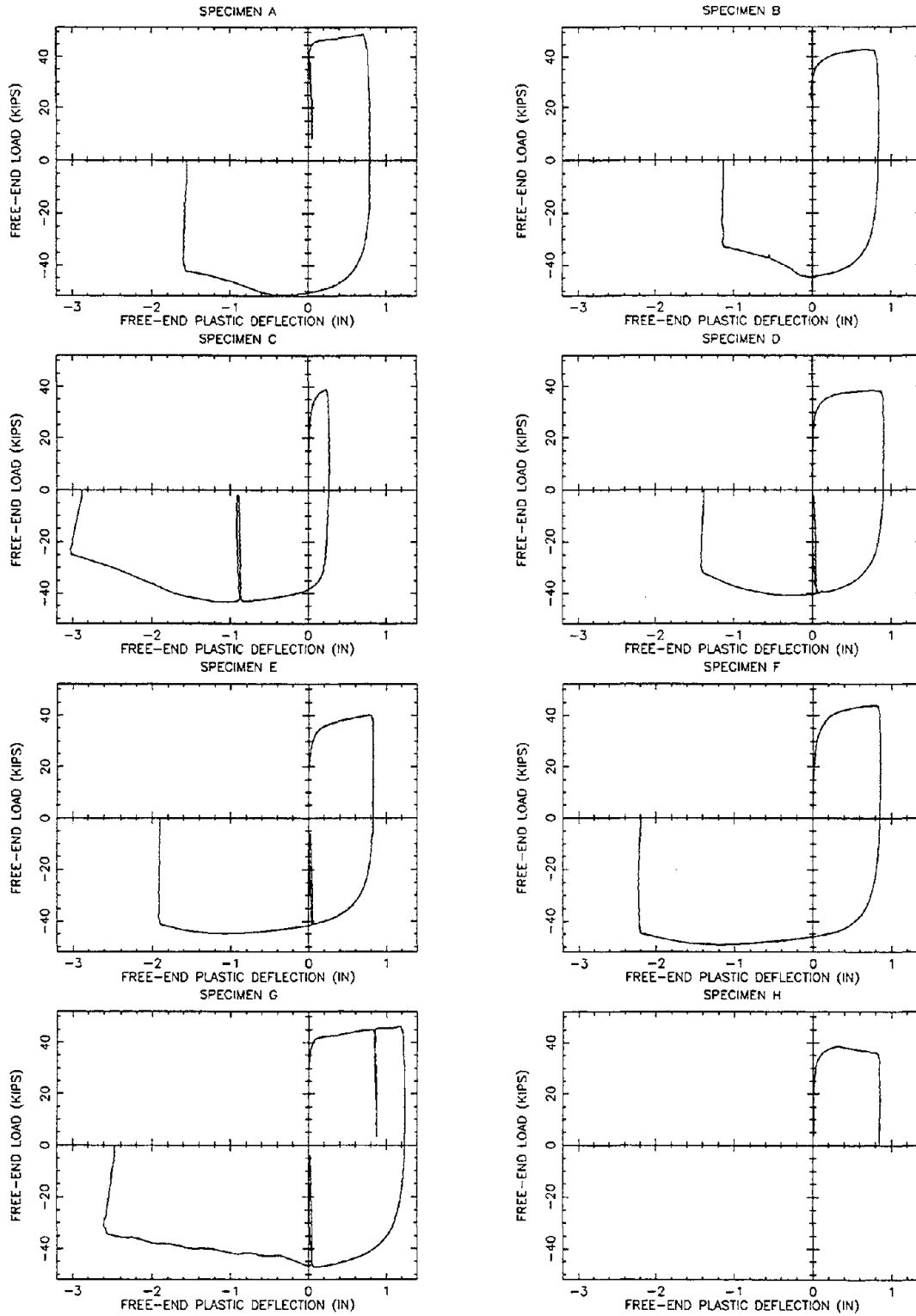


Fig. 3.14: Load-plastic deflection diagrams for Specimens A to H.

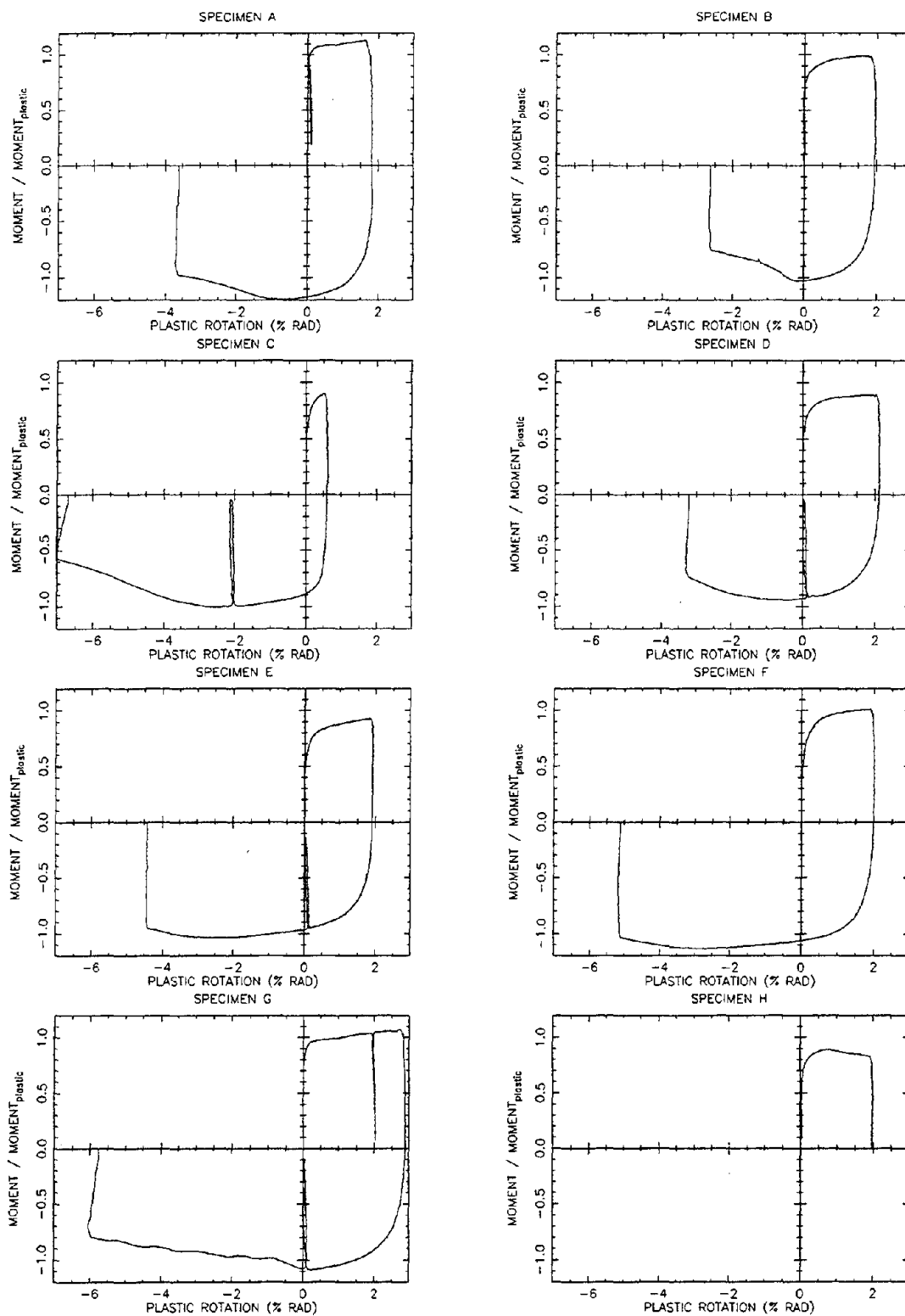


Fig. 3.15: Moment ratio-plastic rotation diagrams for Specimens A to H.

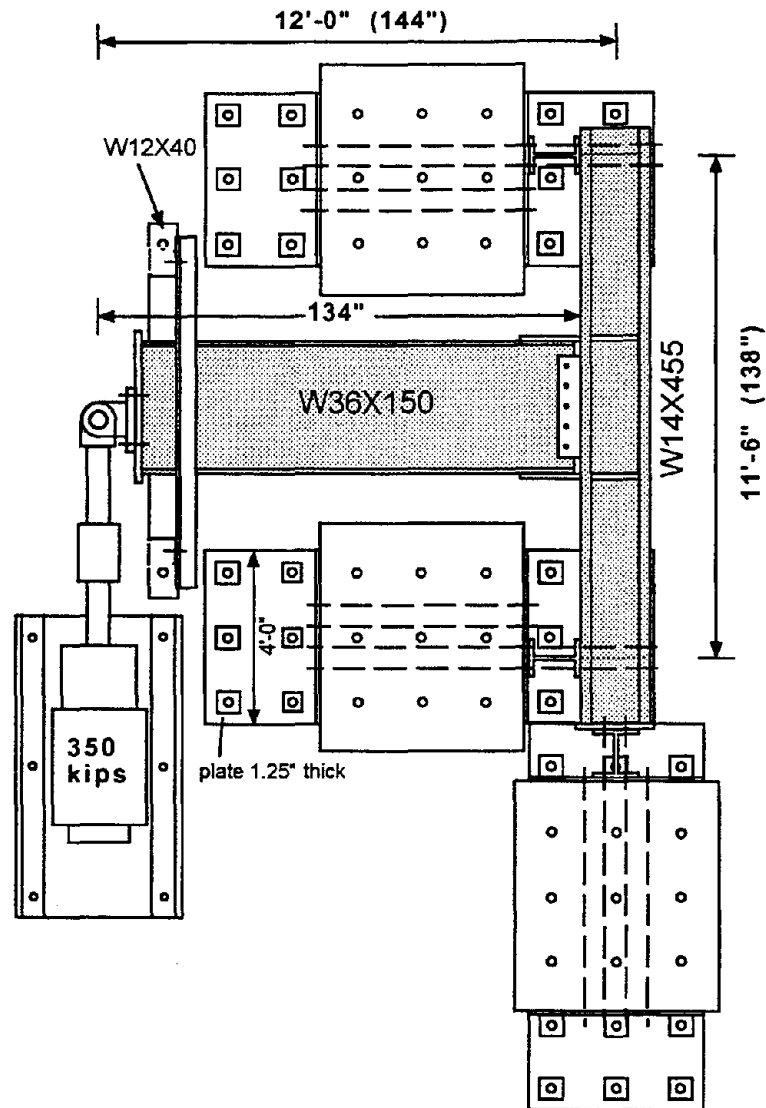


Fig. 3.16: The cyclic test setup and overall dimensions.

Specimen	Material Size	Material Spec	Heat Number	Yield Strength	Tensile Strength
3	W36×150	A36	54940	58 ksi	67 ksi
	W14×455	A572 Gr50	74184	57 ksi	89 ksi
8	W36×150	A36	54940	58 ksi	67 ksi
	W14×455	A572 Gr50	84553	67 ksi	82 ksi

Table 3.2: Material properties of Specimen 3 and 8 (from Mill Certificates).

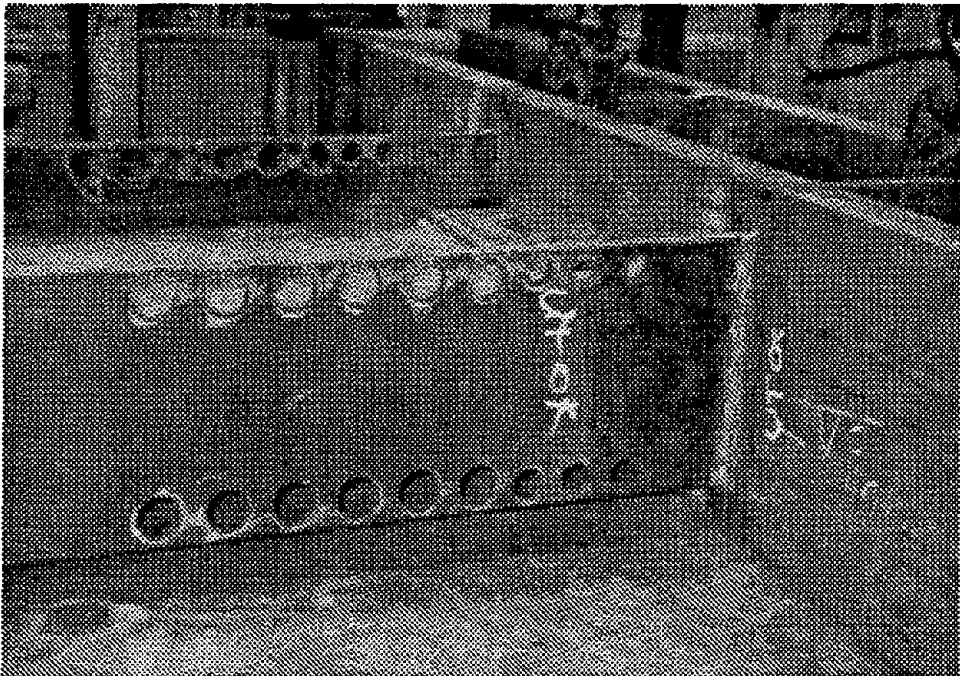


Fig. 3.17: Original hole pattern of Specimen 3.

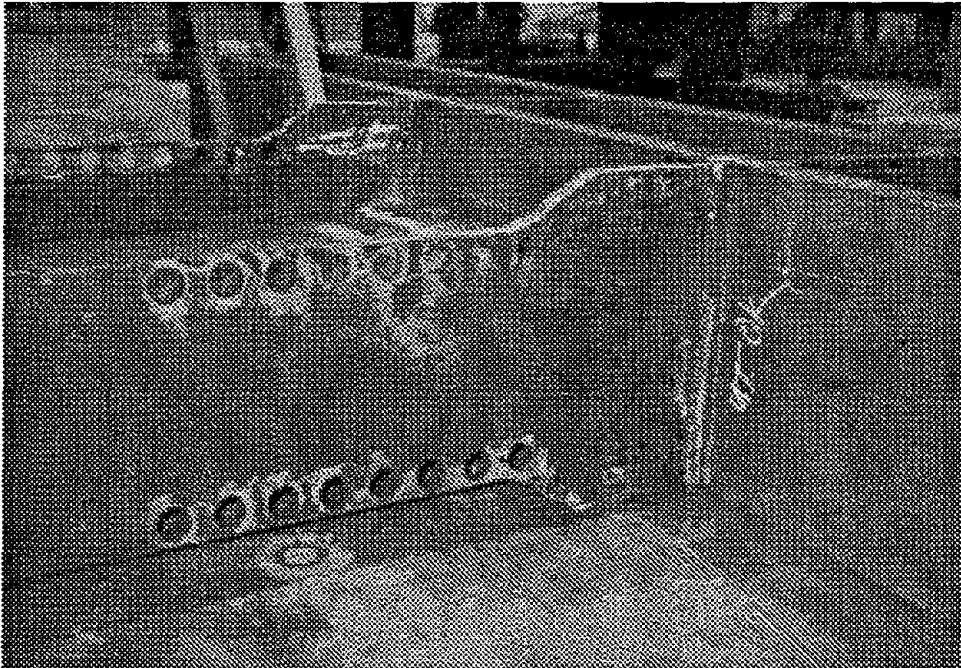


Fig. 3.18: Original hole pattern of Specimen 8.

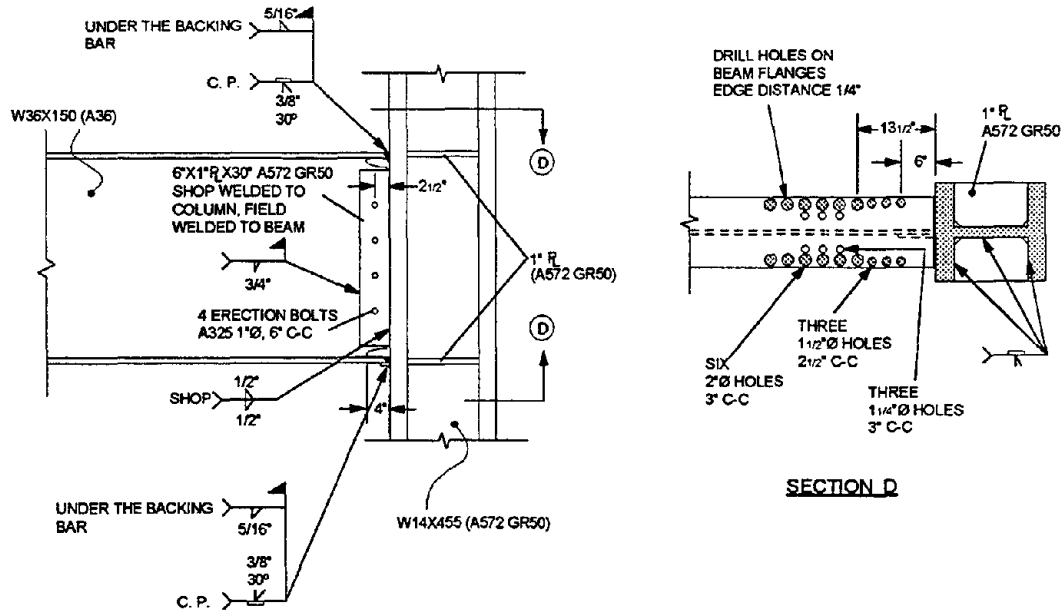


Fig. 3.19: Connection details of Specimen 3.

solve the crucial problem but they also created new problem. The area near these new small holes has a very large stress concentration factor.

Notice in the connection details that the web cope in the beam is larger than a typical design to reduce the triaxial constraint at the connection. Once the constraint is reduced, the area above the web copes can be deformed in the beam axial direction much easier, thus the shear plate can carry much more bending moment. Because of that, the shear plate needs to be thick.

The test procedures and the imposed displacements follow the SAC protocol. The plots of beam tip displacement against tip load for Specimen 3 and 8 are shown in Fig. 3.21. The ultimate connection capacity of Specimen 3 can resist tip load up to 197 kips. The perforated beam section effectively protects the connection from failure. The connection of Specimen 8 with the aid of wings, has a yield capacity of 237 kips tip load. The perforated section also effectively protects the connection. The plots of plastic rotation against plastic moment ratio for Specimen 3 and 8 are shown in Fig. 3.22. Because the beam section is reduced to protect the connection, the beam cannot reach its full plastic capacity. The tested plastic moment ratio is very close to the Z_f/Z ratio at the connection, where Z_f and Z are the plastic modulus of the flange and the whole section, respectively.

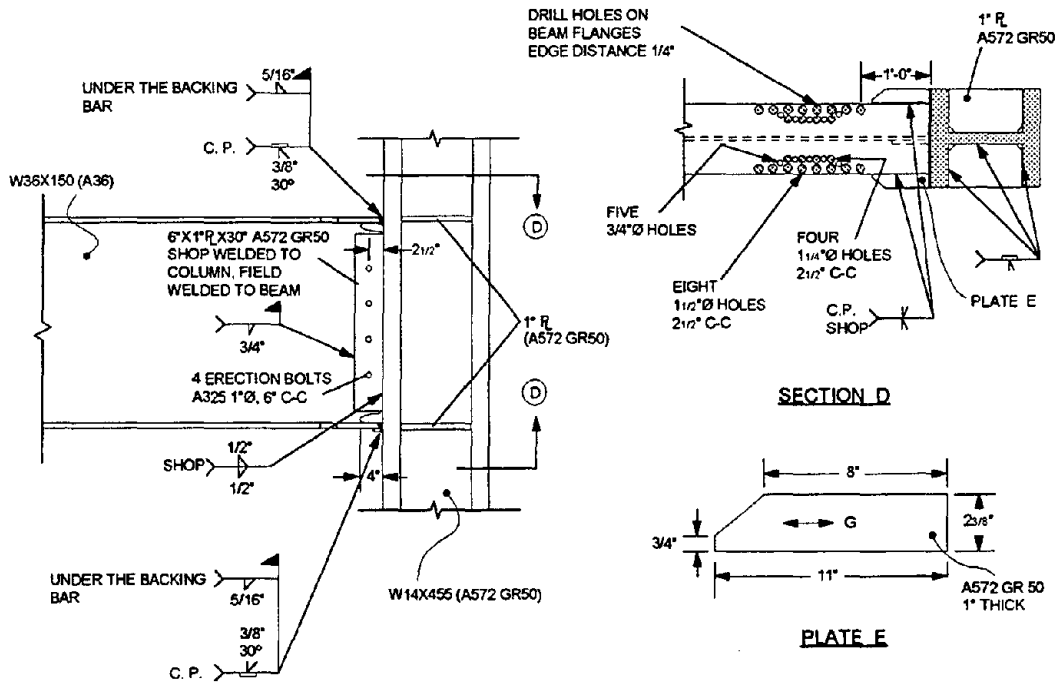


Fig. 3.20: Connection details of Specimen 8.

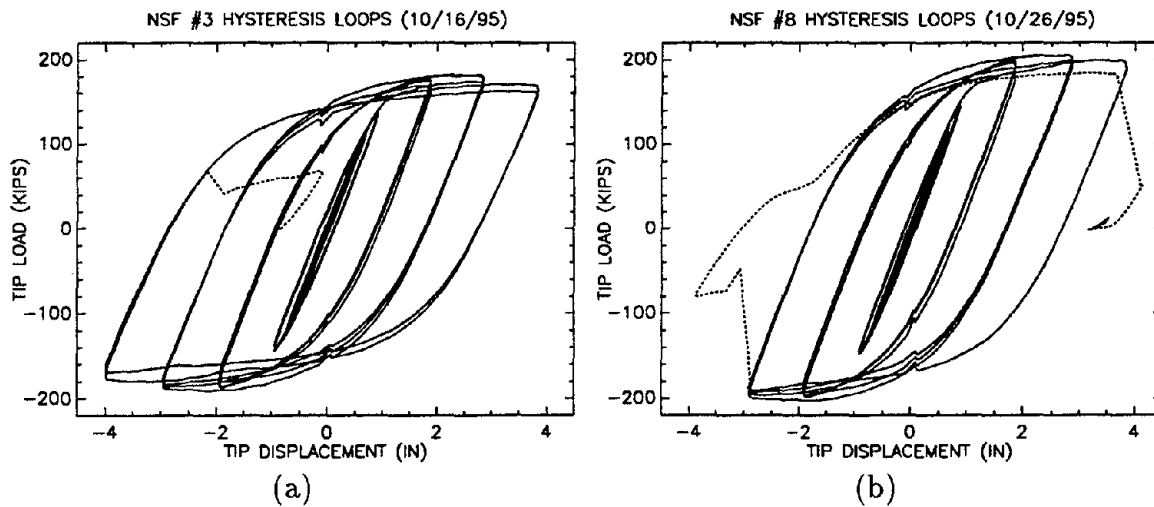


Fig. 3.21: Hysteresis loops for Specimen (a) 3 and (b) 8.

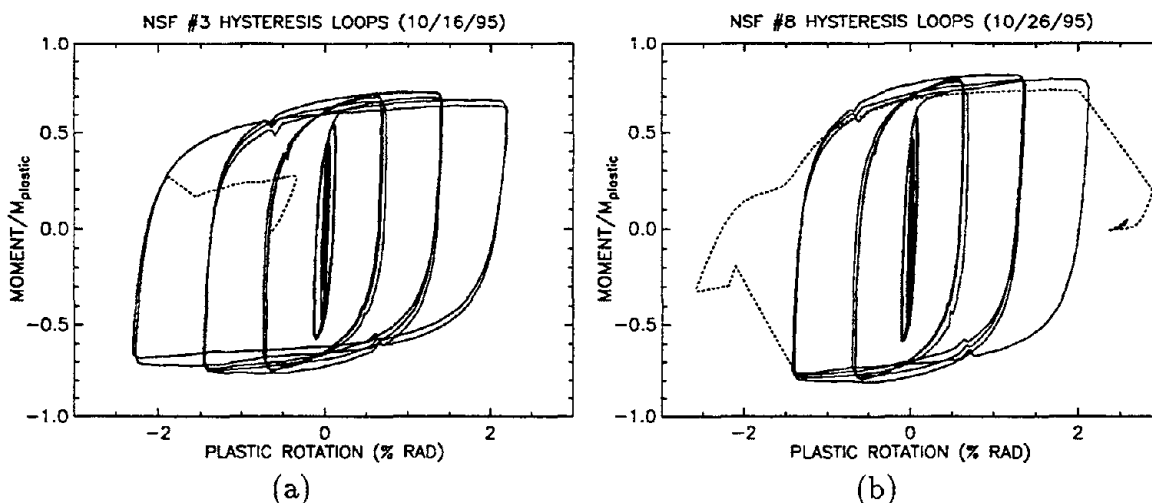


Fig. 3.22: Plastic rotation against moment ratio for Specimen (a) 3 and (b) 8.

A photograph of the white-washed Specimen 3 after the test is shown in Fig. 3.23. Note the superior transfer of web and flange stresses in the perforated area exemplified by the extensive peeling-off of the whitewash. Specimen 8 had a similar appearance (not shown).

Since most of the cyclic tests did not follow the same imposed displacement history, the plastic rotation shown in Fig. 3.22 is not a good indicator of the capability of the connection. The degradation of the hysteresis loops is very important. To combine both effects, the total energy diagrams for both specimens are constructed and shown in Fig. 3.24. The dissipated energy is about 3 times the dissipated energy of the SAC PN specimens discussed in Chapter 2.

Next, the cumulative ductility of both specimens is discussed. By dividing the summation of the plastic displacements by the first positive yield displacement, the cumulative ductility can be obtained. Figure 3.25 shows the cumulative ductility vs. time steps for Specimen 3 and 8. The average cumulative ductility of these two specimens is only 76. If a structure is designed using ductility 8, which corresponds to $R_w = 8$ in the 1994 UBC code, then the structure can withstand only two and a half severe cycles².

² $8(\text{ductility}) \times 4(\text{quadrants}) \times 2.5(\text{cycles}) = 80$



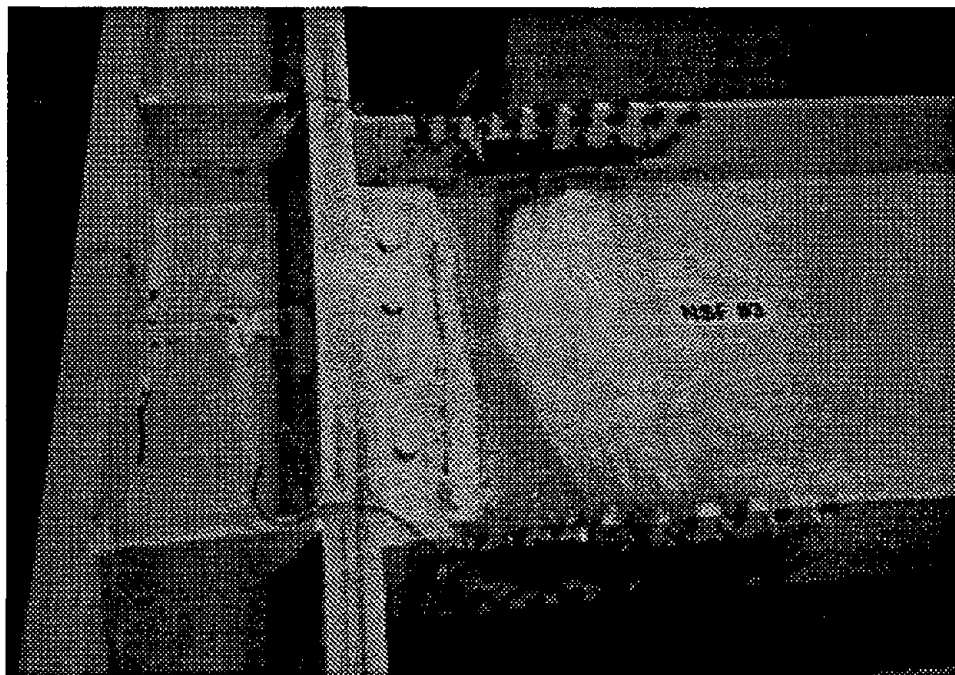


Fig. 3.23: Photograph after test of white-washed Specimen 3.

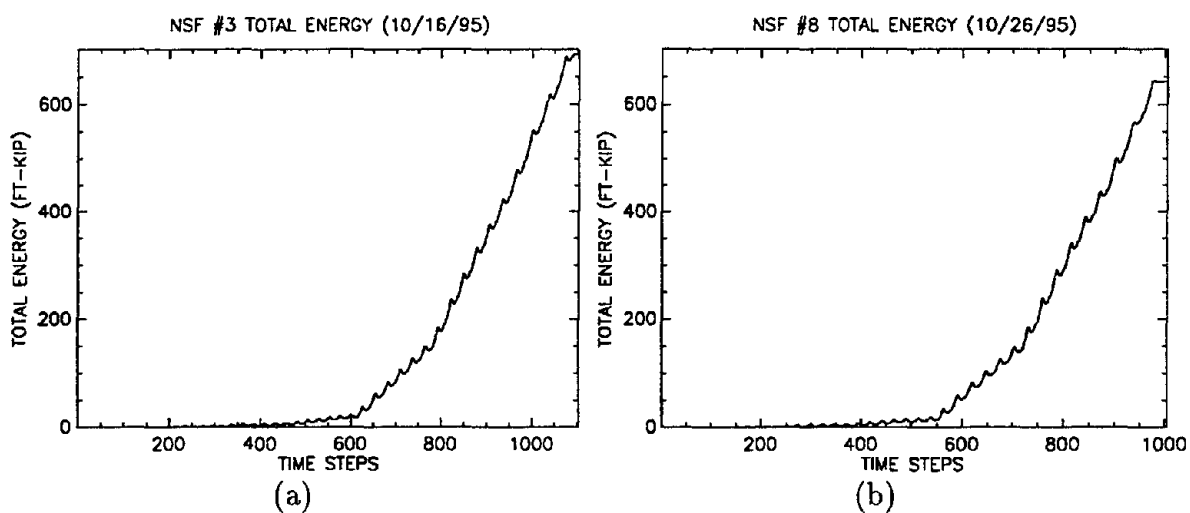


Fig. 3.24: Total energy diagrams for Specimen (a) 3 and (b) 8.

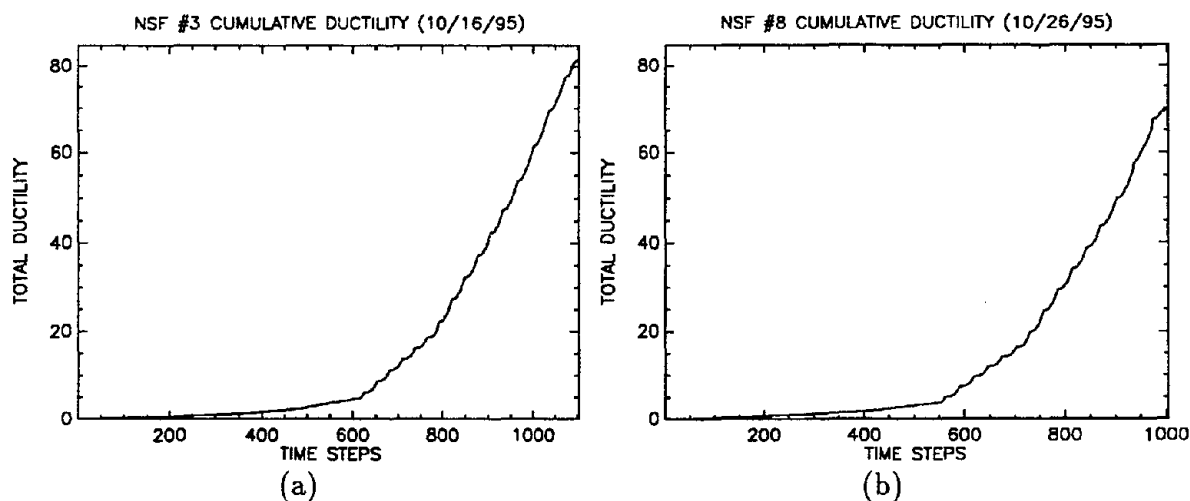


Fig. 3.25: Cumulative ductility diagrams for Specimen (a) 3 and (b) 8.

3.8 Conclusions

Taking out 15% to 40% of the beam flange area near a connection can limit the bending moment transferred from the beam span and protect the connection from brittle failure. The area is removed by a torch cut or by drilling holes.

Several beam flange perforation patterns were studied. Test results show that a well-designed perforated beam can achieve the maximum strength reduction of about 20-30% and increased ductility. Beam stiffness loss due to the perforations is small; the reduction for a good design is only about 2%-6%.

If the reduced area in a beam flange is more than 50%, the beam section becomes unstable. Adding vertical stiffeners to the perforated section can greatly improve its stability and result in large ductility. But such stiffeners add strength to the beam, and the amount of strength added by the stiffeners requires further investigation.

The plastic rotation capacity of a perforated beam section can be determined by a suitable strain hardening factor and by the length of the row of holes. Test results of the moment capacity of the perforated beam show excellent agreement with the theoretical values. The energy dissipating mechanism is achieved either by plastification or by local buckling. These advantages demonstrate that properly designed perforated beam connections can be utilized in moment-resisting frames as a highly effective means for connection protection from brittle fracture and can achieve energy dissipation in certain seismic events.

But the success of a material yielding type connection depends not only on a good design but also on the use of a good material with high ductile behavior. Unfortunately, the structural steel materials tested in the laboratory lack such good ductile behavior. The two large specimens tested have cumulative ductility near 80, which is too small for a big shake. Once the available ductility is exhausted, the connection fails due to brittle fracture.



Chapter 4

Design of Frames with Slotted Bolted Connection

4.1 Introduction

It has been shown previously that conventional welded steel connections are unreliable. Their hysteresis energy capacity is limited. To solve this problem, an alternative method using energy dissipators seems reasonable as long as the added cost is small.

Several different types of passive energy dissipators are now available [8, 29]. From an analytical point of view, passive energy dissipators can be classified into two major categories - viscous type damper and frictional type damper. Material yielding type dissipators have a similar hysteresis behavior as the frictional type. Tune-mass dampers are not energy dissipators because they can only store kinetic energy but cannot dissipate energy. Viscous type dampers have a great advantage in analysis because they are linear (velocity proportional). But a viscous damper cannot resist a static or slowly applied load. This means that a viscous damper cannot resist a static gravity load. Whereas frictional type dampers are nonlinear in analysis (displacement and slip force dependent), but they can resist both static and dynamic loads.

The discussion here is limited to the Slotted Bolted Connection (SBC) as developed at UC Berkeley. SBCs have been tested extensively in earlier work [25, 26, 27, 28]. This chapter gives a brief description of such connections. Most of the chapter concentrates on the design of buildings with such connections.

SLOTTED BOLTED CONNECTION

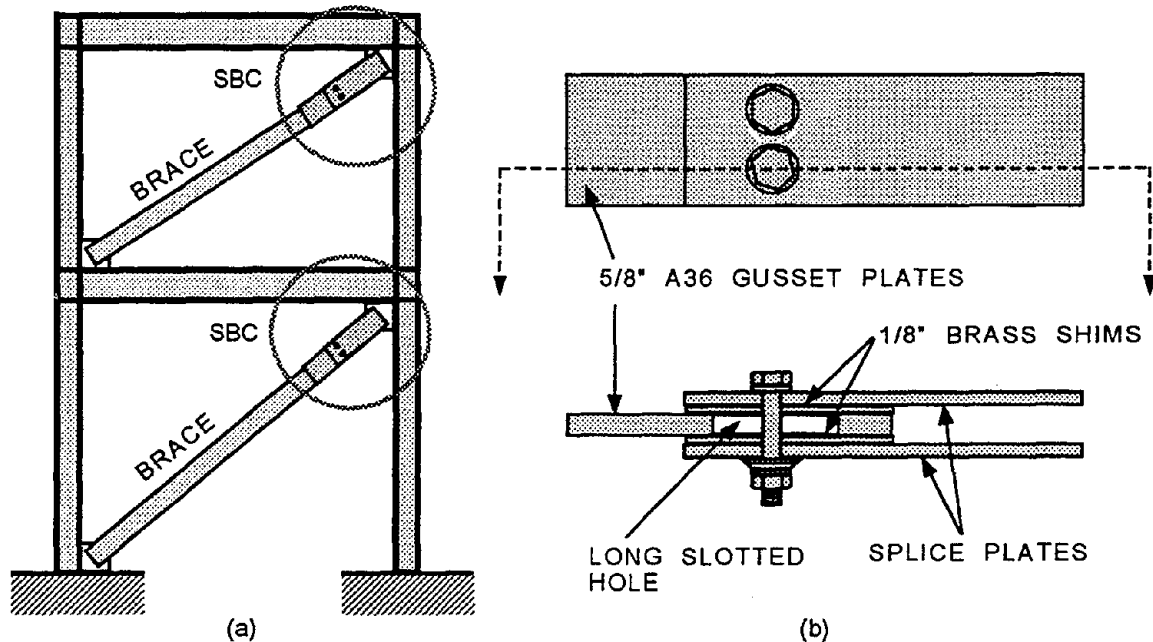


Fig. 4.1: (a) A Concentrically braced frame with SBCs, (b) the top view and side view of an SBC.

4.2 The Slotted Bolted Connection

The SBC is a modified bolted connection designed to dissipate energy through friction during rectilinear tension and compression loading cycles. As an example, an SBC can be placed between a brace end and the frame joint of a building as shown in Fig. 4.1a. The energy input to the building during a strong earthquake is dissipated by friction in the SBC dissipators in axial motion.

An SBC consists of five metal plates and a number of fastener bolts. Figure 4.1b shows a 2-bolted SBC assembly. Each plate, except the gusset plate, has an equal number of circular bolt holes for bolting these five plates together. The elongated holes or slots in the gusset plate, in which the bolts are seated, are parallel to the line of the loading motion. Two brass shims are inserted between the gusset plate and the splice plates in order to develop a constant friction. The friction coefficient of mild steel on brass is 0.3. The steel gusset plate is “sandwiched” directly between

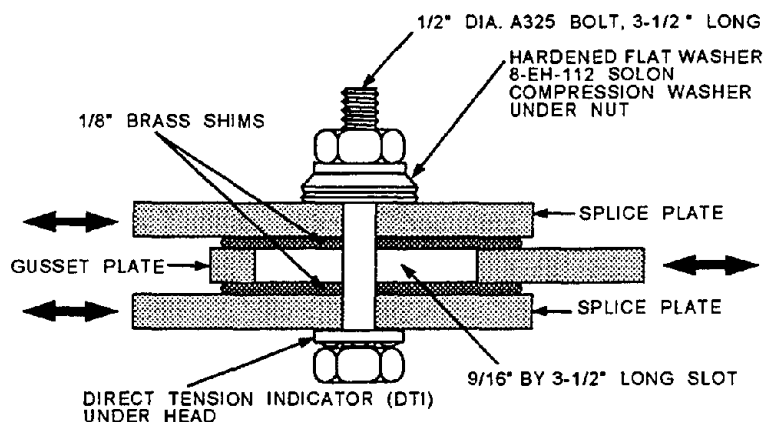


Fig. 4.2: Typical detail of a Slotted Bolted Connection (SBC).

the brass insert plates during an assembly. Typically, the gusset plate and the splice plates are of A36 steel. The brass shims are of the widely available half hard cartridge brass (UNS-260) (see Fig. 4.2). Both materials are inexpensive.

The A325 bolts are $\frac{1}{2}$ in. in diameter and $3\frac{1}{2}$ in. long. The optional Belleville washers placed under each nut are 8-EH-112 Solon compression washers with a hardened washer on top. Belleville washers are initially cone-shaped annular disk springs which flatten when compressed. The purpose of the Belleville washers is to maintain tension in the bolt during slip of the plates. To achieve the desired initial bolt tension, Direct Tension Indicator (DTI) washers are placed under each bolt head. DTIs are specially produced washers with protrusions that flatten as the bolt is tightened. The DTIs for $\frac{1}{2}$ in. diameter bolts are designed to indicate a bolt tension in the range of 12 to 14 kips.

Figure 4.3 shows typical hysteretic test loops for a 2-bolted SBC specimen. When the tensile or compressive force applied to the SBC exceeds the frictional forces developed between the surfaces, the gusset plate slips relative to the brass shims. This process is repeated with slip in the opposite direction upon reversal of the direction of force. Energy is dissipated by means of friction between the sliding surfaces. Slip force in the SBC has been shown to remain relatively constant over the range of interest. The SBC has been shown to be capable of dissipating significant quantities of energy by means of friction. This can satisfy the seismic hysteresis energy demand. Another advantage of the SBC is its low material and fabrication cost. The SBC exhibits great potential as an energy dissipating device in the seismic design and retrofit

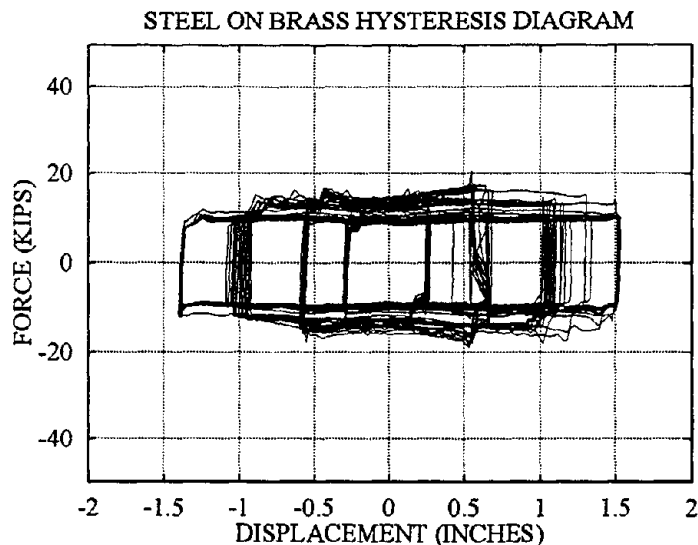


Fig. 4.3: Hysteresis loops for a two-bolted SBC test specimen.

of structures.

The SBC has been used in two seismic strengthening projects at Stanford University [43]. In the strengthening of Building 610, the SBC was used in the in-plane pier to prevent the shear failure of the pier. In the Lou Henry Hoover Building, SBCs were added to the brace connections to prevent the braces from buckling and limit the forces transferred to the vulnerable beams. Many new projects are considering SBCs as primary energy dissipators, including the strengthening project of the Golden Gate Bridge, San Francisco.

Because of the nonlinear behavior of SBCs, it is not necessary for a designer to choose the required sizes and locations. One can adjust the sizes of SBCs by trial-and-error with the aid of nonlinear structural analysis software, but such design iterations may be time-consuming and costly. In the following sections, three design tools will be indicated to assist in the determination of the required SBCs. Such tools can help the designer pick good starting values for the SBCs, thus minimizing the subsequent trial-and-error iterations.

4.3 Analytical Model of SBC

To simplify the analytical model for a building with an SBC, a braced shear building will be used in the following discussion. A shear building is defined as a structure in

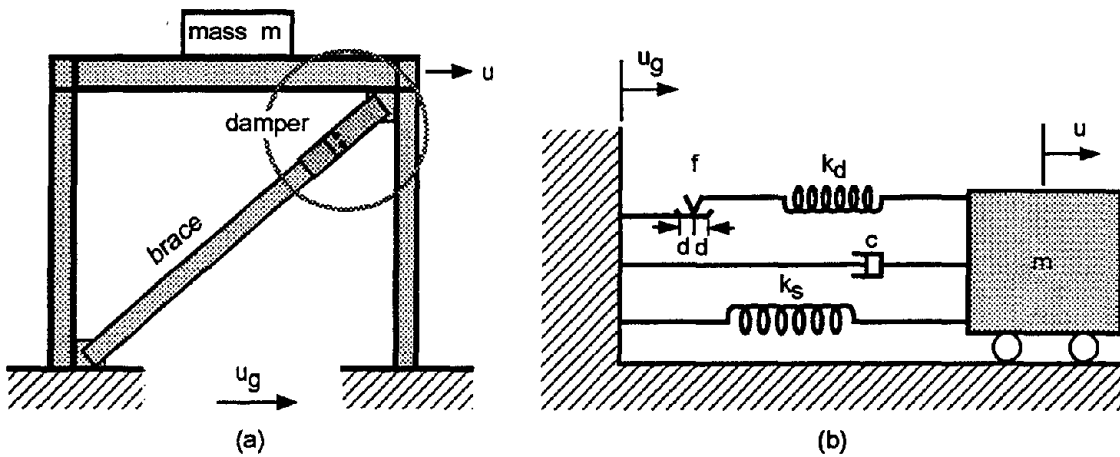


Fig. 4.4: (a) A single-story concentrically braced frame with a friction damper, and (b) the corresponding single degree-of-freedom model.

which there is no rotation of a horizontal section at the floor level. The total mass of the structure is concentrated at the floor levels. Also, the floor diaphragms are assumed to be rigid. Deformation of the structure is independent of the axial forces present in the columns.

Consider a single-story braced shear building with a relative lateral displacement u at the floor level as depicted in Fig. 4.4a. The lateral stiffness of the brace is k_d , and the lateral stiffness of the columns is k_s . The total initial lateral stiffness of the structure is $k = k_d + k_s$. This system corresponds to an SDOF system as shown in Fig. 4.4b. The governing equation for the single degree-of-freedom system can be written as

$$m\ddot{u} + c\dot{u} + k_s u + f_d(u) = -m\ddot{u}_g \quad (4.1)$$

where m is the total mass, c is the viscous damping coefficient, and $-m\ddot{u}_g$ is the earthquake forcing function applied at the floor level. The spring force $f_d(u)$ in Eq. (4.1) is nonlinear. As the frictional damper begins to slip during vibration, the stiffness k_d turns to zero. Thus the total lateral stiffness reduces to k_s . The solution of Eq. (4.1) requires a nonlinear structural analysis computer program.

A brace with a frictional damper attached can be modeled as an elastic-perfectly plastic axial force bar with yield force equal to the slip force f of the damper. The slope of the load-displacement curve is equal to the brace stiffness k_d at the initial

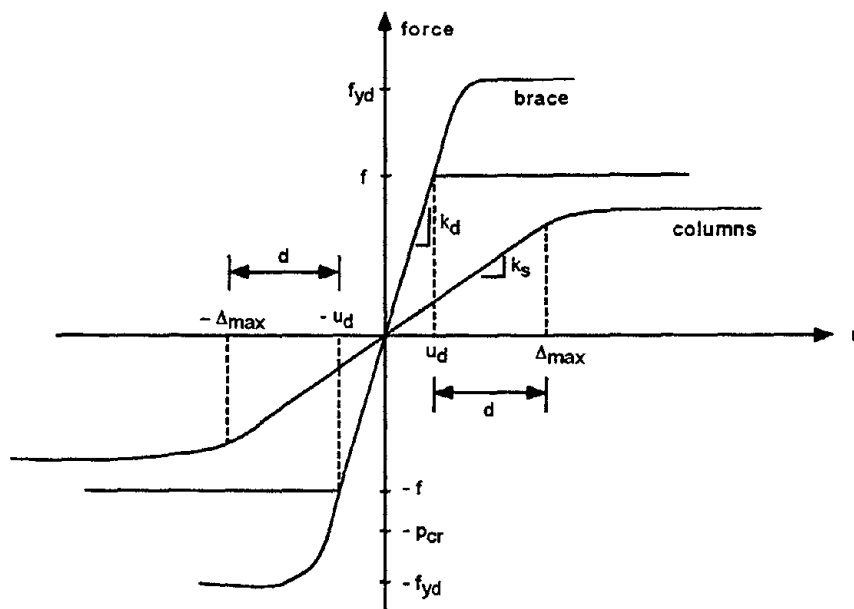


Fig. 4.5: Selection of friction force and slip distance.

stage of the loading. As the load increases to the slip force of the frictional damper, the damper slides and forms a perfectly plastic plateau portion of the curve. The length of the plastic region is equal to one half of the maximum allowable slip length of the damper with the initial origin located at the center of the slip range.

Certain limitations are imposed on the choice of the friction force f and the half slip length d . Figure 4.5 shows the requirements for selecting a frictional damper. If the moment in the column exceeds its moment resisting capacity, a plastic hinge will form in the column. In such a case, some damage occurs in the structure. Thus the damper should start to slip earlier than when the force resisting capacity of any member of the structure is reached. It is also necessary that the slip force of the damper must be less than the buckling load p_{cr} and yielding load f_{yd} of the brace such that no damage or stability problems can arise in the brace. Requirements for the slip length d are not very strict. If the structure is designed to remain in the elastic range, the maximum slip length can be set equal to the displacement Δ_{max} , where the first structural member begins to yield. But if the structural members are to yield to dissipate energy also, there is no slip length restriction. Special studies on the load-displacement relationships are needed for other types of structural-dissipating device configurations.

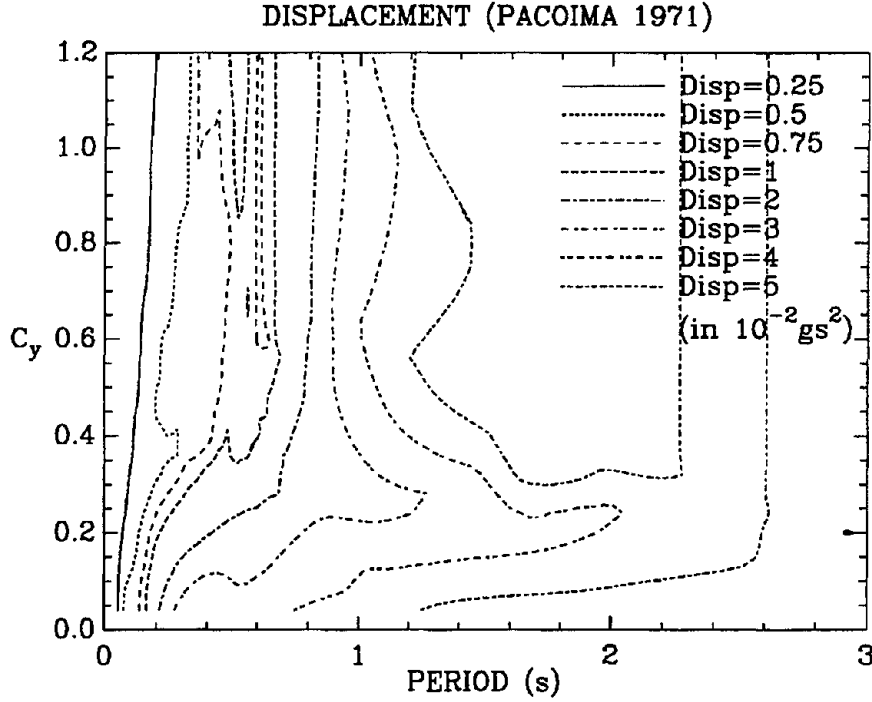


Fig. 4.6: Special displacement spectrum for the 1971 Pacoima earthquake. This spectra is constructed for 5% stiffness ratio and 2% damping ratio.

In order to simplify the design of a structure with a friction energy dissipating device, response spectra for the analytical model described by Eq. (4.1) are constructed. Let elastic stiffness ratio $\alpha_s = k_s/k$, where $k = k_d + k_s$, and $f_d(u) = k_d h_d(u)$. Then Eq. (4.1) becomes:

$$\ddot{u} + \frac{4\pi\xi}{T}\dot{u} + \frac{4\pi^2\alpha_s}{T^2}u + \frac{4\pi^2(1-\alpha_s)}{T^2}h_d(u) = -\ddot{u}_g \quad (4.2)$$

An implicit parameter $C_y (= f/mg)$ is hidden within $h_d(u)$. The period T in the above equation represents the period of the structure with no slip, i.e., $T = 2\pi\sqrt{m/k}$. The stiffness of the structure changes when the frictional damper slips. Hence the vibration frequency of the structure is not constant. For a typical concentrically braced steel frame, the value of α_s is commonly below 10%. By solving Eq. (4.2) over the T - C_y range, a set of displacement response spectra can be constructed. Figs. 4.6 and 4.7 show special displacement spectra with different damping ratios for the 1971 Pacoima earthquake.

These two spectra lead to some interesting findings. If the slip force is large, cor-

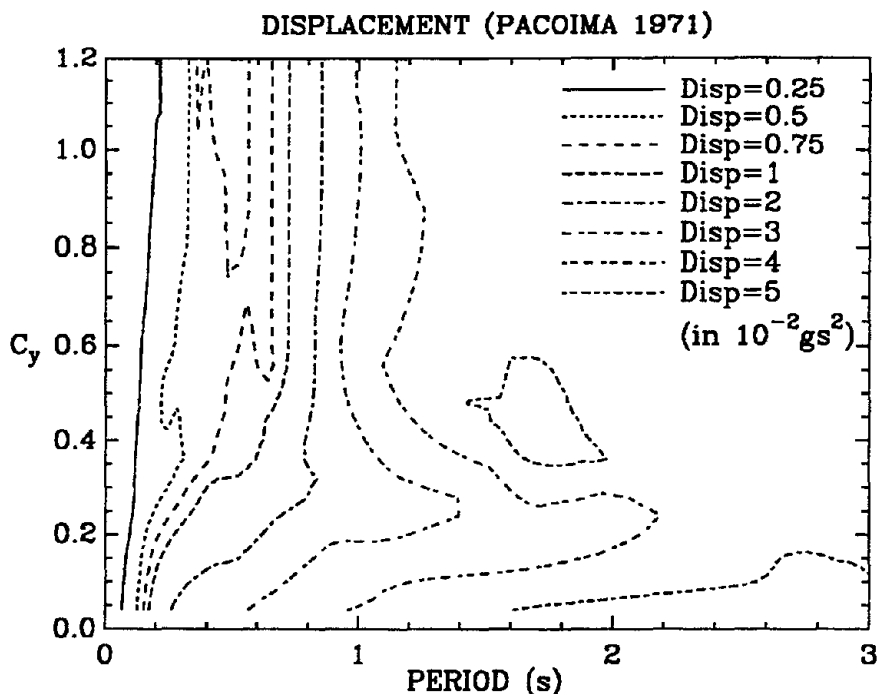


Fig. 4.7: Special displacement spectrum for the 1971 Pacoima earthquake. Both the stiffness and damping ratios are 5%.

responding to large C_y , the damper will not slip, the brace behaves elastically, and the contour line appears parallel to the vertical axis. In other words, the use of a large frictional damper is useless. The most effective range for frictional dampers is for C_y to be below 0.4 for seismic-resisting applications with a short vibration period. For long period structures, the required friction force is smaller. For some moderate earthquakes, the value of C_y is even lower. In this range, several brace-damper combinations lead to the same displacement response. This allows the engineer to select the most economical combination along an equal displacement contour. The same procedure can be used to construct response spectra for other values of stiffness and damping ratios.

4.4 Design Methods

Three methods are devised to design a structure with a frictional damper. They are the displacement spectrum method, the energy-based design method, and the force reduction design method. The selection of a design method depends on the stage of

the design and the availability of the computational software. In this section, only single degree-of-freedom systems are considered. These methods can be extended to the design of multi degrees-of-freedom systems.

4.4.1 Design by Special Spectra

The simplest and most straight-forward method to design a single-story shear building with a frictional damper is by using the special displacement response spectrum as described in the last section.

The design procedure is very simple. First, the columns are designed to support the gravity load of the structure, and the lateral stiffness of the columns is assumed to be 5% of the total lateral stiffness¹. Second, the brace and the damper are designed using the special displacement spectrum of a certain earthquake such as the one shown in Fig. 4.6. Then a desired displacement curve for the design is chosen from the figure. Assume the value of this curve to be u_{max} . This displacement determines the minimum half slip length d of the frictional damper, where this displacement must be smaller than the drift limitation Δ_{max} to protect the gravity supporting columns and the secondary structures, i.e.,

$$u_{max} \leq \Delta_{max} \leq d + \frac{f}{k_d} \quad (4.3)$$

Every point on the displacement curve represents a C_y - T pair, where C_y is related to the slip force by

$$f = mgC_y \quad (4.4)$$

and T is related to the brace stiffness by

$$k_d = m(1 - \alpha_s) \left(\frac{2\pi}{T} \right)^2 \quad (4.5)$$

Once f and k_d have been determined, two more design constraints must be satisfied. The slip force of the frictional damper f must be smaller than the buckling load p_{cr} and the yield load f_{yd} of the brace, i.e.,

$$SF \cdot f \leq p_{cr} \leq f_{yd} \quad (4.6)$$

¹The stiffness ratio depends on the structural form and member arrangement. For different value of stiffness, the special displacement response spectra have to be regenerated.

where SF is the safety factor. This equation reduces to $SF \cdot f \leq f_{yd}$ for a short brace, in which the buckling load is larger than the yield force, and the effect of the buckling load is ignored.

As compared with a traditional MRF design, a frictional damper can provide the required ductility by a suitable slip length d . The frictional damper can also provide an amount of hysteresis energy much larger than the seismic demand. Thus concerns for the available ductility and hysteresis energy capacity as in an MRF design do not enter the problem.

Also, once the size of the brace member is selected in a conventional CBF design, the yield load and the stiffness of the brace are determined. On a bracing frictional damper, the stiffness and the slip load corresponding to the buckling or yield load in the CBF brace, can be selected separately. The slip load can always be made smaller than the buckling load of the brace. In this case, the frictional damper can be considered as either an energy dissipating device or a brace surge protector.

4.4.2 Design by Energy Balance

In designing structures with frictional dampers, the cumulative energy of the ground motion becomes meaningless, since a well-designed frictional damper can always convert kinetic energy and strain energy into heat and dissipate it by air cooling or metal conduction. Based on this concept, the design is very simple for a single degree-of-freedom system.

Let u_{max} and \dot{u}_{max} be the maximum displacement and velocity responses, respectively, of a structure with mass m under a certain ground motion. A frictional damper on the brace with slip force f and slip range $-d$ to $+d$ is attached to the structure. The goal of the design is to select adequate values of f and d . Usually d can be selected to meet the ductility requirement. But it is more direct to use the elastic limit displacement of the columns. Assuming that the brace has been designed, the concentrically braced frame then can be analyzed for an earthquake using a **linear** structural analysis program. The maximum strain energy SE and the maximum kinetic energy KE can be calculated from

$$SE = \frac{1}{2}ku_{max}^2 \quad (4.7)$$

$$KE = \frac{1}{2}mi_{max}^2 \quad (4.8)$$

where $k = k_d + k_s$. In an earthquake, SE and KE will not be equal even for a conservative system because the input energy is transient at all times.

The frictional damper is designed to dissipate most of the maximum strain and kinetic energies. Since SE and KE occur at different times, their combination representing the maximum system energy can be used to design the damper. The simple design rule is

$$\text{maximum system energy} = \text{recoverable strain energy} + \text{dissipated energy} \quad (4.9)$$

The maximum system energy of Eq. (4.9) can be either SE or KE , or some reasonable combinations of SE and KE . Since the phase between the structural motion and the ground motion will change after the frictional damper is inserted, the use of the average of SE and KE is reasonable. For a single degree-of-freedom system, Eq. (4.9) can then be written as (see Fig. 4.5)

$$\frac{1}{2}(SE + KE) = \frac{1}{2}k_s\Delta_{max}^2 + \frac{1}{2}k_d\left(\frac{f}{k_d}\right)^2 + f\left(\Delta_{max} - \frac{f}{k_d}\right) \quad (4.10)$$

from which the slip force f can be determined. It is assumed that the maximum instantaneous energy can be dissipated in quarter cycle. If u_{max} is greater than Δ_{max} , this method cannot be applied, since there is no sliding space for the frictional damper to move (refer to Fig. 4.5).

Using the code spectra to design, the same procedure can be applied. If S_a is the spectral acceleration, the pseudo velocity S_v and pseudo displacement S_d are

$$S_v = \frac{T}{2\pi}S_a \quad (4.11)$$

$$S_d = \frac{T}{2\pi}S_v \quad (4.12)$$

The kinetic and strain energies can be computed and used in determining the slip force f

$$KE = \frac{1}{2}mS_v^2 \quad (4.13)$$

$$SE = \frac{1}{2}kS_d^2 \quad (4.14)$$

4.4.3 Design by Force Reduction

Another good method for designing a frictional damper can be based on the equation of motion

$$m\ddot{u} + c\dot{u} + k_s u + f_d(u) = -m\ddot{u}_g \quad (4.15)$$

where $f_d(u)$ is the force term for the frictional damper. The direction of the f_d is always opposite to the direction of the motion. The structure activates the frictional damper as it is sliding, satisfying the following conditions:

$$f_d(u) = \begin{cases} f \cdot \text{sgn}(\dot{u}) & \text{if } |u| > u_d \\ k_d u & \text{if } |u| \leq u_d \end{cases} \quad (4.16)$$

By moving f_d to the right-hand side of the equation, this term can be interpreted as the reduction of the earthquake force. The remaining terms on the left-hand side represent the original structure without the frictional damper. If the magnitude of the slip force f is about one-half of the applied earthquake force, a ground load reduction factor of 2 is obtained. This design method applies to the original structure without the brace and the frictional damper by considering the frictional damper as an earthquake force reduction device. Only linear elastic analysis is needed if k_s is linearly elastic.

If one wishes to use the code specified spectral acceleration S_a times mass m as the earthquake load, then frictional force can be deducted from it. This means using $(mS_a - f)$ as the design load. The drawback of this method is that the effect of the brace stiffness is ignored. The shift of the structural period needs to be considered carefully.

4.4.4 Design Methods for MDOF system

An n -story shear building with frictional dampers, such as the 3-story one shown in Fig. 4.8, can be formulated as a multi-degree-of-freedom (MDOF) system. The equations of motion are n ordinary differential equations in terms of relative displacement vector \mathbf{u} :

$$\mathbf{M}\ddot{\mathbf{u}} + \mathbf{C}\dot{\mathbf{u}} + \mathbf{K}_s \mathbf{u} + \mathbf{f}_d(\mathbf{u}) = \mathbf{P} \quad (4.17)$$

where \mathbf{M} , \mathbf{C} , and \mathbf{K}_s are the n by n mass matrix, the n by n damping coefficient matrix, and the n by n lateral column stiffness matrix, respectively. The displacement

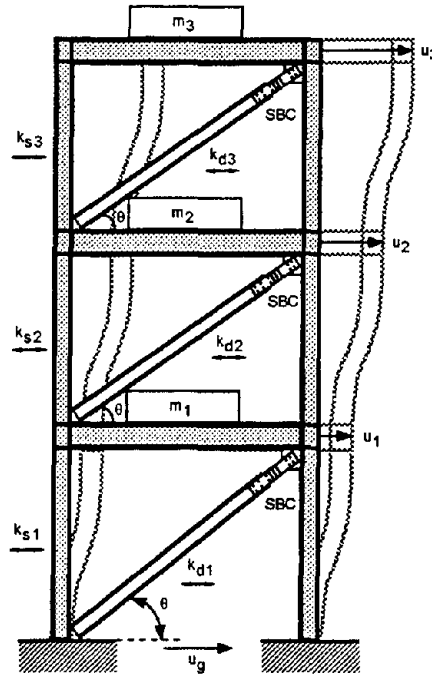


Fig. 4.8: A 3-story shear building with SBC dampers.

\mathbf{u} is an n -component column vector, the i th component is corresponding to the i th level horizontal displacement relative to the ground. \mathbf{f}_d is an n by 1 force vector representing the horizontal force component of the SBC braces. The external load \mathbf{P} is equal to $-\mathbf{M}\mathbf{r}\ddot{u}_g$, the n by 1 constant vector \mathbf{r} has all its elements equal to 1. As before, \ddot{u}_g is the ground acceleration. In a building structure, drifts are more important than displacements. The drift at i th level is defined as

$$\delta_i = u_i - u_{i-1}, \quad i = 1, 2, \dots, n \quad (4.18)$$

where u_0 is zero. Eq. (4.17) is nonlinear and can be solved by step-by-step piece-wise linear integration methods.

Two of the design methods described previously need only linear analysis. In such cases, the modal superposition method is more advantageous, because only the first few modes are required. During the no slip condition, \mathbf{f}_d can be expressed as

$$\mathbf{f}_d = \mathbf{K}_d \mathbf{u} \quad (4.19)$$

where \mathbf{K}_d is the n by n horizontal stiffness matrix for the braces. Defining the total stiffness matrix \mathbf{K} for no slip condition, $\mathbf{K} = \mathbf{K}_s + \mathbf{K}_d$, Eq. (4.17) for this condition

can be expressed as

$$\mathbf{M}\ddot{\mathbf{u}} + \mathbf{C}\dot{\mathbf{u}} + \mathbf{K}\mathbf{u} = -\mathbf{M}\mathbf{r}\ddot{u}_g \quad (4.20)$$

The i th column of the modal matrix Φ , and the corresponding undamped free vibration frequency ω_i for no slip condition, can be obtained by solving the following algebraic eigenproblem

$$\mathbf{K}\phi_i = \omega_i^2 \mathbf{M}\phi_i, \quad i = 1, \dots, n \quad \text{and} \quad \omega_1^2 \leq \dots \leq \omega_n^2 \quad (4.21)$$

The mode shapes (eigenvectors) ϕ_i are orthogonal, i.e.,

$$\phi_i^T \mathbf{M} \phi_j = \begin{cases} \tilde{m}_i & \text{if } i = j \\ 0 & \text{if } i \neq j \end{cases} \quad (4.22)$$

and

$$\phi_i^T \mathbf{K} \phi_j = \begin{cases} \tilde{k}_i & \text{if } i = j \\ 0 & \text{if } i \neq j \end{cases} \quad (4.23)$$

where \tilde{m}_i and \tilde{k}_i are the generalized mass, and the generalized stiffness for the i th mode, respectively. Assuming proportional damping ($\mathbf{C} = a_0 \mathbf{M} + a_1 \mathbf{K}$), such that the damping matrix C can be diagonalized, i.e.,

$$\phi_i^T \mathbf{C} \phi_j = \begin{cases} \tilde{c}_i = 2\xi_i \omega_i \tilde{m}_i & \text{if } i = j \\ 0 & \text{if } i \neq j \end{cases} \quad (4.24)$$

where \tilde{c}_i is the generalized damping coefficient, and ξ_i is the modal damping ratio for the i th mode. The orthogonality properties of the normal (modal) coordinates are used to simplify the equations of motion of the MDOF system. Defining modal amplitude vector \mathbf{z} , such that

$$\mathbf{u} = \Phi \mathbf{z} \quad (4.25)$$

then Eq. (4.20) can be rewritten as

$$\mathbf{M}\Phi\ddot{\mathbf{z}} + \mathbf{C}\Phi\dot{\mathbf{z}} + \mathbf{K}\Phi\mathbf{z} = -\mathbf{M}\mathbf{r}\ddot{u}_g \quad (4.26)$$

Premultiplying both sides of Eq. (4.26) by Φ^T , and defining $\mathbf{L} = \Phi^T \mathbf{M} \mathbf{r}$, the set of equations becomes

$$\Phi^T \mathbf{M} \Phi \ddot{\mathbf{z}} + \Phi^T \mathbf{C} \Phi \dot{\mathbf{z}} + \Phi^T \mathbf{K} \Phi \mathbf{z} = -\mathbf{L} \ddot{u}_g \quad (4.27)$$

Using the orthogonality properties in Eqs. (4.22), (4.23), and (4.24), Eq. (4.27) can be written in uncoupled form

$$\tilde{m}_i \ddot{z}_i + \tilde{c}_i \dot{z}_i + \tilde{k}_i z_i = -l_i \ddot{u}_g, \quad i = 1, \dots, n \quad (4.28)$$

Rewriting this equation in terms of ξ_i and ω_i , Eq. (4.28) becomes

$$\ddot{z}_i + 2\xi_i \omega_i \dot{z}_i + \omega_i^2 z_i = -\frac{l_i}{\tilde{m}_i} \ddot{u}_g, \quad i = 1, \dots, n \quad (4.29)$$

where l_i and z_i are the i th element of vector \mathbf{L} and \mathbf{z} , respectively. By solving these n uncoupled equations, the displacement vector \mathbf{u} can be obtained using modal superposition (Eq. (4.25)). If the CSMIP² earthquake response spectra are used to find the peak response of Eq. (4.29), some modal combination methods have to be used to obtain the solution closer to the exact response.

Two of the design methods, excluding the displacement spectrum method, can be extended for design of frictional dampers for MDOF systems. Due to the nonlinearity of frictional damper systems, the displacement spectrum method cannot be used for designing MDOF systems because the principle of superposition is not valid.

For a planar structure having p frictional dampers, there are 2^p possible friction states. As friction dampers lock and unlock, and the system modal characteristics also change, 2^p different sets of modal data are possible. If p is large, it is almost impossible to consider all of the possible friction states, let alone to design them. In order to design each frictional damper to the proper size, some assumptions have to be made.

In a small earthquake, all of the frictional dampers in the structure are locked, and the structure responds elastically. During a moderate or severe earthquake, some of the frictional dampers are activated but some are not. If a frictional damper cannot be activated by a strong ground motion, then it is not required. The purpose of a frictional damper is to dissipate energy. The greatest efficiency is attained if all of the dampers are sliding simultaneously. Also, if some of the dampers are locked, they provide continuous load paths for an earthquake to transmit force through them to reach vulnerable members. From this point of view, the desired frictional states reduce to two: **all locked**, or **all activated**. The remaining question is how to assign

²California Strong Motion Instrumentation Program (CSMIP), Office of Strong Motion Studies, Div. of Mines and Geology, State of California. 801 K Street, MS 13-35, Sacramento, CA 95814.

proper friction to each of the dampers such that all dampers will be activated at the same time during a strong earthquake and maintain the safety of the structure.

Since the time required for the structure to complete a cycle of vibration in response to a typical earthquake ground motion is very close to the natural period of the structure, the structure is vibrating most of the time in its first mode shape. Higher modes have much less effect on the response unless their frequencies are close to the natural frequency. If the friction forces are assigned proportional to the member force distribution of the first mode shape, then the vibrating shape will be the same for all-locked as well as all-sliding conditions. In other words, the frictional dampers become activated at the same time. In these two states the mode shapes are the same but the vibration frequency (or the velocity) of the structure is reduced toward zero when the dampers are activated.

4.5 Temperature Rise of SBC

When a structure equipped with SBCs is under the excitation of a strong earthquake, the SBCs slide by means of friction. The kinetic energy of the structure must be mostly absorbed by SBCs. This energy appears in SBCs in the form of heat.

The total energy dissipated by an SBC can be expressed as

$$E_d = \int f du_d \quad (4.30)$$

where f is the friction force of the SBC, and u_d is the slip displacement of the SBC. Note that E_d is the energy lost or dissipated; this is the energy absorbed by the SBC. If E_d is expressed in $lb \cdot in$, the heat generated in Btu is

$$H = \frac{E_d}{9,336} \quad (4.31)$$

The temperature rise of the SBC assembly can be approximated by the classic expression

$$\Delta T = \frac{H}{mC} \quad (4.32)$$

where ΔT is the temperature rise in $^{\circ}F$, m is the mass of the SBC parts in lb_m , and C is the specific heat in $lb_m \cdot ^{\circ}F$; C is 0.12 for steel. The temperature-rise equation can be used to explain what happens when an SBC is caused to slide. It is assumed

above that the SBC retains all the heat. However, if the duration of the earthquake is long, there are many variables involved. In such cases, the temperature decay due to ambient temperature, air cooling, and metal conduction must be considered. Usually, the temperature rise is small for a well-designed SBC. If the temperature rise is critical for certain applications, one can increase the steel plate volume (heat sink) to bring the temperature down. Notice that the friction force of an SBC is controlled by the bolts, and not by its volume. Thus the temperature rise problem can be easily solved by using a larger volume SBC.

4.6 Design Examples

4.6.1 Single-story Shear Building with SBC

The analysis methods discussed above are applied to the strengthening of a 42 ft wide and 26 ft tall concentrically braced frame (Fig. 4.9). The original structure is without the SBC. The columns use W12×190 sections ($I_x = 1,890 \text{ in}^4$, $I_y = 589 \text{ in}^4$, depth $h = 14.38 \text{ in}$, length $L_s = 26 \text{ ft}$, and area $A_s = 55.8 \text{ in}^2$). The brace uses W12×72 section ($I_x = 597 \text{ in}^4$, $I_y = 195 \text{ in}^4$, area $A_d = 21.1 \text{ in}^2$, length $L_d = 592.76 \text{ in}$, and $r_y = 3.04 \text{ in}$). After an SBC is inserted at the end of the brace, the structure should have better seismic behavior. The frame supports a 150 kip vertical load, and is designed to resist strong earthquakes similar to the 1971 Pacoima dam earthquake without any of the members yielding. Figures 4.10 and 4.11 are the ground acceleration and the Fourier amplitude spectrum, respectively, of the 1971 Pacoima earthquake. It is also required that the maximum lateral displacement Δ_{max} at roof level must be less than 1.3 inches to reduce non-structural damage. Brace buckling is not permitted. The material for the columns and brace is A36 steel with an assumed 2% internal damping ratio, the yield stress $\sigma_y = 36 \text{ ksi}$, and Young's modulus $E = 29,000 \text{ ksi}$. An SBC frictional damper is attached to the brace and a joint gusset plate. The roof deck is assumed to be much stiffer than the lateral stiffness of the frame and can be considered as rigid. Previously devised methods are used to design this shear building. Structural responses *before* and *after* the strengthening will be compared.

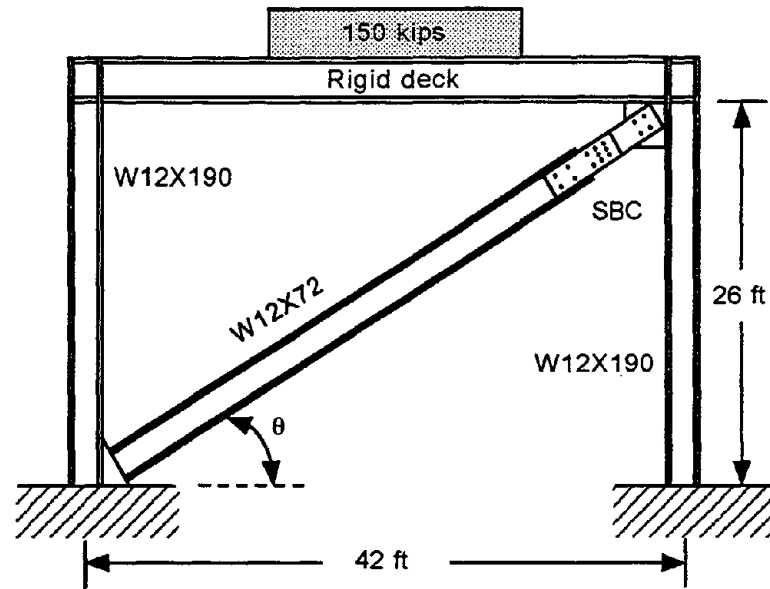


Fig. 4.9: A single-story concentrically braced warehouse frame.

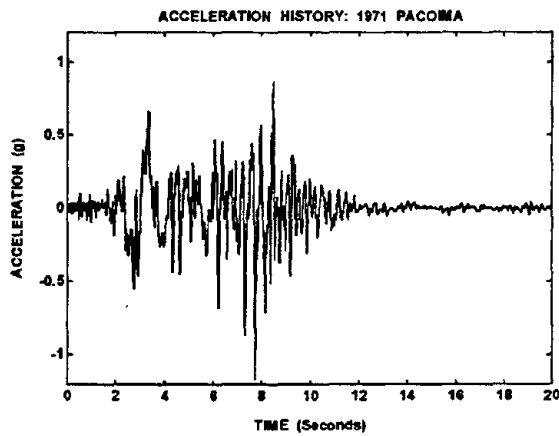


Fig. 4.10: The accelerogram of the 1971 Pacoima earthquake.

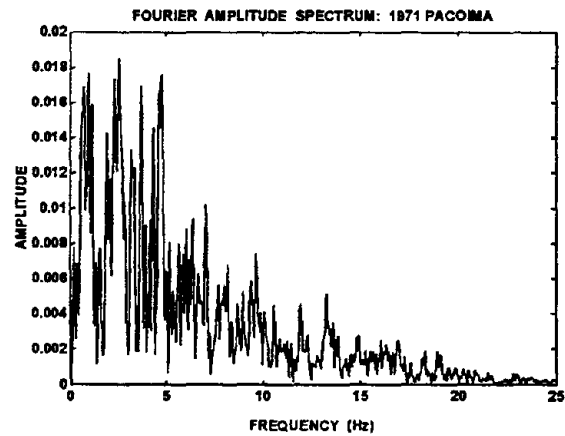


Fig. 4.11: The Fourier amplitude spectrum of the 1971 Pacoima earthquake ground acceleration.

Displacement Spectrum Method

The maximum stress in the column is due to 75 kips vertical load and bending moment caused by 1.3 inches sidesway at the top. The maximum axial stress is

$$\sigma = \frac{75}{A_s} + \frac{12E}{L_s^2} \Delta_{max} \frac{h}{2} = 34.8 \text{ ksi} < \sigma_y$$

The lateral stiffness of the columns and brace can be calculated as

$$k_s = \frac{12EI_x}{L_s^3} * 2 = 43.3 \text{ kips/in}$$

$$k_d = \frac{EA_d}{L_d} \cos^2 \theta = 746.3 \text{ kips/in}$$

where $\cos \theta = 42/\sqrt{42^2 + 26^2}$. The stiffness ratio α_s can be calculated as $43.31/(43.31 + 746.3) = 0.055$. The structural period T is known to be

$$T = 2\pi \sqrt{\frac{150}{g(k_s + k_d)}} = 0.14 \text{ sec}$$

From the special displacement spectrum in Fig. 4.6, for $u = 1.4$ inches ($.33 \times 10^{-2} \text{gs}^2$) contour and $T = 0.14$ sec, one obtains $C_y \approx 0.34$. The horizontal friction force component of the frictional damper is

$$f = mgC_y = 150 * 0.34 = 51 \text{ kips}$$

The needed slip force in the axial direction can be calculated to be $f/\cos \theta = 60$ kips. Checking brace stress σ , buckling load p_{cr} , and L/r ratio

$$\sigma = \frac{60}{A_d} = 2.84 \text{ ksi} < \sigma_y$$

$$p_{cr} = \frac{\pi^2 EI_y}{L_d^2} = 159 \text{ kips} > 60 \text{ kips}$$

$$\frac{L_d}{r_y} = \frac{42 * 12/\cos \theta}{3.04} = 195 < 200$$

Test results show that each $\frac{1}{2}$ inch diameter A325 bolt in an SBC can provide 7.5 kips friction force (see Fig. 4.3). Thus an 8 bolt SBC connection is used here to give 60 kips axial friction force. Required minimum half slip length d can be calculated by

$$d \geq \Delta_{max} - f/k_d = 1.3 - 60/746.3 = 1.22 \text{ in}$$

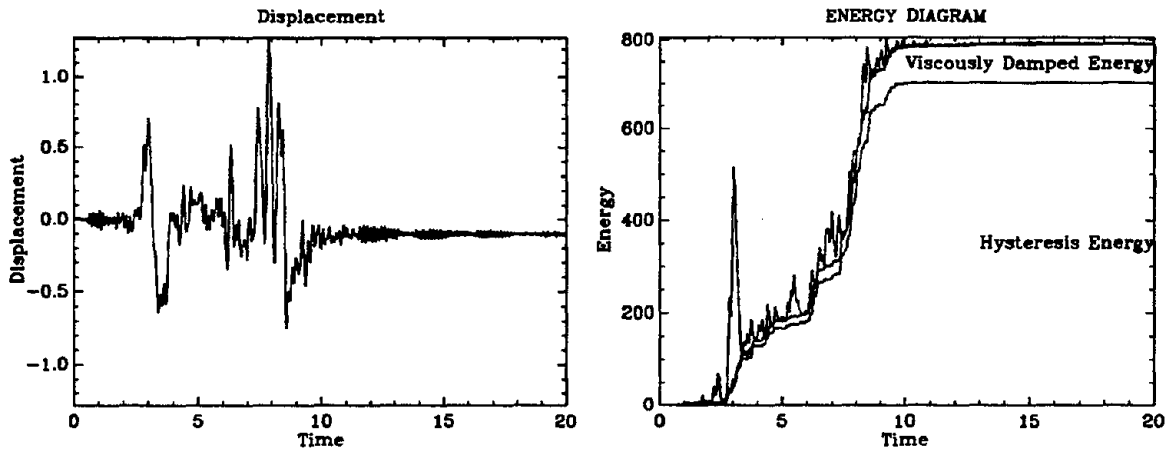


Fig. 4.12: Displacement response, in inches, of the single story building with the SBC for the 1971 Pacoima earthquake. **Fig. 4.13:** Absolute energy history, in kip-inches, of the single story building with the SBC for the 1971 Pacoima earthquake.

Choosing a total slot length of 3 inches ($d = 1.5$ in) satisfies this requirement.

Analysis of the structure is performed using the DANS computer program [75]. The displacement time history is shown in Fig. 4.12. The peak horizontal displacement u_{max} is 1.28 inches. The maximum base shear is 106.6 kips. The absolute energy diagram is shown in Fig. 4.13. Over 88% of the input energy is dissipated by the SBC damper. The hysteresis diagram of the SBC is given in Fig. 4.14.

To verify the adequacy of the analytical model and the capacity of the SBC for the selected earthquake, an SBC specimen with eight $\frac{1}{2}$ inch A325 bolts was fabricated [25]. The specimen was subjected to SBC slip displacement responses derived from the aforementioned analysis. Figure 4.15 shows the experimental hysteresis diagram. By comparing this figure with its analytical counterpart (Fig. 4.14), it is seen that the target slip force of 60 kips is attained.

From Fig. 4.13, the energy dissipated by the SBC is about 700 kip-inches. This amount of energy appears in the form of heat and causes the SBC temperature to rise. This amount of energy can be converted to heat by Eq. 4.31

$$H = \frac{700 \times 1,000}{9,336} = 75 \text{ Btu} \quad (4.33)$$

The main portion of the SBC consists of two $12'' \times 8'' \times \frac{5}{8}''$ steel plates and one $14'' \times 10'' \times \frac{5}{8}''$ steel plate. The mass can be calculated to be 60.2 lb_m . The mass of

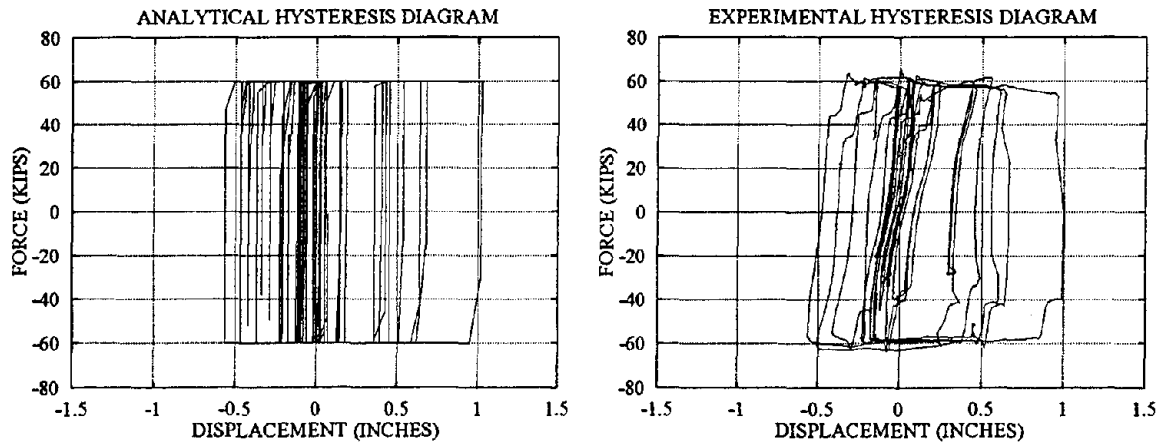


Fig. 4.14: Analytical hysteretic loops of the SBC for the 1971 Pacoima earthquake. **Fig. 4.15:** Experimental hysteretic loops of the SBC for the 1971 Pacoima earthquake. (Tested by C. E. Grigorian)

the brass shims is ignored here. The temperature rise is calculated by Eq. 4.32 to be

$$\Delta T = \frac{75}{0.12 \times 60.2} = 10.4^{\circ}\text{F} \quad (4.34)$$

The insignificant effect of temperature rise can be seen in this example. Notice that the air cooling and metal conducting in the duration of the earthquake are ignored, so the actual temperature rise should be even lower.

It is interesting to study the original CBF without the SBC damper for comparison. The displacement response and the energy diagram are shown in Fig. 4.16 and 4.17 respectively. Although the peak displacement is decreased to 0.55 inch, the base shear is increased to 430 kips, of which 407 kips was taken by the brace. This means that the axial force in the brace is 478 kips, which is much larger than the buckling load of 159 kips. The CBF structure without the SBC would collapse. A stronger brace is needed here to prevent buckling. Cost reduction by using the SBC is evident.

It is also interesting to compare the velocity and frequency of the structure before and after the SBC is inserted. Figure 4.18 is the trajectory of the braced structure without the SBC, where velocity is high but displacements are small. On the other hand, with an SBC, the velocity is small but the displacements are large (Fig. 4.19). The offset of the equilibrium point due to damper sliding can be seen in the figure. Unlike an elastic structure, which vibrates nearly at a constant frequency, the SBC

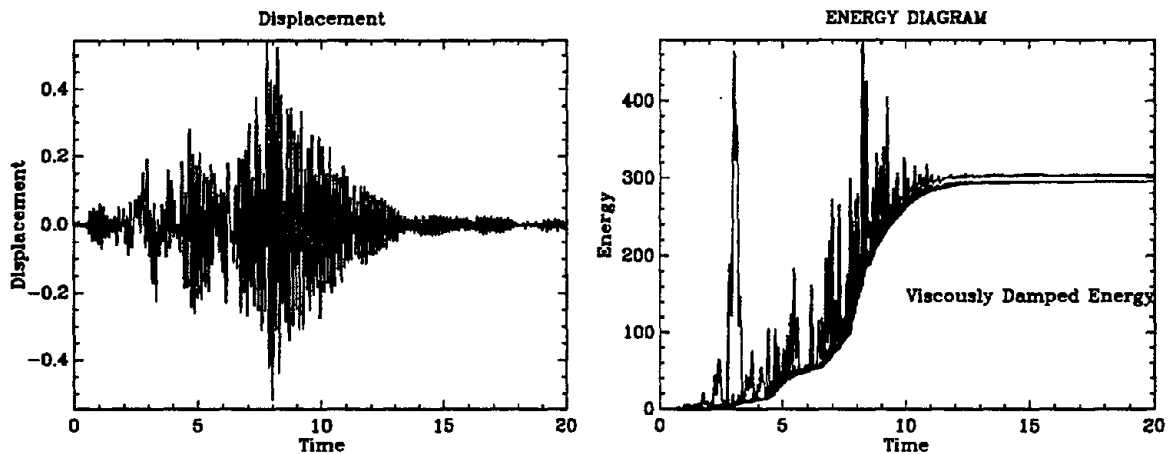


Fig. 4.16: Displacement response, in inches, of the single story building without the SBC for the 1971 Pacoima earthquake.

Fig. 4.17: Absolute energy history, in kip-inches, of the single story building without the SBC for the 1971 Pacoima earthquake.

can dissipate the structural kinetic energy and cause the structure to slow down. To study the frequency response of the original and the SBC equipped systems, the displacement Fourier amplitude spectra for these two systems are constructed (Figs. 4.20 and 4.21). The original building vibrates most of the time near its natural frequency at 7.1 Hz, whereas the vibration frequencies of the building with the SBC have frequencies spreading toward 0 Hz. The speed braking effect of the SBC is evident here. The advantage of a structure equipped with SBCs is the prolongation of its oscillation period. The base-isolated structure has the same merit (long period).

The dynamic response of this single story frame due to other earthquakes has also been studied. Figures 4.22 and 4.23 are the displacement and the SBC slip history, respectively, for the 1989 Loma Prieta earthquake. Figures 4.24 and 4.25 are the displacement and the SBC slip history, respectively, for the 1940 El Centro earthquake times two. The responses for these two earthquakes are feasible.

Energy-Based Design Method

The energy-based design method used in this section requires only linear analysis and is a simple energy balancing method.

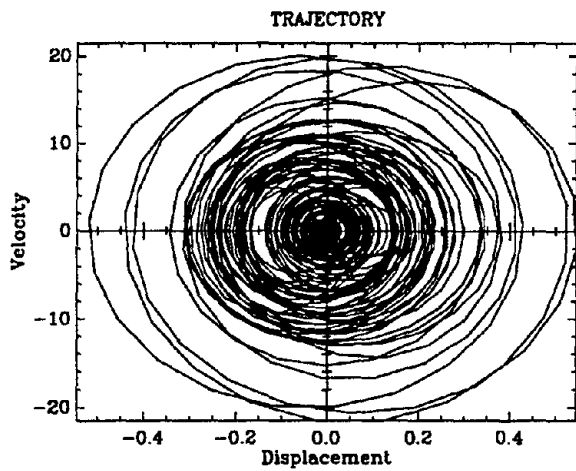


Fig. 4.18: Trajectory diagram, in inches and inches/sec, of the single story building *without* the SBC for the 1971 Pacoima earthquake.

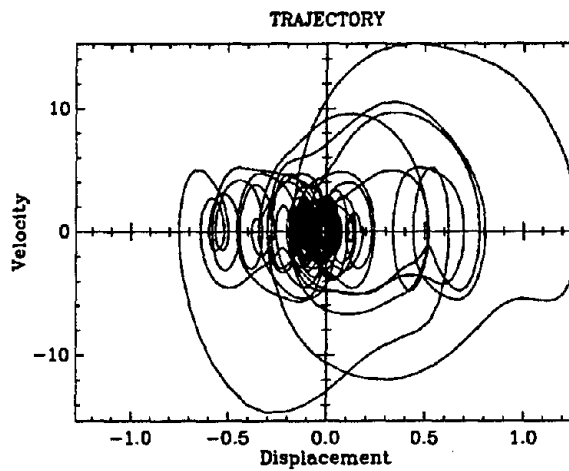


Fig. 4.19: Trajectory diagram, in inches and inches/sec, of the single story building *with* the SBC for the 1971 Pacoima earthquake.

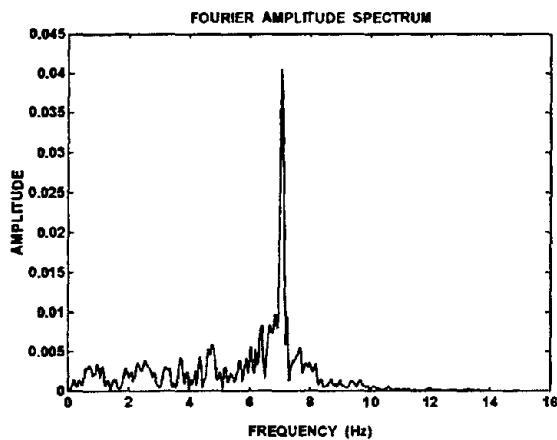


Fig. 4.20: Displacement Fourier amplitude spectrum of the single story building *without* the SBC for the 1971 Pacoima earthquake.

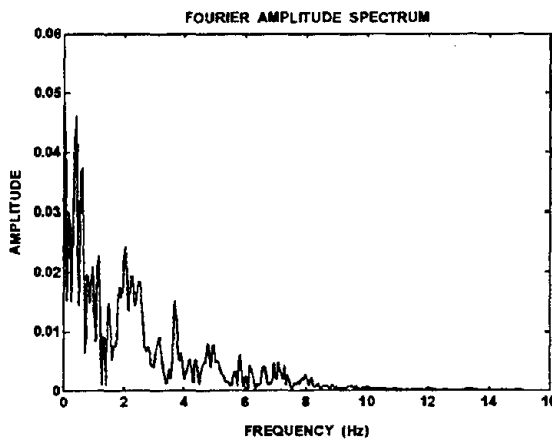


Fig. 4.21: Displacement Fourier amplitude spectrum of the single story building *with* the SBC for the 1971 Pacoima earthquake.

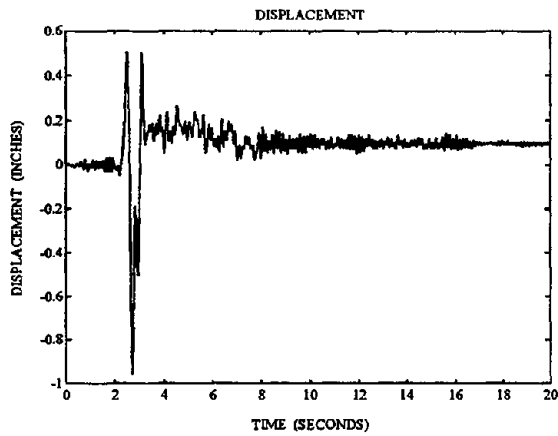


Fig. 4.22: Displacement response of the single story building for the 1989 Loma Prieta earthquake.

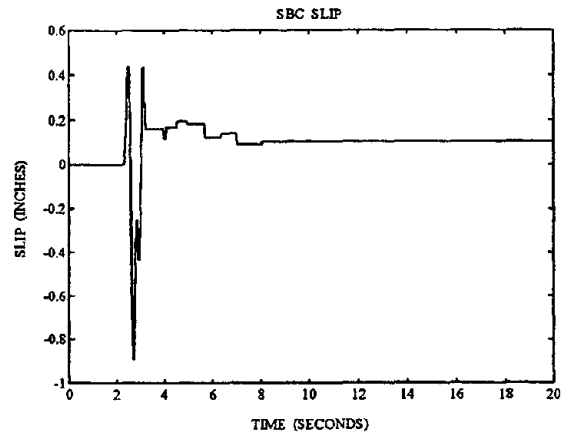


Fig. 4.23: SBC slip history of the single story building for the 1989 Loma Prieta earthquake.

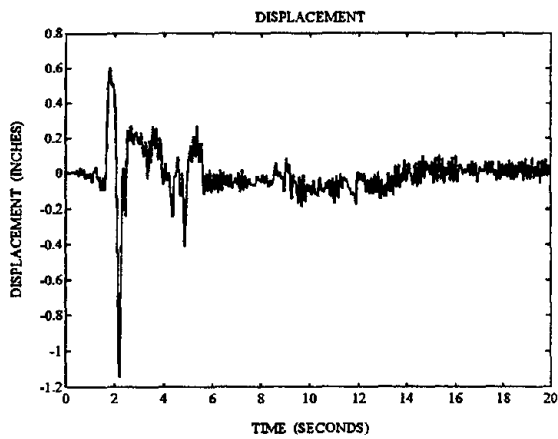


Fig. 4.24: Displacement response of the single story building for the 1940 El Centro earthquake times two.

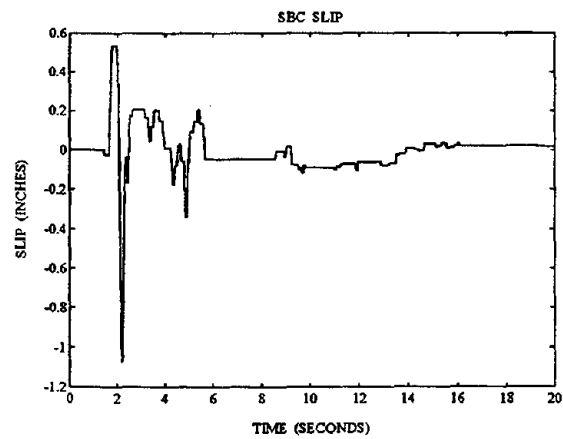


Fig. 4.25: SBC slip history of the single story building for the 1940 El Centro earthquake times two.

As before, the gravity supporting columns are designed first, with W12×190 selected for both columns. The lateral stiffness of the columns is $k_s = 43.3$ kips/inch. By assuming a 5% stiffness ratio, the brace stiffness can be determined. W12×72 section is selected for the brace. The lateral stiffness of the brace is $k_d = 746$ kips/inch. The analysis is then performed using a linear structural analysis program. The maximum magnitude of displacement and velocity can be found to be

$$\begin{aligned}u_{max} &= 0.545 \text{ in} \\ \dot{u}_{max} &= 21.5 \text{ in/sec}\end{aligned}$$

The peak strain energy SE can be calculated as

$$SE = \frac{1}{2}(k_s + k_d)u_{max}^2 = 117 \text{ kip-inches}$$

The maximum kinetic energy KE is

$$KE = \frac{1}{2}m\dot{u}_{max}^2 = 89.4 \text{ kip-inches}$$

Since $u_{max} < \Delta_{max}$, the energy method can be applied. The size of the frictional damper can be selected by applying the equation

$$\frac{1}{2}(SE + KE) = \text{strain energy} + \text{dissipated energy}$$

In this case,

$$0.5(117 + 89.4) = \frac{1}{2}k_s(1.3)^2 + \frac{1}{2}k_d(f/k_d)^2 + (1.3 - f/k_d)f$$

The required friction force is calculated to be $f = 52.8$ kips, or 62 kips in the axial direction, which is very close to the value obtained by the special response spectrum method. If the viscous damping energy is put into consideration, the calculated friction force would be much closer.

Force Reduction Design Method

By moving the friction force to the right-hand-side, Eq. (4.15) can be rewritten as

$$m\ddot{u} + c\dot{u} + k_s u = -m\ddot{u}_g - f_d(u)$$

The presence of $f_d(u)$ makes analysis impossible if only a linear analysis tool is available. One good alternative approach is to analyze the structure without the brace and

damper using a linear analysis software, and determine the maximum base shear V_B . If the design is controlled by the allowable shear force V_a of the columns, the excess part of the base shear must be resisted by the frictional damper, and the required friction force is

$$f = V_B - V_a$$

Of course, if $V_a > V_B$, then there would be no need a damper.

In the design of a structure with two W12×190 columns, the lateral stiffness of the columns k_s is known to be 43.3 kips/in. The linear dynamic analysis for the 1971 Pacoima earthquake shows that the maximum displacement u_{max} is 2.67 inches and the maximum base shear V_B is 116 kips. Since the allowable displacement is 1.3 inches, the force required to reduce the maximum displacement to the allowable value is selected as the horizontal component of the friction force

$$f = k_s(2.67 - 1.3) = 59.3 \text{ kips}$$

This value is acceptable but is much larger, or conservative, than the values found by the previous two methods. The reason is that here the damping force due to the brace is ignored. Also, the vertical supporting structure has a period of 0.59 second, causing different response to the ground motion. However, this quick “back-of-the-envelope” calculation method is suitable for preliminary design.

4.6.2 Multi-story Shear Building with SBCs

In this section, the energy-based method and the force reduction method are applied for designing the SBCs in a 3-story concentrically braced frame. The configuration of the building is shown in Fig. 4.8. This building is modeled as a lumped mass shear building with the following mass and horizontal stiffness properties:

floor mass	$m_1 = m_2 = m_3 = 100/g \text{ kips}$
column stiffness	$k_{s1} = k_{s2} = k_{s3} = 100 \text{ kips/inch}$
brace stiffness	$k_{d1} = k_{d2} = k_{d3} = 1000 \text{ kips/inch}$

The building frame is designed to resist strong earthquakes similar to the 1971 Pacoima earthquake without any of the members yielding. It is also required that the maximum lateral drift Δ_{max} at each floor be less than 1 inch to reduce columns and

non-structural damage. Assuming the internal damping ratio is zero for all modes. Three SBC frictional dampers with friction force f_1 , f_2 , and f_3 are chosen for stories 1, 2, and 3, respectively. The mass matrix \mathbf{M} and stiffness matrices \mathbf{K}_s and \mathbf{K}_d can be shown to be

$$\mathbf{M} = \begin{bmatrix} m_1 & 0 & 0 \\ 0 & m_2 & 0 \\ 0 & 0 & m_3 \end{bmatrix} = \begin{bmatrix} 0.259 & 0 & 0 \\ 0 & 0.259 & 0 \\ 0 & 0 & 0.259 \end{bmatrix}$$

$$\mathbf{K}_s = \begin{bmatrix} k_{s1} + k_{s2} & -k_{s2} & 0 \\ -k_{s2} & k_{s2} + k_{s3} & -k_{s3} \\ 0 & -k_{s3} & k_{s3} \end{bmatrix} = \begin{bmatrix} 200 & -100 & 0 \\ -100 & 200 & -100 \\ 0 & -100 & 100 \end{bmatrix}$$

$$\mathbf{K}_d = \begin{bmatrix} k_{d1} + k_{d2} & -k_{d2} & 0 \\ -k_{d2} & k_{d2} + k_{d3} & -k_{d3} \\ 0 & -k_{d3} & k_{d3} \end{bmatrix} = \begin{bmatrix} 2000 & -1000 & 0 \\ -1000 & 2000 & -1000 \\ 0 & -1000 & 1000 \end{bmatrix}$$

Energy-Based Design Method

The braced 3-story building without the frictional dampers is analyzed by a linear structural analysis program. The maximum drift response is found to be

$$\delta_{max} = \begin{Bmatrix} 1.87 \\ 1.44 \\ .826 \end{Bmatrix} \text{ inches}$$

Because the largest drift is larger than the allowable drift Δ_{max} , the energy-based design method cannot be applied. But this does not mean that the frictional dampers are useless for this structure. It just means that no hysteresis energy can be absorbed at the origin. If the damper slides Δ_{max} in the negative direction first, then there is enough positive slip length available, $2 * \Delta_{max}$, and the energy method is applicable. But this depends on the phase between the structural motion and the random earthquake motion, and the method used does not solve the design problem.

If all the drifts are smaller than Δ_{max} , then the energy method can be used. Note that the ratios between friction forces are known from the first mode member force distribution, and there is only one unknown scaling factor that needs to be determined. This factor can be found by the same design rule as for the SDOF system.

Force Reduction Design Method

Although the energy-based method cannot be used to design this structure, the force reduction method has no such limitation. The 3-story building without the braces is analyzed using a **linear** structural analysis software. The maximum displacement response is

$$\mathbf{u}_{max} = \begin{Bmatrix} 3.32 \\ 6.19 \\ 7.93 \end{Bmatrix} \text{ inches}$$

The maximum story drift vector is calculated to be

$$\delta_{max} = \begin{Bmatrix} 3.32 \\ 3.05 \\ 2.01 \end{Bmatrix} \text{ inches}$$

The maximum drift is calculated by $\delta_i = u_i - u_{i-1}$ for all steps of the displacement response; it cannot be derived from \mathbf{u}_{max} directly. Figure 4.26a shows the structure at extreme drift position; the friction forces are applied at each story level as the equivalent external loads. The maximum story drift is at the first story. Since the allowable drift Δ_{max} is 1 inch, the required total friction force F to reduce the first story drift from 3.32 inches to 1 inch can be calculated by static equilibrium

$$F = k_{s1}(3.32 - \Delta_{max}) = 100 * (3.32 - 1) = 232 \text{ kips} \quad (4.35)$$

where $F = f_1 + f_2 + f_3$. This force is distributed to each story.

The mode shapes and frequencies of this structure without the braces can be obtained by solving the following eigenproblem

$$\mathbf{K}_s \phi_i = \omega_i^2 \mathbf{M} \phi_i, \quad i = 1, \dots, 3 \quad \text{and} \quad \omega_1^2 \leq \omega_2^2 \leq \omega_3^2$$

The free vibration frequencies and eigenvectors are

$$\omega_1 = 8.75 \text{ rad/sec, and } \phi_1 = \begin{Bmatrix} 0.445 \\ 0.802 \\ 1.000 \end{Bmatrix}$$

$$\omega_2 = 24.5 \text{ rad/sec, and } \phi_2 = \begin{Bmatrix} 1.000 \\ 0.445 \\ -0.802 \end{Bmatrix}$$

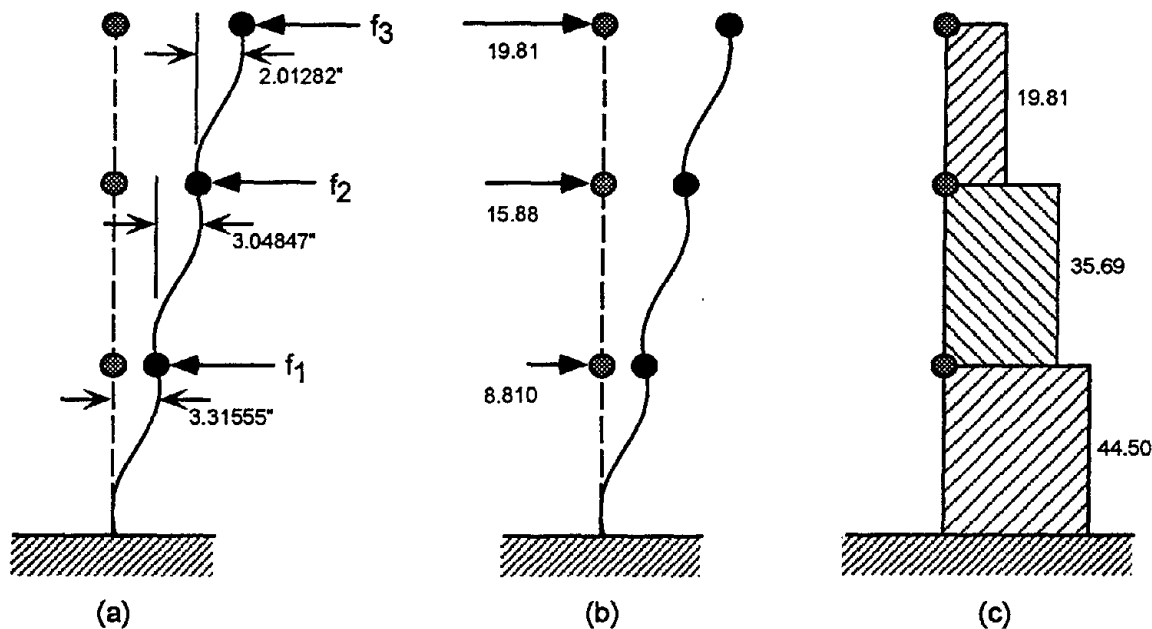


Fig. 4.26: (a) The required friction force f_1 , f_2 , and f_3 are applied as external loads to reduce the largest drift to allowable value. (b) The equivalent static loads calculated from the first mode shape. (c) The shear force distribution calculated from (b).

$$\omega_3 = 35.4 \text{ rad/sec, and } \phi_3 = \begin{Bmatrix} 0.802 \\ -1.000 \\ 0.445 \end{Bmatrix}$$

These mode shapes are shown in Figs. 4.27, 4.28, and 4.29. It is assumed that all of the frictional dampers are either all locked or all activated during the quake. Since the first mode is dominant in seismic response, by ignoring the higher modes, the total friction force F is distributed to each story proportional to the drift of the first mode shape. To explain this, considering the structure is deformed in its first mode shape ϕ_1 (see Fig. 4.26b), the equivalent static load vector is calculated to be

$$\mathbf{f}_s = \mathbf{K}_s \phi_1 = \begin{Bmatrix} 8.81 \\ 15.9 \\ 19.8 \end{Bmatrix}$$

and the corresponding shear force distribution can be calculated by static equilibrium (Fig. 4.26c). The required friction forces have to be assigned in proportion to this

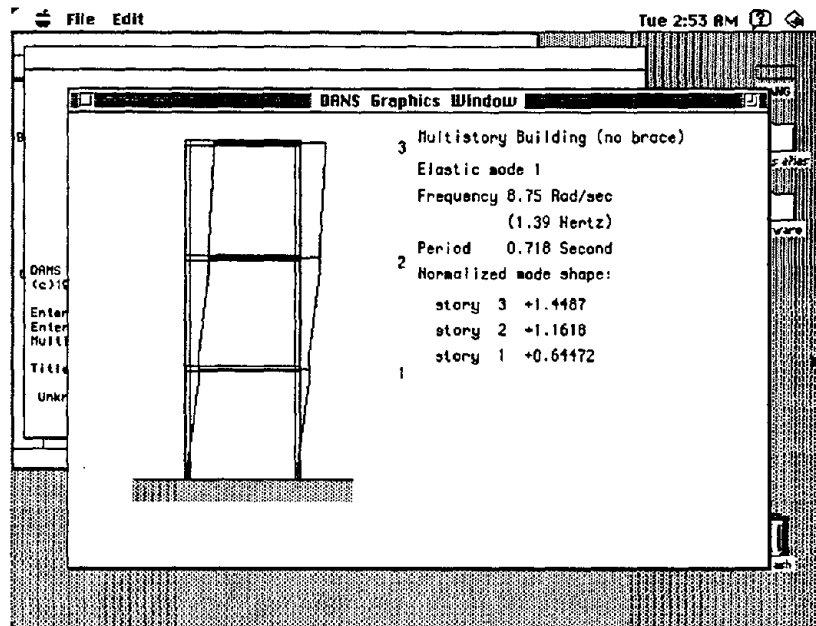


Fig. 4.27: The first mode shape of the 3-story shear building.

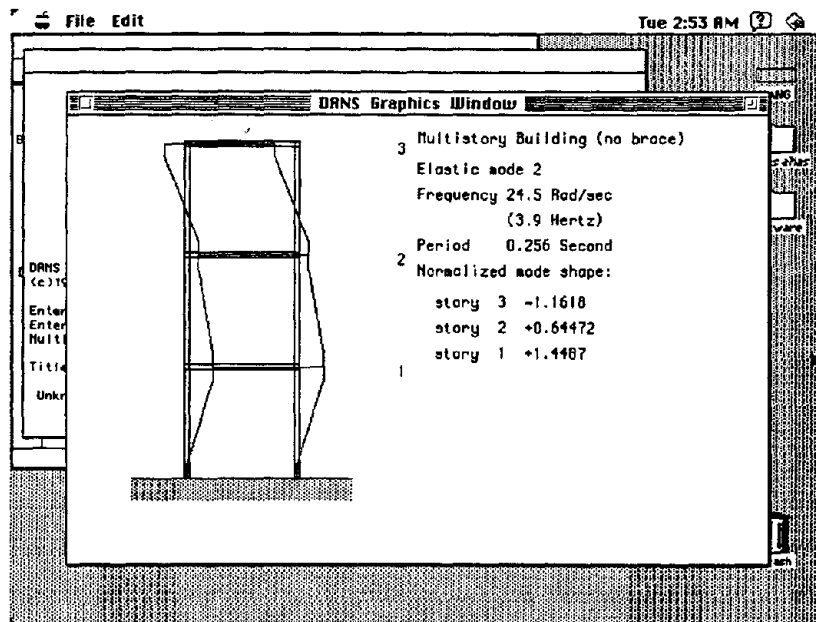


Fig. 4.28: The second mode shape of the 3-story shear building.

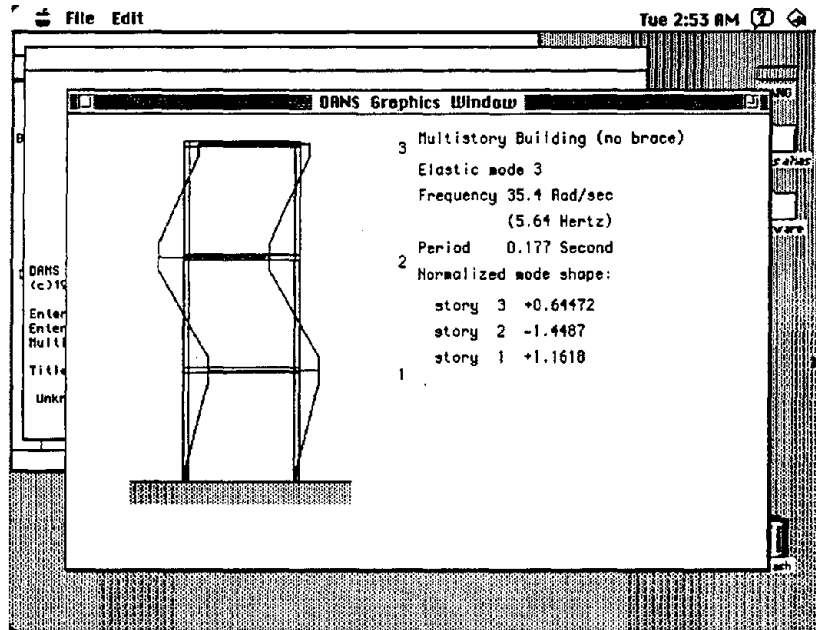


Fig. 4.29: The third mode shape of the 3-story shear building.

shear force distribution in order to be activated simultaneously, i.e.,

$$\begin{Bmatrix} f_1 \\ f_2 \\ f_3 \end{Bmatrix} = \eta \cdot \begin{Bmatrix} 44.5 \\ 35.7 \\ 19.8 \end{Bmatrix} \quad (4.36)$$

where η is a proportional constant and can be determined by the allowable drift. Note that Eq. (4.36) is derived from the first mode shape and, of course, independent of the ground motion. Solving Eqs. (4.35) and (4.36), the frictional forces can be determined

$$\begin{aligned} \eta &= 2.32 \\ f_1 &= \eta \cdot 44.5 \cdot F = 103 \text{ kips} \\ f_2 &= \eta \cdot 35.7 \cdot F = 82.7 \text{ kips} \\ f_3 &= \eta \cdot 19.8 \cdot F = 45.9 \text{ kips} \end{aligned}$$

The design is based on the results of a linear analysis. To verify the accuracy of the design, this braced structure with the frictional dampers is analyzed by a nonlinear

structural analysis program. The maximum story displacements are calculated to be

$$\mathbf{u}_{max} = \begin{Bmatrix} .889 \\ 1.64 \\ 1.98 \end{Bmatrix} \text{ inches}$$

The maximum story drift vector is calculated to be

$$\delta_{max} = \begin{Bmatrix} 0.889 \\ 0.752 \\ 0.365 \end{Bmatrix} \text{ inches}$$

All the drifts are smaller than Δ_{max} . Based on the drift responses, it is seen that the force reduction design method is conservative. The displacement and SBC slip history of this 3-story building for the 1971 Pacoima earthquake are shown in Fig. 4.30. The dynamic responses of the same structure due to the 1989 Loma Prieta earthquake and the 1940 El Centro earthquake times two are also calculated. The displacement and SBC slip history for these two earthquakes are shown in Figs. 4.31 and 4.32, respectively. It can be seen in these figures that the SBC connections are activated almost simultaneously, such that the energy dissipating rate is maximum. Also, all the responses are feasible, although the original design does not consider the effects of the Loma Prieta and the El Centro earthquakes. By inspecting the displacement and drift responses, the structure with the dampers is much better than the one without.

4.7 Conclusions and Remarks

As alternative to using patented expensive energy dissipators, the low-cost Slotted Bolted Connection described in the text can be used to great advantage because it requires smaller members and simpler connections. The design made at peak response is sufficient. The long duration of an earthquake has few unfavorable effects; the cumulative hysteresis energy and a large NYR do not damage the SBC frictional damper. Temperature rise in an SBC is low.

In this study, shear buildings with bracing frictional dampers are considered. Three design procedures described give very good results for the design of SDOF systems with frictional dissipators. These design methods are then extended to the

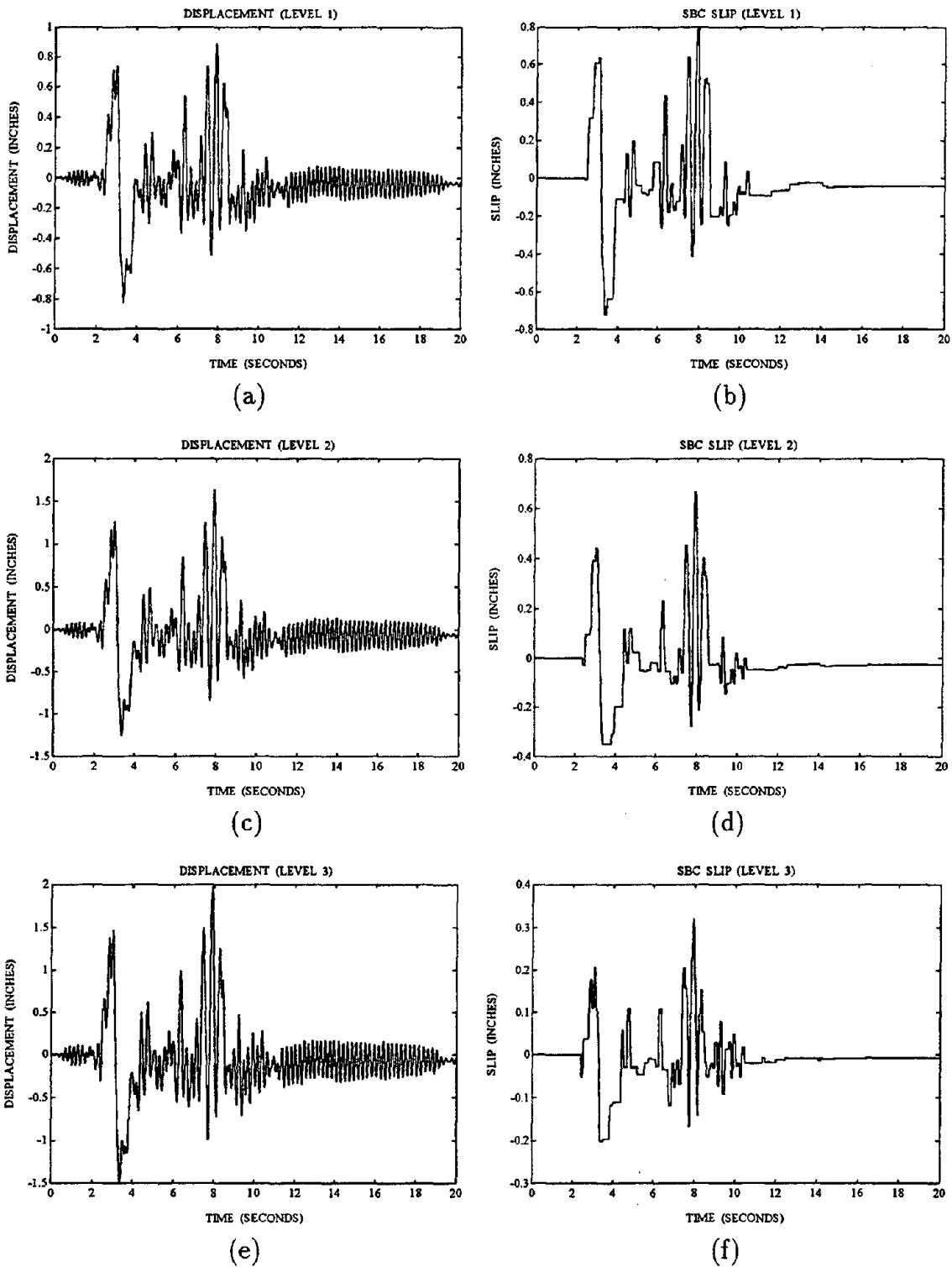


Fig. 4.30: The displacement and SBC slip history of the 3-story shear building for the 1971 Pacoima earthquake.

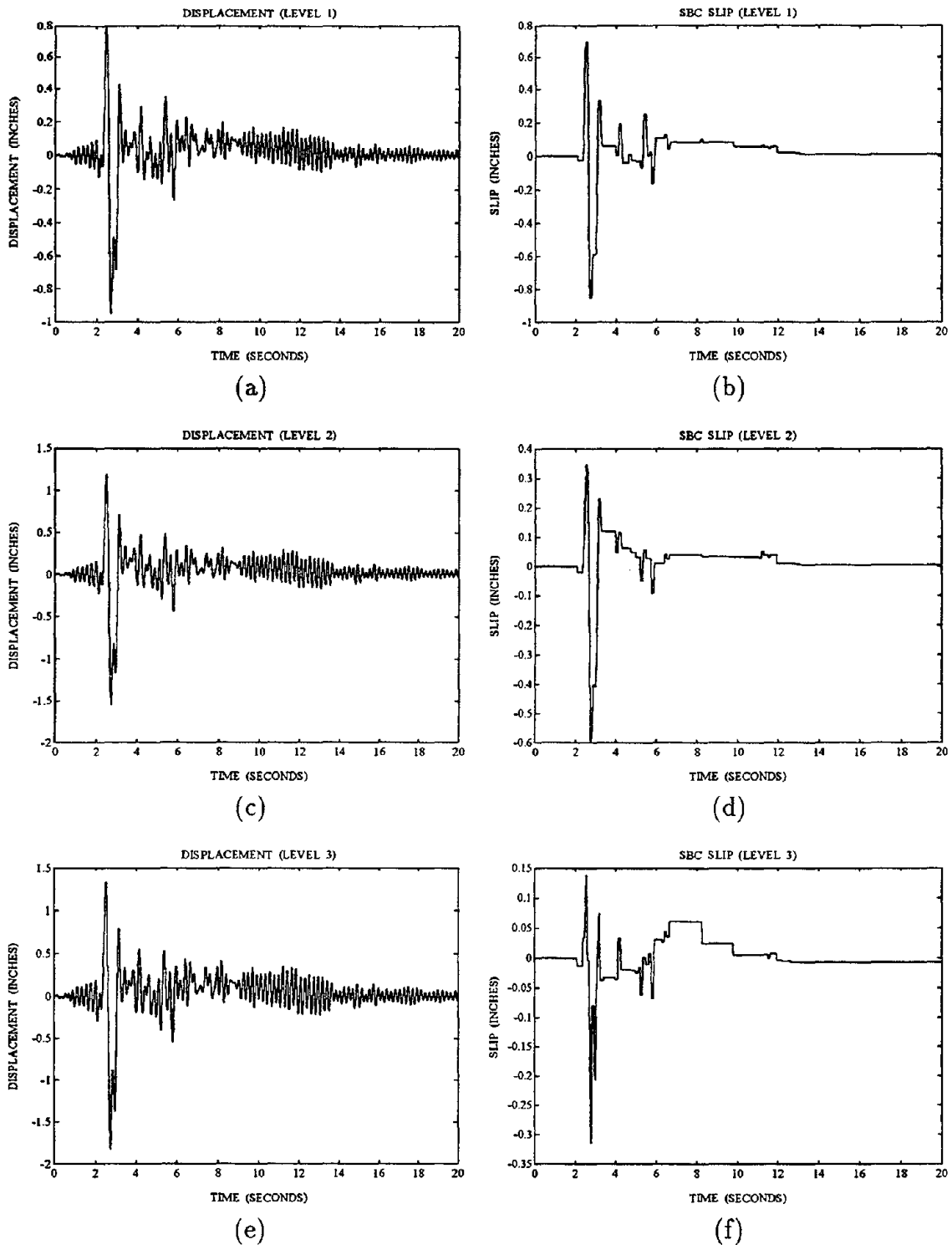


Fig. 4.31: The displacement and SBC slip history of the 3-story shear building for the 1989 Loma Prieta earthquake.

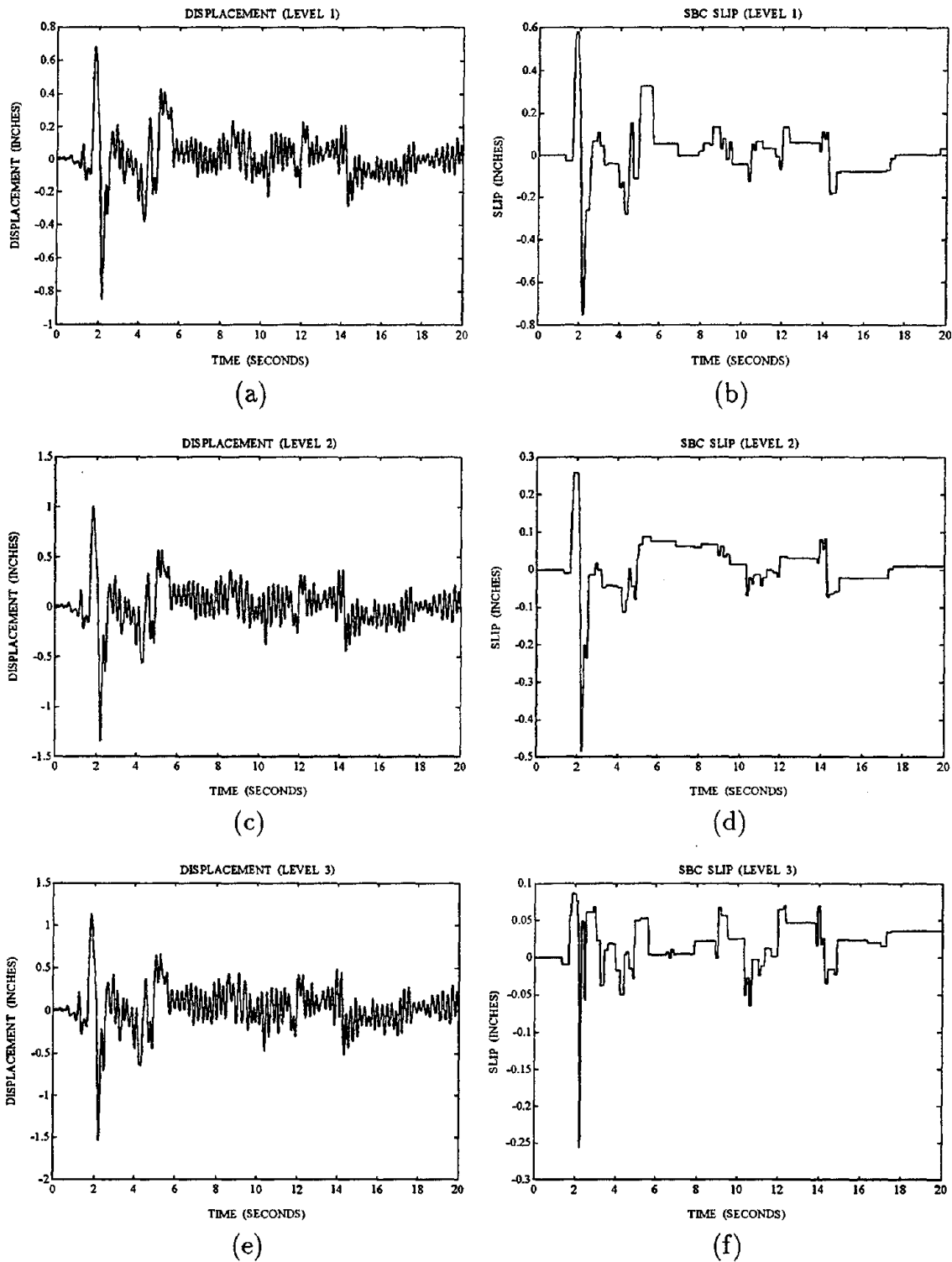


Fig. 4.32: The displacement and SBC slip history of the 3-story shear building for the 1940 El Centro earthquake times two.

design of MDOF systems with p frictional dampers. Instead of considering all of the 2^p possible sliding modes, maximum dissipative rate assumption is made to reduce these modes to only two. To comply with this assumption, the friction forces are chosen proportionally to the first mode member force distribution. The agreement between the analytically determined seismic responses and those based on the proposed assumption, is very good. The suggested design rule is simple and effective. Such a design based on an approximate solution is shown to have excellent seismic response in several major earthquakes.

From the dynamics point of view, the primary disadvantage of braced frames with SBCs is their high stiffness. Such structures have a lower vibration period than moment-resisting frames, and will have a higher acceleration amplification on a firm soil site during an earthquake. This can be seen in the response spectra presented in Chapter 1. To overcome such unfavorable characteristics, the axial friction mechanism of the SBC can be converted to a *rotational* friction mechanism, such that it can be used in moment-resisting frames. The rotational SBC will be presented in the next chapter.

Chapter 5

Rotational Slotted Bolted Connection (RSBC)

5.1 Introduction

The use of braces in a frame is an economical way to provide large lateral resistant capacity in seismic design. The axial motion of a brace member enables the installation of a friction damper. The friction damper in the brace not only prevents the buckling of the brace but also allows energy dissipation during an earthquake. But a structure with large lateral stiffness is not without flaws, as it usually receives higher magnification during an earthquake. Also, there can be aesthetic or functional reasons for a moment resisting frame to be used instead of a braced frame. In such a situation, no axial friction damper can be placed in the MRF. The MRF uses primarily flexure members to resist external load, and it is reasonable to design a rotational friction damper for use on a bending member. Figure 5.1 shows one possible rotational friction damper which acts as a beam-to-column connection. This damper is an adaptation of earlier works on Slotted Bolted Connections (SBCs) as described in the previous chapter, thus it is named the Rotational Slotted Bolted Connection (RSBC). This design places two equal-capacity SBCs on the top and the bottom of a beam. The top and the bottom friction forces are activated by beam rotation and develop moment resistance. A big bolt at the center of the shear plate is the pivot point of rotation.

This chapter describes the design and the test of two RSBCs. A simple constitutive

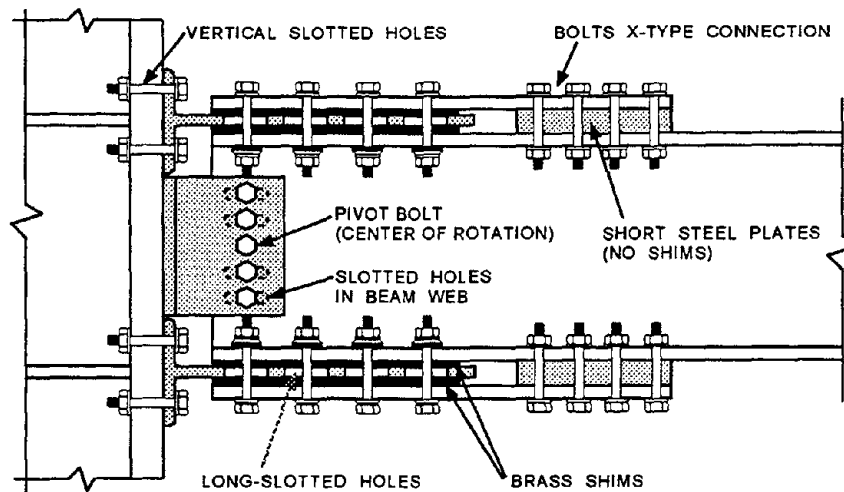


Fig. 5.1: RSBC for Moment Resisting Connections.

model is formulated first. This model resembles an elasto-plastic model. Based on the model, two RSBC specimens were designed, fabricated, and tested. These two RSBCs are bolted connections similar to the one in Fig. 5.1. Test results show that the bending moment capacity is as predicted, the plastic rotation meets the ductility demand, and the hysteresis loops have no degrading after several severe cycles. During the test, RSBCs showed no upper bound on hysteresis energy, and more importantly, both specimens had no damage after severe testing. Therefore, buildings using these connections have no need for retrofit after a strong earthquake.

5.2 The Constitutive Model for RSBC

An RSBC consists of two SBCs as shown in Fig. 5.2. Unlike the SBC using a direct axial force to activate the sliding, an RSBC uses bending moment induced tension and compression in flanges to activate the sliding of two SBCs on the top and on the bottom of a beam. Long slots in the tee stem allow the slip of the connection. Pretensioned bolts in long slots provide the normal force to develop friction during sliding. A large bolt at the center of the shear plate is the rotational center. The constitutive model is very simple because there is no material yielding involved. The Coulomb friction describes the behavior with reasonable accuracy. Thus, the load-deflection relationship can be derived by basic mechanics calculations.

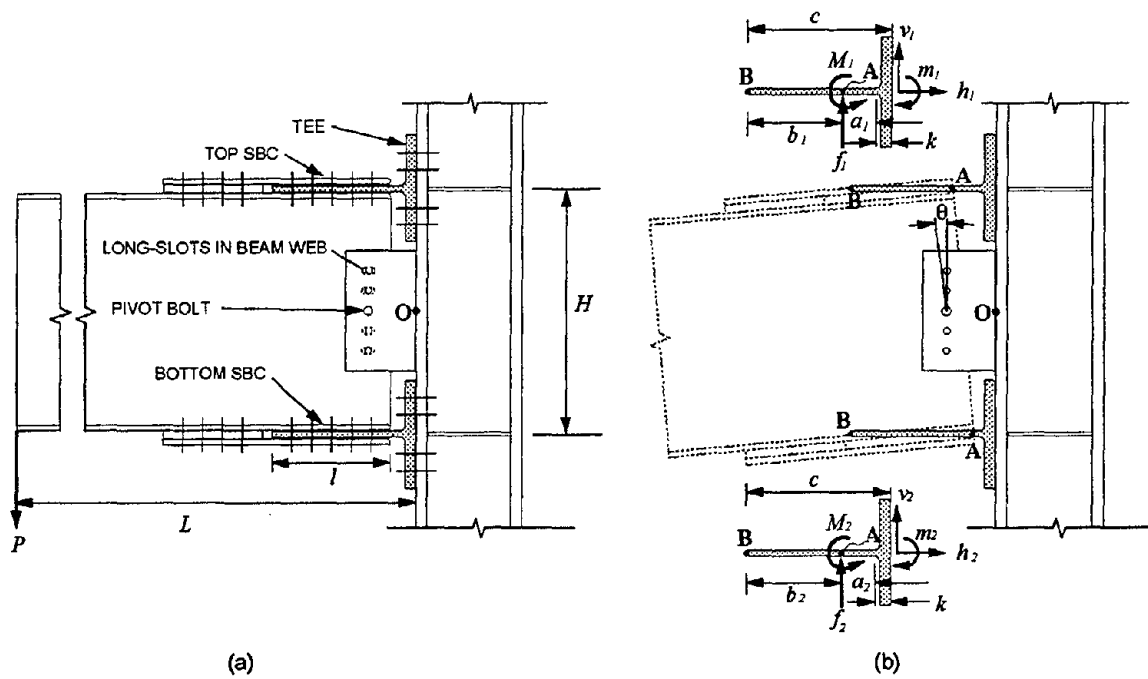


Fig. 5.2: (a) An RSBC consists of two SBCs. (b) Two tees in an RSBC will be bent when the connection rotates.

At the initial stage, the connection rotation angle θ is zero. If there are n bolts pre-tensioned to N kips each in the top SBC, the axial tension force required to activate the top tee can be calculated by Coulomb friction formula

$$h_1 = 2nN\mu_s \tag{5.1}$$

where the multiplier 2 is due to double shear, and μ_s is the static friction coefficient between steel and brass. From previous testing, the value of μ_s is 0.3 for clean mill scale A36 steel against half hard cartridge brass (UNS-260). The kinetic coefficient of friction is about the same for a short distance of slip. The bolt tension N can be achieved by the aid of a Direct Tension Indicator (DTI) during bolt tightening. Table 5.1 gives the range of bolt tension indicated by a DTI washer for A325 and A490 bolts per ASTM F959 [7].

Similarly, the same amount of force is required to activate the bottom tee,

$$h_2 = -2nN\mu_s \tag{5.2}$$

The minus sign indicates the force is compressive. For the dimensions shown in Fig. 5.2a, taking the moment with respect to point O and equating to zero, the tip

DTI size (bolt diameter, in.)	A325 bolt (kips)	A490 bolt (kips)
$\frac{1}{2}$	12 – 14	15 – 18
$\frac{5}{8}$	19 – 23	24 – 29
$\frac{3}{4}$	28 – 34	35 – 42
$\frac{7}{8}$	39 – 47	49 – 59
1	51 – 61	64 – 77
$1\frac{1}{8}$	56 – 67	80 – 96
$1\frac{1}{4}$	71 – 85	102 – 122
$1\frac{3}{8}$	85 – 102	121 – 145
$1\frac{1}{2}$	103 – 124	148 – 178

Table 5.1: Bolt tension range using DTI gap of 0.015 in.

force P to activate both top and bottom tees to slide, denoted as P_1 , can be calculated by

$$P_1 = \frac{H}{2L}(h_1 - h_2) \quad (5.3)$$

where H is the distance between two tee stems.

If the connection develops a small rotation angle θ , the tees will be bent. In that condition, the bending moment of tee needs to be considered in the calculation. For small θ , the beam-tee contact point A remains undeformed, and the contact forces f_1 and f_2 in Fig. 5.2b can be ignored. Since the portion between point A and B is deformed together with the beam, the slope is θ . The internal bending moment of the top tee at point A can be calculated by

$$M_1 = EI \frac{\theta}{a_1} \quad (5.4)$$

where E is Young's modulus, and I is the moment of inertia of the tee stem. For the bottom tee, the internal bending moment at point A is

$$M_2 = EI \frac{\theta}{a_2} \quad (5.5)$$

Dimensions a_1 and a_2 can be obtained approximately by

$$a_1 = c - l - k + H\theta/2 \quad (5.6)$$

$$a_2 = c - l - k - H\theta/2 \quad (5.7)$$

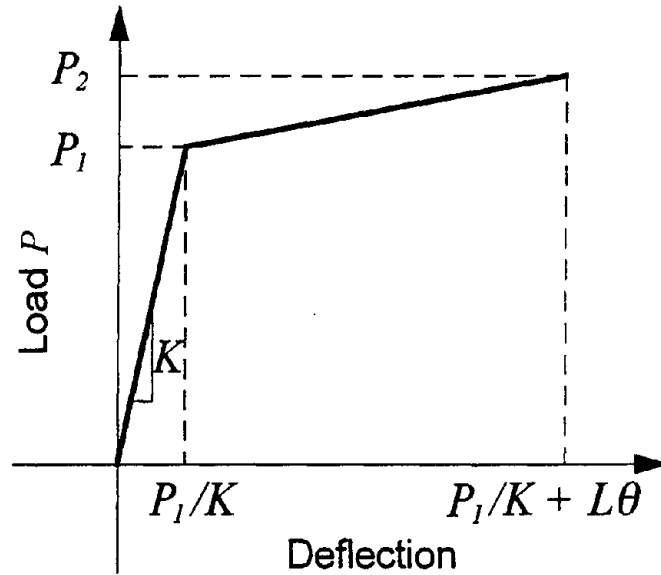


Fig. 5.3: Load-deflection curve for an RSBC.

where c is the length of the tee, l is the original length of the sliding portion, k is the tee flange thickness plus the fillet as given in the AISC manual. For force equilibrium, the bending moment reactions for both tees are

$$m_1 = M_1 \text{ and } m_2 = M_2 \quad (5.8)$$

By taking m_1 and m_2 into account, the tip force, P_2 , required to activate the sliding at angle θ is

$$P_2 = \frac{H}{2L}(h_1 - h_2) + \frac{1}{L}(m_1 + m_2) \quad (5.9)$$

The plot of tip load P vs. tip displacement is shown in Fig. 5.3. In the figure, K is the elastic stiffness of the beam.

If the connection rotates a large angle θ , in addition to the normal tension force exerted by the bolts, the bending of the tees and beam, together with the contact forces f_1 and f_2 , contribute additional normal force to the sliding surfaces, which can dramatically increase the resistance force at the connection. Fortunately, it will be shown in a later section that Eq. 5.9 is reasonably accurate for a rotation angle between $\pm 3\%$ rad, which fulfills the ductility demand for most of the seismic MRFs.

5.3 Specimen Design and Testing

To verify the usefulness of this innovative rotational friction connection, two large-scale specimens resembling the size of the SAC PN specimens were designed and fabricated. The design drawings of these two specimens, designated as Specimen 7A & 7B, are shown in Figs. 5.4-5.9.

Each specimen consists of a 134.5 inches cantilever beam¹ connected to the middle of a column. Specimen 7A was constructed from a W36×135 A36 beam that was bolted to a W14×233 A572 Grade 50 column. Because material yielding was not expected to occur in these two specimens, both specimens shared the same column. Specimen 7B consisted of a smaller A36 beam of size W24×104 bolted to the other side of the same W14×233 column. In the fabrication stage, the WT22×145 section for the tees was unavailable, thus the W36×260 section with one flange cut-off was used in tees for both Specimens 7A and 7B.

The specimen members were designed elastically based on the ASTM specified *minimum* material strength because the real material strengths during design were unknown. Since Specimen 7A was tested first, to avoid any possible failure in the column which was shared with Specimen 7B, Specimen 7A was designed conservatively to attain 75% fixity of the beam based on the 36 ksi strength. Specimen 7B was tested next, therefore, it was designed to reach its full fixity. Two large structural tees with long slotted holes in the stem were bolted to the column. Both sides of the stem of tees are sliding surfaces which must be kept clean and free of oil. For ease of assembly, the bolt holes in the column flange are oversized. Thin brass shims (1/8 in.) were placed on either sides of the tee stem. Two steel cover plates were placed on the outside of the outer brass shims and anchored by an X-type connection in the beam flanges to develop double shear. The X-type connections were designed conservatively with extra fillet welds. To allow the rotation, except for the center bolt hole, the beam web bolt holes for fastening the shear plate were slotted horizontally. The center shear plate bolt is the rotation pivot using a big bolt to resist the unbalanced friction forces in the two tees. To develop axial friction force in tees, ten pretensioned 1 in. bolts were used to provide the normal force in each tee. The distance between these bolts is three times the bolt diameter to avoid the interference between bolts.

¹The length includes the length of the clevis.

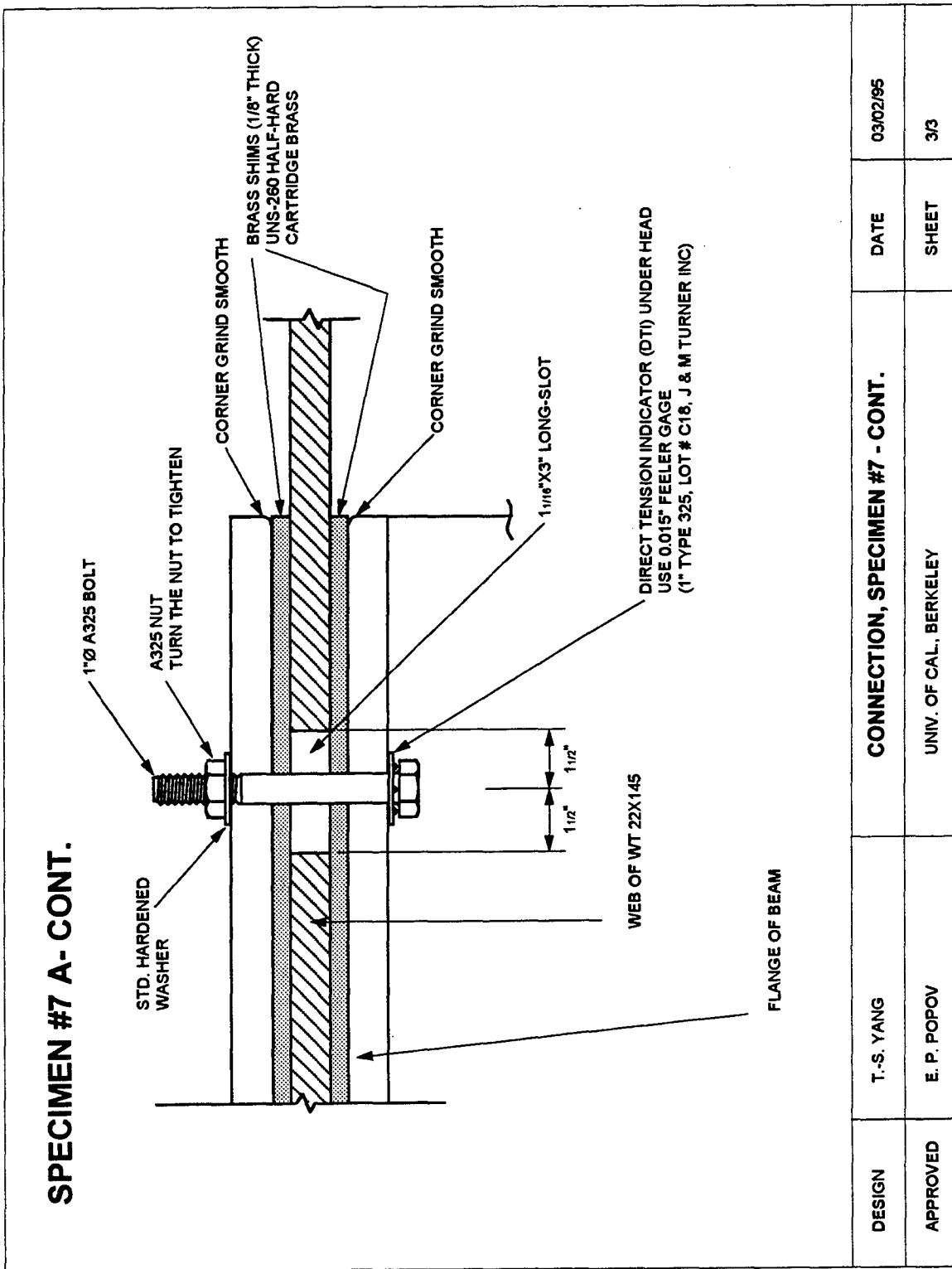


Fig. 5.6: Detail of a rotational friction damper: Specimen 7A (Sheet 3/3).

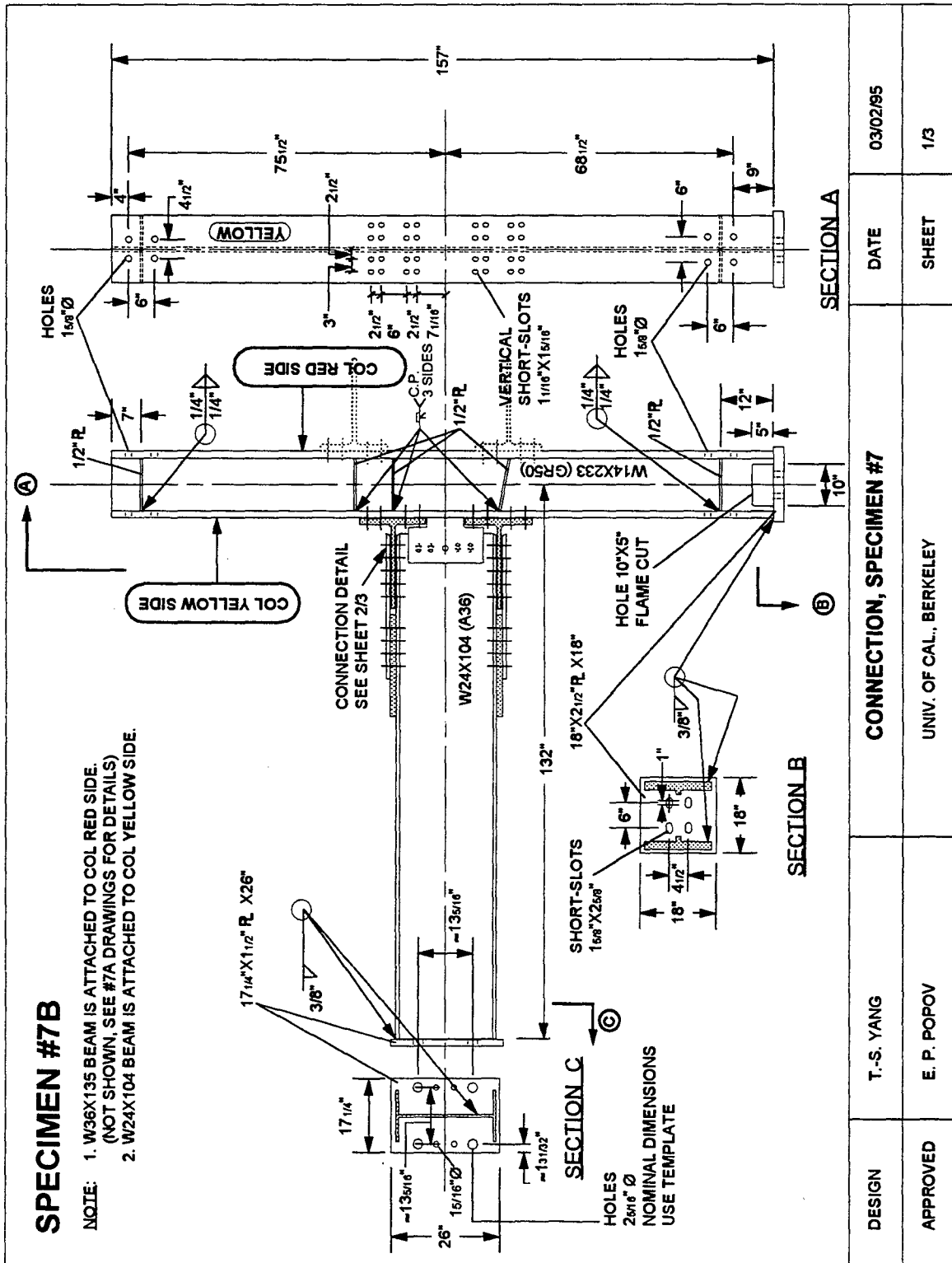


Fig. 5.7: Detail of a rotational friction damper: Specimen 7B (Sheet 1/3).

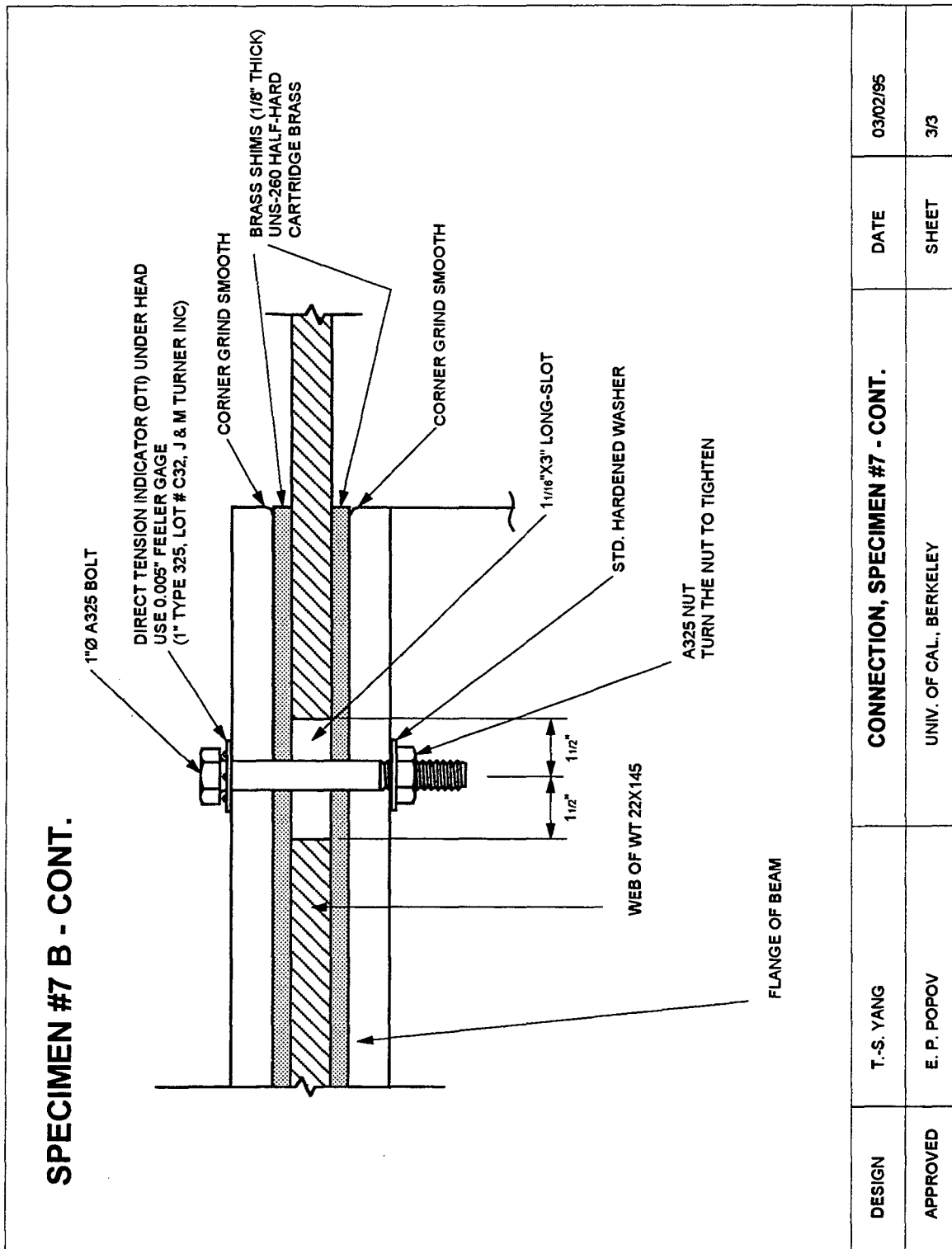


Fig. 5.9: Detail of a rotational friction damper: Specimen 7B (Sheet 3/3).

The smoothness of beam-tee contact point A, as shown in Fig. 5.2, is essential for the tee to slide in and out. Thus, the sharp beam and cover plate corners at point A were ground smooth.

During the assembly, it was found that some of the bolts could not move freely in the long slots. Those long slots were then machined to allow the bolts to move freely inside the slot. Because the length of the long slots in the tee stem is three inches, this allows the one inch diameter bolt at the center to move one inch inside the slot in either direction. If the tee slides so that the bolt reaches the end of a slot, this corresponds to 5.6% of plastic rotation for Specimen 7A and 8.3% of plastic rotation for Specimen 7B. The calculation is obvious: the plastic rotation θ for Specimen 7A can be calculated by

$$\theta = \frac{d}{d^b/2} = \frac{1}{35.55/2} = 0.056 \quad (5.10)$$

where d is the slip distance, and d^b is the depth of the beam. Similarly, the plastic rotation for Specimen 7B can be calculated. Notice that the term “plastic” rotation is due to slip, no actual inelastic deformation is involved.

When the specimens arrived, their material strengths were known to be much higher than the design values (Table 5.2). Fortunately, the connection strength is controlled by the bolts in the long slots and is not affected by the material strength. This is one of the advantages of these connections over the conventional ones.

To ensure correct and uniform tension of the high strength A325 bolts passing through the long slot holes in the tee stem, direct tension indicators (DTIs) were used under the bolt heads. All bolts were of one inch diameter except for the pivot bolt. In order to assure that bolts have been pretensioned to the values required, the bolts with DTI washers in long slots were tightened using Method 1 [69], that is, the bolt was tightened by turning the nut with a DTI under the head. The force indicating values of the DTIs used in these two specimens are shown in Table 5.3. The bolts in Specimen 7A were pretensioned to 0.015 in. DTI gap, which corresponded to 57.1 kips force in each bolt. Because the real material strength for Specimen 7B was much higher than the design value (59 ksi vs. 36 ksi), to effectively use the material, the 0.005 in. DTI gap was applied in tightening the Specimen 7B bolts.

The reason that these two specimens use so many 1 in. bolts instead of using smaller numbers of bigger bolt is due to the tightening tool problem. The impact

Material Properties
(from Mill Certificates)

Specimen Number	Material Size & Spec	Yield Strength F_y (Elongation)	Ultimate Strength F_u (Elongation)
7A Beam	W36×135 A36	53.0 ksi (0.20%)	67.0 ksi (26%)
7B Beam	W24×104 A36	59.0 ksi (0.20%)	74.0 ksi (28%)
Column	W14×233 A572-Gr50	53.0 ksi (0.20%)	73.0 ksi (23%)

Table 5.2: Material properties of Specimen 7A and 7B. Both specimens share the same column.

Specimen Number	DTI size & lot number	Bolt tension 0.015 in. gap	Bolt tension 0.005 in. gap
7A	1 in. A325 C18	57.1 kips	67.0 kips
7B	1 in. A325 C32	56.1 kips	66.0 kips

Table 5.3: Force indicating value of DTIs used in Specimen 7A and 7B.

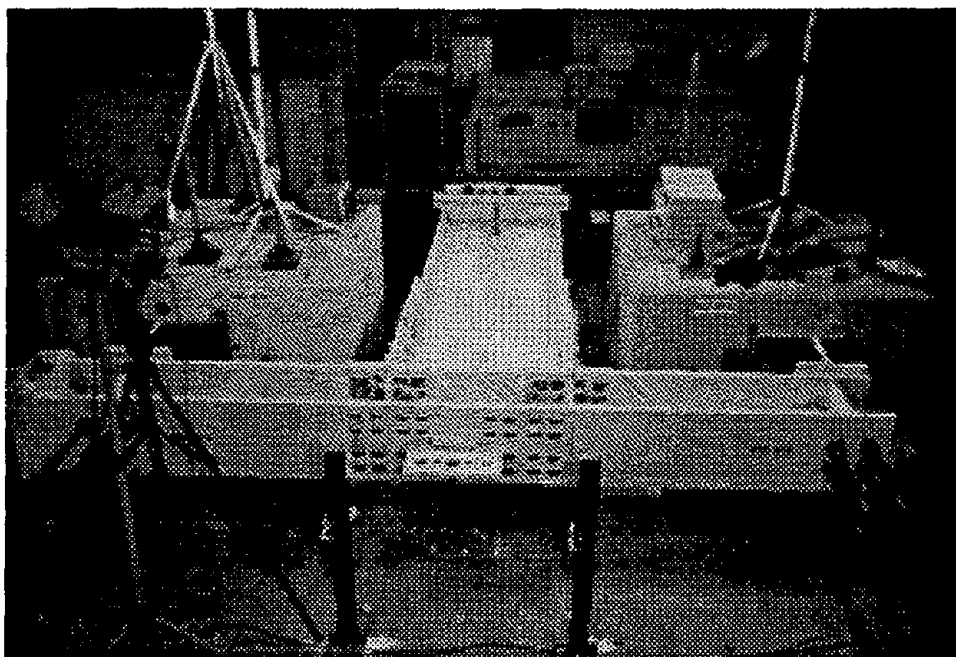


Fig. 5.10: Photograph showing Specimen 7A in testing.

wrench in the university machine shop can only fully tighten bolts up to 5/8 in. in diameter. Larger bolts have to be tightened by a 12 ft wrench manually. During assembly, two husky staff members using the 12 ft wrench could not tighten the 1 in. bolt to the desired tension. Because buying a new tool was too expensive for this limited project budget, a 4X multiplier, together with a big wrench, was used to finish the job. In practical applications, such a problem would not arise and larger bolts could be used to reduce their number².

Figure 5.10 shows Specimen 7A during testing. Bolt holes and the shear plate on the column flange facing the viewer are for the attachment of Specimen 7B beam. One of the sliding tee assemblies is shown in Fig. 5.11. The test results for Specimen 7A and 7B are presented in the next section.

After the test of Specimen 7A, the connection was disassembled. One of the tees shown in Fig. 5.12 reveals no damage. Both surfaces of the tee have brass smears. Due to the stick-slip behavior of the two tees, pivot bolts have to be provided to resist the unbalance force. Since the bolt hole is larger than the pivot bolt, the beam

²Suitable tools for tightening A325 1½ in. bolt are available, for example, from Chicago Pneumatic 614, Ingersoll Rand 5980, and Norbar PT7.

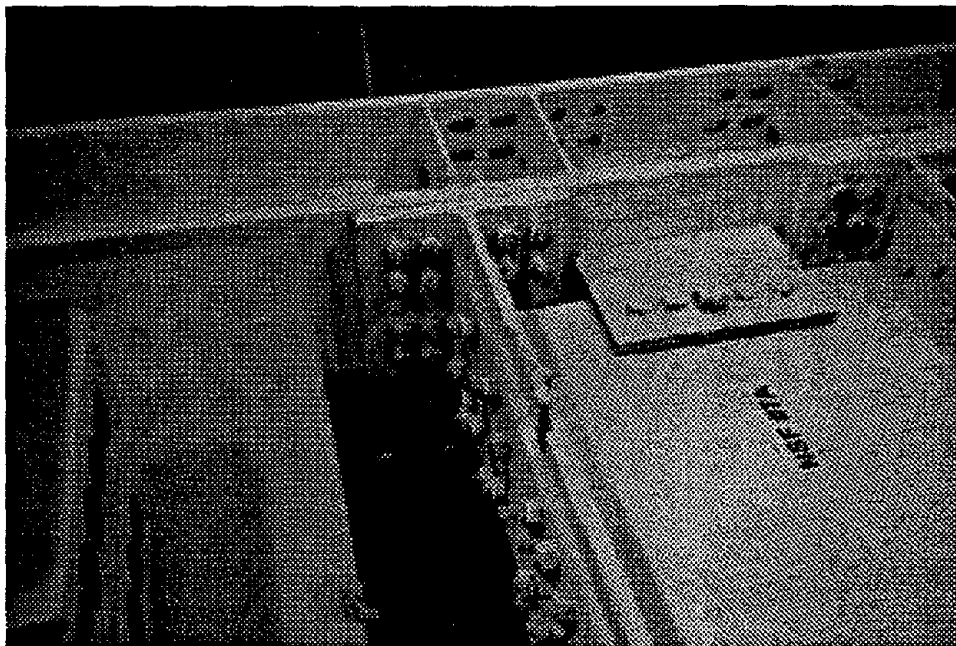


Fig. 5.11: Photograph showing one of the tees for Specimen 7A after the test.

was pulled away from the column about one half inch (see Fig. 5.13). The beam web around the pivot bolt sustained several load reversals, and the bolt hole became enlarged (see Fig. 5.14). Figure 5.15 shows the brass shims and bolts removed from Specimen 7A. The sliding motion scores a series of grooves or scratches on the brass shims. The bolts were not damaged except for the $1\frac{3}{8}$ in. pivot bolt, which was bent by shear. The pivot bolt is shown near the center of Fig. 5.15.

Although the test of Specimen 7A was a great success, there are few minor things that need to be improved:

1. The pivot bolt has to resist beam shear and also the unbalanced friction force of two tees. It is very important to design it conservatively.
2. The pivot bolt hole in the beam web needs to be reinforced in order to bear the pivot bolt.
3. Because the RSBC is relatively more complex than the conventional connection, some special instructions are needed for the shop.

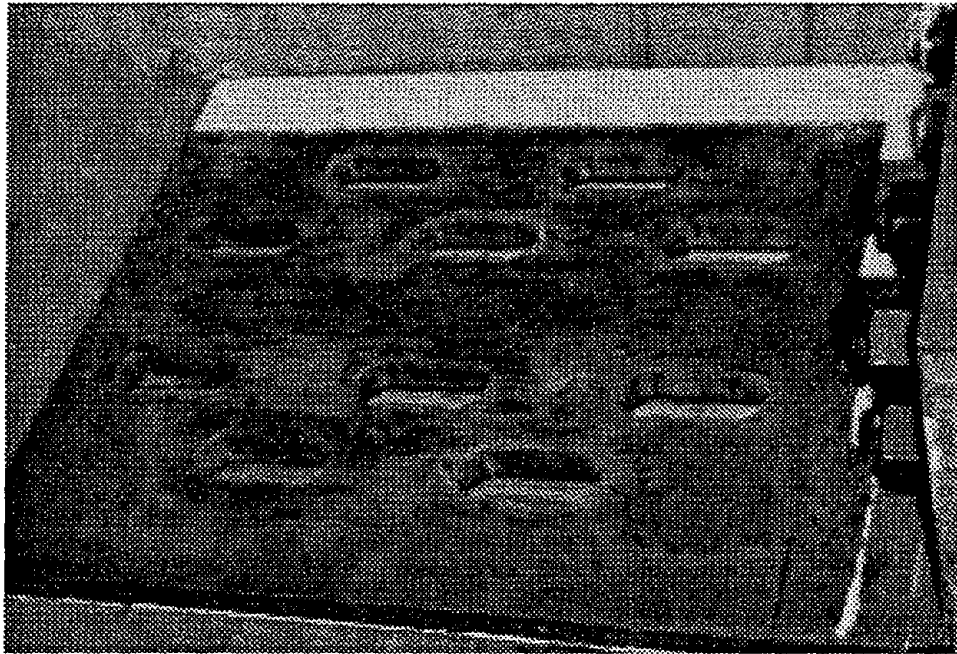


Fig. 5.12: Photograph showing one of the steel tees of Specimen 7A after the test.

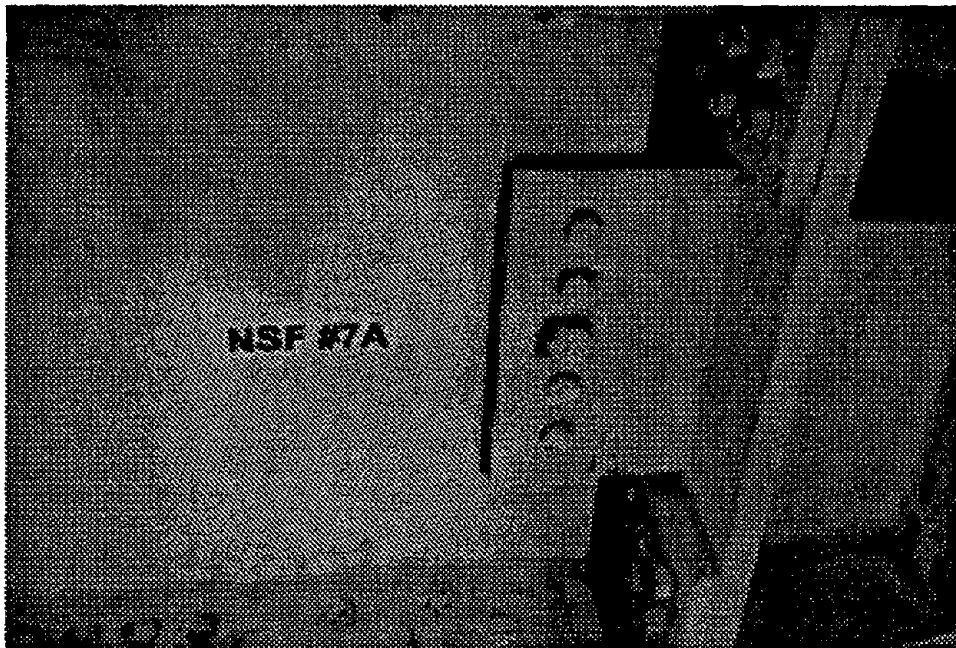


Fig. 5.13: Shear plate of Specimen 7A shows no damage after the test. The beam has been pulled away from the column for half inch.

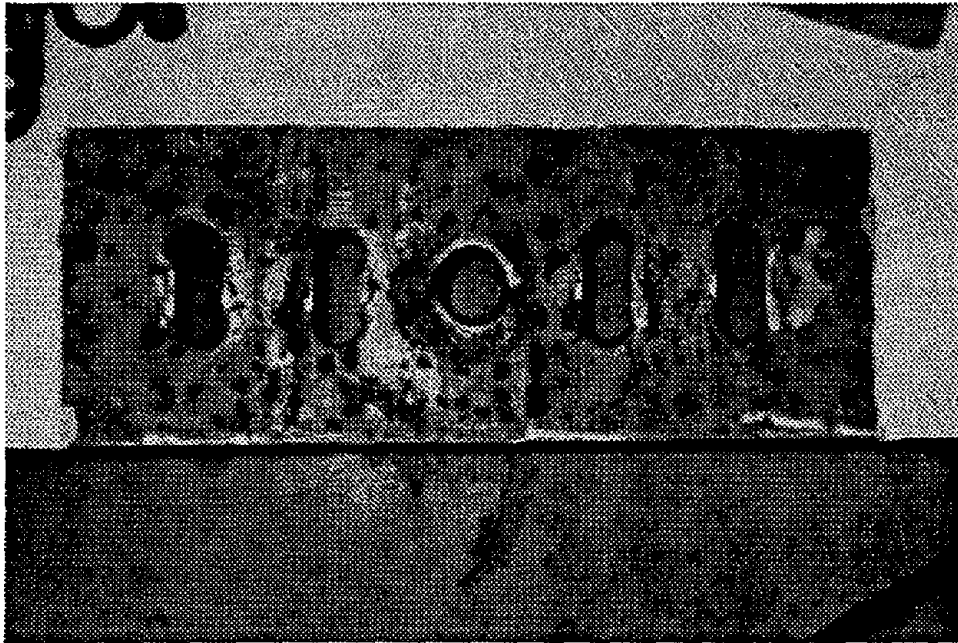


Fig. 5.14: Beam web under the shear plate of Specimen 7A shows no damage after the test. The center pivot bolt hole was enlarged by load reversals.

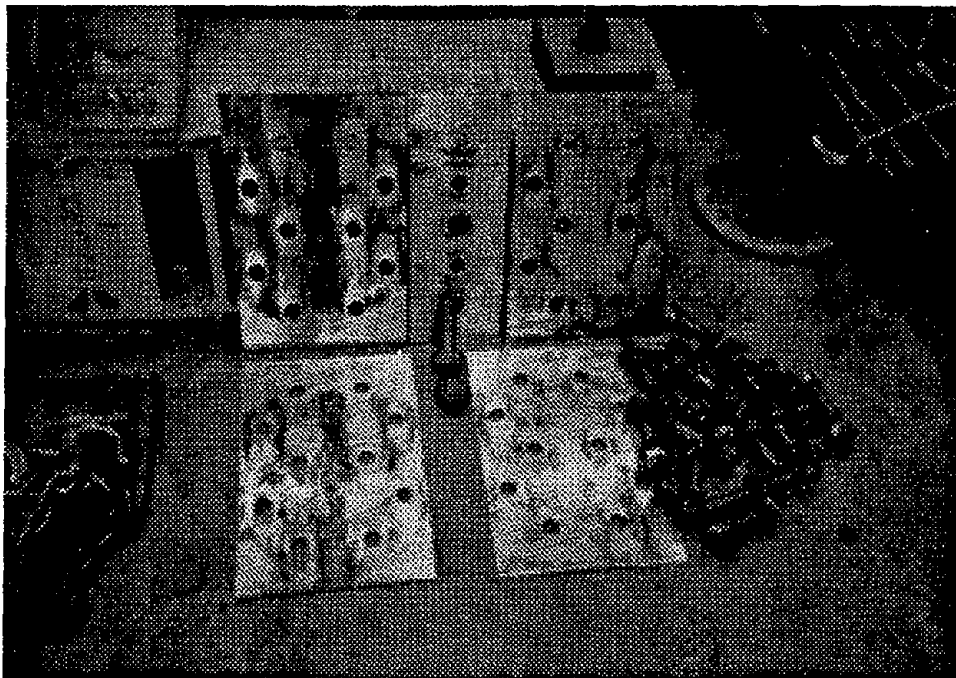


Fig. 5.15: Photograph showing the brass shims and bolts taken out from Specimen 7A after the test.

With the lesson learned from Specimen 7A, Specimen 7B was modified by using a larger pivot bolt, an 1.5 in. diameter A325, and the beam web around the pivot hole was reinforced with a plate (Fig. 5.16). The test of Specimen 7B was very successful. With a large 1.5 in. diameter pivot bolt, the beam was pulled away from the column only 0.2 inch (Fig. 5.17). Close examination of the connection after the test showed no damage after several severe loading cycles (Fig. 5.18). Because the hysteresis energy was dissipated in the form of heat, a mild temperature rise could be sensed on the connection surfaces during the test.

5.4 Structural Test Results

The imposed tip displacements for Specimen 7A & 7B are shown in Fig. 5.19. In order to demonstrate the capacity of the RSBC, the number of applied cycles for Specimen 7A was about double that specified in the SAC protocol. Because no damage was found after the test of Specimen 7A and there is also no apparent upper limit of cycles which RSBC can take, to save testing time, the displacements of the SAC protocol

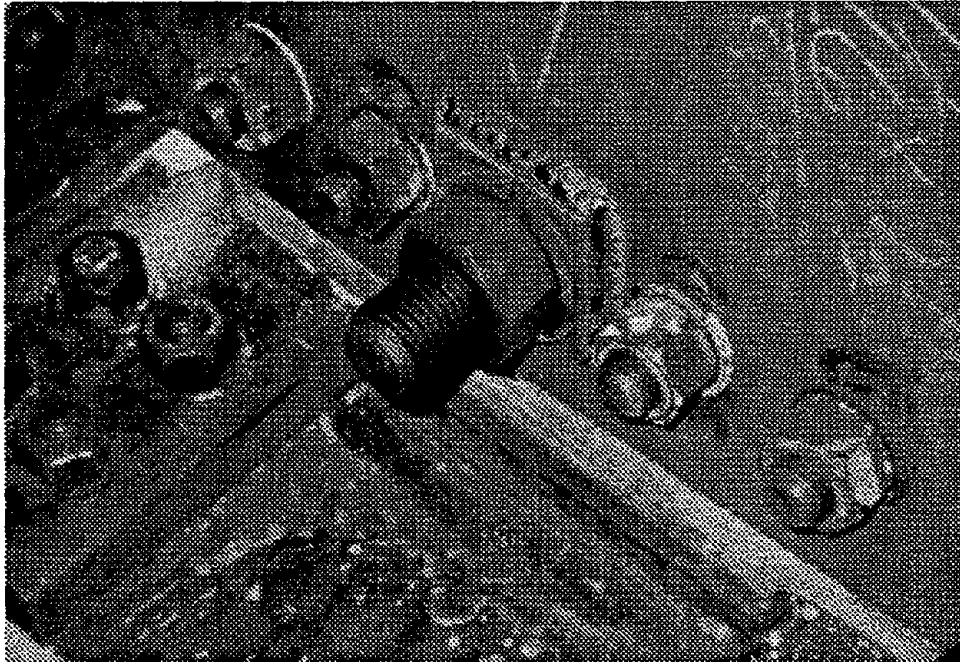


Fig. 5.16: Photograph showing the pivot bolt of Specimen 7B. The bolt hole in beam web is reinforced.

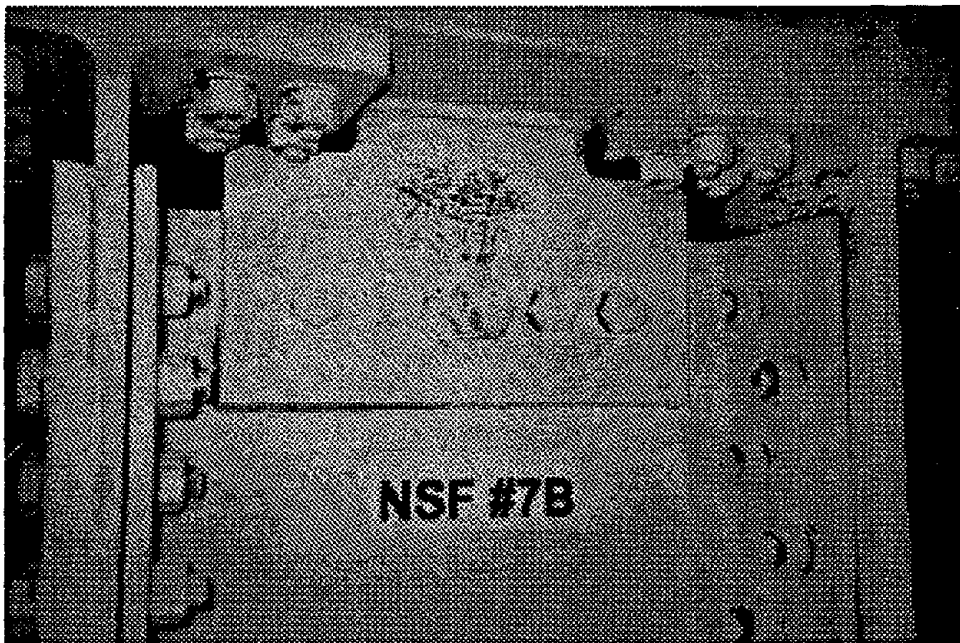


Fig. 5.17: Photograph showing the shear plate and the pivot bolt of Specimen 7B after test.



Fig. 5.18: Photograph showing Specimen 7B after test, the connection is in good condition without damage.

were used in the test of Specimen 7B. The experiments were terminated when the beam tip displacement reached the limiting excursion of the hydraulic actuator.

The exceptionally stable hysteresis loops that were generated by these two specimens during experimentation are shown in Fig. 5.20. The hysteresis loops, generated by steel-on-brass friction, appear to have no degradation after several cycles. Many of the loops overlap each other, which clearly shows the durability and stability of the mechanism. The weird looking shapes at the lower-right and the upper-left corners of the hysteresis loops are due to the small slippage of the brass shims on load reversal because the bolt holes in the brass shim were 1/16 in. larger than the bolt diameter. The analytical hysteresis loops for Specimens 7A and 7B can be constructed using Eqs. 5.1 to 5.9 with reasonable accuracy. For Specimen 7A, $n = 10$, $N = 57.1$ kips, $H = 36.64$ in., $L = 134.5$ in., $c = 22$ in., $l = 18$ in., $k = 2.56$ in., and $\mu_s = 0.3$. The axial tension forces h_1 and h_2 in both tees can be calculated as

$$h_1 = -h_2 = 2nN\mu_s = 343 \text{ kips}$$

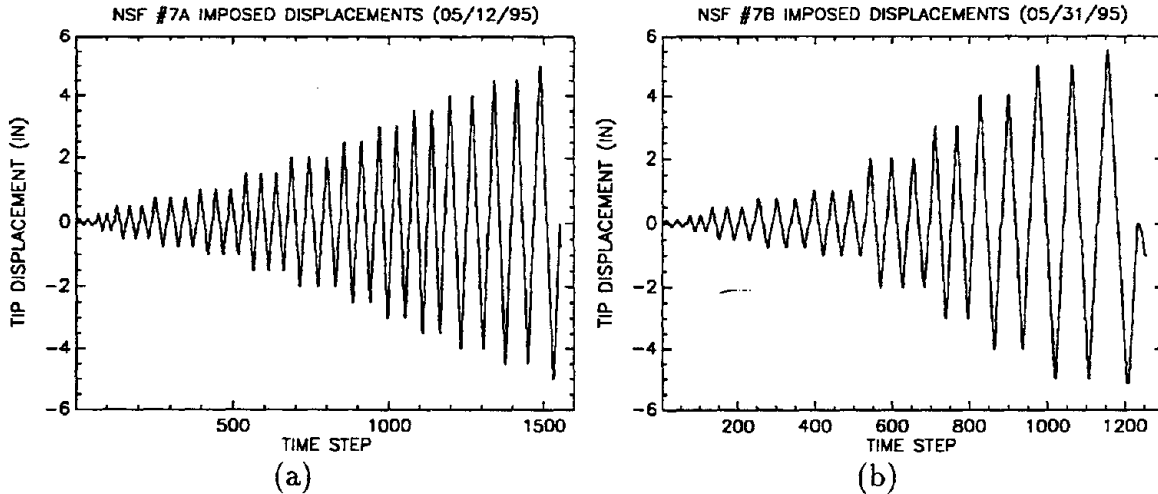


Fig. 5.19: Imposed displacements for Specimen (a) 7A and (b) 7B.

At $\theta = 0.032$ rad, the bending moment reactions m_1 and m_2 for two tees are

$$\begin{aligned}
 m_1 &= EI \frac{\theta}{a_1} = EI \frac{\theta}{c - l - k + H\theta/2} \\
 &= 29,000 \frac{16 \cdot 0.84^3}{12} \frac{0.032}{22 - 18 - 2.56 + 36.64 \cdot 0.032/2} = 362 \text{ kip-in} \\
 m_2 &= EI \frac{\theta}{a_2} = EI \frac{\theta}{c - l - k - H\theta/2} \\
 &= 29,000 \frac{16 \cdot 0.84^3}{12} \frac{0.032}{22 - 18 - 2.56 - 36.64 \cdot 0.032/2} = 862 \text{ kip-in}
 \end{aligned}$$

The required tip loads P_1 and P_2 to activate the sliding of tees at $\theta = 0$ and at $\theta = 0.032$ are

$$\begin{aligned}
 P_1 &= \frac{H}{2L}(h_1 - h_2) = 93.3 \text{ kips} \\
 P_2 &= \frac{H}{2L}(h_1 - h_2) + \frac{1}{L}(m_1 + m_2) = 102 \text{ kips}
 \end{aligned}$$

Similarly, the tip loads for Specimen 7B can be calculated. For Specimen 7B, $n = 10$, $N = 66$ kips, $H = 25.15$ in., $L = 134.5$ in., $c = 22$ in., $l = 18$ in., $k = 2.56$ in., and $\mu_s = 0.3$. The axial tension forces h_1 and h_2 in both tees are

$$h_1 = -h_2 = 2nN\mu_s = 396 \text{ kips}$$

At $\theta = 0.032$, the bending moment reactions m_1 and m_2 for two tees are

$$m_1 = 29,000 \frac{16 \cdot 0.84^3}{12} \frac{0.032}{22 - 18 - 2.56 + 25.15 \cdot 0.032/2} = 399 \text{ kip-in}$$

$$m_2 = 29,000 \frac{16 \cdot 0.84^3}{12} \frac{0.032}{22 - 18 - 2.56 - 25.15 \cdot 0.032/2} = 709 \text{ kip-in}$$

Thus, the required tip loads to activate the sliding of tees are

$$P_1 = \frac{H}{2L}(h_1 - h_2) = 74.0 \text{ kips}$$

$$P_2 = \frac{H}{2L}(h_1 - h_2) + \frac{1}{L}(m_1 + m_2) = 82.3 \text{ kips}$$

The analytical hysteresis loops for Specimens 7A and 7B for θ between ± 0.032 rad are shown in Fig. 5.21. By comparing Figs. 5.20 and 5.21, excellent agreements between experimental and analytical results can be seen. Notice that, for small values of m_1 and m_2 , the hysteresis loops are very close to the elastic-perfectly plastic model.

A small gap between the pivot bolt and bolt hole edge induced the small hysteresis loops which appeared at the center of the hysteresis loop array for Specimen 7A. For Specimen 7B, a larger pivot bolt with a reinforced bearing hole effectively reduced the size of these small hysteresis loops at the center. These phenomena can be clearly seen by looking at the slip diagrams for the two specimens shown in Fig. 5.22, where the top and bottom SBC slip displacements for Specimen 7A & 7B are recorded. It can be seen that the beam for Specimen 7A has been pulled out about 0.5 in., whereas the beam of Specimen 7B has been dragged out only 0.2 in.

The moment-“plastic” rotation diagrams for Specimen 7A & 7B are shown in Fig. 5.23. Both specimens easily exceeded the 3% rotation. Unfortunately, the desirable rotation of 5.6% and 8.3% for Specimen 7A & 7B, respectively, could not be achieved due to the limitation of the test equipment. It is believed that at such a large rotation angle, the simplified constitutive model given in Section 5.2 is no longer valid. Further investigations must be carried out to solve the complicated contact problem. Fortunately, it is rare for an MRF member to require more than 3% rad plastic rotation during severe use.

By integrating the hysteresis loops in Fig. 5.20 step-by-step, the total energy diagrams can be constructed. The energy dissipation efficiency can be seen in Fig. 5.24. The accumulation of energy with each applied cycle virtually is without an upper limit for seismic structural applications. The downward trend in the wavy curve is due to the recovery of the elastic strain energy on load reversal. The irreversible energy is dissipated energy in the form of heat. It is interesting to compare these energy diagrams with those of the conventional welded MRF connections shown in

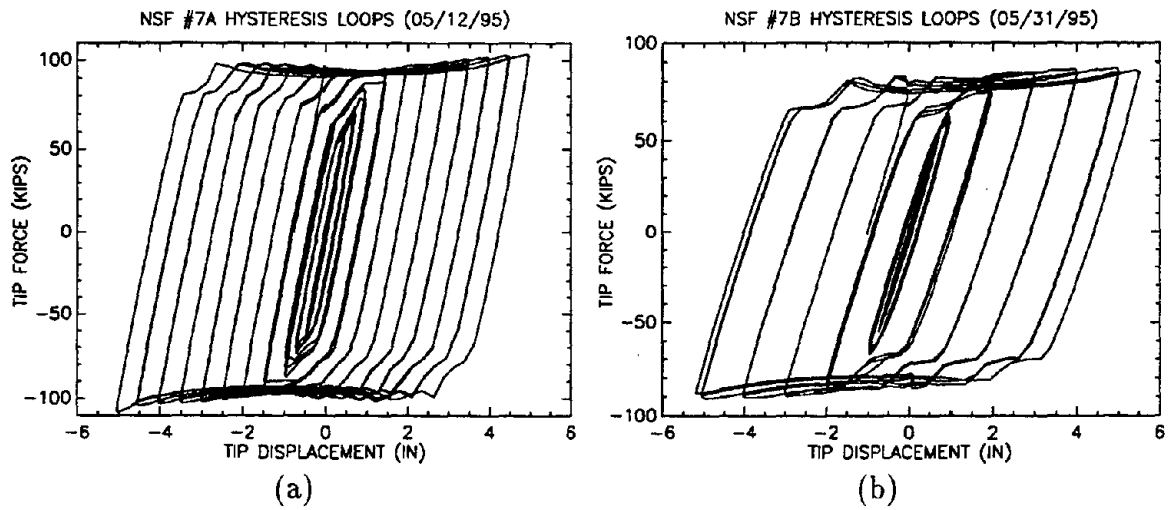


Fig. 5.20: Hysteresis loops for Specimen (a) 7A and (b) 7B.

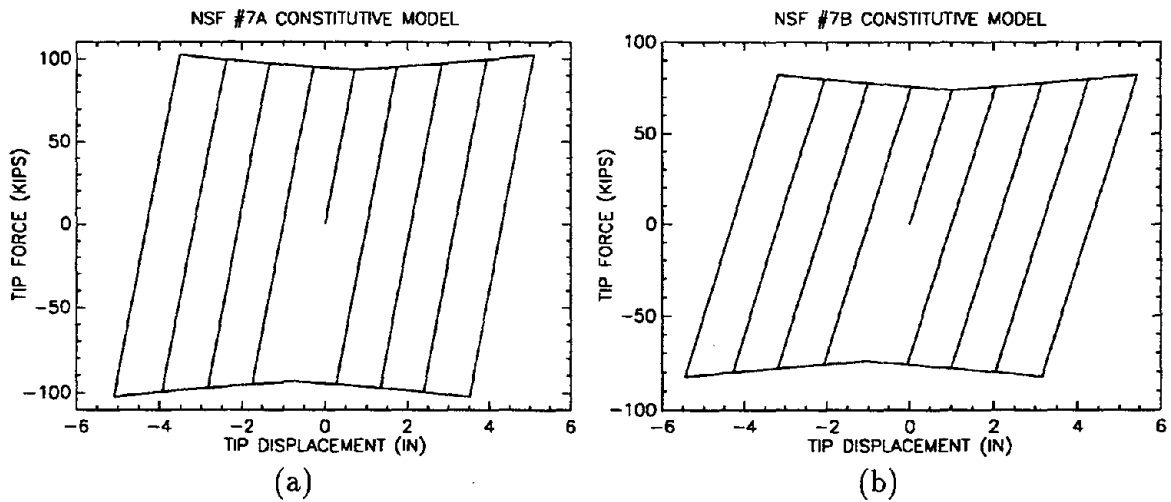


Fig. 5.21: Analytical hysteresis loops for Specimen (a) 7A and (b) 7B.

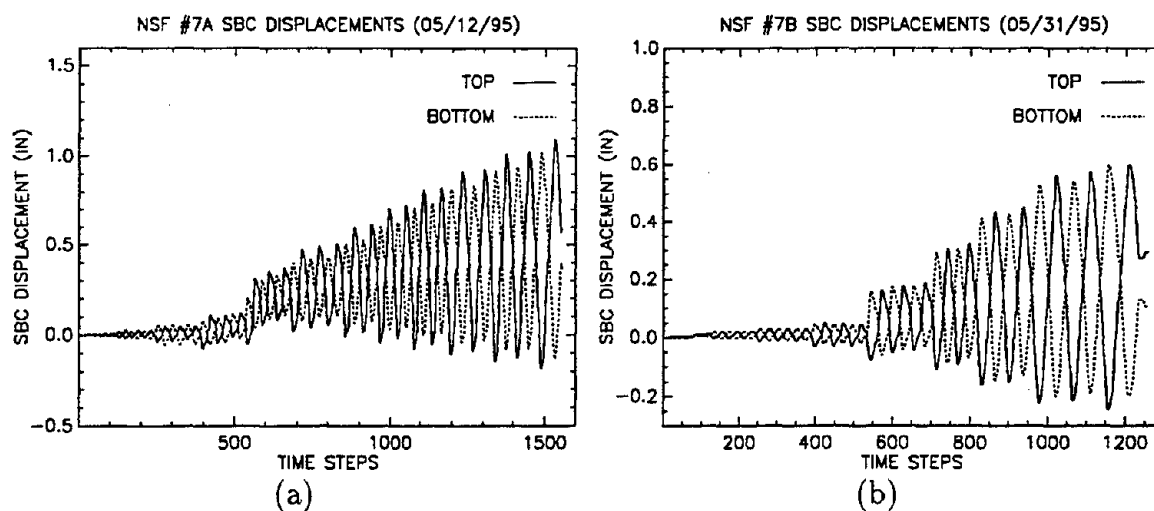


Fig. 5.22: Top and bottom SBC slip for Specimen (a) 7A and (b) 7B.

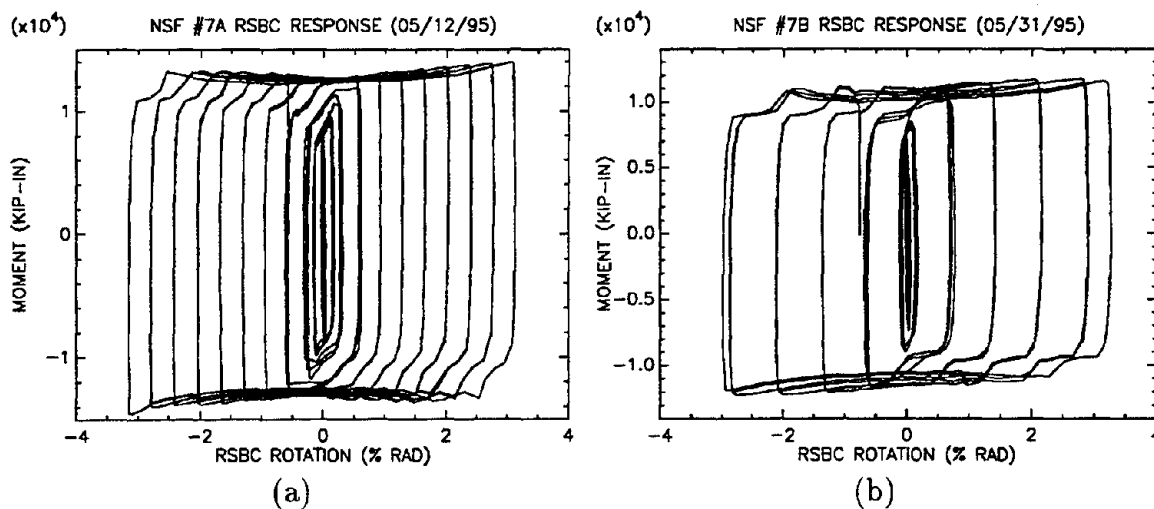


Fig. 5.23: "Plastic" rotations for Specimen (a) 7A and (b) 7B.

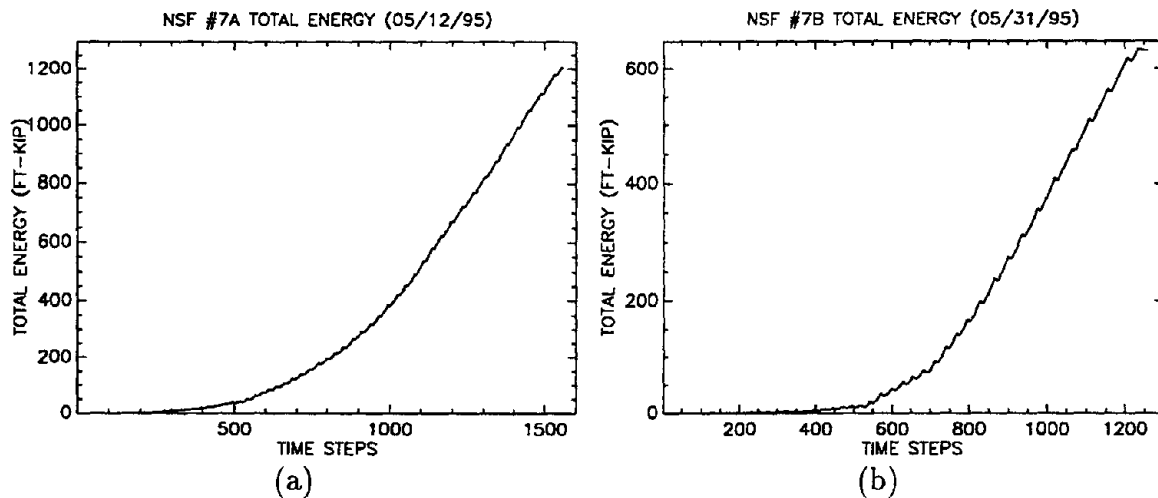


Fig. 5.24: Total strain energy diagram for Specimen (a) 7A and (b) 7B.

Chapter 2 and 3. The amount of dissipated energy of the RSBC is much larger and more stable, but more importantly, the RSBC will not fail.

The RSBC needs many bolts in the beam flange at the most critical section. In order to determine the stress concentration around the bolt holes and the shear taken by the bolts, five strain gauges were placed near the bolt holes on one side of the top cover plate. Figure 5.25 shows the readings of these gauges for Specimen 7A & 7B. These gauges measured the strain in the beam axial direction and were numbered in the direction away from the column, so gauge 1 was the nearest one to the column. It is seen that the stresses were not evenly distributed along the row of bolts. The first and the last bolts took more force than the middle bolts. Because the measured strains were all small, the stress concentrations were not a critical problem.

During the test of Specimen 7A, the white wash kept on peeling off at the root of the two tees. At that time, it was difficult to determine whether the situation was due to large strain or surface rubbing. If it were due to large strain, then it is possible for low cycle fatigue to develop. To solve the puzzle, strain gauges were placed at the tee root surfaces of Specimen 7B (Fig. 5.26). The measurements of these strain gauges are shown in Fig. 5.27. The strain in the beam axial direction is small; the maximum is only 1.1%. Thus, low cycle fatigue failure at the tee root is unlikely to happen.

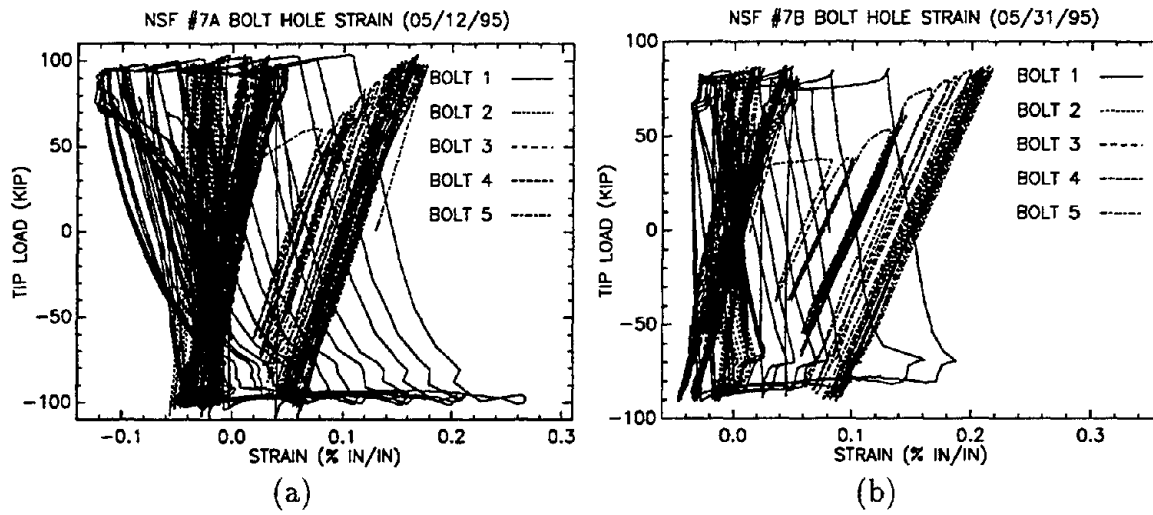


Fig. 5.25: Strain near bolt holes for Specimen (a) 7A and (b) 7B.

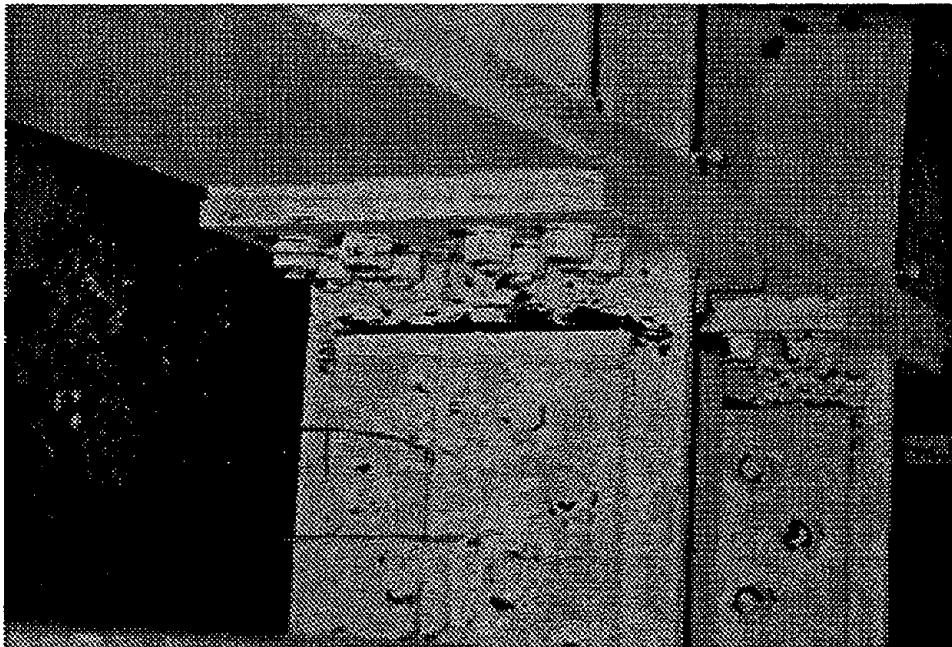


Fig. 5.26: Strain gauge was placed on the tee root surface for Specimen 7B.

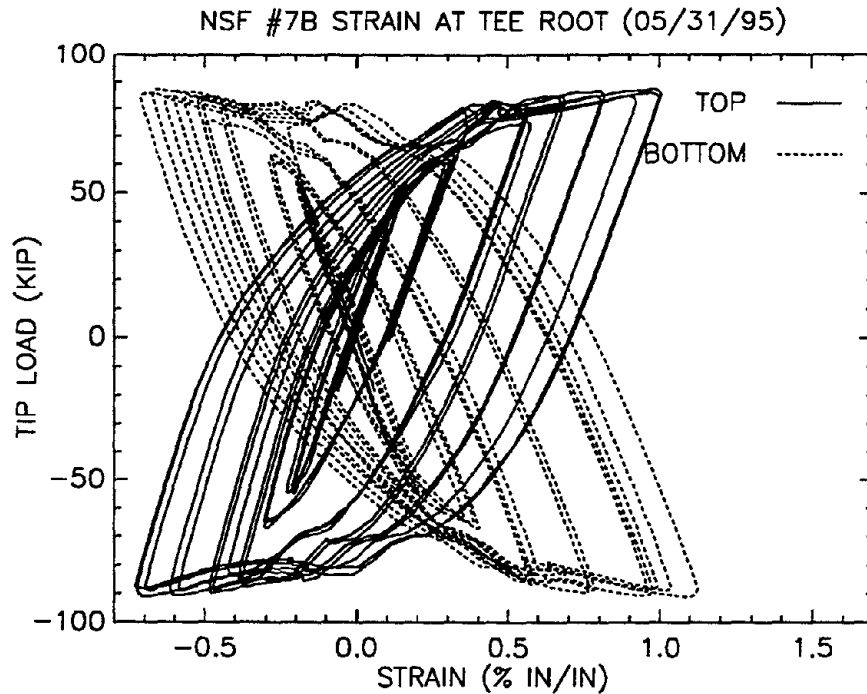


Fig. 5.27: Tee root strains vs. tip load for Specimen 7B.

5.5 Alternative RSBCs

Two RSBCs presented in this chapter are bolted beam-to-column connections. Such connections are very reliable but more expensive than the welded connections. With some modifications, the bolted RSBCs can be easily changed into a welded design. Figure 5.28 shows an alternative RSBC with two tees changed to steel plates, which are groove welded to the column directly. The bolted X-type connection is also changed; the cover plates are fillet welded on the beam flange. The high strength bolts for clamping the sliding surfaces together provide the needed normal force to develop friction, thus they cannot be changed to other forms of assembly. This alternative RSBC is much more easy to construct than the original design. The major parts of the connection can be assembled in the shop; only two groove welds and the shear plate bolting need to be done in the field. An RSBC for the minor axis of the column can use the extension of the continuity plate as the sliding plate.

The RSBC can be easily adapted for use in concrete-steel composite constructions. Figure 5.29 shows an RSBC connected to a reinforced concrete column. The flanges of the tees are buried in the concrete. The shear plate using a tee section also has

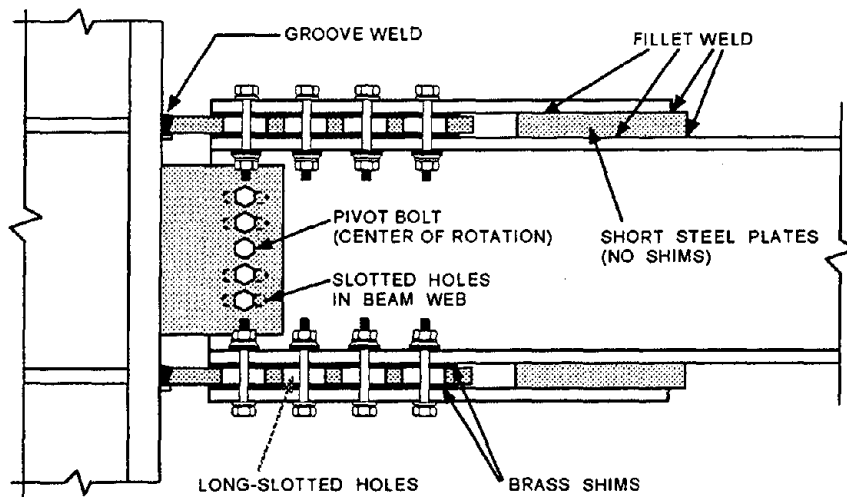


Fig. 5.28: An alternative RSBC for Moment Resisting Connections.

its flange buried in the concrete. To ensure better tension resistance, these tees are surrounded by reinforcing bars. If necessary, these tees can be drilled or have some holes punched for the steel bars to go through. The cover plates can be anchored on the beam flange by either fillet welds or bolting. If a concrete slab is placed on top of the beam, a metal or plastic mold or rubber sheet can cover the RSBC such that the concrete will not block the sliding space. Similar connections for concrete beams and column members are also possible.

5.6 Seismic Structural Design with RSBC

Plastic hinges in structural collapse or shakedown analysis have been used in design for several years [14, 31, 47]. These methods assume the structural materials are ductile and their strength known. But the SAC structural tests show the cumulative ductility of steel is very limited. Also, the behavior of materials beyond the elastic limit is highly variable, and there is no theory which has attempted to deal accurately with this phenomenon. Additionally, today's structural steel has high variation in strength, such that the plastic design theory is inaccurate for metal yielding type connections, especially for severe cyclic yielding conditions. Whereas the analytical model of an RSBC can be described as a *plastic hinge* without any material yielding.

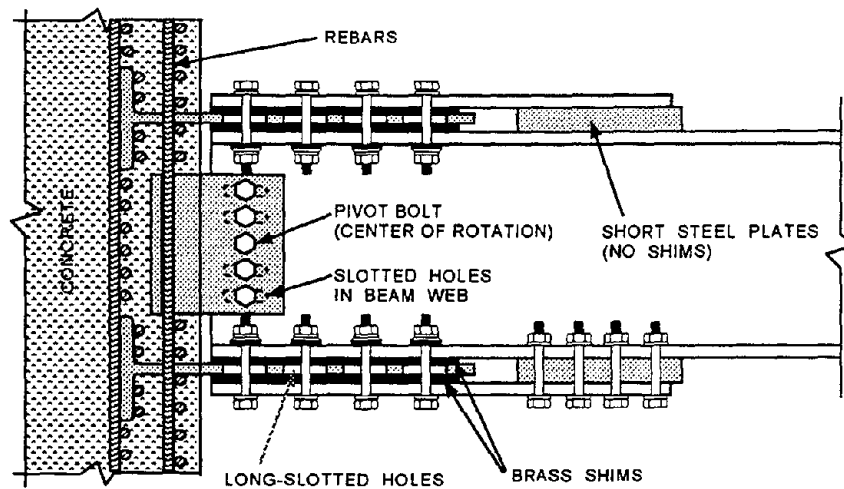


Fig. 5.29: An alternative RSBC for composite construction.

Its strength can be set accurately by an adequate number of bolts, and its ductility can be assigned by using suitable length of slots. The hysteresis loops of RSBC approximate the elastic-perfectly plastic model with reasonable accuracy. It is not only an ideal connection to which the plastic hinge theory can apply, but it is also an outstanding energy dissipator. In other words, the behavior of an RSBC can be accurately analyzed using conventional nonlinear structural analysis programs. Existing seismic codes can be used in designing the RSBCs; the process is similar to the design of conventional steel connections.

5.7 Conclusions and Remarks

On the basis of these limited analytical and experimental studies on non-destructive RSBC connections, the following conclusions can be drawn:

1. The simple Slotted Bolted Connections for braced frames were adapted for use in steel moment-resisting connections. The details for this rotational friction damper are largely conventional, except for the use of long slotted holes in the tees. This design is placed into the public domain. Its low cost and easy fabrication make it very practical for seismic applications.

2. DTI washers were found to be sufficiently accurate indicators for assuring proper tightening of RSBC bolts.
3. By adjusting the long slot length and bolt numbers, the rotation and strength of RSBCs can be accurately determined. The constitutive law is similar to the simple elasto-plastic model. Any nonlinear structural analysis software with an elasto-plastic beam element can be used to simulate the behavior of a structure with RSBCs accurately and easily.
4. The RSBC is an ideal plastic hinge. Plastic design theory can be simply applied to the design of an RSBC without concern of an abrupt fracture or cumulative damage at the connection.
5. The RSBC can be designed to attain the full fixity of the beam, but it is best designed by the allowable stress method to avoid any unreliable material yielding. Only the ASTM specified minimum yield strength is needed in the allowable stress design. The high variation of today's steel strength will not affect the intended performance of the connection because the slip force is controlled by the number of bolts, not by the beam strength. Unlike welded connections, which depend largely on strength and are prone to failure if the actual material strength deviates too much from the design value.
6. The energy dissipation capacity of RSBCs is outstanding. It is better than that of any known moment-resisting connections. The RSBC shows no degradation in hysteresis loops or damage in material after a severe test, it is durable enough to withstand several strong earthquake events without retrofit.
7. The most critical point of an RSBC is at the center of the tee flange and stem juncture due to the bending of the tee stem. In large rotation conditions, the strain can reach 1.1%. However, this moderate strain is not enough to cause fatigue fracture.
8. With some small modifications to the original design, the RSBC can be adapted to be used in welded connections, in concrete-steel composite construction, as well as in joining reinforced or precast concrete members.

The following important issues were not considered in this limited study, and require further research:

1. The simple constitutive model for the RSBC shows reasonable accuracy for rotation angles less than 3% rad. Although it is rare for an MRF connection to deform more than 3% rad of rotation, it is educational to study the load-deflection relationship of the RSBC with large rotations. Suitable details of secondary structures or non-structures undergoing large rotations also require further study.
2. Structural tests of alternative RSBCs as proposed in Section 5.5 are essential to prove their reliability.
3. The choice of brass as a suitable friction surface is not necessarily the only material providing stable hysteresis behavior, thus it is logical to try some alternative shims for a larger coefficient of friction, such that the number of bolts can be reduced.
4. To reduce the corrosion and galvanic effects, it is crucial to test some RSBCs with painted faying surfaces. It is believed that the thin film of paint will rub off in the first few cycles and that the hysteresis loops will be comparable to the ones without paint.
5. The global behavior of an MRF equipped with RSBCs needs to be investigated using shake table tests.

Epilogue

Structural engineers have long been struggling without success for new seismic designs with larger ductility. The reason is simple: structures designed using material which yields to resist the earthquake are conceptually wrong because the available material ductility is very limited. After the cumulative ductility of a structural member exhausts the supply of ductility, the member will fracture. Unfortunately, building codes throughout the world underestimate the strength of earthquakes and still allow the use of material yielding in seismic design.

Between 1970 and 1993, the insurance industry in California collected \$3.4 billion in earthquake premiums, while claims totaled less than \$1 billion. Last year (1994), they took in \$500 million in earthquake premiums and paid out \$11.4 billion for property damage caused by the moderate Northridge earthquake alone³, not to mention the fatalities. It is guaranteed that a stronger, completely different, unexpected earthquake will strike our metropolitan area. San Francisco 1906, Mexico city 1985, Loma Prieta 1989, Northridge 1994, Kobe 1995 are a few examples from the past. Structural failure disasters will replay again and again unless we start to change our structural systems to non-destructive types without material yielding.

Currently, the best known non-destructive structures are base isolation systems. But due to their high cost and their unsuitability for slender buildings, their use is not prevalent. On the other hand, more and more non-destructive energy dissipators are being invented or developed. SBCs and RSBCs belong to this category. Such energy dissipators convert the kinetic energy into heat and prevent the surge of seismic energy from being stored in structural members where they cause damage. The use of energy dissipators greatly reduces the risk of earthquakes. As long as their costs are low, as is

³Base on the authors' observation, the structural retrofit itself is not expensive, it is the interior re-decoration that costs a fortune.

the case with SBCs and RSBCs, their use for practical applications is very promising indeed.

Bibliography

- [1] Aguirre, M. and Sánchez, R., "Structural Seismic Damper," *J. Struct. Eng.*, **118**(5), ASCE, 1158-1171, 1992.
- [2] Aiken, I. D. and Kelly, J. M., "Earthquake Simulator Testing and Analytical Studies of two Energy-Absorbing Systems for Multistory Structures," *Report No. UCB/EERC-90/03*, University of California, Berkeley, 1990.
- [3] Akiyama, H., *Earthquake Resistant Limit-State Design for Buildings*, University of Tokyo Press, 1985.
- [4] Alpsten, G. A., "Thermal Residual Stresses in Hot-Rolled Steel Members," *Fritz Laboratory Report 337.3*, Lehigh University, 1968.
- [5] Anderson, T. L., *Fracture Mechanics, Fundamentals and Applications*, 2nd ed., CRC Press, 1995.
- [6] ASTM, *Standard Test Method for Plane-Strain Fracture Toughness of Metallic Materials*. E399-90, American Society for Testing and Materials, Philadelphia, 1990.
- [7] ASTM, *Standard Specification for Compressible-Washer-Type Direct Tension Indicators for Use with Structural Fasteners*. F959-93a, American Society for Testing and Materials, Philadelphia, 1993.
- [8] ATC 17-1. *Seminar on Seismic Isolation, Passive Energy Dissipation, and Active Control*, Vol. 2, Applied Technology Council, San Francisco, March 1993.
- [9] Barsom, J. M., "Development of the AASHTO Fracture Toughness Requirements for Bridge Steels," *Engineering Fracture Mechanics*, **7**, 605-618, 1975.
- [10] Bathe, K. J., Ramm, E., and Wilson, E. L., "Finite Element Formulations for Large Deformation Dynamic Analysis," *Int. J. Num. Meth. Eng.*, **9**, 373, 1975.
- [11] Bathe, K. J. and Ozdemir, H., "Elastic-Plastic Large Deformation Static and Dynamic Analysis," *Computers & Structures*, **6**(2), 81, 1976.

- [12] Bathe, K. J., "Static and Dynamic Geometric and Material Nonlinear Analysis Using ADINA," Report 82448-2, Acoustics and Vibration Laboratory, Mechanical Engineering Department, Massachusetts Institute of Technology, 1976.
- [13] Bathe, K. J. *Finite Element Procedures in Engineering Analysis*, Prentice-Hall, Englewood Cliffs, New Jersey 07632, 1982.
- [14] Beedle, L. S., *Plastic Design of Steel Frames*, John Wiley and Sons, Inc., New York, 1958.
- [15] Beedle, L. S. and Tall, L., "Basic Column Strength," *Proc. Am. Soc. Civil Engrs.*, **86** (ST-7), 139, July 1960.
- [16] Bertero, V. V., Anderson, J. C., and Krawinkler, H., "Performance of Steel Building Structures During the Northridge Earthquake," *Report No. UCB/EERC-94/09*, Earthquake Engineering Research Center, University of California, Berkeley, 1994.
- [17] Blackman, B., *Studies of Seismic Steel Beam-to-Column Moment Connections*, M. Eng. Thesis, Dept. of Civil Engineering, University of California, Berkeley, 1995.
- [18] Bleich, F., *Buckling Strength of Metal Structures*, McGraw-Hill, New York, 1952.
- [19] Broek, D., *Elementary Engineering Fracture Mechanics*, Martinus Nijhoff, The Hague, 1986.
- [20] Chen, S. J. and Yeh, C. H., "Enhancement of Ductility of Steel Beam-to-Column Connections for Seismic Resistance", *SSRC 1994 Task Group Meeting & Technical Session*, Lehigh University, 1994.
- [21] Dawance, G., "Nouvelles recherches expérimentales sur la plasticité des éléments de construction métallique," *New Experimental Researches on Plasticity of Metal Structural Elements*, *Ann. Inst. Tech. Batiment Trav. Publ.*, **14** 130, 1950.
- [22] Feder, D. and Lee, G. C., "Residual Stress and the Strength of Members of High Strength Steel," *Fritz Laboratory Report 269.2*, Lehigh University, 1959.
- [23] Goudreau, G. L. and Taylor, R. L., "Evaluation of Numerical Integration methods in Elastodynamics," *Comp. Meth. Appl. Mech. Eng.*, **2**, 59-67, 1972.
- [24] Griffith, A. A., "The Phenomena of Rupture and Flow in Solids," *Philosophical Transactions, Royal Society of London*, **A221**, 163-198, 1920.

- [25] Grigorian, C. E., Yang, T.-S., and Popov, E. P., "Slotted Bolted Connection Energy Dissipators," *Report No. UCB/EERC-92/10*, University of California, Berkeley, 1992.
- [26] Grigorian, C.E. and Popov, E. P., "Slotted bolted connections for energy dissipation," *Proceedings of seminar on seismic isolation, passive energy dissipation, and active control*, ATC 17-1, Vol. 2, 545-556, 1992.
- [27] Grigorian, C.E., Yang, T.-S. and Popov, E. P., "Slotted bolted connection energy dissipators," *Earthquake Spectra*, **9**(3), 491-504, 1993.
- [28] Grigorian, C.E. and Popov, E. P., "Energy dissipation with slotted bolted connections," *Report UCB/EERC-94/02*, Earthquake Engineering Research Center, University of California, Berkeley, CA, 1994.
- [29] Hanson, R. D. (Ed.) Theme issue: Passive Energy Dissipation, *Earthquake Spectra*, **9**(3), 1993.
- [30] Hibbitt, Karlsson, and Sorensen, Inc., *ABAQUS Version 5.4*.
- [31] Horne, M. R., *Plastic Theory of Structures*, 2nd Edition, Pergamon Press, Oxford, 1979.
- [32] Hughes, T. J. R., Pister, K. S., and Taylor, R. L., "Implicit-Explicit Finite Elements in Nonlinear Transient Analysis," *Comp. Meth. Appl. Mech. Eng.*, **17/18**, 1979.
- [33] International Conference of Building Officials (ICBO), *Uniform Building Code (UBC)*, Whittier, CA, 1994.
- [34] Irwin, G. R., "Onset of Fast Crack Propagation in High Strength Steel and Aluminum Alloys," *Sagamore Research Conference Proceedings*, **2**, 289-305, 1956.
- [35] Irwin, G. R., "Analysis of Stresses and Strains near the End of a Crack Traversing a Plate," *Journal of Applied Mechanics*, **24**, 361-364, 1957.
- [36] Irwin, G. R., "A Summary of Fracture Mechanics Concepts," *Journal of Testing & Evaluation*, **11**, 56-65, 1983.
- [37] Kasai, K. and Popov, E. P., "General Behavior of WF Steel Shear Link Beams," *J. of Struct. Eng.*, ASCE, **112**(2), 362-382, 1986.
- [38] Kelly, J. M. and Skinner, M. S., "The Design of Steel Energy Absorbing Restrainers and their Incorporation into Nuclear Power Plants for Enhanced Safety," *Report No. UCB/EERC-79/10*, University of California, Berkeley, 1979.

- [39] Kirkaldy, D., *Results of an Experimental Inquiry into the Tensile Strength and Other Properties of Various Kinds of Wrought-Iron and Steel*, 2nd ed., London, Hamilton, Adams & co. 1862.
- [40] Kumai, T., "Elastic Stability of the Square Plate with a Central Circular Hole under Edge Thrust," *Reports of Research Institute for Applied Mechanics*, Kyusyu University, 1(2), 1-10, Japan, 1952.
- [41] Ling, C.-B., "On the Stresses in a Plate Containing Two Circular Holes," *J. Applied Physics*, 19, 1, 77-82, 1948.
- [42] Ling, C.-B., "The Stresses in a Plate Containing an Overlapped Circular Hole," *J. Applied Physics*, 19, 4, 405-411, 1948.
- [43] Lizundia, B., "Seismic Strengthening with Steel Slotted Bolt Connections," *Steel Tips*, Structural Steel Educational Council, January, 1995.
- [44] Ludwik, P. and Scheu, R., "Über Kerbwirkungen bei Flusseisen," *Stahl und Eisen*, 1923.
- [45] MacGregor, C. W., "The Yield Point of Mild Steel," *Transactions of the American Society of Mechanical Engineers*, APM-53-15, 187-200, 1931.
- [46] Mahin, S. A. and Lin, J., "Construction of Inelastic Response Spectra for Single-Degree-of-Freedom Systems," *Report No. UCB/EERC-83/17*, University of California, Berkeley, 1983.
- [47] Neal, B. G., *The Plastic Methods of Structural Analysis*, Chapman and Hall, London, 1956.
- [48] Neuber, H., *Kerbspannungslehre*, 2nd ed., Springer-Verlag, Berlin, 1958.
- [49] Newmark, N. M., "A Method of Computation for Structural Dynamics," *J. Eng. Mech. Div.*, 85, EM3, ASCE, 67-94, 1959.
- [50] Newmark, N. M. and Hall, W. J., "Procedures and Criteria for Earthquake Resistant Design," *Building Science Series* 46, 209-236, Building Practices for Disaster Mitigation, National Bureau of Standards, February, 1973.
- [51] Novak, S. R., "Resistance to Plane-Stress Fracture (R-Curve Behavior) of A572 Structural Steel," *ASTM STP 591*, American Society for Testing and Materials, Philadelphia, 1976.
- [52] Peterson, R. E., *Stress Concentration Factors for Design*, Wiley, New York, 1974.

- [53] Plumier, A., "Modelling and Design of Steel Structures in the Eurocode 8 Context," *Experimental and Numerical Methods in Earthquake Engineering*, 319-349, 1991.
- [54] Popov, E. P. and Pinkney, R. B., "Cyclic Yield Reversal in Steel Building Connections," *Journal of Structural Division, ASCE*, **95**, ST3, 327-353, 1969.
- [55] Popov, E. P. and Stephen, R. M., "Cyclic Loading of Full Size Steel Connections," *American Iron and Steel Institute, Steel Research for Construction Bulletin No. 21*, 1972.
- [56] Popov, E. P., Yang, T.-S. and Grigorian, C. E., "New Directions in Structural Seismic Design," *Earthquake Spectra*, **9**(4), 845-875, November 1993.
- [57] Popov, E. P., Grigorian, C. E. and Yang, T.-S. "Developments in Seismic Structural Analysis and Design," *Engineering Structures*, **17**(3), 187-197, 1995.
- [58] Rice, J. R., "A Path Independent Integral and the Approximate Analysis of Strain Concentration by Notches and Cracks," *Journal of Applied Mechanics*, **35**, 379-386, June, 1968.
- [59] Ricles, J. M. and Popov, E. P., "Composite Action in Eccentrically Braced Frames," *J. Struct. Engrg.*, ASCE, **115**(8), 2046-2066, 1989.
- [60] Roeder, C. W. and Popov, E. P., "Eccentrically Braced Steel Frames for Earthquakes," *J. Struct. Div.*, ASCE, **104**, ST3, 391-412, 1978.
- [61] Rolfe, S. T. and Barsom, J. M., *Fracture and Fatigue Control in Structures, Applications of Fracture Mechanics*, 2nd ed., Prentice-Hall, Englewood Cliffs, N.J., 1987.
- [62] Roberts, R., Irwin, G. R., Krishna, G. V. and Yen, B. T., "Fracture Toughness of Bridge Steels - Phase II Final Report," *Fritz Engineering Laboratory Report No. 379.2*, Lehigh University, June 1974.
- [63] Savin, G. N., *Stress Concentration Around Holes*, International Series of Monographs in Aeronautics and Astronautics, Pergamon Press, London, 1961.
- [64] Schoultz, K. I., *Over den Spanningstoestand in Doorborde Platen*, Diss. Techn. Hochschule, Delft, 1941.
- [65] Skinner, R. I., Kelly, J. M., and Heine, A. J., "Hysteretic Dampers for Earthquake Resistant Structures," *Earthquake Engineering and Structural Dynamics*, **3**, 1975.

- [66] Stiemer, S. F., Godden, W. G., and Kelly, J. M., "Experimental Behavior of Spatial Piping Systems with Steel Energy Absorbers Subjected to a Simulated Differential Seismic Input," *Report No. UCB/EERC-81/09*, University of California, Berkeley, 1981.
- [67] Suresh, S., *Fatigue of Materials*, Cambridge University Press, 1991. (Reprint 1994)
- [68] Timoshenko, S., *Strength of Material, Part II, Advanced Theory and Problems*, 3rd ed., D. Van Nostrand Company, Inc., 1956.
- [69] J & M Turner Inc., *Instruction Manual for Installing High-Strength Bolts with Direct Tension Indicators*, May 1993.
- [70] Uang C. M. and Bertero, V. V., "Implications of Recorded Earthquake Ground Motions on Seismic Design of Building Structures," *Report No. UCB/EERC-88/13*, University of California, Berkeley, 1988.
- [71] Uang, C. M. and Bertero, V. V., "Use of Energy as a Design Criterion in Earthquake-Resistant Design," *Report No. UCB/EERC-88/18*, University of California, Berkeley, 1988.
- [72] Westergaard, H. M., "Bearing Pressures and Cracks," *Journal of Applied Mechanics*, 6, 49-53, 1939.
- [73] Whittaker, A., Uang C. M., and Bertero, V. V., "Earthquake Simulation Tests and Associated Studies of a 0.3-scale model of a Six-story Eccentrically Report No. UCB/EERC-87/02, University of California, Berkeley, 1987.
- [74] Whittaker, A., Bertero, V. V., Alonso, J., and Thompson, C., "Earthquake Simulator Testing of Steel Plate Added Damping and Stiffness Elements," *Report No. UCB/EERC-89/02*, University of California, Berkeley, 1989.
- [75] Yang, T.-S., "DANS, A computer program for the dynamic analysis of nonlinear shear buildings," *CE 299 Project*, University of California, Berkeley, 1991.
- [76] Youssef, N. F. G., Bonowitz, D. and Gross, J. L., "A Survey of Steel Moment-Resisting Frame Buildings Affected by the 1994 Northridge Earthquake," *National Institute of Standards and Technology, Report No. NISTIR 5625*, US Department of Commerce, April 1995.

Appendix A

Nonlinear Dynamic Response Analysis

The nonlinear dynamic equilibrium equation can be expressed in terms of nodal displacement vector \mathbf{u} as

$$\mathbf{M}\ddot{\mathbf{u}} + \mathbf{C}\dot{\mathbf{u}} + \mathbf{F}(\mathbf{u}) = \mathbf{P}(t) \quad (\text{A.1})$$

where matrix \mathbf{M} is the structural mass matrix, \mathbf{C} is the damping matrix, and $\mathbf{P}(t)$ are the applied forces. Dots denote differentiation in time. The term $\mathbf{F}(\mathbf{u})$ is the internal forces opposing the displacement of the structure. For linear elastic structures

$$\mathbf{F}(\mathbf{u}) = \mathbf{K}\mathbf{u} \quad (\text{A.2})$$

where \mathbf{K} is the stiffness matrix of the structure. For non-linear cases, \mathbf{F} must be calculated from the stress distribution:

$$\mathbf{F}(\mathbf{u}) = \int_V \mathbf{B}^T \boldsymbol{\sigma} dV \quad (\text{A.3})$$

where $\boldsymbol{\sigma}$ are the non-linear stresses and \mathbf{B} is the matrix expressing the strains in terms of nodal displacements.

Equation (A.1) can be solved by step-by-step integration methods. The Newmark integration method [49] is used here. The non-linear restoring forces \mathbf{F} must be calculated at each stage of the computation. In order for the displacement and stresses to satisfy the non-linear conditions of the problem, it is necessary to perform an equilibrium iteration sequence in each time step.

The Newmark method is an implicit method. If the solution is known for time t , the non-linear equilibrium equations are considered at time step $t + \Delta t$

$$\mathbf{M}\ddot{\mathbf{u}}_{t+\Delta t} + \mathbf{C}\dot{\mathbf{u}}_{t+\Delta t} + \mathbf{F}_{t+\Delta t} = \mathbf{P}_{t+\Delta t} \quad (\text{A.4})$$

The velocity and displacement vectors are assumed to be interpolated by

$$\dot{\mathbf{u}}_{t+\Delta t} = \dot{\mathbf{u}}_t + [(1 - \gamma)\ddot{\mathbf{u}}_t + \gamma\ddot{\mathbf{u}}_{t+\Delta t}]\Delta t \quad (\text{A.5})$$

$$\mathbf{u}_{t+\Delta t} = \mathbf{u}_t + \dot{\mathbf{u}}_t\Delta t + [(\frac{1}{2} - \beta)\ddot{\mathbf{u}}_t + \beta\ddot{\mathbf{u}}_{t+\Delta t}]\Delta t^2 \quad (\text{A.6})$$

where β and γ are parameters that can be determined to obtain integration accuracy and stability. When $\beta = 1/4$ and $\gamma = 1/2$, it is commonly called the Newmark Beta method or average acceleration method. If $\beta = 1/6$ and $\gamma = 1/2$, it reduces to the linear acceleration method. By solving Eqs. (A.4), (A.5) and (A.6), the acceleration, velocity, and displacement vectors at time $t + \Delta t$ can be obtained.

The equilibrium nodal forces, $\mathbf{F}_{t+\Delta t}$, at time $t + \Delta t$ can be estimated as

$$\mathbf{F}_{t+\Delta t} = \mathbf{F}_t + \mathbf{K}_t\delta\mathbf{u} \quad (\text{A.7})$$

where \mathbf{K}_t is the tangential stiffness matrix evaluated from conditions at time t . It is assumed that the displacement increment $\delta\mathbf{u}$ is linear between times t and $t + \Delta t$,

$$\delta\mathbf{u} = \mathbf{u}_{t+\Delta t} - \mathbf{u}_t \quad (\text{A.8})$$

Substituting Eq. (A.7) in Eq. (A.4) gives

$$\mathbf{M}\ddot{\mathbf{u}}_{t+\Delta t} + \mathbf{C}\dot{\mathbf{u}}_{t+\Delta t} + \mathbf{K}_t\delta\mathbf{u} = \mathbf{P}_{t+\Delta t} - \mathbf{F}_t \quad (\text{A.9})$$

The solution of (A.9) gives approximate displacement increment $\delta\mathbf{u}$. It is necessary to employ iterations within each time step in order to maintain the equilibrium. With the superscripts $i - 1$ and i being the values at two successive equilibrium iterations, Eq. (A.9) can be rewritten as

$$\mathbf{M}\ddot{\mathbf{u}}_{t+\Delta t}^i + \mathbf{C}\dot{\mathbf{u}}_{t+\Delta t}^i + \Delta\mathbf{u}^i = \mathbf{P}_{t+\Delta t} - \mathbf{F}_{t+\Delta t}^{i-1}, \quad i = 1, 2, 3, \dots \quad (\text{A.10})$$

$$\Delta\mathbf{u}^i = \delta\mathbf{u}_{t+\Delta t}^i - \delta\mathbf{u}_{t+\Delta t}^{i-1} \quad (\text{A.11})$$

The first iteration ($i = 1$) in Eq. (A.10) corresponds to the solution of Eq. (A.9), where $\Delta\mathbf{u}^1 = \delta\mathbf{u}$, $\mathbf{u}_{t+\Delta t}^0 = \mathbf{u}_t$, $\dot{\mathbf{u}}_{t+\Delta t}^1 = \dot{\mathbf{u}}_{t+\Delta t}$, $\ddot{\mathbf{u}}_{t+\Delta t}^1 = \ddot{\mathbf{u}}_{t+\Delta t}$, and $\mathbf{F}_{t+\Delta t}^0 = \mathbf{F}_t$. If a pseudo-force formulation is followed, the stiffness matrix \mathbf{K}_t is kept at a constant value, with

dynamic equilibrium being maintained by successive iteration with a varying pseudo-force (right-hand-side in Eq. (A.11)). If the tangent stiffness method is used, the stiffness matrix \mathbf{K}_t is allowed to vary in the computation, with the term $\mathbf{F}_{t+\Delta t}^{i-1}$ being replaced by an equilibrium correction term.

Details of the non-linear solution procedure for the Newmark method are summarized by the following steps [10, 11, 12, 13, 23, 32]:

1. Initialize \mathbf{u}_0 , $\dot{\mathbf{u}}_0$, and $\ddot{\mathbf{u}}_0$ at time $t = t_0$.
2. Choose β , γ , and time increment Δt and calculate the following constants:

$$b_0 = \frac{1}{\beta\Delta t^2} \quad b_2 = \frac{1}{\beta\Delta t} \quad b_4 = \frac{\gamma}{\beta} - 1$$

$$b_1 = \frac{\gamma}{\beta\Delta t} \quad b_3 = \frac{1}{2\beta} - 1 \quad b_5 = \Delta t\left(\frac{\gamma}{2\beta} - 1\right)$$

3. Form the structural mass matrix \mathbf{M} and viscous damping matrix \mathbf{C} .
4. Calculate the tangential stiffness matrix \mathbf{K}_t at time t and form the effective stiffness matrix $\hat{\mathbf{K}}_t$

$$\hat{\mathbf{K}}_t = b_0\mathbf{M} + b_1\mathbf{C} + \mathbf{K}_t \quad (\text{A.12})$$

5. Form the effective load vector $\hat{\mathbf{P}}_{t+\Delta t}$

$$\hat{\mathbf{P}}_{t+\Delta t} = \mathbf{P}_{t+\Delta t} + \mathbf{M}(b_2\dot{\mathbf{u}}_t + b_3\ddot{\mathbf{u}}_t) + \mathbf{C}(b_4\dot{\mathbf{u}}_t + b_5\ddot{\mathbf{u}}_t) - \mathbf{F}_t \quad (\text{A.13})$$

6. Solve for displacement increments $\delta\mathbf{u}$

$$\delta\mathbf{u} = \hat{\mathbf{K}}_t^{-1}\hat{\mathbf{P}}_{t+\Delta t} \quad (\text{A.14})$$

7. Let $i = 0$

8. $i \leftarrow i + 1$

9. Evaluate accelerations, velocities, and displacements as

$$\ddot{\mathbf{u}}_{t+\Delta t}^i = b_0\delta\mathbf{u} - b_2\dot{\mathbf{u}}_t - b_3\ddot{\mathbf{u}}_t \quad (\text{A.15})$$

$$\dot{\mathbf{u}}_{t+\Delta t}^i = b_1\delta\mathbf{u} - b_4\dot{\mathbf{u}}_t - b_5\ddot{\mathbf{u}}_t \quad (\text{A.16})$$

$$\mathbf{u}_{t+\Delta t}^i = \mathbf{u}_t + \delta\mathbf{u} \quad (\text{A.17})$$

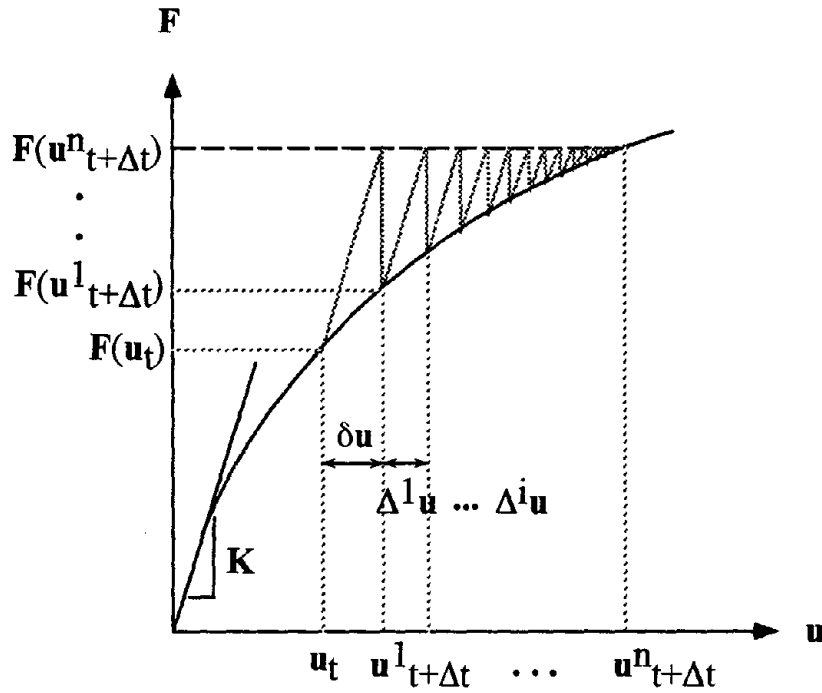


Fig. A.1: Newton iterations in a time-step.

10. Evaluate the residual forces $\hat{\mathbf{r}}^i_{t+\Delta t}$

$$\hat{\mathbf{r}}^i_{t+\Delta t} = \mathbf{P}_{t+\Delta t} - [\mathbf{M}\ddot{\mathbf{u}}^i_{t+\Delta t} + \mathbf{C}\dot{\mathbf{u}}^i_{t+\Delta t} + \mathbf{F}(\mathbf{u}^i_{t+\Delta t})] \quad (\text{A.18})$$

11. Solve for displacement corrections and update displacement increments (see Figure A.1)

$$\Delta \mathbf{u}^i = \hat{\mathbf{K}}_t^{-1} \hat{\mathbf{r}}^i_{t+\Delta t} \quad (\text{A.19})$$

$$\delta \mathbf{u} \leftarrow \delta \mathbf{u} + \Delta \mathbf{u}^i \quad (\text{A.20})$$

12. Check convergence. If $\frac{|\Delta \mathbf{u}^i|}{|\mathbf{u}_t + \delta \mathbf{u}|} > \text{threshold}$, go to step 8.

13. Compute next time step $t \leftarrow t + \Delta t$, go to step 4.

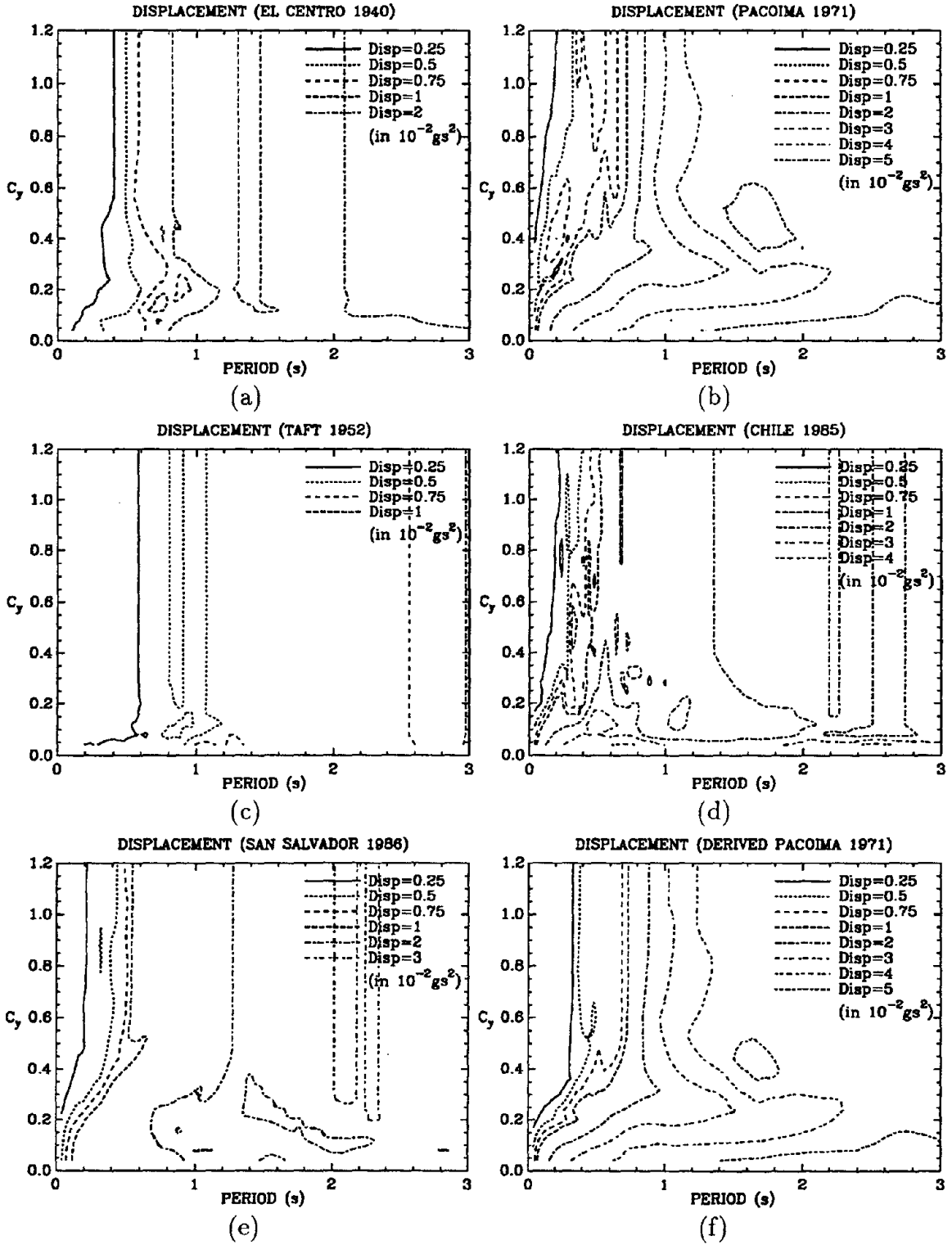
Appendix B

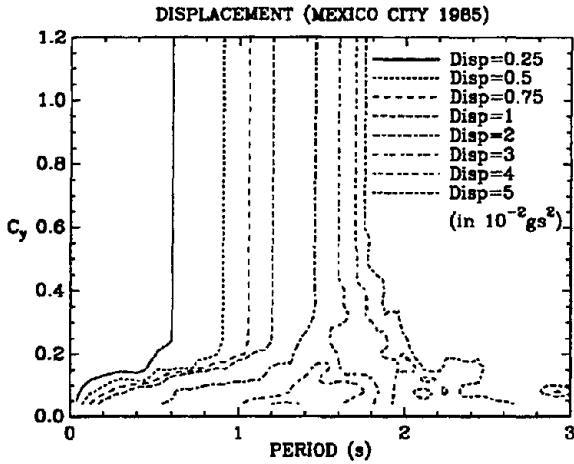
Seismic Response Spectra

This Appendix shows the seismic response spectra for the following earthquake records: (a) 1940 El Centro, (b) 1971 Pacoima, (c) 1952 Taft, (d) 1985 Chile, (e) 1986 San Salvador, (f) 1971 Derived Pacoima, (g) 1985 Mexico City, (h) 1992 Landers, (i) 1978 Miyagi-Ken-Oki, (j) 1989 Loma Prieta, (k) 1940 El Centro \times 1.5, and (l) 1952 Taft \times 4. These spectra are displayed in the following sections:

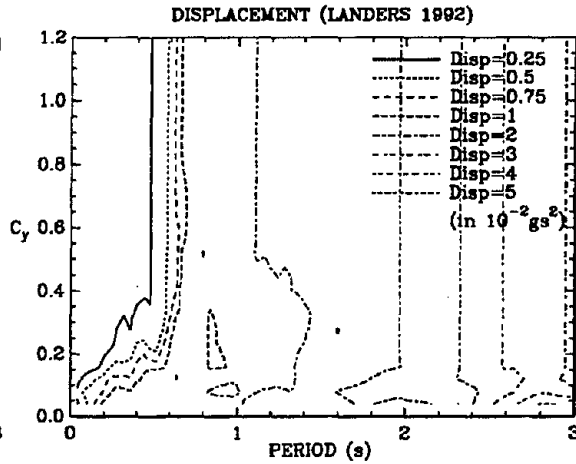
- B.1 - Displacement Response Spectra
- B.2 - Displacement Ductility Response Spectra
- B.3 - Number of Yield Reversals Spectra
- B.4 - Absolute Seismic Input Energy Spectra
- B.5 - Hysteresis Energy Spectra

B.1 Displacement Spectra Diagrams

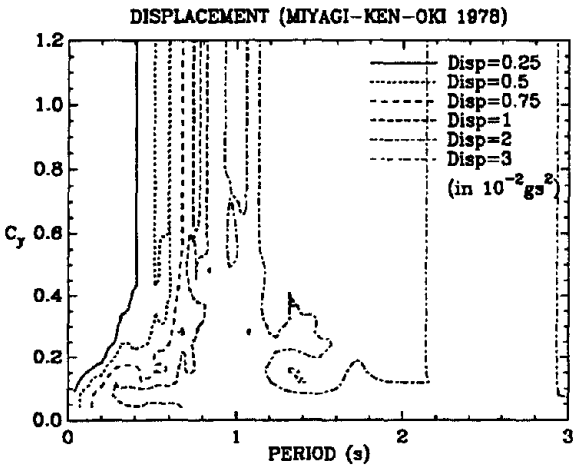




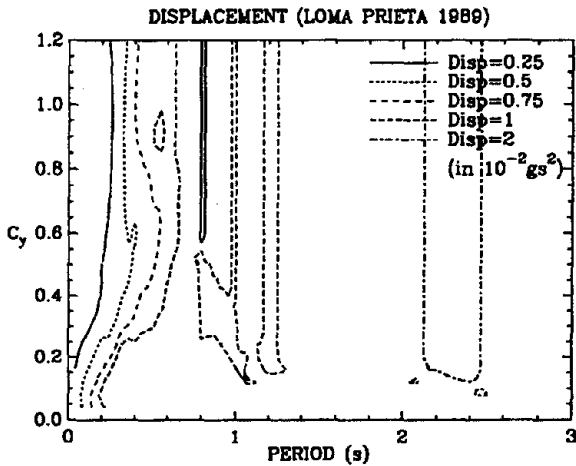
(g)



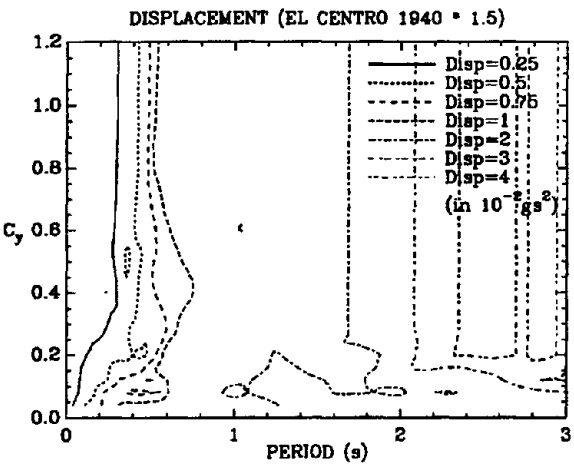
(h)



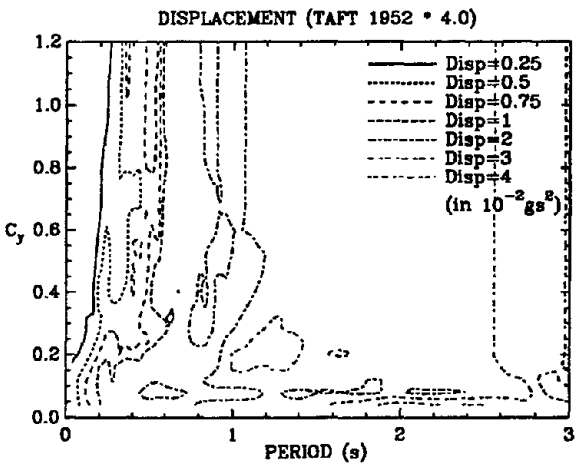
(i)



(j)

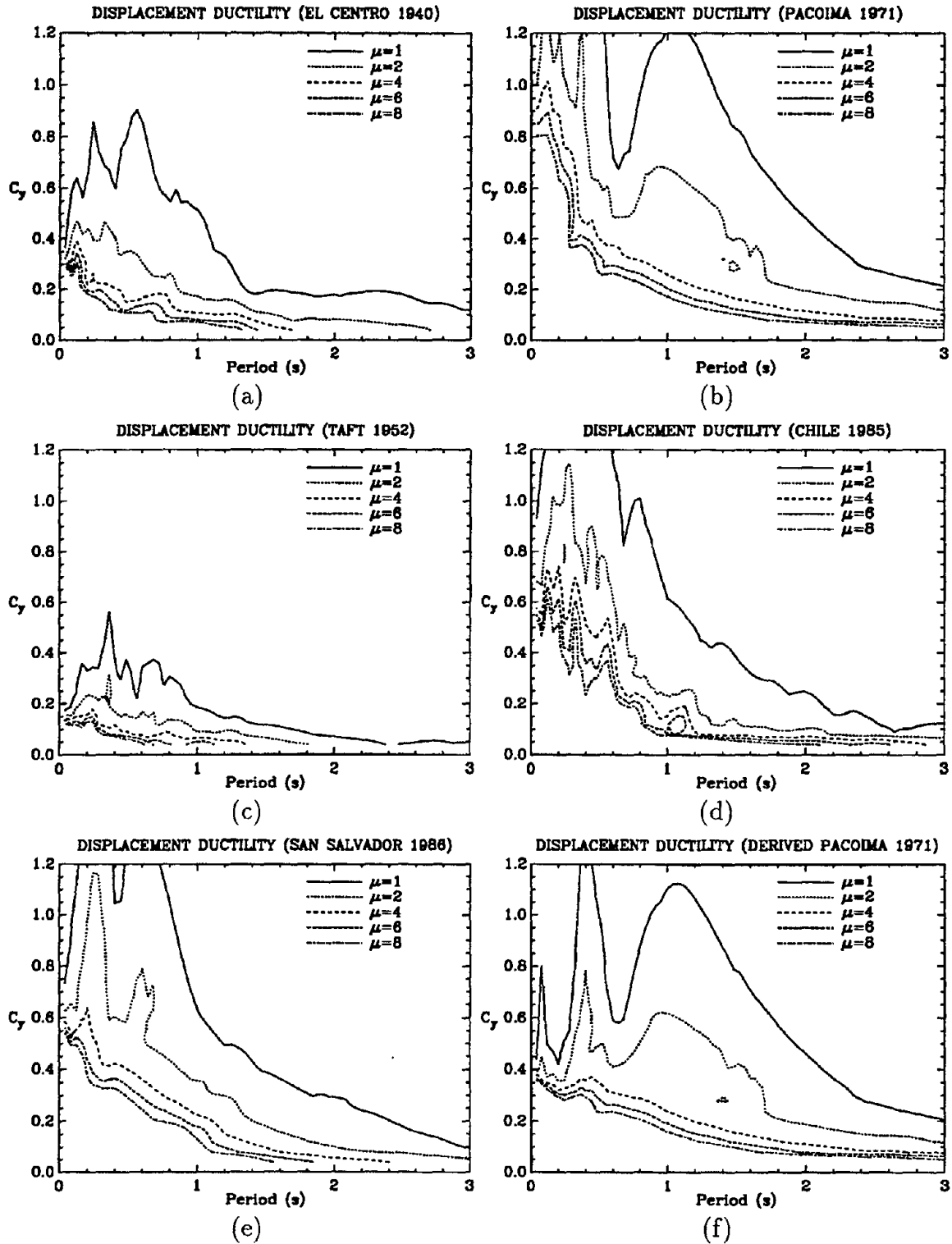


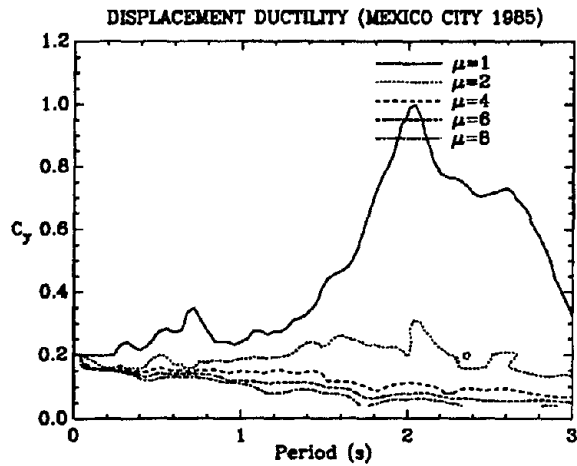
(k)



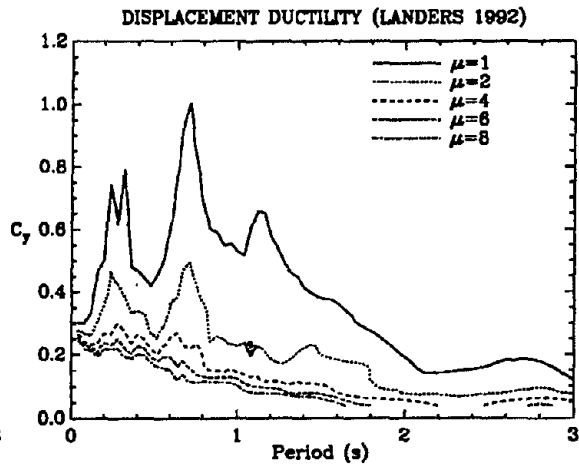
(l)

B.2 Displacement Ductility Diagrams

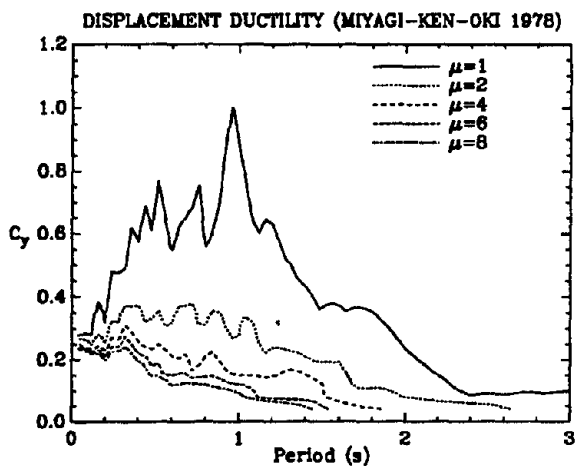




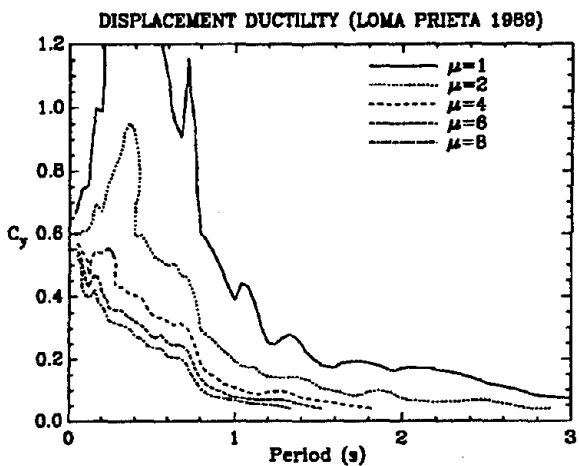
(g)



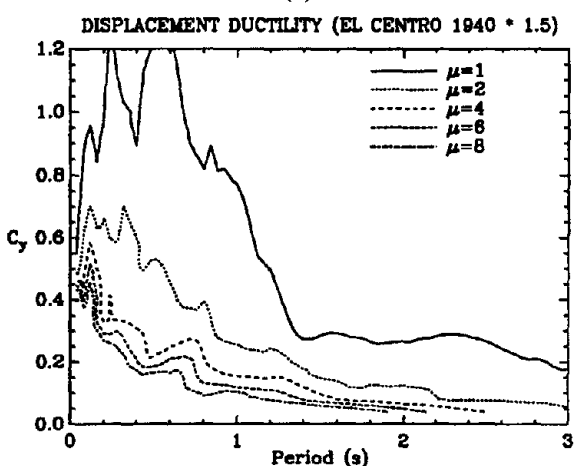
(h)



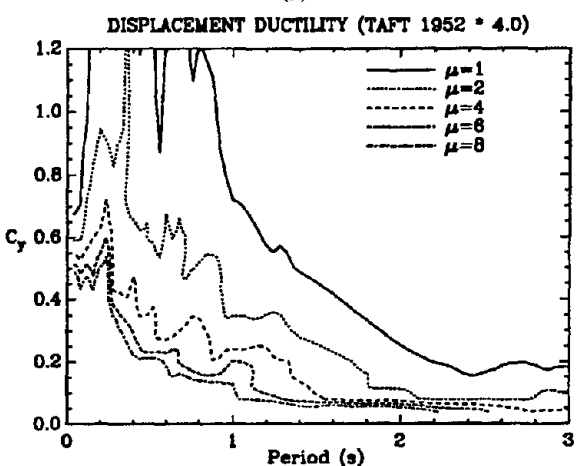
(i)



(j)

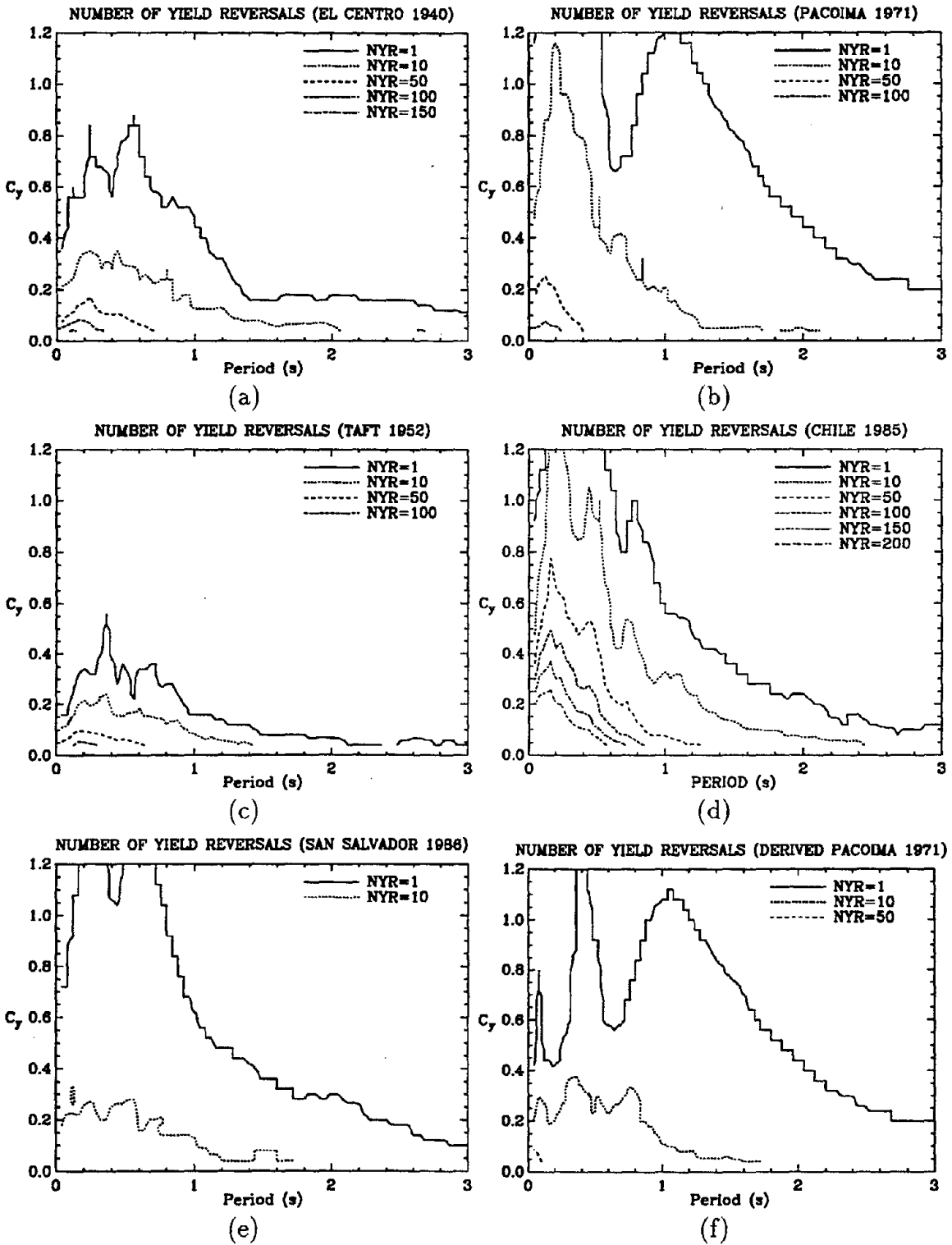


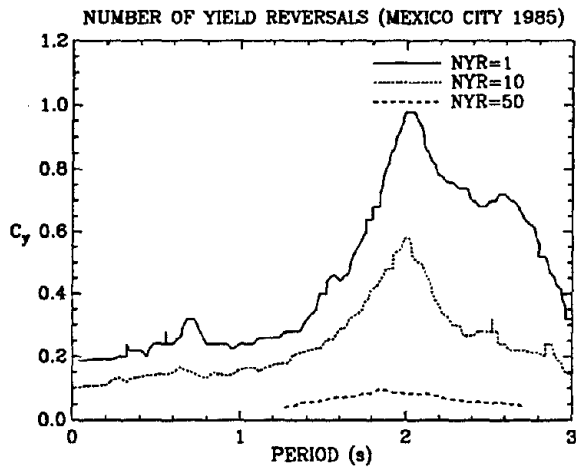
(k)



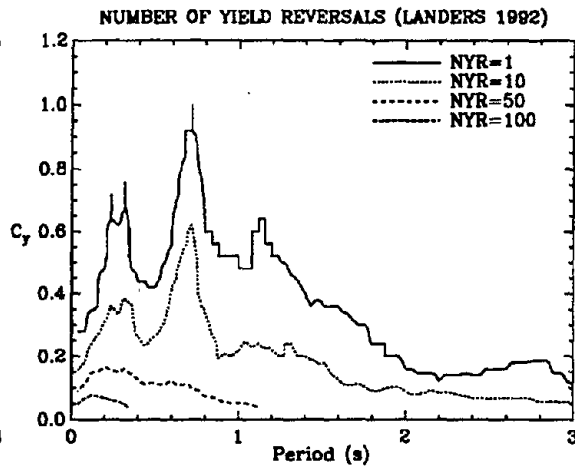
(l)

B.3 Number of Yield Reversals Diagrams

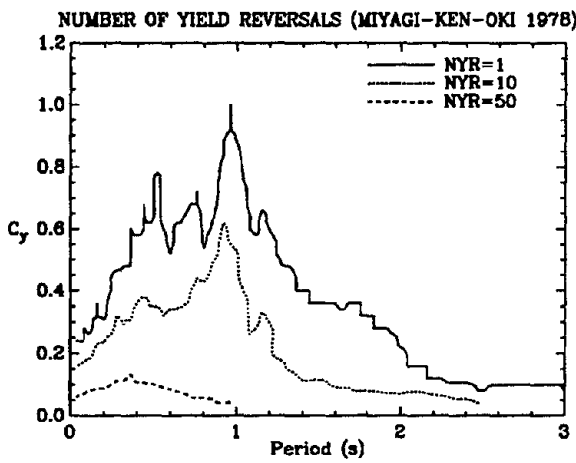




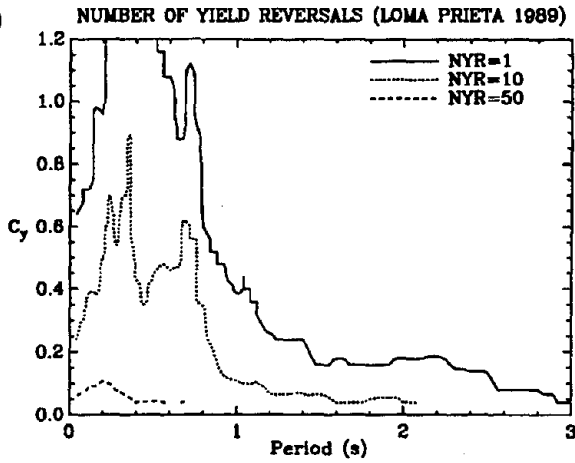
(g)



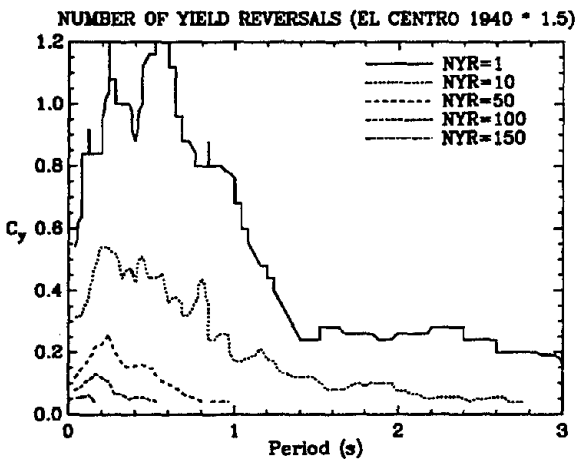
(h)



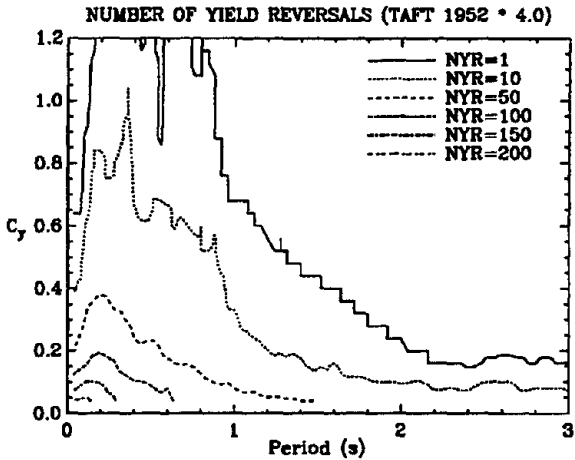
(i)



(j)

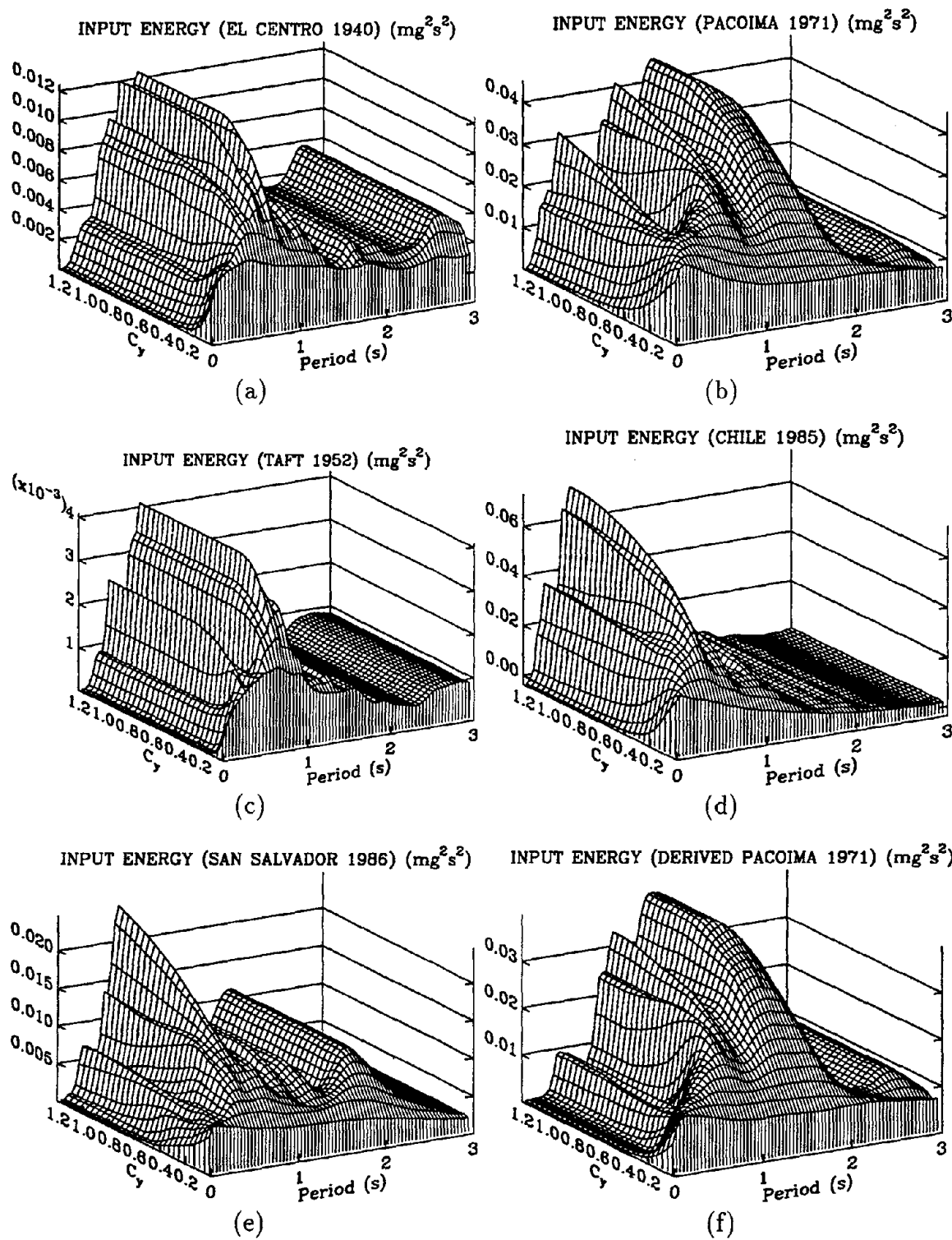


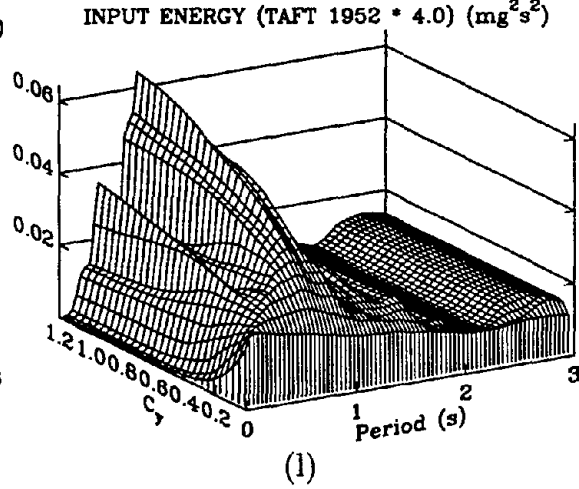
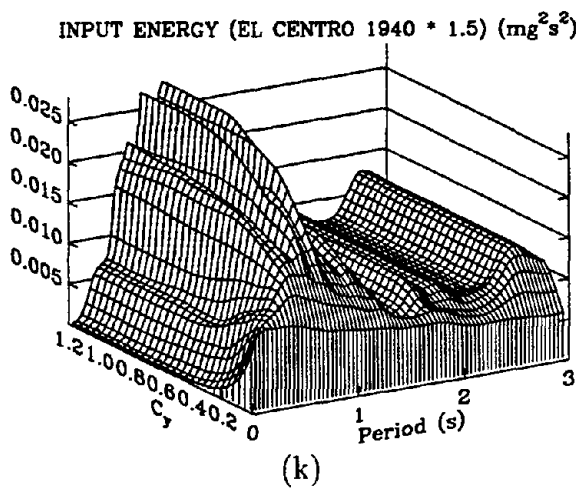
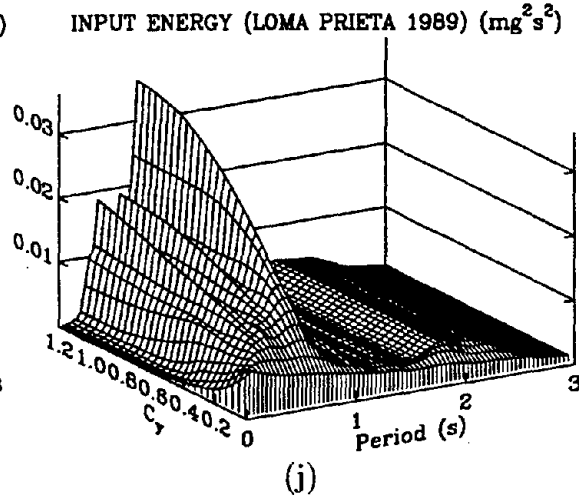
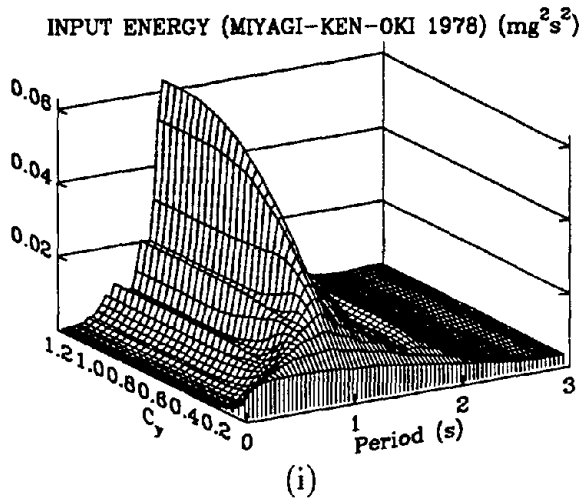
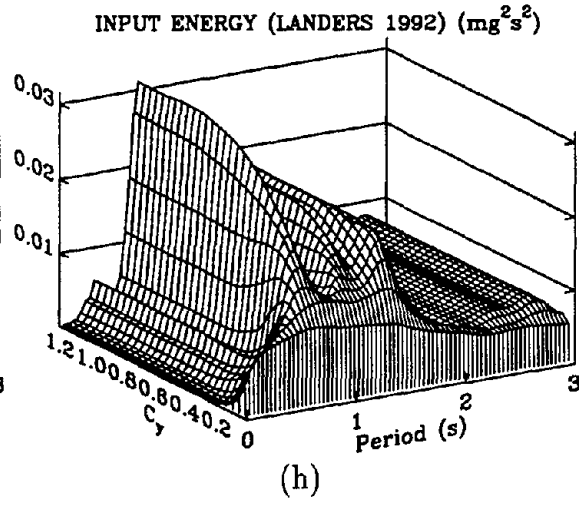
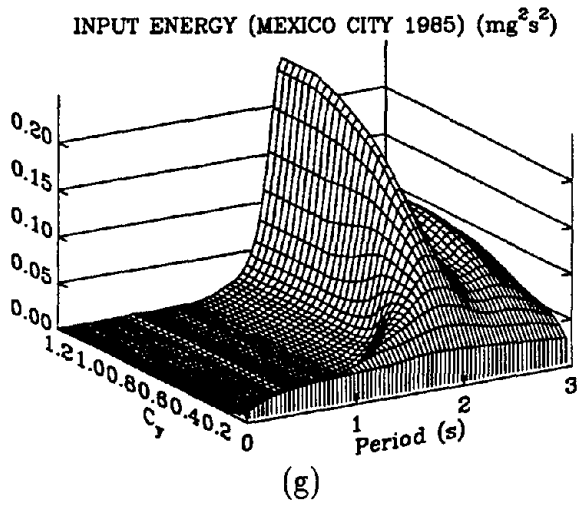
(k)



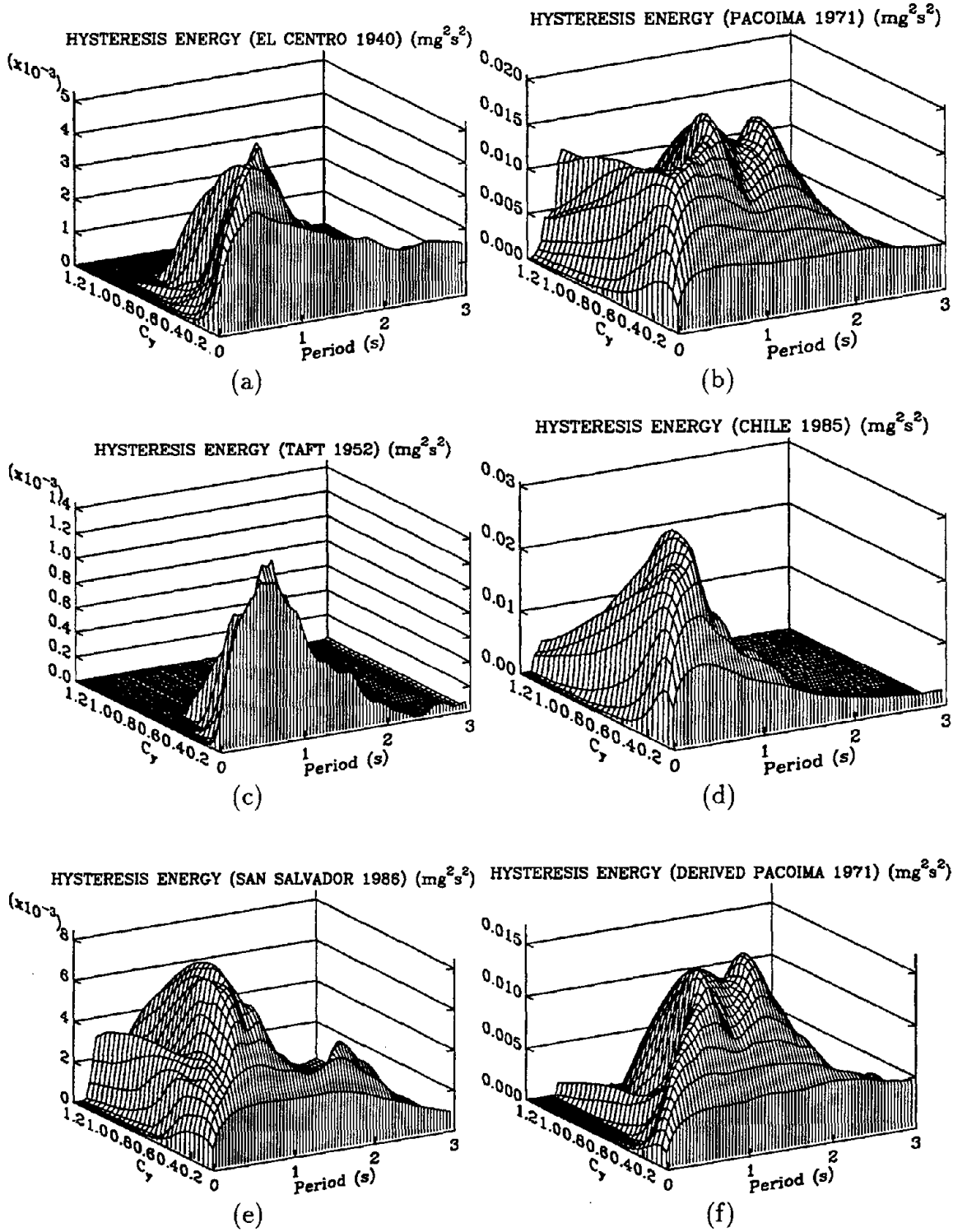
(l)

B.4 Seismic Input Energy Mesh Diagrams

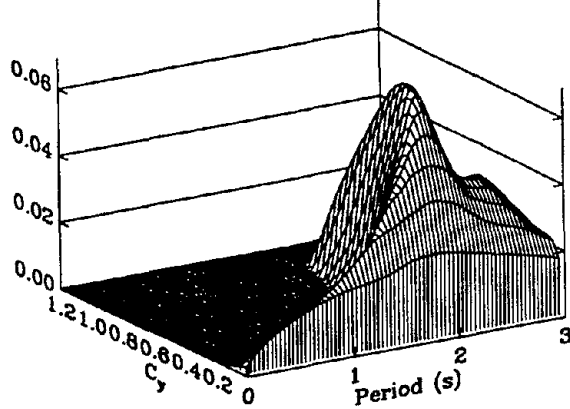




B.5 Hysteresis Energy Mesh Diagrams

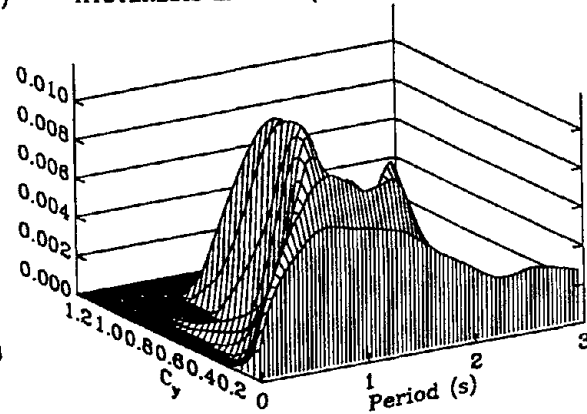


HYSTERESIS ENERGY (MEXICO CITY 1985) (mg^2s^2)



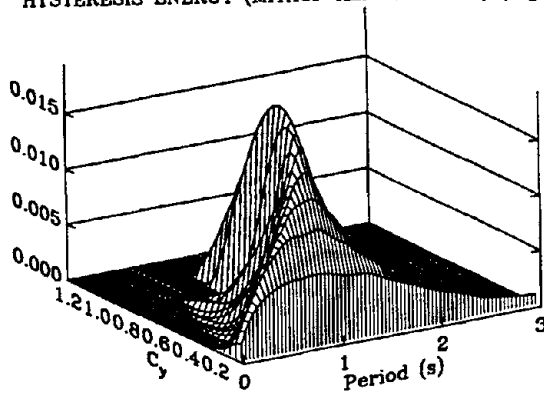
(g)

HYSTERESIS ENERGY (LANDERS 1992) (mg^2s^2)



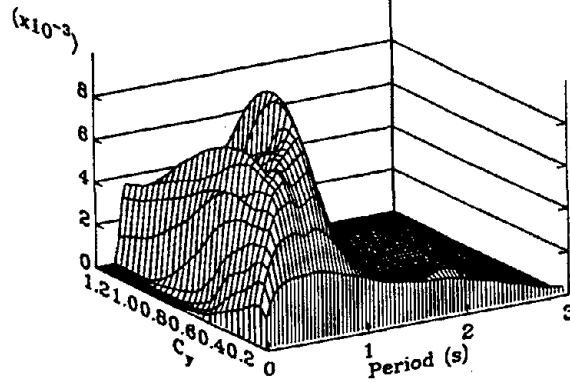
(h)

HYSTERESIS ENERGY (MIYAGI-KEN-OKI 1978) (mg^2s^2)



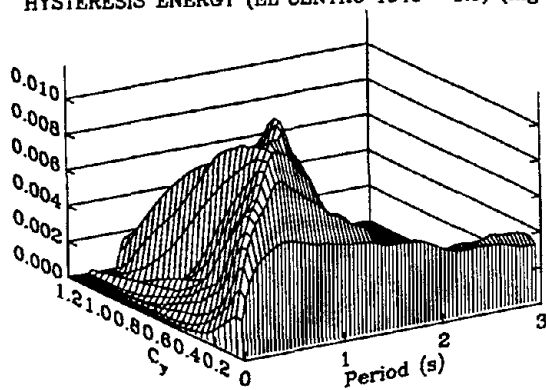
(i)

HYSTERESIS ENERGY (LOMA PRIETA 1989) (mg^2s^2)



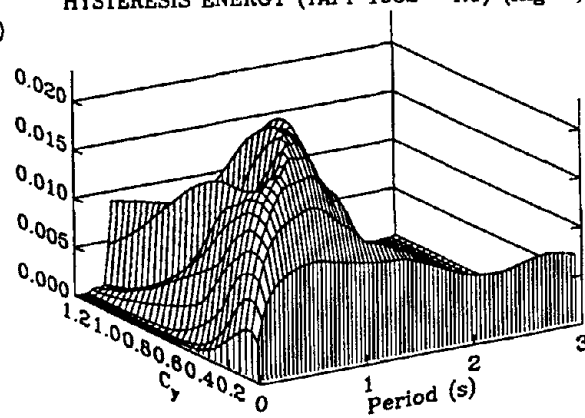
(j)

HYSTERESIS ENERGY (EL CENTRO 1940 * 1.5) (mg^2s^2)



(k)

HYSTERESIS ENERGY (TAFT 1952 * 4.0) (mg^2s^2)



(l)

EARTHQUAKE ENGINEERING RESEARCH CENTER REPORT SERIES

EERC reports are available from the National Information Service for Earthquake Engineering (NISEE) and from the National Technical Information Service (NTIS). Numbers in parentheses are Accession Numbers assigned by the National Technical Information Service; these are followed by a price code. Contact NTIS, 5285 Port Royal Road, Springfield Virginia, 22161 for more information. Reports without Accession Numbers were not available from NTIS at the time of printing. For a current complete list of EERC reports (from EERC 67-1) and availability information, please contact University of California, EERC, NISEE, 1301 South 46th Street, Richmond, California 94804-4698.

- UCB/EERC-84/01 "Pseudodynamic Test Method for Seismic Performance Evaluation: Theory and Implementation," by Shing, P.-S.B. and Mahin, S.A., January 1984, (PB84 190 644)A08.
- UCB/EERC-84/02 "Dynamic Response Behavior of Kiang Hong Dian Dam," by Clough, R.W., Chang, K.-T., Chen, H.-Q. and Stephen, R.M., April 1984, (PB84 209 402)A08.
- UCB/EERC-84/03 "Refined Modelling of Reinforced Concrete Columns for Seismic Analysis," by Kaba, S.A. and Mahin, S.A., April 1984, (PB84 234 384)A06.
- UCB/EERC-84/04 "A New Floor Response Spectrum Method for Seismic Analysis of Multiply Supported Secondary Systems," by Asfura, A. and Der Kiureghian, A., June 1984, (PB84 239 417)A06.
- UCB/EERC-84/05 "Earthquake Simulation Tests and Associated Studies of a 1/5th-scale Model of a 7-Story R/C Frame-Wall Test Structure," by Bertero, V.V., Aktan, A.E., Charney, F.A. and Sause, R., June 1984, (PB84 239 409)A09.
- UCB/EERC-84/06 "Unassigned," by Unassigned, 1984.
- UCB/EERC-84/07 "Behavior of Interior and Exterior Flat-Plate Connections Subjected to Inelastic Load Reversals," by Zee, H.L. and Moehle, J.P., August 1984, (PB86 117 629/AS)A07.
- UCB/EERC-84/08 "Experimental Study of the Seismic Behavior of a Two-Story Flat-Plate Structure," by Moehle, J.P. and Diebold, J.W., August 1984, (PB86 122 553/AS)A12.
- UCB/EERC-84/09 "Phenomenological Modeling of Steel Braces under Cyclic Loading," by Ikeda, K., Mahin, S.A. and Dermitzakis, S.N., May 1984, (PB86 132 198/AS)A08.
- UCB/EERC-84/10 "Earthquake Analysis and Response of Concrete Gravity Dams," by Fenves, G.L. and Chopra, A.K., August 1984, (PB85 193 902/AS)A11.
- UCB/EERC-84/11 "EAGD-84: A Computer Program for Earthquake Analysis of Concrete Gravity Dams," by Fenves, G.L. and Chopra, A.K., August 1984, (PB85 193 613/AS)A05.
- UCB/EERC-84/12 "A Refined Physical Theory Model for Predicting the Seismic Behavior of Braced Steel Frames," by Ikeda, K. and Mahin, S.A., July 1984, (PB85 191 450/AS)A09.
- UCB/EERC-84/13 "Earthquake Engineering Research at Berkeley - 1984," by EERC, August 1984, (PB85 197 341/AS)A10.
- UCB/EERC-84/14 "Moduli and Damping Factors for Dynamic Analyses of Cohesionless Soils," by Seed, H.B., Wong, R.T., Idriss, I.M. and Tokimatsu, K., September 1984, (PB85 191 468/AS)A04.
- UCB/EERC-84/15 "The Influence of SPT Procedures in Soil Liquefaction Resistance Evaluations," by Seed, H.B., Tokimatsu, K., Harder, L.F. and Chung, R.M., October 1984, (PB85 191 732/AS)A04.
- UCB/EERC-84/16 "Simplified Procedures for the Evaluation of Settlements in Sands Due to Earthquake Shaking," by Tokimatsu, K. and Seed, H.B., October 1984, (PB85 197 887/AS)A03.
- UCB/EERC-84/17 "Evaluation of Energy Absorption Characteristics of Highway Bridges Under Seismic Conditions - Volume I (PB90 262 627)A16 and Volume II (Appendices) (PB90 262 635)A13," by Imbsen, R.A. and Penzien, J., September 1986.
- UCB/EERC-84/18 "Structure-Foundation Interactions under Dynamic Loads," by Liu, W.D. and Penzien, J., November 1984, (PB87 124 889/AS)A11.
- UCB/EERC-84/19 "Seismic Modelling of Deep Foundations," by Chen, C.-H. and Penzien, J., November 1984, (PB87 124 798/AS)A07.
- UCB/EERC-84/20 "Dynamic Response Behavior of Quan Shui Dam," by Clough, R.W., Chang, K.-T., Chen, H.-Q., Stephen, R.M., Ghanaat, Y. and Qi, J.-H., November 1984, (PB86 115177/AS)A07.
- UCB/EERC-85/01 "Simplified Methods of Analysis for Earthquake Resistant Design of Buildings," by Cruz, E.F. and Chopra, A.K., February 1985, (PB86 112299/AS)A12.
- UCB/EERC-85/02 "Estimation of Seismic Wave Coherency and Rupture Velocity using the SMART 1 Strong-Motion Array Recordings," by Abrahamson, N.A., March 1985, (PB86 214 343)A07.
- UCB/EERC-85/03 "Dynamic Properties of a Thirty Story Condominium Tower Building," by Stephen, R.M., Wilson, E.L. and Stander, N., April 1985, (PB86 118965/AS)A06.
- UCB/EERC-85/04 "Development of Substructuring Techniques for On-Line Computer Controlled Seismic Performance Testing," by Dermitzakis, S. and Mahin, S., February 1985, (PB86 132941/AS)A08.
- UCB/EERC-85/05 "A Simple Model for Reinforcing Bar Anchorages under Cyclic Excitations," by Filippou, F.C., March 1985, (PB86 112 919/AS)A05.
- UCB/EERC-85/06 "Racking Behavior of Wood-framed Gypsum Panels under Dynamic Load," by Oliva, M.G., June 1985, (PB90 262 643)A04.

- UCB/EERC-85/07 "Earthquake Analysis and Response of Concrete Arch Dams," by Fok, K.-L. and Chopra, A.K., June 1985, (PB86 139672/AS)A10.
- UCB/EERC-85/08 "Effect of Inelastic Behavior on the Analysis and Design of Earthquake Resistant Structures," by Lin, J.P. and Mahin, S.A., June 1985, (PB86 135340/AS)A08.
- UCB/EERC-85/09 "Earthquake Simulator Testing of a Base-Isolated Bridge Deck," by Kelly, J.M., Buckle, I.G. and Tsai, H.-C., January 1986, (PB87 124 152/AS)A06.
- UCB/EERC-85/10 "Simplified Analysis for Earthquake Resistant Design of Concrete Gravity Dams," by Fenves, G.L. and Chopra, A.K., June 1986, (PB87 124 160/AS)A08.
- UCB/EERC-85/11 "Dynamic Interaction Effects in Arch Dams," by Clough, R.W., Chang, K.-T., Chen, H.-Q. and Ghanaat, Y., October 1985, (PB86 135027/AS)A05.
- UCB/EERC-85/12 "Dynamic Response of Long Valley Dam in the Mammoth Lake Earthquake Series of May 25-27, 1980," by Lai, S. and Seed, H.B., November 1985, (PB86 142304/AS)A05.
- UCB/EERC-85/13 "A Methodology for Computer-Aided Design of Earthquake-Resistant Steel Structures," by Austin, M.A., Pister, K.S. and Mahin, S.A., December 1985, (PB86 159480/AS)A10 .
- UCB/EERC-85/14 "Response of Tension-Leg Platforms to Vertical Seismic Excitations," by Liou, G.-S., Penzien, J. and Yeung, R.W., December 1985, (PB87 124 871/AS)A08.
- UCB/EERC-85/15 "Cyclic Loading Tests of Masonry Single Piers: Volume 4 - Additional Tests with Height to Width Ratio of 1," by Sveinsson, B., McNiven, H.D. and Sucuoglu, H., December 1985, (PB87 165031/AS)A08.
- UCB/EERC-85/16 "An Experimental Program for Studying the Dynamic Response of a Steel Frame with a Variety of Infill Partitions," by Yanev, B. and McNiven, H.D., December 1985, (PB90 262 676)A05.
- UCB/EERC-86/01 "A Study of Seismically Resistant Eccentrically Braced Steel Frame Systems," by Kasai, K. and Popov, E.P., January 1986, (PB87 124 178/AS)A14.
- UCB/EERC-86/02 "Design Problems in Soil Liquefaction," by Seed, H.B., February 1986, (PB87 124 186/AS)A03.
- UCB/EERC-86/03 "Implications of Recent Earthquakes and Research on Earthquake-Resistant Design and Construction of Buildings," by Bertero, V.V., March 1986, (PB87 124 194/AS)A05.
- UCB/EERC-86/04 "The Use of Load Dependent Vectors for Dynamic and Earthquake Analyses," by Leger, P., Wilson, E.L. and Clough, R.W., March 1986, (PB87 124 202/AS)A12.
- UCB/EERC-86/05 "Two Beam-To-Column Web Connections," by Tsai, K.-C. and Popov, E.P., April 1986, (PB87 124 301/AS)A04.
- UCB/EERC-86/06 "Determination of Penetration Resistance for Coarse-Grained Soils using the Becker Hammer Drill," by Harder, L.F. and Seed, H.B., May 1986, (PB87 124 210/AS)A07.
- UCB/EERC-86/07 "A Mathematical Model for Predicting the Nonlinear Response of Unreinforced Masonry Walls to In-Plane Earthquake Excitations," by Mengi, Y. and McNiven, H.D., May 1986, (PB87 124 780/AS)A06.
- UCB/EERC-86/08 "The 19 September 1985 Mexico Earthquake: Building Behavior," by Bertero, V.V., July 1986.
- UCB/EERC-86/09 "EACD-3D: A Computer Program for Three-Dimensional Earthquake Analysis of Concrete Dams," by Fok, K.-L., Hall, J.F. and Chopra, A.K., July 1986, (PB87 124 228/AS)A08.
- UCB/EERC-86/10 "Earthquake Simulation Tests and Associated Studies of a 0.3-Scale Model of a Six-Story Concentrically Braced Steel Structure," by Uang, C.-M. and Bertero, V.V., December 1986, (PB87 163 564/AS)A17.
- UCB/EERC-86/11 "Mechanical Characteristics of Base Isolation Bearings for a Bridge Deck Model Test," by Kelly, J.M., Buckle, I.G. and Koh, C.-G., November 1987, (PB90 262 668)A04.
- UCB/EERC-86/12 "Effects of Axial Load on Elastomeric Isolation Bearings," by Koh, C.-G. and Kelly, J.M., November 1987, PB88-179015(A06).
- UCB/EERC-87/01 "The FPS Earthquake Resisting System: Experimental Report," by Zayas, V.A., Low, S.S. and Mahin, S.A., June 1987, (PB88 170 287)A06.
- UCB/EERC-87/02 "Earthquake Simulator Tests and Associated Studies of a 0.3-Scale Model of a Six-Story Eccentrically Braced Steel Structure," by Whittaker, A., Uang, C.-M. and Bertero, V.V., July 1987, (PB88 166 707/AS)A18.
- UCB/EERC-87/03 "A Displacement Control and Uplift Restraint Device for Base-Isolated Structures," by Kelly, J.M., Griffith, M.C. and Aiken, I.D., April 1987, (PB88 169 933)A04.
- UCB/EERC-87/04 "Earthquake Simulator Testing of a Combined Sliding Bearing and Rubber Bearing Isolation System," by Kelly, J.M. and Chalhoub, M.S., December 1990, PB92-192962(A09).
- UCB/EERC-87/05 "Three-Dimensional Inelastic Analysis of Reinforced Concrete Frame-Wall Structures," by Moazzami, S. and Bertero, V.V., May 1987, (PB88 169 586/AS)A08.
- UCB/EERC-87/06 "Experiments on Eccentrically Braced Frames with Composite Floors," by Ricles, J. and Popov, E., June 1987, (PB88 173 067/AS)A14.
- UCB/EERC-87/07 "Dynamic Analysis of Seismically Resistant Eccentrically Braced Frames," by Ricles, J. and Popov, E., June 1987, (PB88 173 075/AS)A16.
- UCB/EERC-87/08 "Undrained Cyclic Triaxial Testing of Gravels-The Effect of Membrane Compliance," by Evans, M.D. and Seed, H.B., July 1987, (PB88 173 257)A19.

- UCB/EERC-87/09 "Hybrid Solution Techniques for Generalized Pseudo-Dynamic Testing," by Thewalt, C. and Mahin, S.A., July 1987, (PB 88 179 007)A07.
- UCB/EERC-87/10 "Ultimate Behavior of Butt Welded Splices in Heavy Rolled Steel Sections," by Bruneau, M., Mahin, S.A. and Popov, E.P., September 1987, (PB90 254 285)A07.
- UCB/EERC-87/11 "Residual Strength of Sand from Dam Failures in the Chilean Earthquake of March 3, 1985," by De Alba, P., Seed, H.B., Retamal, E. and Seed, R.B., September 1987, (PB88 174 321/AS)A03.
- UCB/EERC-87/12 "Inelastic Seismic Response of Structures with Mass or Stiffness Eccentricities in Plan," by Bruneau, M. and Mahin, S.A., September 1987, (PB90 262 650/AS)A14.
- UCB/EERC-87/13 "CSTRUCT: An Interactive Computer Environment for the Design and Analysis of Earthquake Resistant Steel Structures," by Austin, M.A., Mahin, S.A. and Pister, K.S., September 1987, (PB88 173 339/AS)A06.
- UCB/EERC-87/14 "Experimental Study of Reinforced Concrete Columns Subjected to Multi-Axial Loading," by Low, S.S. and Moehle, J.P., September 1987, (PB88 174 347/AS)A07.
- UCB/EERC-87/15 "Relationships between Soil Conditions and Earthquake Ground Motions in Mexico City in the Earthquake of Sept. 19, 1985," by Seed, H.B., Romo, M.P., Sun, J., Jaime, A. and Lysmer, J., October 1987, (PB88 178 991)A06.
- UCB/EERC-87/16 "Experimental Study of Seismic Response of R. C. Setback Buildings," by Shahrooz, B.M. and Moehle, J.P., October 1987, (PB88 176 359)A16.
- UCB/EERC-87/17 "The Effect of Slabs on the Flexural Behavior of Beams," by Pantazopoulou, S.J. and Moehle, J.P., October 1987, (PB90 262 700)A07.
- UCB/EERC-87/18 "Design Procedure for R-FBI Bearings," by Mostaghel, N. and Kelly, J.M., November 1987, (PB90 262 718)A04.
- UCB/EERC-87/19 "Analytical Models for Predicting the Lateral Response of R C Shear Walls: Evaluation of their Reliability," by Vulcano, A. and Bertero, V.V., November 1987, (PB88 178 983)A05.
- UCB/EERC-87/20 "Earthquake Response of Torsionally-Coupled Buildings," by Hejal, R. and Chopra, A.K., December 1987, PB90-208638(A15).
- UCB/EERC-87/21 "Dynamic Reservoir Interaction with Monticello Dam," by Clough, R.W., Ghanaat, Y. and Qiu, X-F., December 1987, (PB88 179 023)A07.
- UCB/EERC-87/22 "Strength Evaluation of Coarse-Grained Soils," by Siddiqi, F.H., Seed, R.B., Chan, C.K., Seed, H.B. and Pyke, R.M., December 1987, (PB88 179 031)A04.
- UCB/EERC-88/01 "Seismic Behavior of Concentrically Braced Steel Frames," by Khatib, I., Mahin, S.A. and Pister, K.S., January 1988, (PB91 210 898/AS)A11.
- UCB/EERC-88/02 "Experimental Evaluation of Seismic Isolation of Medium-Rise Structures Subject to Uplift," by Griffith, M.C., Kelly, J.M., Coveney, V.A. and Koh, C.G., January 1988, (PB91 217 950/AS)A09.
- UCB/EERC-88/03 "Cyclic Behavior of Steel Double Angle Connections," by Astaneh-Asl, A. and Nader, M.N., January 1988, (PB91 210 872)A05.
- UCB/EERC-88/04 "Re-evaluation of the Slide in the Lower San Fernando Dam in the Earthquake of Feb. 9, 1971," by Seed, H.B., Seed, R.B., Harder, L.F. and Jong, H.-L., April 1988, (PB91 212 456/AS)A07.
- UCB/EERC-88/05 "Experimental Evaluation of Seismic Isolation of a Nine-Story Braced Steel Frame Subject to Uplift," by Griffith, M.C., Kelly, J.M. and Aiken, I.D., May 1988, (PB91 217 968/AS)A07.
- UCB/EERC-88/06 "DRAIN-2DX User Guide.," by Allahabadi, R. and Powell, G.H., March 1988, (PB91 212 530)A12.
- UCB/EERC-88/07 "Theoretical and Experimental Studies of Cylindrical Water Tanks in Base-Isolated Structures," by Chalhoub, M.S. and Kelly, J.M., April 1988, (PB91 217 976/AS)A05.
- UCB/EERC-88/08 "Analysis of Near-Source Waves: Separation of Wave Types Using Strong Motion Array Recording," by Darragh, R.B., June 1988, (PB91 212 621)A08.
- UCB/EERC-88/09 "Alternatives to Standard Mode Superposition for Analysis of Non-Classically Damped Systems," by Kusainov, A.A. and Clough, R.W., June 1988, (PB91 217 992/AS)A04.
- UCB/EERC-88/10 "The Landslide at the Port of Nice on October 16, 1979," by Seed, H.B., Seed, R.B., Schlosser, F., Blondeau, F. and Juran, I., June 1988, (PB91 210 914)A05.
- UCB/EERC-88/11 "Liquefaction Potential of Sand Deposits Under Low Levels of Excitation," by Carter, D.P. and Seed, H.B., August 1988, (PB91 210 880)A15.
- UCB/EERC-88/12 "Nonlinear Analysis of Reinforced Concrete Frames Under Cyclic Load Reversals," by Filippou, F.C. and Issa, A., September 1988, (PB91 212 589)A07.
- UCB/EERC-88/13 "Implications of Recorded Earthquake Ground Motions on Seismic Design of Building Structures," by Uang, C.-M. and Bertero, V.V., November 1988, (PB91 212 548)A06.
- UCB/EERC-88/14 "An Experimental Study of the Behavior of Dual Steel Systems," by Whittaker, A.S., Uang, C.-M. and Bertero, V.V., September 1988, (PB91 212 712)A16.
- UCB/EERC-88/15 "Dynamic Moduli and Damping Ratios for Cohesive Soils," by Sun, J.I., Goleorkhi, R. and Seed, H.B., August 1988, (PB91 210 922)A04.

- UCB/EERC-88/16 "Reinforced Concrete Flat Plates Under Lateral Load: An Experimental Study Including Biaxial Effects," by Pan, A. and Moehle, J.P., October 1988, (PB91 210 856)A13.
- UCB/EERC-88/17 "Earthquake Engineering Research at Berkeley - 1988," by EERC, November 1988, (PB91 210 864)A10.
- UCB/EERC-88/18 "Use of Energy as a Design Criterion in Earthquake-Resistant Design," by Uang, C.-M. and Bertero, V.V., November 1988, (PB91 210 906/AS)A04.
- UCB/EERC-88/19 "Steel Beam-Column Joints in Seismic Moment Resisting Frames," by Tsai, K.-C. and Popov, E.P., November 1988, (PB91 217 984/AS)A20.
- UCB/EERC-88/20 "Base Isolation in Japan, 1988," by Kelly, J.M., December 1988, (PB91 212 449)A05.
- UCB/EERC-89/01 "Behavior of Long Links in Eccentrically Braced Frames," by Engelhardt, M.D. and Popov, E.P., January 1989, (PB92 143 056)A18.
- UCB/EERC-89/02 "Earthquake Simulator Testing of Steel Plate Added Damping and Stiffness Elements," by Whittaker, A., Bertero, V.V., Alonso, J. and Thompson, C., January 1989, (PB91 229 252/AS)A10.
- UCB/EERC-89/03 "Implications of Site Effects in the Mexico City Earthquake of Sept. 19, 1985 for Earthquake-Resistant Design Criteria in the San Francisco Bay Area of California," by Seed, H.B. and Sun, J.I., March 1989, (PB91 229 369/AS)A07.
- UCB/EERC-89/04 "Earthquake Analysis and Response of Intake-Outlet Towers," by Goyal, A. and Chopra, A.K., July 1989, (PB91 229 286/AS)A19.
- UCB/EERC-89/05 "The 1985 Chile Earthquake: An Evaluation of Structural Requirements for Bearing Wall Buildings," by Wallace, J.W. and Moehle, J.P., July 1989, (PB91 218 008/AS)A13.
- UCB/EERC-89/06 "Effects of Spatial Variation of Ground Motions on Large Multiply-Supported Structures," by Hao, H., July 1989, (PB91 229 161/AS)A08.
- UCB/EERC-89/07 "EADAP - Enhanced Arch Dam Analysis Program: Users's Manual," by Ghanaat, Y. and Clough, R.W., August 1989, (PB91 212 522)A06.
- UCB/EERC-89/08 "Seismic Performance of Steel Moment Frames Plastically Designed by Least Squares Stress Fields," by Ohi, K. and Mahin, S.A., August 1989, (PB91 212 597)A05.
- UCB/EERC-89/09 "Feasibility and Performance Studies on Improving the Earthquake Resistance of New and Existing Buildings Using the Friction Pendulum System," by Zayas, V., Low, S., Mahin, S.A. and Bozzo, L., July 1989, (PB92 143 064)A14.
- UCB/EERC-89/10 "Measurement and Elimination of Membrane Compliance Effects in Undrained Triaxial Testing," by Nicholson, P.G., Seed, R.B. and Anwar, H., September 1989, (PB92 139 641/AS)A13.
- UCB/EERC-89/11 "Static Tilt Behavior of Unanchored Cylindrical Tanks," by Lau, D.T. and Clough, R.W., September 1989, (PB92 143 049)A10.
- UCB/EERC-89/12 "ADAP-88: A Computer Program for Nonlinear Earthquake Analysis of Concrete Arch Dams," by Fenves, G.L., Mojtahedi, S. and Reimer, R.B., September 1989, (PB92 139 674/AS)A07.
- UCB/EERC-89/13 "Mechanics of Low Shape Factor Elastomeric Seismic Isolation Bearings," by Aiken, I.D., Kelly, J.M. and Tajirian, F.F., November 1989, (PB92 139 732/AS)A09.
- UCB/EERC-89/14 "Preliminary Report on the Seismological and Engineering Aspects of the October 17, 1989 Santa Cruz (Loma Prieta) Earthquake," by EERC, October 1989, (PB92 139 682/AS)A04.
- UCB/EERC-89/15 "Experimental Studies of a Single Story Steel Structure Tested with Fixed, Semi-Rigid and Flexible Connections," by Nader, M.N. and Astaneh-Asl, A., August 1989, (PB91 229 211/AS)A10.
- UCB/EERC-89/16 "Collapse of the Cypress Street Viaduct as a Result of the Loma Prieta Earthquake," by Nims, D.K., Miranda, E., Aiken, I.D., Whittaker, A.S. and Bertero, V.V., November 1989, (PB91 217 935/AS)A05.
- UCB/EERC-90/01 "Mechanics of High-Shape Factor Elastomeric Seismic Isolation Bearings," by Kelly, J.M., Aiken, I.D. and Tajirian, F.F., March 1990.
- UCB/EERC-90/02 "Javid's Paradox: The Influence of Preform on the Modes of Vibrating Beams," by Kelly, J.M., Sackman, J.L. and Javid, A., May 1990, (PB91 217 943/AS)A03.
- UCB/EERC-90/03 "Earthquake Simulator Testing and Analytical Studies of Two Energy-Absorbing Systems for Multistory Structures," by Aiken, I.D. and Kelly, J.M., October 1990, (PB92 192 988)A13.
- UCB/EERC-90/04 "Unassigned," by Unassigned, 1990.
- UCB/EERC-90/05 "Preliminary Report on the Principal Geotechnical Aspects of the October 17, 1989 Loma Prieta Earthquake," by Seed, R.B., Dickenson, S.E., Riemer, M.F., Bray, J.D., Sitar, N., Mitchell, J.K., Idriss, I.M., Kayen, R.E., Kropp, A., Harder, L.F., Jr. and Power, M.S., April 1990, (PB 192 970)A08.
- UCB/EERC-90/06 "Models of Critical Regions in Reinforced Concrete Frames Under Seismic Excitations," by Zulficar, N. and Filippou, F.C., May 1990.
- UCB/EERC-90/07 "A Unified Earthquake-Resistant Design Method for Steel Frames Using ARMA Models," by Takewaki, I., Conte, J.P., Mahin, S.A. and Pister, K.S., June 1990, PB92-192947(A06).
- UCB/EERC-90/08 "Soil Conditions and Earthquake Hazard Mitigation in the Marina District of San Francisco," by Mitchell, J.K., Masood, T., Kayen, R.E. and Seed, R.B., May 1990, (PB 193 267/AS)A04.

- UCB/EERC-90/09 "Influence of the Earthquake Ground Motion Process and Structural Properties on Response Characteristics of Simple Structures," by Conte, J.P., Pister, K.S. and Mahin, S.A., July 1990, (PB92 143 064)A15.
- UCB/EERC-90/10 "Experimental Testing of the Resilient-Friction Base Isolation System," by Clark, P.W. and Kelly, J.M., July 1990, (PB92 143 072)A08.
- UCB/EERC-90/11 "Seismic Hazard Analysis: Improved Models, Uncertainties and Sensitivities," by Araya, R. and Der Kiureghian, A., March 1988, PB92-193010(A08).
- UCB/EERC-90/12 "Effects of Torsion on the Linear and Nonlinear Seismic Response of Structures," by Sedarat, H. and Bertero, V.V., September 1989, (PB92 193 002/AS)A15.
- UCB/EERC-90/13 "The Effects of Tectonic Movements on Stresses and Deformations in Earth Embankments," by Bray, J. D., Seed, R. B. and Seed, H. B., September 1989, PB92-192996(A18).
- UCB/EERC-90/14 "Inelastic Seismic Response of One-Story, Asymmetric-Plan Systems," by Goel, R.K. and Chopra, A.K., October 1990. (PB93 114 767)A11.
- UCB/EERC-90/15 "Dynamic Crack Propagation: A Model for Near-Field Ground Motion.," by Seyyedian, H. and Kelly, J.M., 1990.
- UCB/EERC-90/16 "Sensitivity of Long-Period Response Spectra to System Initial Conditions," by Blasquez, R., Ventura, C. and Kelly, J.M., 1990.
- UCB/EERC-90/17 "Behavior of Peak Values and Spectral Ordinates of Near-Source Strong Ground-Motion over a Dense Array," by Niazi, M., June 1990, (PB93 114 833)A07.
- UCB/EERC-90/18 "Material Characterization of Elastomers used in Earthquake Base Isolation," by Papoulia, K.D. and Kelly, J.M., 1990, PB94-190063(A08).
- UCB/EERC-90/19 "Cyclic Behavior of Steel Top-and-Bottom Plate Moment Connections," by Harriott, J.D. and Astaneh-Asl, A., August 1990, (PB91 229 260/AS)A05.
- UCB/EERC-90/20 "Seismic Response Evaluation of an Instrumented Six Story Steel Building," by Shen, J.-H. and Astaneh-Asl, A., December 1990, (PB91 229 294/AS)A04.
- UCB/EERC-90/21 "Observations and Implications of Tests on the Cypress Street Viaduct Test Structure," by Bollo, M., Mahin, S.A., Moehle, J.P., Stephen, R.M. and Qi, X., December 1990, (PB93 114 775)A13.
- UCB/EERC-91/01 "Experimental Evaluation of Nitinol for Energy Dissipation in Structures," by Nims, D.K., Sasaki, K.K. and Kelly, J.M., 1991.
- UCB/EERC-91/02 "Displacement Design Approach for Reinforced Concrete Structures Subjected to Earthquakes," by Qi, X. and Moehle, J.P., January 1991, (PB93 114 569/AS)A09.
- UCB/EERC-91/03 "A Long-Period Isolation System Using Low-Modulus High-Damping Isolators for Nuclear Facilities at Soft-Soil Sites," by Kelly, J.M., March 1991, (PB93 114 577/AS)A10.
- UCB/EERC-91/04 "Dynamic and Failure Characteristics of Bridgestone Isolation Bearings," by Kelly, J.M., April 1991, (PB93 114 528)A05.
- UCB/EERC-91/05 "Base Sliding Response of Concrete Gravity Dams to Earthquakes," by Chopra, A.K. and Zhang, L., May 1991, (PB93 114 544/AS)A05.
- UCB/EERC-91/06 "Computation of Spatially Varying Ground Motion and Foundation-Rock Impedance Matrices for Seismic Analysis of Arch Dams," by Zhang, L. and Chopra, A.K., May 1991, (PB93 114 825)A07.
- UCB/EERC-91/07 "Estimation of Seismic Source Processes Using Strong Motion Array Data," by Chiou, S.-J., July 1991, (PB93 114 551/AS)A08.
- UCB/EERC-91/08 "A Response Spectrum Method for Multiple-Support Seismic Excitations," by Der Kiureghian, A. and Neuenhofer, A., August 1991, (PB93 114 536)A04.
- UCB/EERC-91/09 "A Preliminary Study on Energy Dissipating Cladding-to-Frame Connection," by Cohen, J.M. and Powell, G.H., September 1991, (PB93 114 510)A05.
- UCB/EERC-91/10 "Evaluation of Seismic Performance of a Ten-Story RC Building During the Whittier Narrows Earthquake," by Miranda, E. and Bertero, V.V., October 1991, (PB93 114 783)A06.
- UCB/EERC-91/11 "Seismic Performance of an Instrumented Six-Story Steel Building," by Anderson, J.C. and Bertero, V.V., November 1991, (PB93 114 809)A07.
- UCB/EERC-91/12 "Performance of Improved Ground During the Loma Prieta Earthquake," by Mitchell, J.K. and Wentz, Jr., F.J., October 1991, (PB93 114 791)A06.
- UCB/EERC-91/13 "Shaking Table - Structure Interaction," by Rinawi, A.M. and Clough, R.W., October 1991, (PB93 114 917)A13.
- UCB/EERC-91/14 "Cyclic Response of RC Beam-Column Knee Joints: Test and Retrofit," by Mazzoni, S., Moehle, J.P. and Thewalt, C.R., October 1991, (PB93 120 277)A03.
- UCB/EERC-91/15 "Design Guidelines for Ductility and Drift Limits: Review of State-of-the-Practice and State-of-the-Art in Ductility and Drift-Based Earthquake-Resistant Design of Buildings," by Bertero, V.V., Anderson, J.C., Krawinkler, H., Miranda, E. and The CUREe and The Kajima Research Teams, July 1991, (PB93 120 269)A08.
- UCB/EERC-91/16 "Evaluation of the Seismic Performance of a Thirty-Story RC Building," by Anderson, J.C., Miranda, E., Bertero, V.V. and The Kajima Project Research Team, July 1991, (PB93 114 841)A12.

- UCB/EERC-91/17 "A Fiber Beam-Column Element for Seismic Response Analysis of Reinforced Concrete Structures," by Taucer, F., Spacone, E. and Filippou, F.C., December 1991, (PB94 117 629AS)A07.
- UCB/EERC-91/18 "Investigation of the Seismic Response of a Lightly-Damped Torsionally-Coupled Building," by Boroschek, R. and Mahin, S.A., December 1991, (PB93 120 335)A13.
- UCB/EERC-92/01 "Studies of a 49-Story Instrumented Steel Structure Shaken During the Loma Prieta Earthquake," by Chen, C.-C., Bonowitz, D. and Astaneh-Asl, A., February 1992, (PB93 221 778)A08.
- UCB/EERC-92/02 "Response of the Dumbarton Bridge in the Loma Prieta Earthquake," by Fenves, G.L., Filippou, F.C. and Sze, D.T., January 1992, (PB93 120 319)A09.
- UCB/EERC-92/03 "Models for Nonlinear Earthquake Analysis of Brick Masonry Buildings," by Mengi, Y., McNiven, H.D. and Tanrikulu, A.K., March 1992, (PB93 120 293)A08.
- UCB/EERC-92/04 "Shear Strength and Deformability of RC Bridge Columns Subjected to Inelastic Cyclic Displacements," by Aschheim, M. and Moehle, J.P., March 1992, (PB93 120 327)A06.
- UCB/EERC-92/05 "Parameter Study of Joint Opening Effects on Earthquake Response of Arch Dams," by Fenves, G.L., Mojtahedi, S. and Reimer, R.B., April 1992, (PB93 120 301)A04.
- UCB/EERC-92/06 "Seismic Behavior and Design of Semi-Rigid Steel Frames," by Nader, M.N. and Astaneh-Asl, A., May 1992, PB93-221760(A17).
- UCB/EERC-92/07 "A Beam Element for Seismic Damage Analysis," by Spacone, E., Ciampi, V. and Filippou, F.C., August 1992, (PB95-192126)A06.
- UCB/EERC-92/08 "Nonlinear Static and Dynamic Analysis of Reinforced Concrete Subassemblages," by Filippou, F.C., D'Ambrisi, A. and Issa, A., August 1992, PB95-192175(A09).
- UCB/EERC-92/09 "Evaluation of Code Accidental-Torsion Provisions Using Earthquake Records from Three Nominally Symmetric-Plan Buildings," by De la Llera, J.C. and Chopra, A.K., September 1992, (PB94 117 611)A08.
- UCB/EERC-92/10 "Slotted Bolted Connection Energy Dissipators," by Grigorian, C.E., Yang, T.-S. and Popov, E.P., July 1992, (PB92 120 285)A03.
- UCB/EERC-92/11 "Mechanical Characteristics of Neoprene Isolation Bearings," by Kelly, J.M. and Quiroz, E., August 1992, (PB93 221 729)A07.
- UCB/EERC-92/12 "Application of a Mass Damping System to Bridge Structures," by Hasegawa, K. and Kelly, J.M., August 1992, (PB93 221 786)A06.
- UCB/EERC-92/13 "Earthquake Engineering Research at Berkeley - 1992," by EERC, October 1992, PB93-223709(A10).
- UCB/EERC-92/14 "Earthquake Risk and Insurance," by Brillinger, D.R., October 1992, (PB93 223 352)A03.
- UCB/EERC-92/15 "A Friction Mass Damper for Vibration Control," by Inaudi, J.A. and Kelly, J.M., October 1992, (PB93 221 745)A04.
- UCB/EERC-92/16 "Tall Reinforced Concrete Buildings: Conceptual Earthquake-Resistant Design Methodology," by Bertero, R.D. and Bertero, V.V., December 1992, (PB93 221 695)A12.
- UCB/EERC-92/17 "Performance of Tall Buildings During the 1985 Mexico Earthquakes," by Terán-Gilmore, A. and Bertero, V.V., December 1992, (PB93 221 737)A11.
- UCB/EERC-92/18 "Dynamic Analysis of Nonlinear Structures using State-Space Formulation and Partitioned Integration Schemes," by Inaudi, J.A. and De la Llera, J.C., December 1992, (PB94 117 702/AS/A05).
- UCB/EERC-93/01 "Seismic Performance of an Instrumented Six-Story Reinforced-Concrete Building," by Anderson, J.C. and Bertero, V.V., 1993.
- UCB/EERC-93/02 "Evaluation of an Active Variable-Damping-Structure," by Polak, E., Meeker, G., Yamada, K. and Kurata, N., 1993, (PB93 221 711)A05.
- UCB/EERC-93/03 "An Experimental Study of Flat-Plate Structures under Vertical and Lateral Loads," by Hwang, S.-H. and Moehle, J.P., February 1993, (PB94 157 690/AS)A13.
- UCB/EERC-93/04 "Seismic Performance of a 30-Story Building Located on Soft Soil and Designed According to UBC 1991," by Terán-Gilmore, A. and Bertero, V.V., 1993, (PB93 221 703)A17.
- UCB/EERC-93/05 "Multiple-Support Response Spectrum Analysis of the Golden Gate Bridge," by Nakamura, Y., Der Kiureghian, A. and Liu, D., May 1993, (PB93 221 752)A05.
- UCB/EERC-93/06 "On the Analysis of Structures with Viscoelastic Dampers," by Inaudi, J.A., Zambrano, A. and Kelly, J.M., August 1993, PB94-165867(A06).
- UCB/EERC-93/07 "Earthquake Analysis and Response of Concrete Gravity Dams Including Base Sliding," by Chávez, J.W. and Fenves, G.L., December 1993, (PB94 157 658/AS)A10.
- UCB/EERC-93/08 "Model for Anchored Reinforcing Bars under Seismic Excitations," by Monti, G., Spacone, E. and Filippou, F.C., December 1993, PB95-192183(A05).
- UCB/EERC-93/09 "A Methodology for Design of Viscoelastic Dampers in Earthquake-Resistant Structures," by Abbas, H. and Kelly, J.M., November 1993, PB94-190071(A10).
- UCB/EERC-93/10 "Tuned Mass Dampers Using Viscoelastic Dampers," by Inaudi, J.A., Lopez-Almansa, F. and Kelly, J.M., December 1993.

- UCB/EERC-93/11 "Nonlinear Homogeneous Dynamical Systems," by Inaudi, J.A. and Kelly, J.M., December 1993.
- UCB/EERC-93/12 "Synthesized Strong Ground Motions for the Seismic Condition Assessment of the Eastern Portion of the San Francisco Bay Bridge," by Bolt, B.A. and Gregor, N.J., December 1993, PB94-165842(A10).
- UCB/EERC-93/13 "On the Analysis of Structures with Energy Dissipating Restraints," by Inaudi, J.A., Nims, D.K. and Kelly, J.M., December 1993, PB94-203619(A07).
- UCB/EERC-94/01 "Preliminary Report on the Seismological and Engineering Aspects of the January 17, 1994 Northridge Earthquake," by EERC, January 1994, (PB94 157 666/AS)A05.
- UCB/EERC-94/02 "Energy Dissipation with Slotted Bolted Connections," by Grigorian, C.E. and Popov, E.P., February 1994, PB94-164605.
- UCB/EERC-94/03 "The Influence of Plate Flexibility on the Buckling Load of Elastomeric Isolators," by Kelly, J.M., March 1994, PB95-192134(A04).
- UCB/EERC-94/04 "Insitu Test Results from Four Loma Prieta Earthquake Liquefaction Sites: SPT, CPT, DMT and Shear Wave Velocity," by Mitchell, J.K., Lodge, A.L., Coutinho, R.Q., Kayen, R.E., Seed, R.B., Nishio, S. and Stokoe II, K.H., April 1994, PB94-190089(A09).
- UCB/EERC-94/05 "Seismic Response of Steep Natural Slopes," by Sitar, N. and Ashford, S.A., May 1994, PB94-203643(A10).
- UCB/EERC-94/06 "Small-Scale Testing of a Self-Centering Friction Energy Dissipator for Structures," by Nims, D.K. and Kelly, J.M., August 1994.
- UCB/EERC-94/07 "Accidental and Natural Torsion in Earthquake Response and Design of Buildings," by De la Llera, J.C. and Chopra, A.K., June 1994, PB94-203627(A14).
- UCB/EERC-94/08 "Preliminary Report on the Principal Geotechnical Aspects of the January 17, 1994 Northridge Earthquake," by Stewart, J.P., Bray, J.D., Seed, R.B. and Sitar, N., June 1994, PB94203635(A12).
- UCB/EERC-94/09 "Performance of Steel Building Structures During the Northridge Earthquake," by Bertero, V.V., Anderson, J.C. and Krawinkler, H., August 1994, PB95-112025(A10).
- UCB/EERC-94/10 "Manual for Menshin Design of Highway Bridges: Ministry of Construction, Japan," by Sugita, H. and Mahin, S., August 1994, PB95-192100(A08).
- UCB/EERC-94/11 "Earthquake Analysis and Response of Two-Level Viaducts," by Singh, S.P. and Fenves, G.L., October 1994, (A09).
- UCB/EERC-94/12 "Response of the Northwest Connector in the Landers and Big Bear Earthquakes," by Fenves, G.L. and Desroches, R., December 1994, PB95-192001(A08).
- UCB/EERC-95/01 "Geotechnical Reconnaissance of the Effects of the January 17, 1995, Hyogoken-Nanbu Earthquake, Japan," by , August 1995.
- UCB/EERC-95/02 "The Attenuation of Strong Ground Motion Displacement," by Gregor, N.J., June 1995.
- UCB/EERC-95/03 "Upgrading Bridge Outrigger Knee Joint Systems," by Stojadinovic, B. and Thewalt, C.R., June 1995.
- UCB/EERC-95/04 "Earthquake Hazard Reduction in Historical Buildings Using Seismic Isolation," by Gacovski, M., June 1995.
- UCB/EERC-95/05 "Final Report on the International Workshop on the Use of Rubber-Based Bearings for the Earthquake Protection of Building," by Kelly, J.M., May 1995.
- UCB/EERC-95/06 "Seismic Rehabilitation of Framed Buildings Infilled with Unreinforced Masonry Walls Using Post-Tensioned Steel Braces," by Terán-Gilmore, A., Bertero, V.V. and Youssef, N., June 1995.
- UCB/EERC-95/07 "Earthquake Analysis and Response of Concrete Arch Dams," by Tan, H. and Chopra, A.K., August 1995.
- UCB/EERC-95/08 "Behavior of Pre-Northridge Moment Resisting Steel Connections," by Yang, T.-S. and Popov, E.P., August 1995.
- UCB/EERC-95/09 "Seismic Behavior and Retrofit of Older Reinforced Concrete Bridge T-Joints," by Lowes, L.N. and Moehle, J.P., September 1995.
- UCB/EERC-95/10 "Seismological and Engineering Aspects of the 1995 Hyogoken-Nanbu (Kobe) Earthquake," by EERC, November 1995.
- UCB/EERC-95/11 "Studies in Steel Moment Resisting Beam-to-Column Connections for Seismic-Resistant Design," by Blackman, B. and Popov, E.P., October 1995.
- UCB/EERC-95/12 "Natural Rubber Isolation Systems for Earthquake Protection of Low-Cost Buildings," by Taniwangsa, W., Clark, P. and Kelly, J.M., December 1995.
- UCB/EERC-95/13 "Analytical and Experimental Studies of Steel Connections and Energy Dissipators," by Yang, T.-S. and Popov, E.P., December 1995.

NTIS does not permit return of items for credit or refund. A replacement will be provided if an error is made in filling your order, if the item was received in damaged condition, or if the item is defective.

Reproduced by NTIS

National Technical Information Service
Springfield, VA 22161

*This report was printed specifically for your order
from nearly 3 million titles available in our collection.*

For economy and efficiency, NTIS does not maintain stock of its vast collection of technical reports. Rather, most documents are printed for each order. Documents that are not in electronic format are reproduced from master archival copies and are the best possible reproductions available. If you have any questions concerning this document or any order you have placed with NTIS, please call our Customer Service Department at (703) 487-4660.

About NTIS

NTIS collects scientific, technical, engineering, and business related information — then organizes, maintains, and disseminates that information in a variety of formats — from microfiche to online services. The NTIS collection of nearly 3 million titles includes reports describing research conducted or sponsored by federal agencies and their contractors; statistical and business information; U.S. military publications; audiovisual products; computer software and electronic databases developed by federal agencies; training tools; and technical reports prepared by research organizations worldwide. Approximately 100,000 *new* titles are added and indexed into the NTIS collection annually.

For more information about NTIS products and services, call NTIS at (703) 487-4650 and request the free *NTIS Catalog of Products and Services*, PR-827LPG, or visit the NTIS Web site
<http://www.ntis.gov>.

NTIS

***Your indispensable resource for government-sponsored
information—U.S. and worldwide***



U.S. DEPARTMENT OF COMMERCE
Technology Administration
National Technical Information Service
Springfield, VA 22161 (703) 487-4650
